

**ENGINEERING A β -TURN MIMETIC TORSION BALANCE
FOR CONFORMATIONAL CONTROL:
DESIGN, SYNTHETIC STRATEGIES AND NMR ANALYSIS**

by

Alyssa B. Lypson, M.S.

B.S. in Biochemistry and Psychology, Allegheny College, 2009

M.S. in Chemistry, University of Pittsburgh, 2018

Submitted to the Graduate Faculty of
The Dietrich School of Arts and Sciences in partial fulfillment
of the requirements for the degree of
Doctor of Philosophy

University of Pittsburgh

2018

UNIVERSITY OF PITTSBURGH
DIETRICH SCHOOL OF ARTS AND SCIENCES

This dissertation was presented

by

Alyssa B. Lypson, M.S.

It was defended on

October 30, 2018

and approved by

Dr. Dennis Curran, Distinguished Service Professor of Chemistry & Bayer Professor,
Department of Chemistry

Dr. Barry Gold, PhD, Professor and Co-Director of Drug Discovery Institute, School of
Pharmacy

Dr. W. Seth Horne, Associate Professor, Department of Chemistry

Committee Chair: Dr. Craig S. Wilcox, Professor, Department of Chemistry; Research
Integrity Officer, Research Conduct & Compliance

Copyright © by Alyssa B. Lypson, M.S.

2018

**ENGINEERING A β -TURN MIMETIC TORSION BALANCE
FOR CONFORMATIONAL CONTROL:
DESIGN, SYNTHETIC STRATEGIES AND NMR ANALYSIS**

Alyssa B. Lypson, Ph.D.

University of Pittsburgh, 2018

The molecular torsion balance concept was applied to a peptide-hybrid balance to accurately investigate the effects of amino acid changes on antiparallel β -sheet configuration and stability for applications in molecular recognition and computational drug design. In this study, we report an engineered design of that balance for improved interchain alignment by introduction of noncovalent steric constraint at the reverse turn. Our design utilizes a restricted N-aryl bond rotation to impose a two-state folded model by incorporating an (*ortho*-tolyl)amide into a locked biaryl system. The turn mimetic nucleates hairpin formation in an antiparallel β -sheet configuration upon attachment of peptide sequences, providing a minimal model system to investigate biologically interesting epitopes. Bromine installation *ortho* to peptide chain attachment sites imposed an additional degree of conformational control for improved thermodynamic stability in the folded conformation. Our design approach, which relied upon Monte Carlo simulations of substituted native chorismate pyruvate lyase (CPL₇₅₋₉₃), is described along with solution-phase and solid-phase synthetic strategies. ¹H and 2D NMR experiments revealed improved interchain alignment to promote hydrogen bond formation in the conformationally controlled synthetic peptidomimetic torsion balance hybrid compared to a control molecule. Line shape analysis of low temperature ¹H NMR data approximated rotational restriction around the aryl ether bond to be 11 kcal/mol at 193 K in CD₂Cl₂. ¹H NMR AND 2D ROESY analyses reveal an improved shape to mimic the ends of an antiparallel β -sheet. Hydrogen

bond formation has been identified between NH amide proton of the upper side chain (proton donor) and glycine acetamide of the lower side chain (proton donor) and glycine acetamide of the lower side chain (proton acceptor). Results confirm bromine substituents impose noncovalent steric constraints *ortho* to the peptide side chains to reduce conformational entropy of the upper peptide chains.

TABLE OF CONTENTS

LIST OF TABLES	XI
LIST OF FIGURES	XIII
LIST OF SCHEMES	XVII
LIST OF ABBREVIATIONS	XIX
1.0 INTRODUCTION.....	1
1.1 PEPTIDE-BASED THERAPEUTICS	2
1.2 THE MOLECULAR TORSION BALANCE AS A MINIMAL MODEL SYSTEM FOR STUDYING PROTEIN FOLDING	3
1.2.1 The Torsion Balance Concept.....	4
1.2.2 First Generation Torsion Balance	6
1.2.2.1 Aryl and alkyl CH- π interactions	7
1.2.2.2 Amide and organic fluorine interactions	9
1.2.3 Second Generation Torsion Balance	10
1.2.3.1 Alkyl CH- π interactions	11
1.2.3.2 Halogen bonding	12
1.2.3.3 Salt bridge stability	13
1.2.3.4 Neighboring group effects in hydrophobic surface association.....	14
1.2.4 Third Generation Torsion Balance: A Novel Peptide Hybrid Torsion Balance	16
2.0 DESIGN AND SYNTHESIS OF A CONFORMATIONALLY CONTROLLED β -TURN MIMETIC TORSION BALANCE	18

2.1	PEPTIDOMIMETICS	19
2.1.1	Conformationally Controlled Hybrid Synthetic Natural Peptides as β -Sheet Mimetics.....	20
2.2	DESIGN STRATEGY OF A CONFORMATIONALLY CONTROLLED β-TURN MIMETIC TORSION BALANCE.....	25
2.2.1	Peptide Structure and Sequence Survey of Antiparallel β -Sheets.....	27
2.2.1.1	Structural analysis of chorismate pyruvate lyase	28
2.2.2	β -Turn Mimetic Template Design	31
2.2.2.1	SUBSTITUTION OF CPL ₇₅₋₉₃ WITH BIARYL (<i>ORTHO</i> -TOLYL)AMIDE-AMINO ACID SUBUNIT	32
2.2.2.2	β -Turn Mimetic Template.....	38
2.3	SYNTHESIS OF A CONFORMATIONALLY CONTROLLED β-TURN MIMETIC TORSION BALANCE CORE.....	39
2.3.1	Asymmetrical Synthesis.....	40
2.3.1.1	Method I	40
2.3.1.2	Method II.....	41
2.3.2	Symmetrical Synthesis.....	43
3.0	EVALUATION AND VALIDATION OF THE WILCOX β-TURN MIMETIC TORSION BALANCE DESIGN	45
3.1	CONFORMATIONAL ANALYSIS OF CORE STRUCTURE	45
3.2	INVESTIGATION OF CONFORMATIONAL CONSTRAIN IN THE DIBROMO TORSION BALANCE	48

3.2.1	Evaluation of Biaryl Benzyloxycarbonyl Diether 58 and Aryl Ether Bond Rotation.....	49
3.2.2	Synthesis and Analysis of Biaryl Isopropyl Diether 71	53
3.2.2.1	Synthesis of biaryl isopropyl diether 71.....	53
3.2.2.2	Analysis of biaryl isopropyl diether 71	54
3.3	CONFORMATIONAL ANALYSIS OF THE DIBROMO β -TURN MIMETIC TORSION BALANCE CORE.....	58
4.0	SYNTHESIS AND NMR STUDIES OF MONOMETHYLAMIDE TARGET 43 AND CONTROL 44.....	61
4.1	RETROSYNTHETIC ANALYSIS OF MONOMETHYLAMIDE TARGET 43 AND CONTROL 44	62
4.2	SYNTHESIS OF MONOMETHYLAMIDE TARGET 43 AND CONTROL 44	62
4.3	NMR ASSIGNMENTS AND COMPARISON OF MONOMETHYLAMIDE TARGET 43 AND CONTROL 44	64
4.4	ANALYSIS OF MONOMETHYLAMIDE TARGET 43.....	71
4.4.1	Folding Preference of Monomethylamide Target 43.....	71
4.4.2	Evaluation of Hydrogen Bond Formation in Monomethylamide Target 43	73
4.5	SUMMARY OF STUDIES OF MONOMETHYL TARGET 43 AND CONTROL 44.....	74
5.0	ADVANCED β -TURN MIMETIC TARGETS 76-78.....	76

5.1	DESIGN AND RETROSYNTHETIC ANALYSIS OF ADVANCED β-TURN MIMETIC TARGETS 76-78	76
5.1.1	Polypeptide Derivatives	76
5.1.2	Zwitterion Derivatives	84
5.2	UPPER SIDE CHAIN PROTECTION STRATEGIES	86
5.2.1	Allyl Protection of Hydroxycarbonyl Ethers	86
5.2.2	Incorporation of Allyloxycarbonyl Ethers	88
5.3	UPPER SIDE CHAIN EXTENSION STRATEGY	90
5.3.1	Initial Evaluation of SPPS Strategy	91
5.3.2	Evaluation of Upper Side Chain Deprotection	93
5.3.3	Evaluation of Allyl Deprotection Conditions Off-Resin	93
5.3.4	Evaluation of Allyl Deprotection Conditions On-Resin	94
5.3.5	Evaluation of Amino Acid Coupling	95
5.3.6	Evaluation of Resin Loading Efficiency	97
5.4	SUMMARY AND CONCLUSION OF PROGRESS TOWARD ADVANCED DERIVATIVES 77-79	99
6.0	ADVANCED β-TURN MIMETIC TARGETS 122-125	101
6.1	DESIGN AND RETROSYNTHETIC ANALYSIS OF ADVANCED β-TURN MIMETIC TARGETS 122-126	101
6.1.1	Polypeptide Derivatives	101
6.2	SYNTHESIS OF BIARYL ACID 140	105
6.2.1	Synthetic Strategies for Extension of Resin Attachment Site	105
6.2.1.1	Incorporation of <i>t</i>-butyloxycarbonyl ester in biaryl acid 103	106

6.2.1.2	Incorporation of <i>t</i> -butyloxycarbonyl ester in 113.....	106
6.2.1.3	Incorporation of allyloxycarbonyl ethers in 130.....	108
6.3	SYNTHESIS OF 141.....	108
6.3.1	Solid-Phase Synthesis.....	108
6.3.2	Resin Loading.....	110
6.3.3	Resin Cleavage	111
6.3.4	Optimization of Resin Loading and Cleavage Steps.....	112
6.3.5	Optimized Synthesis of 141	115
6.4	SYNTHESIS OF SPPS PRECURSOR BIARYL ACID 127.....	117
6.4.1	Synthesis of Acid 113	117
6.4.1.1	Optimization of biaryl methyl ester cleavage.....	118
6.4.2	Incorporation of Lower Peptide Chain.....	119
6.5	SUMMARY OF PROGRESS TOWARD ADVANCED DERIVATIVES 122-	
126	122
7.0	EXPERIMENTAL	123
7.1	GENERAL	123
7.1.1	General information for SPPS protocols	124
7.1.1.1	Purification and Characterization	125
7.1.2	Monte Carlo Simulations and Dynamics	125
7.2	EXPERIMENTAL PROCEDURES.....	126
APPENDIX A	164
APPENDIX B	168
BIBLIOGRAPHY	247

LIST OF TABLES

Table 1. Experimental folding energies for esters 2-3 in CDCl ₃ at 25 °C	8
Table 2. Folding energies for methyl (4), phenyl (5), and isopropyl esters (6) in CDCl ₃ at 25 °C to support an investigation of electrostatic potential of the aromatic face ring and the strength of edge-to-preferentially folded	9
Table 3. Folding energies for torsion balances 12a-f at 25 °C to examine hydrophobic effects in D ₂ O	11
Table 4. Folding energies for esters 13-16 at 5 °C to determine effects of halogenated bond on XH- π	12
Table 5. Folding energies for esters 19-26 at 5 °C to measure nearest neighbor group effects in hydrophobic surfaces	15
Table 6. N-Aryl and aryl amide N-C(O) rotational barriers in 64-67	48
Table 7. Parameters employed for ¹ H NMR simulation of 58	52
Table 8. Aryl C-O rotational barriers in 58 , 70 and 71	58
Table 9. Target 44 and control 43 ¹ H (700 MHz, CD ₂ Cl ₂) assignments and ¹³ C (600 MHz, CD ₂ Cl ₂) assignments	66
Table 10. Resins considered for SPPS.....	81
Table 11. Phenol reactivity test and results of alkylation to form 111	89
Table 12. Results of allyl deprotection to form 102	94
Table 13. Results of solid-state amino acid coupling to upper side chains to form 102	96
Table 14. Results of resin loading to form 111	99

Table 15. Reactivity of biaryl carboxylic acid **113** and results of alkylation to form **130** 107

LIST OF FIGURES

Figure 1. Wilcox molecular torsion balance	5
Figure 2. Tröger's base	6
Figure 3. First generation torsion balances	7
Figure 4. Torsion balance derivatives (7-9) used by Diederich et al. to measure preferential folding amongst $C_{sp^2}-F\cdots C(O)$ and $C_{sp^3}-F\cdots C(O)$ dipole interactions	10
Figure 5. Second generation torsion balance scaffold	11
Figure 6. (a) Ammonium-carboxylate torsion balance 17 and guanidinium-carboxylate 18 used to measure salt bridge stability; (b) Minimized structure modeled using force field MMFF94s	13
Figure 7. Wilcox β -turn mimetic torsion balance	17
Figure 8. Examples of cyclic and acyclic β -turn mimics	23
Figure 9. Kelly's biphenyl-amino acid unit to nucleate β -sheets via a hydrogen-bonded hydrophobic cluster conformation	24
Figure 10. Robinson's cyclic biphenyl amino acid templates as cationic macrocyclic peptidomimetics of PG-1	25
Figure 11. (a) Representation of design requirements for the (b) Wilcox β -turn mimetic torsion balance	27
Figure 12. Chorismate pyruvate lyase-vanillate internal ligand-binding pocket	28
Figure 13. Structural analysis of CPL-vanillate binding site	30
Figure 14. N-aryl and aryl-aryl restricted rotation	32

Figure 15. Chemical structure of a native and mutant CPL ₇₅₋₉₃ β -hairpin for modeling the Wilcox β -turn mimetic torsion balance	33
Figure 16. (a) Native CPL ₇₅₋₉₃ (I); truncated CPL ₇₇₋₉₃ gives CPL ₇₅₋₈₀ and CPL ₈₈₋₉₃ (II); overlay of biaryl (<i>ortho</i> -tolyl)amide-amino acid template to link CPL ₇₅₋₈₀ and CPL ₈₈₋₉₃ (III; IV). (b) Averaged backbone torsion angles benchmarked within the Ramachadran plot.	35
Figure 17. Minimized structures of the β -turn mimetic torsion balance from the top (left) and bottom (right) views of (a) the core scaffold and (b) tetrapeptide CPL derivative.....	36
Figure 18. Conformationally controlled β -turn mimetic torsion balance core targets and control analogs	38
Figure 19. Orthogonal protection sites of conformationally controlled asymmetrical (37) and symmetrical (39) β -turn mimetic torsion balance core scaffolds.....	39
Figure 20. Systems studied to determine folding preferences of the β -turn mimetic torsion balance scaffold.....	46
Figure 21. Conformational analysis of biaryl benzyloxycarbonyl diether 58	50
Figure 22. Simulated and experimental ¹ H NMR data of biaryl benzyloxycarbonyl diether 58 in CD ₂ Cl ₂ (400 MHz) at 183 K.	51
Figure 23. Aryl ether rotational barrier of Yoshimura's silyl ketene acetal 70	53
Figure 24. Conformational analysis of biaryl isopropyl diether 71	55
Figure 25. Experimental (top) and simulated (bottom) ¹ H NMR spectra of biaryl isopropyl diether 71 in CD ₂ Cl ₂ (400 MHz) at 193 K using iNMR.....	57
Figure 26. ¹ H NMR spectra of Gly target 39 in CDCl ₃ (bottom) and CD ₂ Cl ₂ (top) at 298 K on a 700 MHz NMR	59
Figure 27. Two conformers of Gly target 39 by rotation around the aryl amide N-C(O) bond. .	60

Figure 28. Representation of Gly target 44 and control 43 with atom numbering (hydrogen or carbon) for spectroscopic assignment.....	65
Figure 29. ROESY and EXSY (700 MHz, CD ₂ Cl ₂) assignments data for 43	65
Figure 30. Summary of ROESY/EXSY data (left) and ¹ H NMR spectra (right) of gly target 43 and control 44 in CD ₂ Cl ₂ at 298 K for amide proton ¹ H NMR assignment of the major (B) and minor (C) conformers	67
Figure 31. Selected ROESY data of 43 (left) versus 44 (right) in CD ₂ Cl ₂ at 298 K for ¹ H assignment of (a) aryl methyl protons and of (b) upper side chain methylene protons.....	69
Figure 32. CPK models of Gly target 43 and control 44	70
Figure 33. Models of Gly target 43 and control 44	71
Figure 34. ¹ H NMR spectra of 43 (700 MHz) in CDCl ₃ (bottom), CD ₂ Cl ₂ (middle) and C ₇ D ₈ (top) at 298 K.....	72
Figure 35. The effect of temperature on the ¹ H NMR of N-methyl protons in 43 in C ₇ D ₈ from 298 K to 338 K.....	74
Figure 36. Advanced polypeptides of the symmetrical dibromo β -turn mimetic torsion balance for detection of two (75-76) and five (77) interchain hydrogen bonds.	77
Figure 37. GB1 β -turn sequence modification for torsion balance derivatives 78 and 79	78
Figure 38. Zwitterions 97-98 and control amides 99-100 of symmetrical dibromo β -turn mimetic to determine salt bridge effects on rates of N-aryl bond rotation.	85
Figure 39. Beer-Lambert plot of 103 in ACN at $\lambda = 298$ nm.	98
Figure 40. Advanced polypeptides of the symmetrical dibromo β -turn mimetics for detection of two (121-122) and five (124-126) interchain hydrogen bonds.	102
Figure 41. Cleavage sites in resin-bound substrate 142-i	112

Figure 42. Resin coupling reagents for activation of acid 140	113
Figure 43. Analytical HPLC-DAD chromatograms (280 nm) and NMR data (700 MHz, CD ₃ CN) at room temperature of Rink amide resin cleavage experiments.....	115
Figure 44. HPLC chromatogram of alanine 141 (A ₂₈₀) from SPPS protocol in Scheme 28.	116
Figure SI-45. ROESY/EXSY data of alanine 141 in CD ₃ CN (1.0 mM) at 298 K	165
Figure SI-46. ROESY/EXSY data of gly target 44 (left) and control (right) 43 in CD ₂ Cl ₂ (0.1 mM) at 298 K.....	166
Figure SI-47. ESI-MS data for test allyl deprotection	167

LIST OF SCHEMES

Scheme 1. Synthesis toward asymmetrical β -turn mimetic torsion balance 37	40
Scheme 2. Synthesis of the torsion balance biaryl 57	42
Scheme 3. Three conformers of torsion balance 44 and control 43	42
Scheme 4. Successful completion of the symmetrical glycine core 39	44
Scheme 5. Synthesis of biaryl isopropyl diether 71	54
Scheme 6. Retrosynthetic pathway to target 43 and control 44	62
Scheme 7. Synthesis of symmetrical torsion balance derivative 43	63
Scheme 8. Synthetic steps to control 44	63
Scheme 9. Three conformers of gly target 43 and control 44 (enantiomers not shown).	64
Scheme 10. (a) The symmetrical dibromo β -turn mimetic torsion balance scaffold. (b) Retrosynthetic analysis of the torsion balance core Gly target 39	79
Scheme 11. Target SPPS precursor 83	82
Scheme 12. Retrosynthetic analysis of 75-77 using solid- and solution-phase methods.....	83
Scheme 13. Retrosynthetic analysis of zwitterions 97-98 and control amides 59-60	86
Scheme 14. Reaction conditions for upper side chain protection.....	87
Scheme 15. Test reaction conditions for upper side chain protection.....	87
Scheme 16. Synthesis of carboxylic acid 103 for upper side chain protection.....	90
Scheme 17. Test reaction conditions for resin loading	91
Scheme 18. Initial attempt of upper side chain extension using SPPS.....	92
Scheme 19. SPPS test conditions for upper side chain extension.....	95
Scheme 20. Resin loading conditions for biaryl aromatic acid 103 with bromo Wang resin.....	97

Scheme 21. Target SPPS acid precursors 83 and 127 . (a) Initial SPPS strategy using biaryl acid 83 and bromo Wang resin (80b); (b) Alternate SPPS strategy using biaryl acetic acid 127 and Rink amide resin 81	103
Scheme 22. Retrosynthetic analysis of 122-123 using solid- and solution-phase methods.....	104
Scheme 23. Synthetic strategies to <i>t</i> -butyloxycarbonyl ester 129	106
Scheme 24. Synthesis of symmetrical ether 129 and acid 140	108
Scheme 25. Preparation of symmetrical Ala derivative 141	109
Scheme 26. Solid-phase synthesis of amide 142	111
Scheme 27. Control test for formation of resin-linker cleavage product 153	112
Scheme 28. Synthesis of alanine target 141	116
Scheme 29. SPPS precursor 127	117
Scheme 30. Attempted synthetic strategies of acid 154	118
Scheme 31. Improved synthesis of acid 113 enroute to 129	119
Scheme 32. Synthesis toward advanced derivatives 81-85	122

LIST OF ABBREVIATIONS

Ac	Acetyl
ACN	Acetonitrile
Ac ₂ O	Acetic anhydride
Ala	Alanine
Bn	Benzyl
Boc	<i>Tert</i> -butyloxycarbonyl
BOP	(Benzotriazol-1-yloxy)tris(dimethylamino)phosphonium hexafluorophosphate
DBU	1,8-Diazabicyclo[5.4.0]undec-7-ene
DCM	dichloromethane
DIC	<i>N,N'</i> -Diisopropylcarbodiimide
DIEA	<i>N,N'</i> -Diisopropylethylamine
DMF	<i>N,N'</i> -Dimethylformamide
DMS	Dimethylsulfate
DMSO	Dimethyl sulfoxide
EDCI	<i>N</i> -Ethyl- <i>N'</i> -(3-dimethylaminopropyl)carbodiimide hydrochloride
EDT	Ethane dithiol
EI	Electron ionization
equiv	Equivalents
ESI	Electrospray ionization
Et	Ethyl
Fmoc	9-Fluorenylmethyloxycarbonyl
Gly	Glycine
HBTU	<i>N,N,N',N'</i> -Tetramethyl-O-(1H-benzotriazol-1-yl)uronium hexafluorophosphate
HCTU	2-(6-Chloro-1H-benzotriazol-1-yl)- <i>N,N,N',N'</i> -tetramethylaminium hexafluoro-phosphate
HOBt	1-Hydroxybenzotriazole
HPLC	High performance liquid chromatography
HRMS	High resolution mass spectrometry
IR	Infrared spectroscopy
LRMS	Low resolution mass spectrometry
MALDI-TOF	Matrix-assisted laser desorption ionization – time of flight
Me	Methyl
MS	Mass spectrometry
n/d	Not detected
NMP	1-Methyl-2-pyrrolidinone
NMR	Nuclear magnetic resonance
NOESY	Nuclear overhauser effect spectroscopy
Ph	Phenyl
Pd(PPh ₃) ₄	Tetrakis(triphenylphosphine)palladium(0)

Py	Pyridine
PyAOP	7-Azabenzotriazol-1-yloxy)trispyrrolidinophosphonium hexafluorophosphate
PyBOP	(Benzotriazol-1-yloxy)tripyrrolidinophosphonium hexafluorophosphate
Q-TOF	Quadrupole time-of-flight
ROESY	Rotating-frame nuclear overhauses effect correlation spectroscopy
rt	Room temperature
SPhos	2-Dicyclohexylphosphino-2',6'-dimethoxybiphenyl
SPPS	Solid-phase peptide synthesis
TBAF	Tetrabutylammonium fluoride
TBSCl	<i>Tert</i> -butyldimethylsilyl chloride
TFA	Trifluoroacetic acid
THF	Tetrahydrofuran
TIS	Triisopropylsilane
TLC	Thin layer chromatography

ACKNOWLEDGEMENTS

In reflection, it is impossible to fully capture and express my gratitude to all who supported me and impacted my graduate school experience. First and foremost, I am grateful for my advisor, Professor Craig Wilcox; not only has he supported and challenged me, but above all, believed in me. Dr. Wilcox's commitment to rigorous science as well as his mentorship and patience have enabled me to become a better scientist and scientific writer. His diligence, integrity, and selflessness are traits that I hope to keep with me throughout my future endeavors. It is rare in graduate school to find an advisor as supportive and compassionate as Dr. Wilcox, and for that, I am forever grateful.

My committee members - Professor Dennis Curran, Professor Seth Horne and Professor Barry Gold - have also been instrumental to my success in graduate school. Dr. Horne, also my collaborator, has been extremely helpful and accessible in guiding a subproject of this work. In addition to his wealth of scientific wisdom he imparted, I will always remember to consider the "big picture" when I find myself distracted by the details. Without these advisors, I would not be the scientist I am today.

Additional faculty and staff at the University of Pittsburgh have been instrumental to my success. My proposal advisor, Professor Tara Meyer, pushed me to think outside-the-box and believed in me throughout my time at graduate school. Professor Stephen Weber also played a critical role in my graduate school experience. I thank him for all his support and in shaping me into a better teacher, student mentor and scientific communicator, and, for helping me to see the versatility of my education and training. I would also like to thank Professor Toby Chapman, Professor Kay Brummond, Dr. Carol Fortney, and Jay Auses for their support

and encouragement. I am also appreciative to Professor Peter Wipf and Dr. Matthew LaPorte, as well as NMR and MS instrumental facilities personnel for their technical support, including Dr. Damodaran Krishan, Dr. Viswanathan Elumalai, and Dr. Bhaskar Godugu. My gratitude further extends to the Pitt Department of Chemistry for their support and funding as well as to the NIH for funding.

I must also acknowledge my undergraduate chemistry and biochemistry advisors at Allegheny College, Professor Shaun Murphree and Professor Martin Serra. Dr. Murphree was fundamental to my career path in organic chemistry, and I am grateful to him for the impact his scientific zest instilled in me many years ago and still does to this day.

To my past group members and friends in the department: Dr. Nicole Kennedy - a dear friend and colleague – to whom I am forever in-debt to for being my backbone throughout all the ups and downs of graduate school. I could not imagine surviving graduate school without her friendship. I would also like to thank past Wilcox group members for their thoughtful discussions; specifically, Dr. Sandra Keyser for her mentorship. Thank you to Halina Werner of the Horne group for assisting me with SPPS methods. I would also like to acknowledge Kim Kowalis and Megan Breski.

Of course, I must thank my friends outside the Department and my family for their enormous amounts of support. Their encouragement and care were critical to my success. A special thank you to my parents: I will never be able to fully express my gratitude for all you have done for me. Thank you for shaping me into the person I am today.

1.0 INTRODUCTION

Biomolecular recognition processes are orchestrated by a combination of biochemical interactions and equilibria. Biomolecular interactions are essential for cellular function and biological processes, both physiological and pathological. Fundamental understanding of the mechanisms of such interactions is a goal in both basic and applied research. For a given event, the molecular function, or binding, of each molecular component is determined by its molecular shape, or folding. Hence, intermolecular interactions rely upon intramolecular stabilization, and, are further influenced by energetic contributions from solvation.^{1,2} As such, it is challenging to accurately measure the quantitative energetic differences of the component forces of interactions due to the thermodynamic substates present in macromolecular systems.¹⁻³ However, such an endeavor is of significant interest for advancements in computational drug design and molecular recognition.

Understanding molecular conformation preferences in solution can greatly assist in developing new methods to modulate conformation-dependent properties in drug design. Generally, the conformational variability of an enzyme is determined by the flexibility of rotatable bonds in the peptide backbone and amino acid side chains. Moreover, drug-like compounds adopt a variety of conformations even in solid states as evident in the Protein Data Bank (PDB)⁴ and Cambridge Structural Database (CSD).⁵ Molecular dynamics simulations used to accurately measure complexities between structure, electrostatic interactions, solvation and energetics are limited by the force field applied during calculations.^{3,6} Comparisons between NMR experiments

and molecular dynamics are instrumental to benchmark simulations to further our understanding of biomolecular interactions critical to folding, such as hydrogen bonds, salt bridges and hydrophobic clusters.^{7,8} Furthermore, construction of minimal model systems, which isolate chemical components critical to interactions in macromolecular systems, provides powerful biological templates to test computational models and molecular recognition theories in a controlled manner.

1.1 PEPTIDE-BASED THERAPEUTICS

Many complex diseases, such as cancer, metabolic and neurodegenerative diseases,⁷ are a result of aberrant protein-protein interactions (PPIs) or enzyme deficiencies, in which conventional therapeutics are too non-specific for treatment.⁸ As a result, the attractive pharmacological profile of proteins and peptides, such as high selectivity, efficacy, safety and tolerability, has led to the emergence of novel biologic-based therapeutics, or amino-acid based drugs.⁹⁻¹² Amino acid-based therapeutics are defined as proteins, peptides and peptidomimetics.

Enthusiasm has wavered for peptide-derived therapeutics since the advent of insulin therapy in the 1920s.¹³ Physiological and chemical limitations of native peptides as therapeutics, such as short plasma half-life, poor bioavailability, membrane impermeability and stability, were first overcome by implementation of small molecules as therapeutics for ligand receptor binding and selective modulation.^{9,10} Though combinatorial libraries, high-throughput screening (HTS) technologies,^{11,13} and structural biology.^{9-11,15} revolutionized drug discovery, small molecules developed from lead compounds present their own set of drawbacks in terms of druggability.^{10,14} Modern day synthetic strategies mitigate the inherent limitations of native peptides, allowing for

pharmacokinetic modulation¹⁵⁻¹⁷ by sequence and peptide backbone modification,¹⁸⁻²¹ incorporation of canonical and non-canonical amino acids^{18b,19,21,22} as well as improved solubility²³ and half-life by conjugation.²⁴ Moreover, formulary advancements offer improved stability and permeability, with peptide-based candidates of up to 40 amino acids in length entering clinical development.^{25,26}

Advances in molecular engineering have enabled peptide-derived drug discovery and development to keep pace with scientific innovation, leading to 60 approved peptide-based pharmaceuticals in global markets to-date that are known to disrupt PPIs, inhibit intracellular pathways and target receptor tyrosine kinases.⁹ With 150 and 250 drug candidates in clinical and pre-clinical development, respectively, the projected market opportunity of future peptide and peptidomimetic pharmaceuticals is expected to exceed \$50 billion by 2024 (from under \$30 billion in 2018).⁹

1.2 THE MOLECULAR TORSION BALANCE AS A MINIMAL MODEL SYSTEM FOR STUDYING PROTEIN FOLDING

As the barriers to entry are substantial for the preclinical and clinical development of any drug, the combination of theoretical and experimental investigations designed to predict biomolecular structure, folding, binding and catalysis, are necessary to lower basic scientific impediments to progress. The molecular torsion balance is used for measuring molecular folding energies to gain understanding of preferred physical forces that stabilize the folded state of a biomolecule; such forces include Keesom forces,⁹ Debye forces¹⁰ and solvation effects in folded biomolecules.^{1,2} The torsion balance molecular scaffold was designed to have accessible modification to allow

evaluation of the many possible variables that influence non-covalent interactions, and, to give unambiguous spectroscopic data that would not require time-consuming analysis.

1.2.1 The Torsion Balance Concept

The Wilcox torsion balance was developed in 1994 as a molecular tool to measure isolated non-covalent interactions critical to molecular recognition and protein folding (Figure 1).²⁹ The torsion balance molecular design allowed for gently restricted rotation ($\Delta G^\ddagger = 14$ to 24 kcal/mol) of the top asymmetrical aryl ring about a Tröger's base analog. That barrier is low enough to allow conformational equilibration at room temperature but high enough to study the populations of two conformations, folded and unfolded, by ^1H NMR. In Figure 1, the folded and unfolded states of the first generation torsion balance are illustrated on the left and right, respectively. We note the upper and lower halves are shown in blue and black, respectively. In the folded state, the phenyl subunit of the phenyl ester is orientated perpendicular to the toluenic ring to form a compact structure; whereas in the unfolded state, the phenyl subunit of the phenyl ester is oriented away from the toluenic ring. Here, interconversion of the rotatable bond allowed for investigation of substituent effects on preferential folding. Thus allowing for direct comparison of small-molecule drug-receptor interactions and residue side-chain interactions. If there is an attractive force, there is a deviation from a 1:1 ratio between the two orientations of the top ring. That deviation is detectable by ^1H NMR studies. Furthermore, changes in environmental media, such as solvent, temperature, and pH, were carried out to probe those effects on folding and are summarized in Chapter 1.2.2 and 1.2.3.

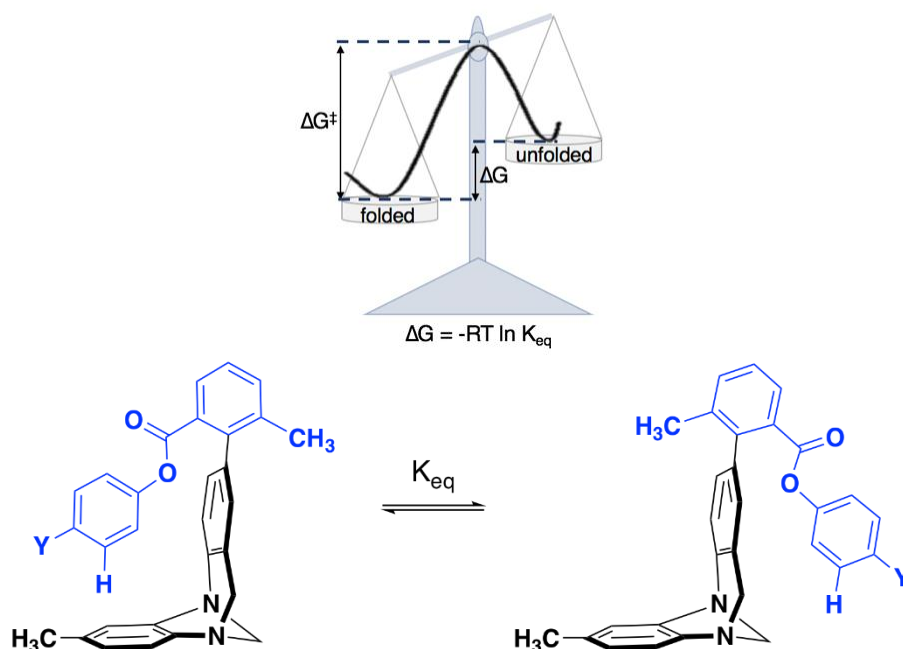


Figure 1. Wilcox molecular torsion balance. Folded (left) and unfolded (right) conformational states of aryl esters in the first generation molecular torsion balance. Restricted rotation ($\Delta G^\ddagger = 16$ kcal/mol at 298 K) allows for two distinct sets of NMR signals. The upper and lower halves of the balance are shown in blue and black, respectively.

Analogs of 2,3-dimethyldibenzodiazocine (Tröger's base; Figure 2) are known as ideal templates for biomimetic systems due to their relative rigidity, unique cleft-shape and potential to direct functionalities towards the cleft through substitution at C2 and C8.^{30,31} The scaffold has many applications,³² including but not limited to receptors for benzenoid substrates,³⁰ hydrogen bonding hosts in diacids,^{31,33,34} ligands in asymmetric catalysis,³¹ drug candidates,³⁵ and new materials for optical applications.³⁶ Although the Tröger's base was originally synthesized by Carl Julius Ludwig Tröger in 1887,³⁷ the Tröger's base structure was not described until 1935.³⁸ Finally, in 1987, Dr. Craig S. Wilcox established the structure by crystallographic analysis.³⁹ The C₂-symmetrical molecule owes its chirality to the two configurationally stable amines. The structure is concave and V-shaped with an angle of 89-104° between the two aryl rings.³⁰ That

angle provides flexibility at the bridge and allows for optimal distance requirements for stabilized non-covalent interactions.

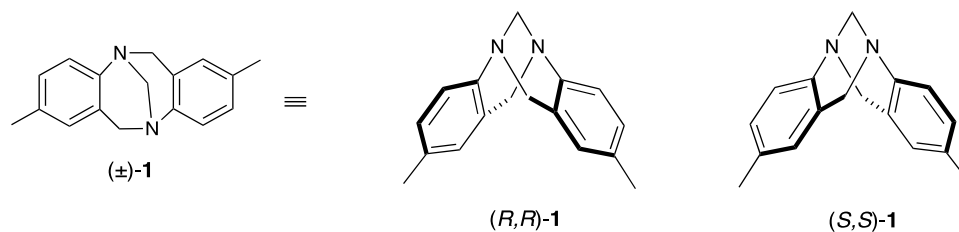


Figure 2. Tröger's base.

1.2.2 First Generation Torsion Balance

The first generation torsion balances were studied in non-polar solvents to evaluate the benzene dimer edge-to-face, aryl and alkyl CH- π , cation- π (Figure 3) and fluorination effects on the folding ratio. Using ^1H NMR data, folding free energies of synthesized derivatives were measured by integration and line-shape analysis.⁴⁰ A brief synopsis of the first generation torsion balance is described in Chapter 1.2.2.1.

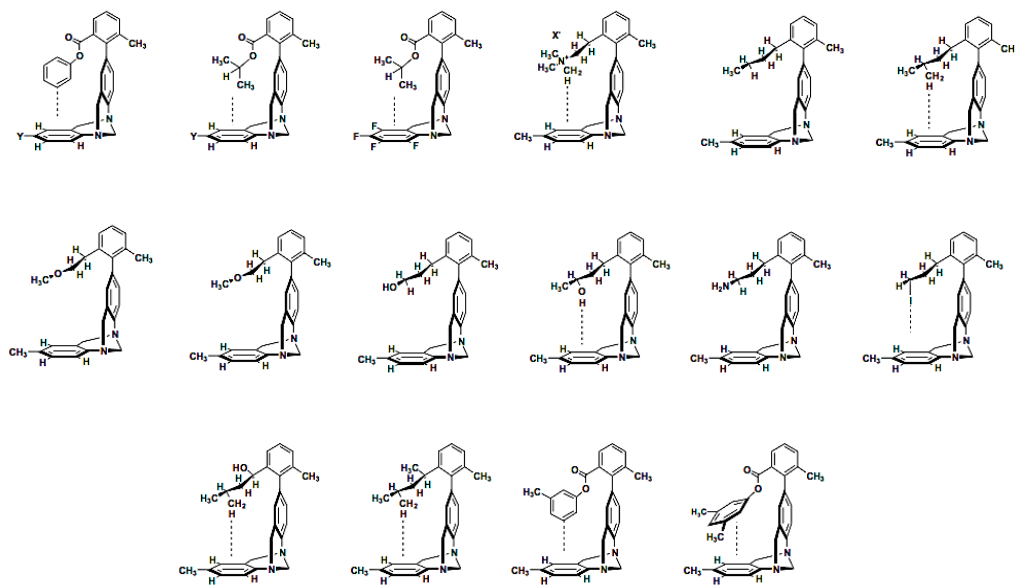
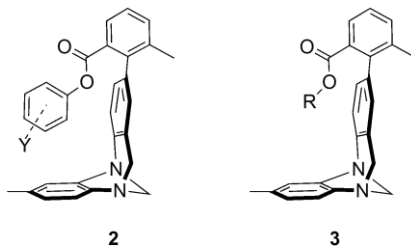


Figure 3. First generation torsion balances.

1.2.2.1 Aryl and alkyl CH- π interactions

Initially, the torsion balance was used to measure the stability of the tilted-T edge-to-face interaction and effects of substitution on preferential folding (Table 1).²⁹ Here, deactivation of the phenyl ester phenyl subunit by electron withdrawing groups (**2d-e**) were shown to perturb the folding ratio. In considering the alkyl groups (**3a-c**), the *t*-butyl-aryl interaction (**3c**) was discovered to be as significant as the edge-to-face interaction.

Table 1. Experimental folding energies for esters **2-3** in CDCl₃ at 25 °C.²⁹ First-generation torsion balances for investigation of benzene dimer tilted-T edge-to-face interactions.

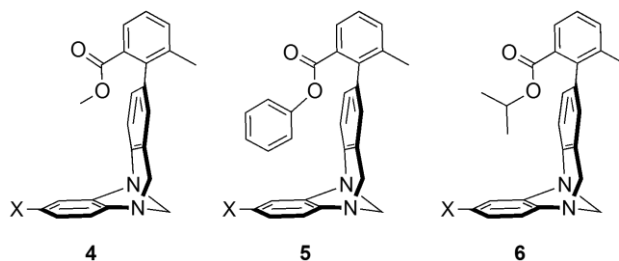


Ester	Y	R	$-\Delta G^{a,b}$
2a	H	-	0.24
2b	<i>p</i> -CH ₃	-	0.37
2c	<i>p</i> -OCH ₃	-	0.24
2d	<i>p</i> -CN	-	0.65
2e	<i>p</i> -NO ₂	-	0.65
2f	<i>p</i> -I	-	0.65
2g	<i>m</i> -CH ₃	-	0.00
2h	<i>m</i> -CN	-	0.24
2i	3,5-dimetl	-	-0.37
3a		CH ₃	0.00
3b		cyclohexyl	0.37
3c		<i>t</i> -butyl	0.82

a) $\pm 10\%$ error. b) kcal/mol.

Further interest in the forces contributing to the aryl and alkyl CH- π interactions led to ¹H NMR studies of substituted phenyl, methyl and isopropyl esters (**4-6**; Table 2).⁴¹ Folding was preferred in the isopropyl ester (**6**) over the phenyl ester (**5**) at room temperature. Because there was no evidence of substitution effects, the data negated the significance of electrostatic potential on preferential folding. It was apparent that edge-to-face interactions are a result of London dispersion forces.

Table 2. Folding energies for methyl (**4**), phenyl (**5**), and isopropyl esters (**6**) in CDCl₃ at 25 °C to support an investigation of electrostatic potential of the aromatic face ring and the strength of edge-to-preferentially folded.⁴¹



X	$-\Delta G^{a,b}$ (4)	$-\Delta G^{a,b}$ (5)	$-\Delta G^{a,b}$ (6)
NO ₂	-0.11	0.21	0.51
CN	-0.06	0.30	0.64
I	0.06	0.23	0.46
Br	-0.02	0.26	0.54
OCH ₃	0.04	0.27	0.44
OH	0.03	0.23	0.47
NH ₂	0.06	0.18	0.34

a) $\pm 10\%$ error. b) kcal/mol.

1.2.2.2 Amide and organic fluorine interactions

The discovery of a characteristic geometry of an organic fluorine orthogonal to a carbonyl in many complexes in the CSD and PDB was described by Diederich and coworkers.⁴² The exchange of hydrogen for fluorine is common in medicinal chemistry due to improvements in absorption, distribution, metabolism, excretion and toxicity (ADMET).^{43,44} Diederich et al. employed the torsion balance to measure the C-F \cdots C(O) dipole interaction, in combination with the double mutant cycle approach, to support an investigation of improved efficacy in fluorine-substituted synthetic drug candidates (Figure 4).^{45,46} Solvent effects on the C-F \cdots C(O) dipole interaction between trifluorophenyl and methyl amide derivatives **7-9** revealed evidence of an attractive

noncovalent dipole $C_{sp2}-F\cdots C(O)$ and $C_{sp2}-F\cdots C(O)$ interactions between organic fluorine and amide groups.

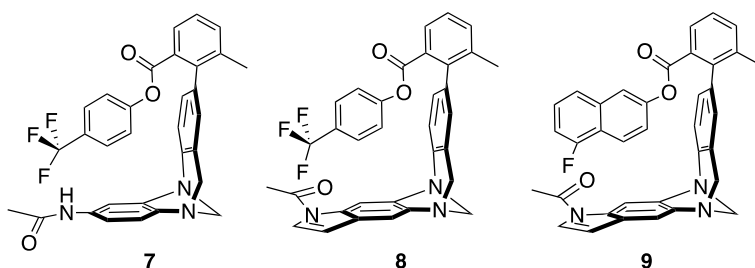


Figure 4. Torsion balance derivatives (**7-9**) used by Diederich et al. to measure preferential folding amongst $C_{sp2}-F\cdots C(O)$ and $C_{sp3}-F\cdots C(O)$ dipole interactions.^{45,46} (**7-9**) used by Diederich et al. to measure preferential folding amongst $C_{sp2}-F\cdots C(O)$ and $C_{sp3}-F\cdots C(O)$ dipole interactions.^{45,46} Note the indole and naphthyl incorporation in torsion balances **8** and **9**, respectively.

1.2.3 Second Generation Torsion Balance

A second generation torsion balance (Figure 5) was designed to measure noncovalent interactions in water.⁴⁷ Until this point, the design of the torsion balance scaffold incorporated a rotatable asymmetrical alkyl or aryl 3-methyl benzoate atop a Tröger's base derivative. For these experiments to be successful, it was necessary to improve solubility and prevent solvation from disrupting the folding ratio. To improve solubility, isophthalates were decorated with hydrophilic groups along the torsion balance rotational axis and revealed the desired result without imposing energetic differences in folding preference. To prevent solvation from disrupting the folding ratio, the symmetry of the upper half of the balance was improved. Asymmetry in the methyl benzoate creates a difference in dipole moments. To avoid any consequential deviations in isomeric ratio from polarity changes, the methyl group was replaced with a methyl ester.⁴⁷

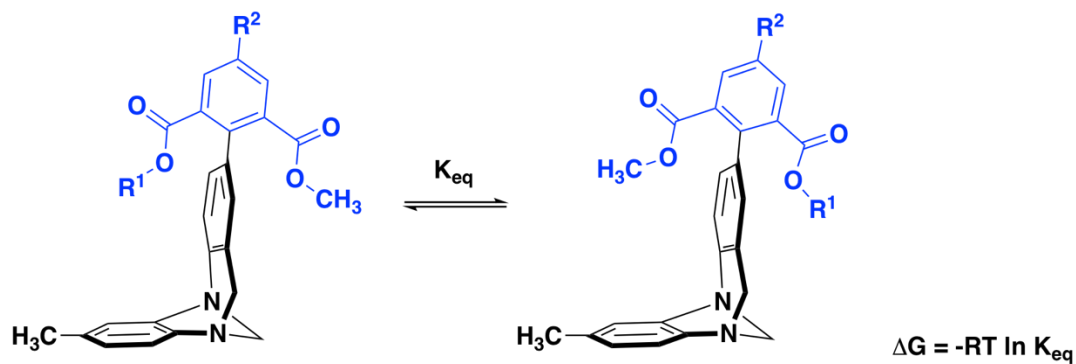


Figure 5. Second generation torsion balance scaffold.

1.2.3.1 Alkyl CH- π interactions

In comparing the difference between the folding energies of the torsion balance in D₂O and nonpolar solvents, Bhayana showed the hydrophobic assistance to folding was significant. Specifically, the greater the size of the alkyl substituent, the greater the folding ratio.⁴⁷

Table 3. Folding energies for torsion balances **12a-f** at 25 °C to examine hydrophobic effects in D₂O.⁴⁷ Torsion balances **10-12** were also used in this study.

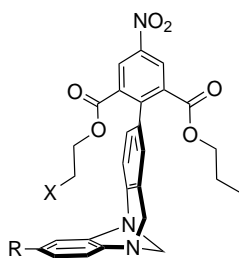
Ester	Y	$-\Delta G_{\text{fold}} [\text{CDCl}_3]^{\text{a,b}}$	$-\Delta G_{\text{fold}} [\text{D}_2\text{O}]^{\text{a,b}}$
12a	(CH ₃) ₂ HC	0.50	0.72
12b	(CH ₃) ₃ C	0.65	0.92
12c	cyclohexyl	0.36	0.67
12d	1-adamantyl	0.55	0.68
12e	1-adamantyl	0.00	0.90
12f	CH ₃	-	0.00

a) $\pm 10\%$ error. b) kcal/mol.

1.2.3.2 Halogen bonding

The second generation torsion balance was used to evaluate the halogenated bond effect⁴⁸ on the XH- π interaction (**13-16**; Table 4).⁴⁹ Preferential folding was observed for derivatives forming an intramolecular hydrogen bond over the halogen bond. Carbamate and hydroxyalkyl substituents had similar acceptor ability, which was improved in tertiary carbamates **16a** and **16b**. Contrary to expected halogen bond strength, folding ratios were higher for bromides and chlorides derivatives than iodides.

Table 4. Folding energies for esters **13-16** at 5 °C to determine effects of halogenated bond on XH- π .⁴⁹



13-16

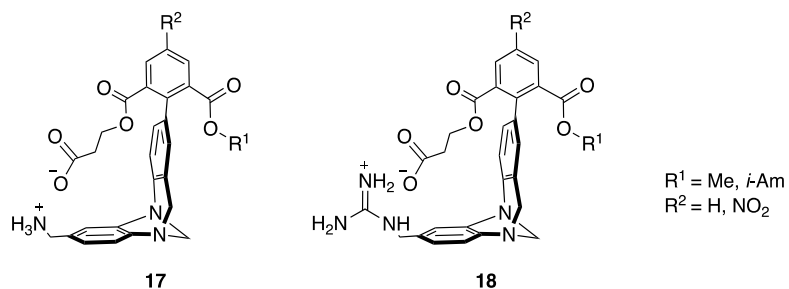
Ester	R	X	$-\Delta G_{\text{fold}}[\text{CDCl}_3]^{\text{a,b}}$
13a	BocNH	Br	0.18
13b	BocNH	Cl	0.2
13c	BocNH	OH	0.37
14a	HOCH ₂	Br	0.21
14b	HOCH ₂	Cl	0.18
14c	HOCH ₂	OH	0.48
15a	Me ₂ NOCCH ₂	Br	0.25
15b	Me ₂ NOCCH ₂	Cl	0.26
15c	Me ₂ NOCCH ₂	OH	0.71
15d	Me ₂ NOCCH ₂	I	0.13
16a	BocNMe	Br	0.36
16b	BocNMe	Cl	0.37

a) $\pm 15\%$ error. b) kcal/mol.

1.2.3.3 Salt bridge stability

Salt bridges are important for protein stability, recognition and regulation. Buried salt bridges are known to stabilize the protein-folded state.⁵⁰ Yet, an accurate description of surface, or partially or fully solvent exposed, salt bridges in the protein-folded state is still elusive. Experimental data from an investigation of salt bridge stability in torsion balance derivatives revealed no change in stabilization between buried and solvent exposed salt bridges in ammonium-carboxylate **17** and guanidinium-carboxylate **18** ($-\Delta G_{\text{fold}} = 0.3$ to 0.5 kcal/mol; Figure 6).⁴⁹ In addition, temperature changes from 5-25 °C and pD changes from 3.1 to 10.0 offered negligible effects on preferential folding. Results of these temperature studies disputed Thomas and Elcock's theory that salt bridges are stabilized at higher temperatures.⁵¹

(a)



(b)

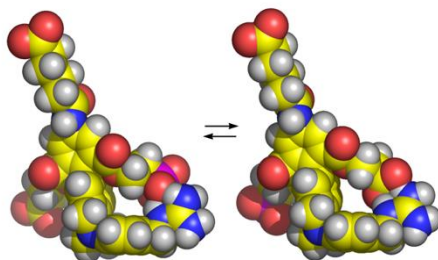


Figure 6. (a) Ammonium-carboxylate torsion balance **17** and guanidinium-carboxylate **18** used to measure salt bridge stability. (b) Minimized structure modeled using force field MMFF94s.⁴⁹

The use of molecular dynamics studies to accurately measure complexities between salt bridge structure, solvation and energetics is limited by the force field applied during calculations.^{50d} This computational impediment was confirmed by the same torsion balance salt bridge stability study (Figure 6b). Experimental data revealed small differences in stabilizing energy between salt bridges in ammonium-carboxylate **17** and guanidinium-carboxylate **18**, whereas dynamic modeling using force field MMFF94s indicated larger differences, or stronger interactions, in **18** compared to **17**.⁴⁹ Results of this torsion balance study demonstrate the importance of NMR experiments to assess the energetic contributions of salt bridge formation and to validate the accuracy of simulations calculated by predictive models.

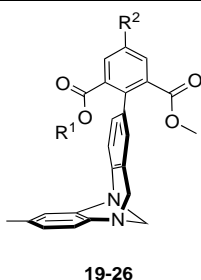
1.2.3.4 Neighboring group effects in hydrophobic surface association

The second generation balance was used to investigate polar neighboring group effects on hydrophobically-assisted folding (Table 5).⁵² Specifically, the water structure at the molecular surface was examined to determine effects of polarity in hydrophobic surface association. Based on Lum-Chandler-Weeks (LCW) theory,⁵³ Ling hypothesized an effect would arise from polarity differences on structure and orderliness of water at the hydrophobic surface. If the polar group influenced the excess free energy of water at the nearby hydrophobic surface, changes in folding energies would indicate the contribution of desolvation in preferential folding.

Though torsion balances bearing a bicyclo[2.2.2]octyl subunit were preferably folded to those bearing trans-cyclohexyl units, the neighboring group effect on contact surfaces in torsion balances **19-26** was negligible. Results showed branching functionalities increased folding compared to linear functionality in MeOD; however, the difference in folding energy between branched and linear derivatives was diminished in D₂O.⁵² Data from NMR experiments in D₂O reveal higher folding energies compared to MeOD. Therefore, London dispersion forces appear to

be enhanced more in water for poorly bound surfaces than for tightly bound surfaces. In addition, evaluation of alkyl chain length effects, revealed excess surface free energy (γ) of the interacting surfaces is not significantly changed as the surface is extended in torsion balances **19-26**. This is interesting because LCW theory predicts γ is different among hydrophobic spheres of changing size.⁵³

Table 5. Folding energies for esters **19-26** at 5 °C to measure nearest neighbor group effects in hydrophobic surfaces.⁵²



Ester	R ¹	R ²	$-\Delta G_{\text{fold}}$ [CDCl ₃] ^{a,b}	$-\Delta G_{\text{fold}}$ [MeOD] ^{b,c}
19a	Bco-H	NO ₂	1.9	
19b	Bco-H	NH ₂	1.3	
19c	Bco-H	NHCO(CH ₂) ₃ CO ₂ H		2.3
20a	Cy-Me	NO ₂	1.2	
20b	Cy-Me	NH ₂	1.1	
20c	Cy-Me	NHCO(CH ₂) ₃ CO ₂ H		1.7
21a	Bco-CO ₂ Et	NO ₂	2.2	
21b	Bco-CO ₂ Et	NH ₂	2.2	
21c	Bco-CO ₂ Et	NHCO(CH ₂) ₃ CO ₂ H		3.0
22a	Cy-CO ₂ Et	NO ₂	1.4	
22b	Cy-CO ₂ Et	NH ₂	1.5	
22c	Cy-CO ₂ Et	NHCO(CH ₂) ₃ CO ₂ H		1.9
23a	Bco-CO ₂ Bn	NO ₂	2.4	
23b	Bco-CO ₂ Bn	NH ₂	1.6	
23c	Bco-CO ₂ H	NHCO(CH ₂) ₃ CO ₂ H		3.3
24a	Cy-CO ₂ Bn	NO ₂	1.4	
24b	Cy-CO ₂ Bn	NH ₂	0.3	
24c	Cy-CO ₂ H	NHCO(CH ₂) ₃ CO ₂ H		2.3
25a	Bco-CH ₂ OBn	NO ₂	0.9	
25b	Bco-CH ₂ OBn	NH ₂	1.6	
25c	Bco-CH ₂ OH	NHCO(CH ₂) ₃ CO ₂ H		2.3
26a	Cy-CH ₂ OBn	NO ₂	0.7	
26b	Cy-CH ₂ OBn	NH ₂	0.7	
26c	Cy-CH ₂ OH	NHCO(CH ₂) ₃ CO ₂ H		1.4

a) Error = ±0.2 kJ/mol. b) kJ/mol. c) Error = ±0.2-0.5 kJ/mol.

1.2.4 Third Generation Torsion Balance: A Novel Peptide Hybrid Torsion Balance

The design of compounds capable of interfering with PPIs requires understanding of sources of affinity and specificity in each interface. Most interfaces are composed of two relatively large protein surfaces with the correct shape and electrostatic complementarity for binding. Computational techniques, directly correlating protein-protein binding energy with buried hydrophobic surface area, failed to accurately measure the energetic contributions of individual residues in binding.^{55b} Despite the large size of binding interfaces, single residues contribute a large fraction of binding free energy in a domain, known as hotspots.⁵⁵ Such hot spot residues often cluster near the center of the interface and are surrounded by energetically less important residues. Still, energetically important interactions can be grouped into independent clusters, having additive contributions.⁵⁴ We applied the torsion balance concept to experimentally probe the energetic contributions of amino acid residues in protein binding.

A novel peptide torsion balance hybrid was designed to support an investigation of pairwise amino acid interactions in antiparallel orientation of a β -sheet and the effects of changes in amino acids on a short β -strand. Though moderately high risk compared to the previous work by the Wilcox group, the third generation balance potentially offers a robust experimental tool relevant to testing current computational methods and theories of biological recognition and in identifying guiding principles for biological drug design. Stated otherwise, can the molecular torsion balance concept be applied to evaluate competitive binding between biologically relevant domains larger and richer in detail than amino acid side-chain interactions and small-molecule drug-receptor interactions? In this study, we describe the design (Chapter 2), synthesis (Chapters 2.3, 4.1, 5, 6)

and NMR analysis (Chapters 3, 4, 6) toward a hybrid synthetic-natural peptide that incorporates a conformationally controlled torsion balance.

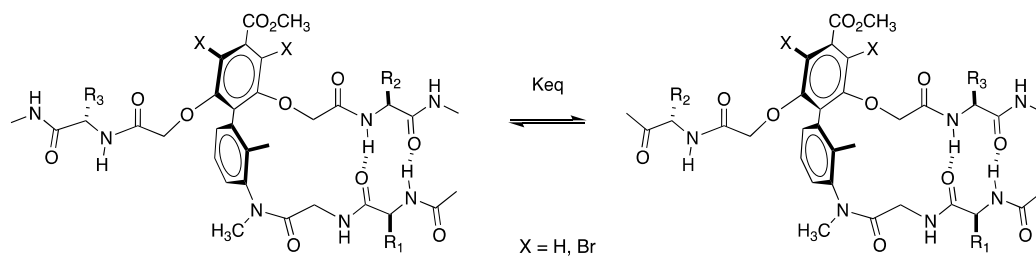


Figure 7. Wilcox β -turn mimetic torsion balance. Folded (left) and unfolded (right). Each R group represents a different amino acid side chain. Restricted rotation around the N-aryl bond ($\Delta G^\ddagger = 21$ kcal/mol) allows for two distinct sets of NMR signals.

2.0 DESIGN AND SYNTHESIS OF A CONFORMATIONALLY CONTROLLED β -TURN MIMETIC TORSION BALANCE

The results in this chapter have been published in:

Lypson, A.B. Wilcox, C.S. "Synthesis and NMR Analysis of a Conformationally Controlled β - Turn Mimetic Torsion Balance." *Journal of Organic Chemistry*, **2017**, 82, 898-909.

Computational techniques are instrumental to designing amino acid-based therapeutics.⁵⁵⁻⁵⁹ However, docking of a highly flexible peptide into a protein remains a major challenge.⁵⁵ The degrees of freedom arising from rotatable bonds in the peptide backbone and residue side chains can generate an infinite number of configurations for a single amino acid sequence.^{1,2} Traditional protocols developed for docking small molecules, such as AutoDock, Vina⁵⁶ and MOE-Dock,⁵⁷ have been used to dock peptides to protein receptors.^{57a-e,59} Though, such methods are challenged by the growing quantity and complexity of experimental data. Comparisons between simulation and experimental data remain necessary to assess the accuracy of computational methods to predict protein folding.

Many strategies exist for designing proteins and amino-acid based targets.⁶¹ Traditional methods for protein design, such as template-based design, rely upon a three-dimensional structure of a predefined template to adapt into a sequence.⁵⁸ This strategy eliminates the ambiguity of predicting the fold of an unknown sequence. For example, if the template is reliable and the framework is stabilized by the connected amino acid side chains, the fold is unaltered. Hirschman introduced this concept for cyclic somatostatin derivatives.⁵⁹ Alternatively, de novo design⁶⁰ alters

amino acid arrangement to produce a novel protein sequence and structure. More recently rational-based designed has been applied to peptidomimetics and is categorized as target-based design and ligand-based design methods.⁶¹ The latter can be further classified into subcategories, including sequence-based design. Such subcategories were recently described in *Drug Design, Development and Theory*.⁶²

2.1 PEPTIDOMIMETICS

Paramount to the function of any active biomolecule is its three-dimensional folded structure. Mimicking that structure, and thereby function, of biological peptides using non-peptidic scaffolds has become an established method to modulate specific PPIs and to improve the pharmacokinetic drawbacks of peptides. Strategies for modulating PPIs include the development of non-canonical amino acid containing α -peptides as well as unnatural polyamide-based and non-polyamide-based secondary structure mimics.^{18-23, 59,62}

Gellman, Horne, and others have used sequence-based design to develop peptide-like structures.^{18,63} Such models are based on a combination of natural and synthetic amino acids to induce peptide interactions of a protein folded state. As defined by Gellman, secondary structures with non-canonical amino acid monomers, or foldamers, are “any polymer with a strong tendency to adopt a specific compact conformation.”⁶⁴ In the biological environment, peptidomimetic structures can accurately provide the desired shape and function of the secondary structural elements (α -helices, β -strands, and reverse turns) to mimic the parent in its native environment, or, to bind off-target. The traditional peptidomimetic approach is based upon the design of synthetic molecules to mimic unique secondary structural motifs for incorporation into

biologically relevant sequences. In example, we highlight design requirements for synthetic templates to mirror intramolecular and intermolecular interactions ubiquitous in hydrogen-bonded antiparallel β -sheet domains.⁶⁵

Formation of pairwise interchain interactions requires perpendicular orientation of amino acid side chains between two β -strands. The adopted geometry enforces both intramolecular (local and non-local) and intermolecular interactions between residues. Specifically, the intramolecular interactions are critical to protein shape, while intermolecular stacking of these structures executes function. We note β -sheets are well-known to be implicated in pathogenesis of cancer as well as Alzheimer's and Parkinson's disease, and are therefore of significant interest in peptidomimetics.^{8,66} However, development of accurate β -sheet mimics has been slow compared to progress made in development of α -helix mimics.²¹ Nevertheless, efforts to accurately design structures modeling antiparallel β -sheets have been successful and are discussed in Chapter 2.1.1.

2.1.1 Conformationally Controlled Hybrid Synthetic Natural Peptides as β -Sheet

Mimetics

Of the secondary protein structures, reverse-turns (α -, β -, γ -, δ - and π -turns) are well-known to govern peptide and protein folding and therefore are accessible for protein modification.⁶⁶ Because turns typically reside at the surface, or solvent-exposed location, within a globular protein, turns are well-suited for mimetic design. The most common of the turns is the β -turn. The β -turn is formed by four adjacent residues, where $i + 1$ and $i + 3$ are less than 7 Å apart, ideal for nucleating the formation of β -sheets. These structural motifs are defined by the backbone torsion angles ϕ and ψ of residues $i + 1$ and $i + 2$. Folded β -hairpin structural stability is determined by the β -turn

conformation as well as intermolecular forces between the β -turn-linked β -strands, such as hydrogen bonds, salt bridges, and hydrophobic clusters. Moreover, forces of interactions affecting the number of thermodynamic substates of a folded conformation are confounded by solvation, sequence, chain length and environmental effects.^{2,3} Thus, the β -turn structural motif provides an excellent model for probing thermodynamics of ligand binding and molecular recognition in biological systems.

In order to accurately study determinants of hairpin formation and to probe the importance of bioactive epitopes, designed sequences must be contained in the context of a compact folded structure.³ Yet, rational design, based on X-ray crystallography and theoretical calculations, of a truncated peptide is limited by the elusive affinity and intrinsic flexibility of peptides. The enthalpy change of secondary interactions may be unable to compensate for the entropy loss during folding. Energetic contributions from conformational entropy of the unfolded state can be reduced by restricting the freely rotatable peptide bonds necessary for folding. Modification of synthetic templates to increase molecular rigidity is common in template-based design to enforce residue alignment.^{21,59} Introduction of rotational restraint, such as using a semi rigid linker or template, to connect natural or unnatural bioactive man can provide the compact conformation needed for investigating bioactive and thermodynamic properties.

Approaches have been developed to transfer hairpin sequences from folded proteins onto semirigid hairpin-stabilizing templates to afford macrocyclic, conformationally restrained protein epitope mimetics (PEM).⁶⁹ Conformational restriction, induced by covalent and non-covalent constraints, provides higher binding potency and target selectivity than its native parent.⁶⁸ In 2004, the Verdine group introduced the idea of a locked structure design to stabilize α -helices in targeting B-cell lymphoma 2 (BCL-2).⁸ The combination of constrain-based design strategies provides

cooperatively stabilized hairpin conformations via backbone cyclization, template-imposed conformational bias and hairpin loop size and sequence effects.

Exhaustive efforts have been put forth by the chemical community to develop β -turn mimics for nucleating β -sheets with conformational constraint as a key design requirement.^{18,69-73} Cyclic and acyclic structures as well as metal chelates have been exploited to nucleate the hairpin motif and to measure folding by 1D and 2D NMR studies. We show a small representative collection of these structures (Figure 8) to convey the diverse approaches to such scaffolds. Kelly and coworkers incorporated dibenzofuran propionic acid at the $i + 1$ and $i + 2$ residues of the turn in both peptide and protein substructures to facilitate hairpin formation in CDCl_3 .⁶⁹ Upon improving solubility of that template, results of NMR studies showed similar free energies of solvation for the mimetic and wild-type sequences in D_2O .²³ Gellman also used NMR studies in water to compare thermodynamic differences in folding parameters of *trans*-5-amino-3,4-dimethylpent-3-enoate conformations. Nowick et al. applied a peptide/oligourea/azapeptide hybrid to adopt a β -turn by forming two intramolecular hydrogen bonds in chloroform. Later, Nowick showed hairpin formation by replacing a β -turn peptide sequence with an artificial amino acid, “Orn(*i*-PrCO- Hao)”.⁶⁵

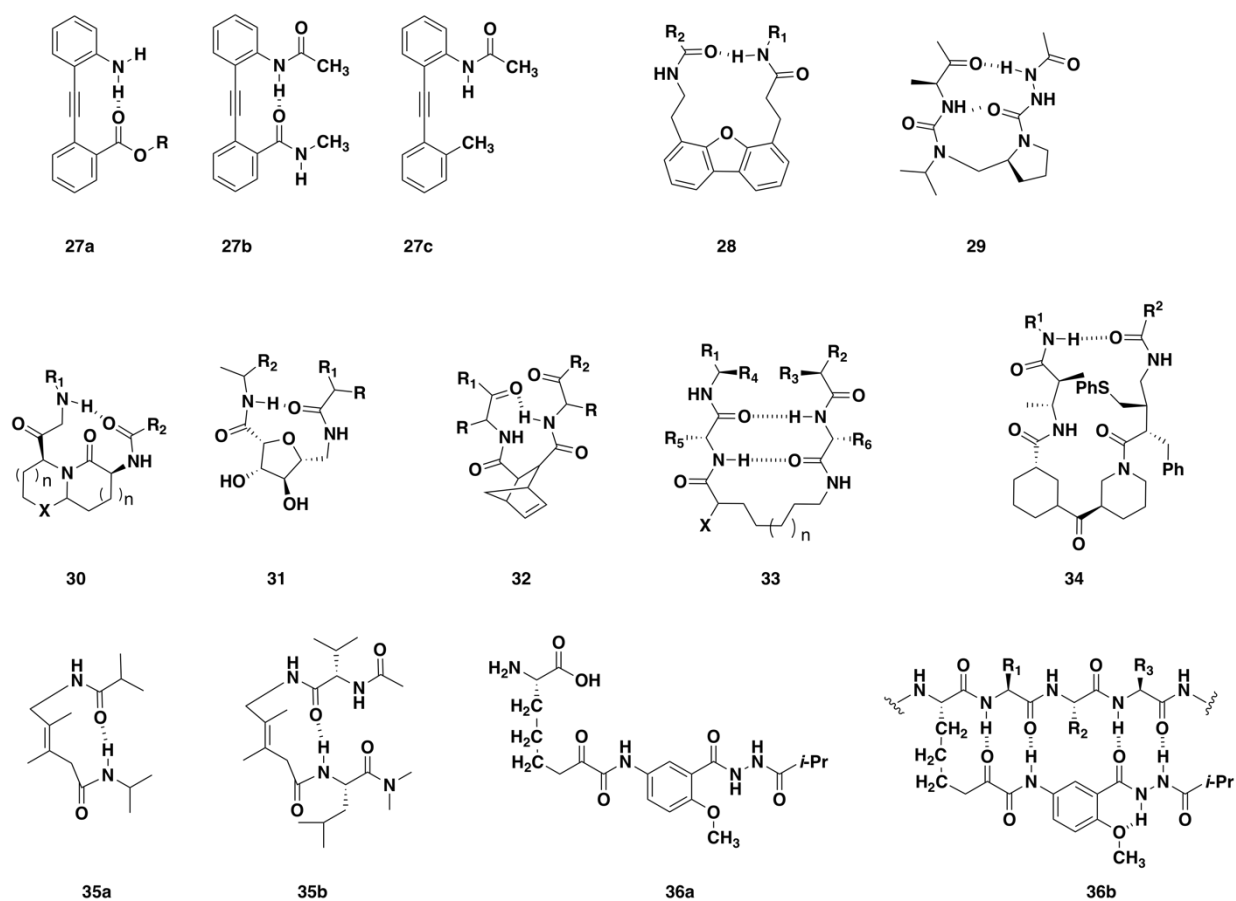


Figure 8. Examples of cyclic and acyclic β -turn mimics.⁶⁵

Of interest to our mimetic design is the biaryl amino acid unit, which has been incorporated into many turn mimetics.^{18b,66-69} Biaryls occur in peptide natural products, such as the glycopeptide antibiotic vancomycin and the peptide-based antibiotic WS-43708A.⁹ The rigid structure makes for an attractive template to control the conformation of the folded substrate.⁷⁴ Kemp's pioneer study used a disubstituted diphenylacetylene as a β -turn mimic to nucleate hydrogen-bonded β -sheet formation (**27a-c**; Figure 8).⁶⁷ Since, the oligophenyl scaffold has been pursued for both helical²¹ and sheet-like^{64,68,72-73} templates. The rigid structures of sequential aromatic rings linked by a single bond are not in the same molecular plane and are therefore asymmetrical.

Kelly and colleagues⁷² used the template-based design concept to develop a biphenyl-amino acid unit to nucleate β -sheets via a hydrogen-bonded hydrophobic cluster conformation (Figure 9). Hydrophobic clusters are important intermediates in folding and are known to reduce the local entropy penalty for folding by preorganizing the unfolded state.^{53,72} Destabilization of the hairpin conformation occurred when phenyl amides replaced the phenyl ethyl unit. The amide subunit restricted flexibility of the peptide chains compared to the ethyl subunit, preventing hydrophobic cluster formation between the phenyl and α -hydrophobic amino acid.

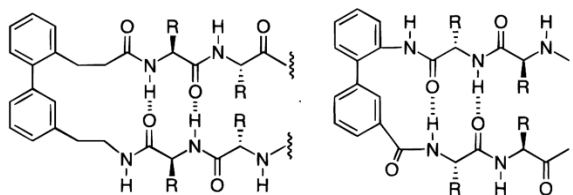


Figure 9. Kelly's biphenyl-amino acid unit to nucleate β -sheets via a hydrogen-bonded hydrophobic cluster conformation.⁷²

Brandmeier,^{73b} Suich^{73a} and Robinson⁶⁸ studied biphenyl-amino acid scaffolds in *o,o'*-biphenyl, *o,m'*-biphenyl and *m,m'*-biphenyl scaffolds as macrocyclic turn mimics. Robinson showed the rate of atropisomer interconversion around the biaryl link could not be slowed down in *o,o'*-biphenyl templates of macrocyclic peptidomimetics of PG-1 compared to *o,m'*-biphenyl and *m,m'*-biphenyl scaffolds (Figure 10).⁶⁸ Conformational analysis relied upon 2D NMR data to investigate folding because ¹H NMR data of *o,o'*-biphenyl tetrapeptide derivatives revealed only the *trans* amide conformation. A comparison of ϕ and ψ angles of several amino acid-substituted macrocyclic *o,o'*-biphenyl tetrapeptides indicated many residues were prohibited by the Ramachandran plot for β -turns due to imposed cyclic strain. That result was not observed for *o,m'*-biphenyl and *m,m'*-biphenyl derivatives.

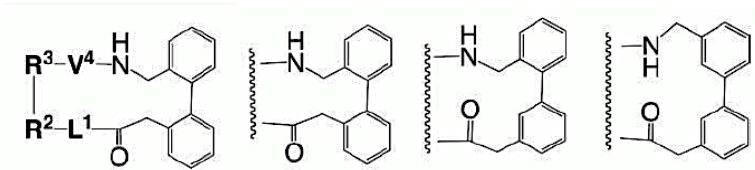


Figure 10. Robinson's cyclic biphenyl amino acid templates as cationic macrocyclic peptidomimetics of PG-1. *o,o'*-Biphenyl tetrapeptide (left) was destabilized compared to the *o,m'*-biphenyl and *m,m'*-biphenyl hexapeptides.^{68c}

We exploit the use of restricted rotation in a biaryl amino acid unit to develop the β -turn mimetic torsion balance for investigating the forces of interactions and effects of the molecular environment on folding for competing pairwise amino acids, as well as, peptide sequences in the antiparallel β -sheet motif.

2.2 DESIGN STRATEGY OF A CONFORMATIONALLY CONTROLLED β -TURN MIMETIC TORSION BALANCE

Our design of the β -turn mimetic torsion balance allows for the direct comparison of two different competing amino acid interactions and further lends itself to comparing two different competing peptide sequences in a compact hairpin structure (Figure 11). We emphasize that rather than imitate a β -turn, our goal was to ensure the turn scaffold enforced the hydrogen-bonded antiparallel β -sheet motif. Stated otherwise, the design demand required that our scaffold (1) match the ends of an antiparallel β -sheet and (2) establish the distances and orientations required for interchain peptidomimetic hydrogen bond formation. The illustration in Figure 11 represents our design.

Like the first and second generation torsion balances,^{29,41} our approach provides two configurations, imposed by restricted rotation about a single rotatable bond, for observation of folded and unfolded states by 1D and 2D NMR. The upper and lower β -strands of a native β -

hairpin sequence (shown in magenta) are covalently connected by the torsion balance. Sequence modulation introduces a mutation into the native peptide sequence (shown in green). The design allows covalent attachment of the mutant sequence along the torsion balance rotatable axis, opposite the upper native sequence. Incorporating the rotational axis into the β -turn allows the preferential pairwise interactions between the upper and lower strands as well as the corresponding energetic differences to be identified by NMR and line shape analysis.⁴⁰ An example of two possible folded configurations used to probe substitution of α -amino acid hydrophobic residues (Ala vs Leu) on preferential folding is shown (Figure 11B). The upper chains maintain a similar level of hydrophobicity and therefore, do not alter the charge. We discuss a detailed account of our approach to design the turn template and third generation balance, here.

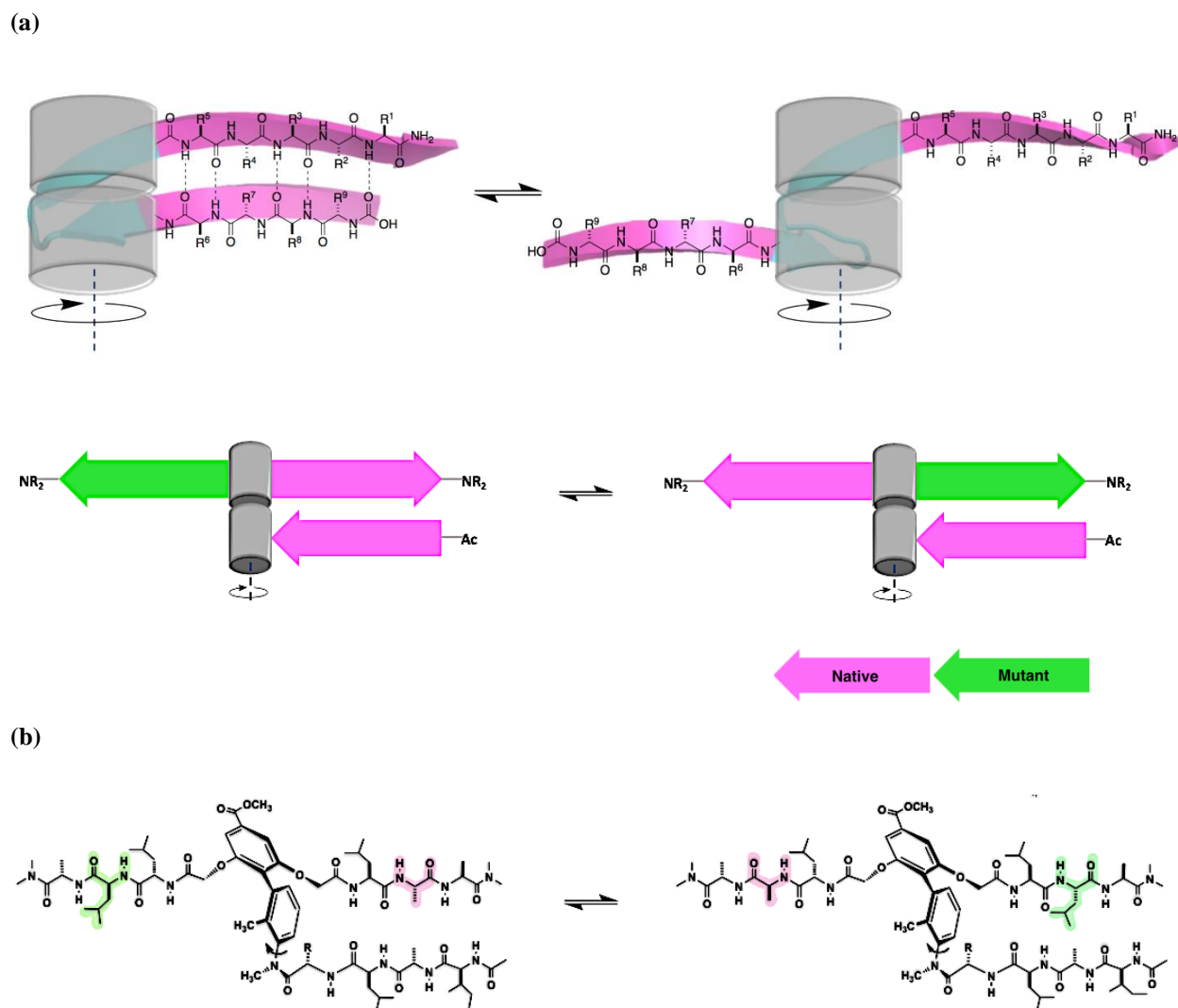


Figure 11. (a) Representation of design requirements for the (b) Wilcox β -turn mimetic torsion balance.

2.2.1 Peptide Structure and Sequence Survey of Antiparallel β -Sheets

Several well-defined β -sheet substructures of enzymes in the PDB, including examples from bovine pancreatic trypsin inhibitor, lysozyme,⁷⁴ barnase, and chorismate pyruvate lyase (CPL),^{75a} were studied to test our concept and take inventory of the interactions that provide conformational stability, such as salt bridge and hydrophobic interactions. Lysozyme has six surface salt bridges

that contribute toward the stability of the protein. Mutational analysis of lysozyme revealed little contribution from salt bridges upon solvation, while desolvation provided a large contribution, emulating a buried salt bridge. Moreover, CPL-vanillate (VNL) inhibition was of interest to probe both enzymatic stability and conformation necessary for its unusual internal ligand binding technique, shown in Figure 12. Because the CPL-VNL complex was most important for modeling the torsion balance, a detailed structural analysis is provided.

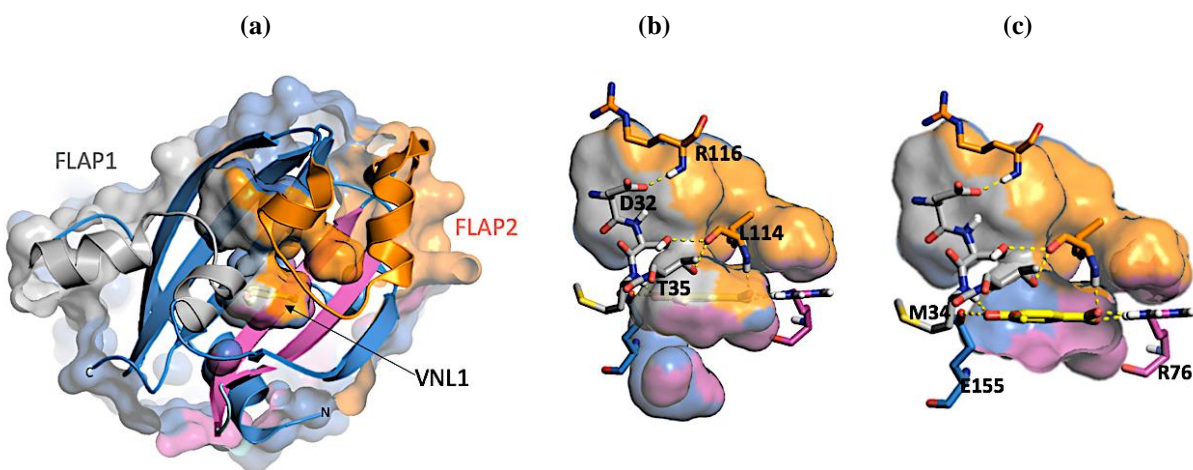


Figure 12. Chorismate pyruvate lyase-vanillate internal ligand-binding pocket. (a) Flaps 1 (residues 21-40) and 2 (residues 97-119) are colored in grey and orange, respectively. The ligand, VNL, is shown buried in the internal ligand-binding site behind flaps 1 and 2. (b) and (c) Internal binding cavity and nearby pockets with key flap and binding site residues. Residues are colored to match the CPL structure in (a). Hydrogen bonding interactions are displayed as yellow dashed lines. The opening and closing of flaps is dependent upon 3 residues of flap 1 (D₃₂, S₃₃, and T₃₅) hydrogen bonding to flap 2 (L₁₁₄ and R₁₁₆). Complexation forms at sidechains of R₇₆ (2 H-bonds) and E₁₅₅, as well as backbone amides of M₃₄ and L₁₁₄. PDB: 1XLR.^{75a}

2.2.1.1 Structural analysis of chorismate pyruvate lyase

CPL catalyzes the cleavage of the pyruvate group from chorismate to provide 4-hydroxybenzoate (4HB), the key intermediate for ubiquinone biosynthesis.^{75b} CPL has two interior flaps (shown in

orange and grey in Figure 12) comprised of hydrophobic residues, located adjacent to the central β -sheet of the enzyme. Mutation and modeling studies of the binding and release mechanism indicate three hydrogen bonds that are pivotal for keeping the flaps together; flap 1 residues (D₃₂, S₃₃, and T₃₅) hydrogen bond to flap 2 (L₁₁₄ and R₁₁₆; Figure 12B).^{75b-d} Enzyme activation and inhibition occur upon flap opening and subsequent 4HB and VNL binding to the densely packed hydrophobic pocket, respectively. We show ligand binding requires hydrogen bond formation between VNL and sidechains, R₇₆ and E₁₅₅, as well as backbone amides, M₃₄ and K₁₁₄. Of most interest to us were the hydrophobic and hydrophilic residues neighboring the binding cavity (Figure 13).

Interchain hydrophobic clusters from main chain hydrogen bonded residues within the central β -sheet provide stability to the binding pocket. Specifically, amide backbone of I₇₈ and L₈₀ form hydrogen bonds to L₈₈ and A₉₀, respectively. These pairwise interactions orient the residue sidechains directly toward vanillate, indicating the ideal radius for van der Waals interactions between each structure. This compact hydrophobic cluster appears to shape, or tile, the cavity surface (Figure 13E). Formation of tightly packed hydrophobic clusters in the core of a protein is a common practice for optimizing van der Waals interaction via substitution with non-polar residues to enhance the protein stability. Further stabilization to this region of the folded β -sheet is provided by interchain salt bridge formation between R₉₁ and E₇₇ (Figure 13B). Altogether, the structural knowledge available for the enzyme receptor-ligand binding provided a feasible structure for our torsion balance model to probe interactions of protein hotspots buried beneath the surface.

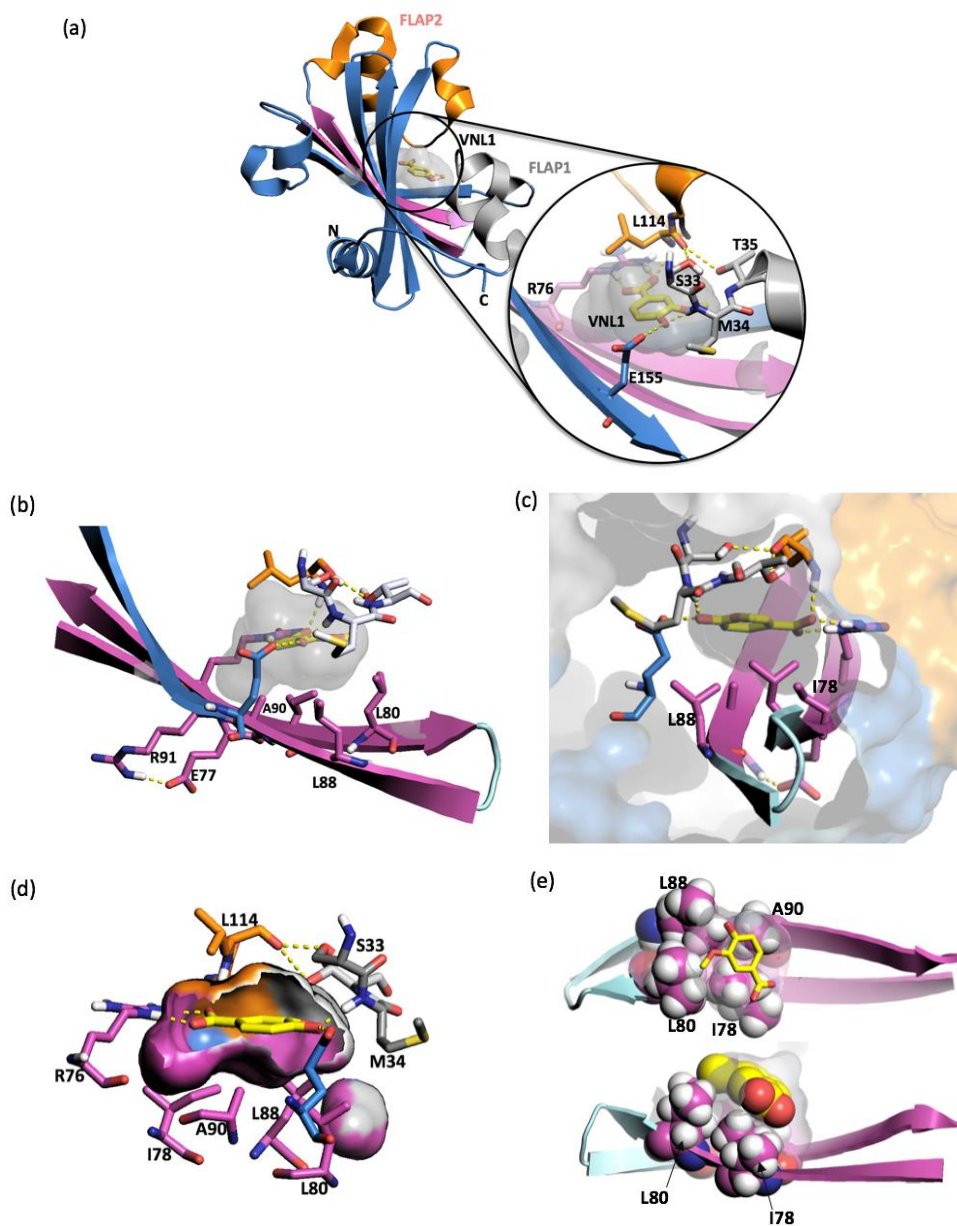


Figure 13. Structural analysis of CPL-vanillate binding site. (a) CPL is complexed with VNL (yellow) in coordination site (grey surface). Flaps 1 and 2 are colored in grey and orange, respectively, and the β -structure of interest is colored in magenta. The inset shows the five hydrogen bonding interactions (yellow dashed lines) between VNL with labeled residues of CPL, and two interactions to L114 main chain amide of flap 1. (b, c) View of the β -sheet of interest with hydrophobic residues (I₇₈, L₈₀, L₈₈, and A₉₀) and hydrophilic residues (R₉₁ and E₇₇) in magenta. Interaction between R₉₁ and E₇₇ offer additional stabilization to the folded β -sheet. (d) Binding cavity and surrounding hydrophobic residues with β -sheet removed for clarity. (e) Formation of hydrophobic cluster between alkyl side chain residues in folded CPL₇₅₋₉₃. neighboring residues appears to shape, or tile, the cavity surface as shown by above (top) and side (bottom) views. PDB: 1XLR.^{75a}

2.2.2 β -Turn Mimetic Template Design

Monte Carlo simulations were applied to model the dibenzodiazocine scaffold with the β -sheet template structure CPL₇₅₋₉₃. It was determined that the dibenzodiazocine architecture did not have the correct shape to match the ends of the hydrogen-bonded antiparallel β -sheet.

In order to construct a β -turn mimetic that would structurally complement the hydrogen-bonded antiparallel β -sheet motif, we turned to a biaryl (*ortho*-tolyl)amide-amino acid core template. The use of biphenyl alkylamino acid subunits to nucleate β -sheets has been described by Kelly,⁷² Robinson,⁶⁸ and Hamilton,²¹ amongst others⁷³ (discussed in Chapter 2.1). However, NMR data revealed orthogonal arrangement of the biphenyl gave poor alignment of amino acid side chains for some examples (Chapter 2.1).⁶⁸ We exploit this knowledge by imposing a rotational barrier in a biaryl-amino acid derivative to give two competing conformational states.

Our biaryl (*ortho*-tolyl)amide-amino acid core design imposes restricted rotation around an N-aryl bond ($\Delta G^\ddagger = 15$ to 20 kcal/mol). An *ortho* substituent is well-known to constrain rotation about the N-aryl bond. This was reported by Mislow^{76a} for acyclic and cyclic (*ortho*-tolyl)amides (Figure 14) and by the Curran group^{76b} for *o*-haloanilide atropisomers in asymmetric radical cyclizations ($\Delta G^\ddagger = 28$ -31 kcal/mol). The design also incorporated an *o,o,o'*-trisubstituted biphenyl unit as an additional site of restricted single bond rotation. Although *ortho*-substituents are mostly responsible for the biaryl bond restriction, the attachment of additional *meta*-substituents is known to introduce further rotational restriction due to a “buttressing effect” (Figure 14). Computer simulations were carried out, based upon Kawano’s work on methyl-2,2',6-trimethoxy-[1,1'-biphenyl]-3-carboxylate, to predict the biaryl rotational barrier to be approximately 27 kcal/mol at 343 K.^{77c}

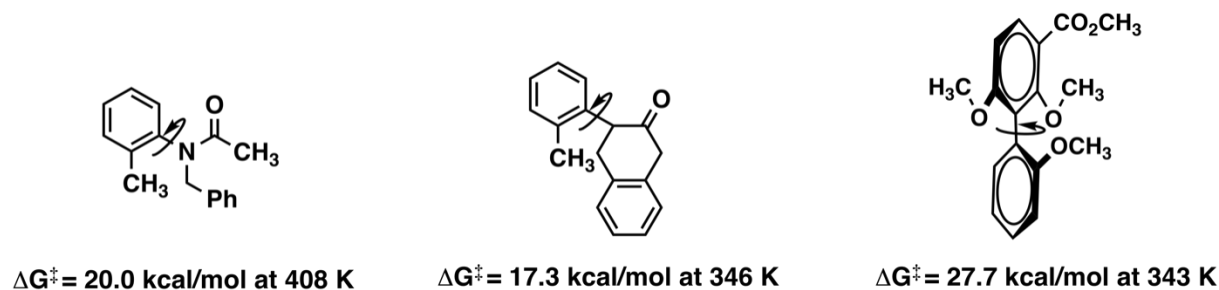


Figure 14. N-aryl and aryl-aryl restricted rotation. (a) Mislow's acyclic and cyclic (*ortho*-tolyl) amide.^{76a} (b) Kawano's *o,o,m,o'*-biphenyl.^{77c} The meta substituent offers increased rotational restriction due to a "buttressing effect."

2.2.2.1 Substitution of CPL₇₅₋₉₃ with biaryl (*ortho*-tolyl)amide-amino acid subunit

The shape of the biaryl(*ortho*-tolyl)amide-amino acid was tested using mutational analysis in CPL₇₅₋₉₃ to answer whether the torsion balance template had the correct orientation to match an antiparallel β -sheet. Modeling showed replacement of amino acids CPL₈₁₋₈₇ with the biaryl (*ortho*-tolyl)amide-amino acid template gave the correct native CPL₈₀₋₇₅ and CPL₈₈₋₉₃ β -strands on the top and bottom halves of the scaffold, respectively. We remind the reader that our goal was not to model the turn, but rather to enforce the desired conformation for interchain hydrogen bonding in the antiparallel β -sheet motif. Figure 15 shows this model and the relationship to the primary CPL₇₅₋₉₃ β -hairpin sequence. The biaryl (*ortho*-tolyl)amide-amino acid scaffold replaces CPL₈₇₋₈₁ and links residues L₈₀ and L₈₈, reinforcing the antiparallel β -sheet orientation. We anticipated our strategy could accommodate considerable amino acid sequence variation, permitting the use of our method to reproduce structures of other β -sheets. This can be achieved by attaching the appropriate amino acid side chains on the top and bottom halves of the balance and replacing the turn sequence with our turn scaffold.

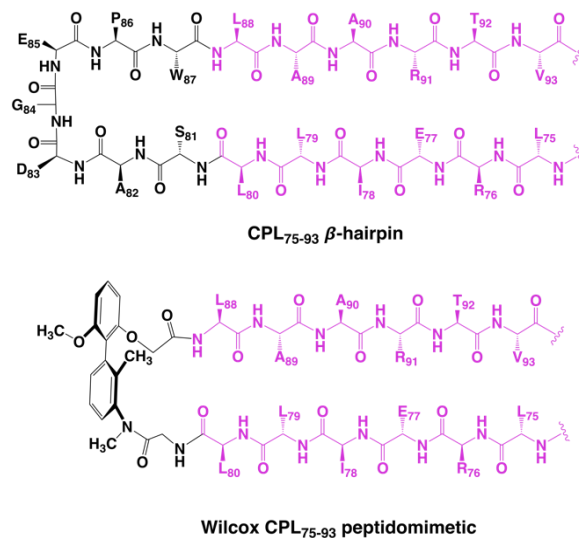


Figure 15. Chemical structure of a native and mutant CPL₇₅₋₉₃ β -hairpin for modeling the Wilcox β -turn mimetic torsion balance. The biaryl (*ortho*-tolyl)amide-amino acid template links truncated CPL hairpin strands at L₈₀ and L₈₈. The strands are colored to match the cartoon of design requirements in Figure 11A as well as the CPL structural analysis (Figure 12; Figure 13).

Computational models revealed that our peptide-torsion balance hybrid template, derived from CPL₇₅₋₉₃, can directly reproduce the primary (Figure 15) and secondary (Figure 16) structures of a hydrogen-bonded antiparallel β -sheet motif. Figure 16 shows the native and truncated three-dimensional hairpin structures of CPL₇₇₋₉₃ in **I** and **II**, respectively. Though most turn mimetics are designed to replace $i + 1$ and $i + 2$ residues, modeling revealed that replacement of CPL₈₁₋₈₇ provided the optimal geometry for our template to mimic the antiparallel β -sheet motif. It was not our goal to mimic the sequence of CPL₈₁₋₈₇, but rather to connect the strands at the correct angles and distances for interchain alignment to promote hydrogen bonding.

Modeling revealed backbone modification with the torsion balance template gave dihedral angles within normal limits to connect two antiparallel β -strands, as indicated by the Ramachandran plot⁷⁸ (Figure 16). Initially, the emulation shown in **III** indicated the backbone of L₈₀ did not match the orientation of our template to mimic CPL₈₀₋₇₅ in a CPL₉₃₋₇₅ hairpin. Small changes in alignment of the lower C-N main chain of amide carbonyls, ranging from $\phi = 109^\circ$ in **III** to $\phi =$

129° in **IV**, improved alignment and did not cause the native peptide sequences to adopt an unnatural conformation. The clustered points within the plot represent the average backbone torsion angles for modeled conformers between values $\phi = 109^\circ$ and $\phi = 129^\circ$. These are representative of conformers modeled between **III** and **IV**, and, correspond to the allowed regions of the Ramachandran plot β -sheet conformation. Modeling predicted the global minimum for the template structure as 86.5 kcal/mol (Figure 17).

The two conformational states of the torsion balance are observed upon introduction of the mutant CPL₈₈₋₉₃ sequence to the upper aromatic ring. The nonnative sequence is covalently linked to compete against the native top strand for pairwise amino acid hydrogen bond formation with the lower strand (Figure 11; Figure 13). The α -carbonyl ethers connecting the upper phenyl substructure to peptides adopts a low energy perpendicular conformation where the aliphatic C-O bond in the phenyl methoxy ether fragment is oriented perpendicular to the plane of the aromatic ring. Molecular dynamics studies incorporating our scaffold indicated that conformational preference makes it feasible for one of the upper peptide side chains to hydrogen bond with the lower peptide side chain, leading to a compact hydrogen-bonded structure. We considered the possibility of upper chains hydrogen bonding but did not find evidence of this (discussed in Chapter 5). The test strategy would allow us to test if the torsion balance design was feasible to measure amino acid interactions in a hydrogen-bonded antiparallel β -sheet configuration. An example of the folded and unfolded torsion balance, shown in Figure 11B, compares the effects of leucine insertion on reverse turn stabilization.

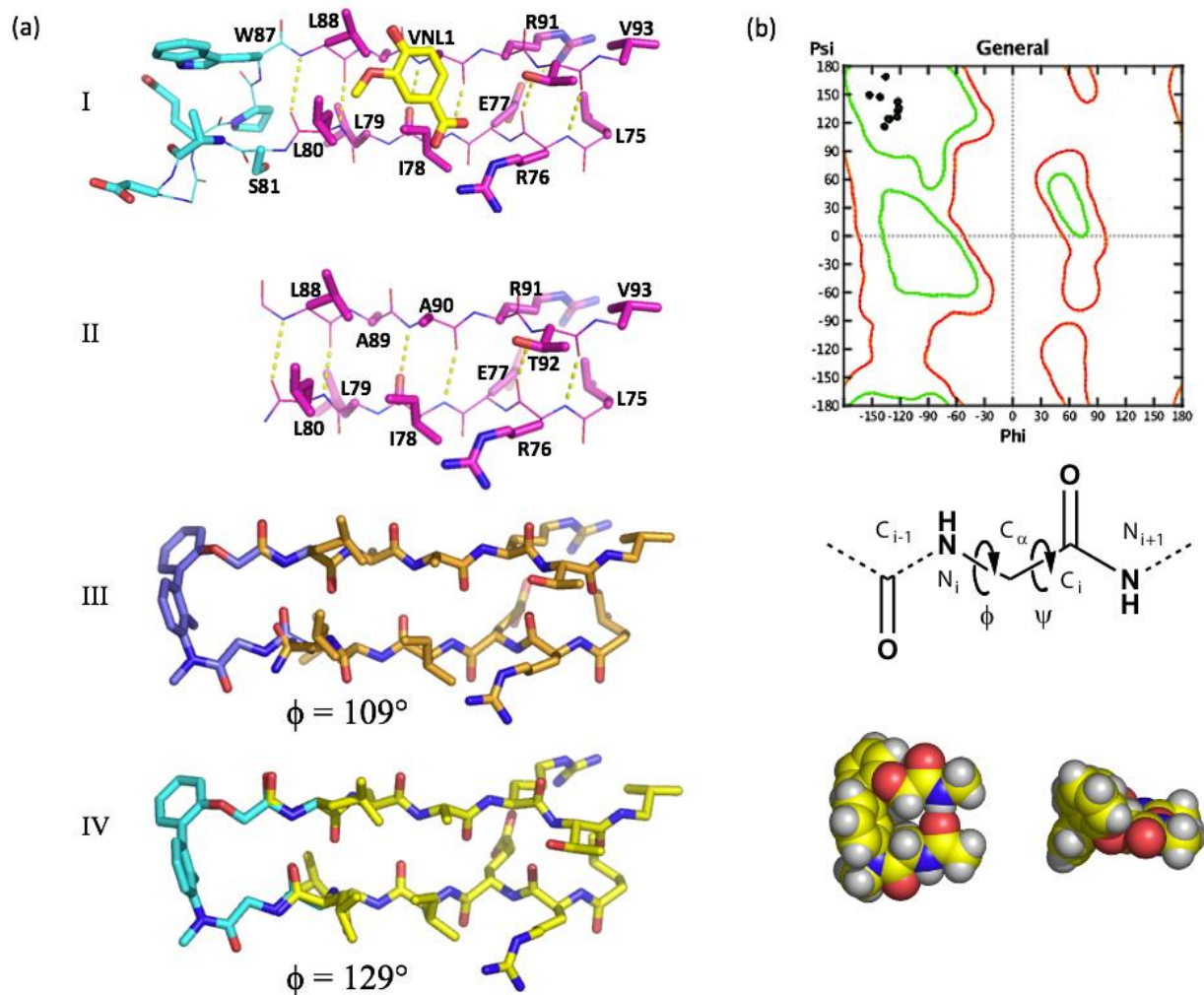


Figure 16. (a) Native CPL₇₅₋₉₃ (I); truncated CPL₇₇₋₉₃ gives CPL₇₅₋₈₀ and CPL₈₈₋₉₃ (II); overlay of biaryl (*ortho*-tolyl)amide-amino acid template to link CPL₇₅₋₈₀ and CPL₈₈₋₉₃ (III; IV). (b) Averaged backbone torsion angles benchmarked within the Ramachadran plot. The torsion is defined as C_{*i*-1}-C-1-C-1'-C-*i*-1' from NHC(O) to C(O)NH. Rotation of the truncated strands from $\phi = 109^\circ$ to $\phi = 129^\circ$ (from III and IV) enforces desired strand/strand alignment in allowed region for β -sheets. Minimized structure of the biaryl(*ortho*-tolyl)amide amino acid template for β -turn mimetic torsion balance scaffold from the side and bottom views.

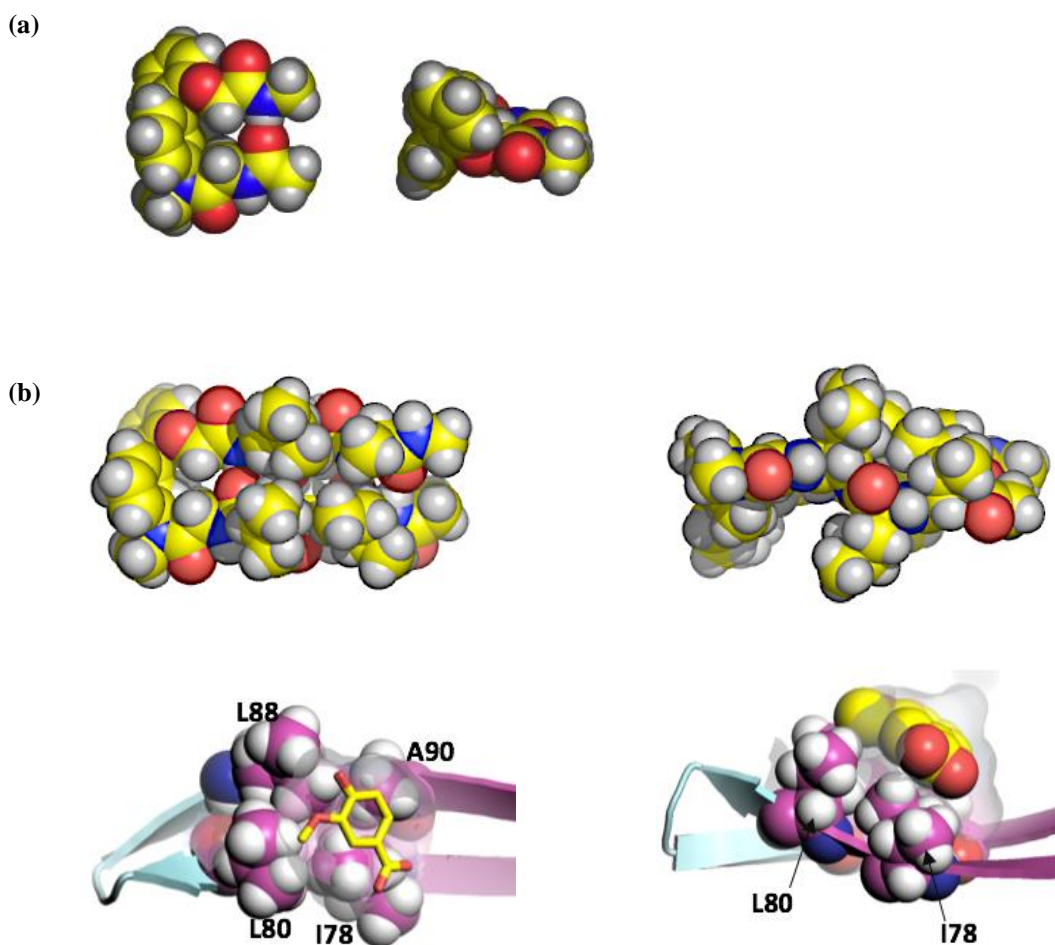


Figure 17. Minimized structures of the β -turn mimetic torsion balance from the top (left) and bottom (right) views of (a) the core scaffold and (b) tetrapeptide CPL derivative. (c) Formation of hydrophobic cluster between alkyl side chain residues in folded CPL₇₅₋₉₃ reproduced from Figure 13 for comparison to the hexapeptide mimetic. PDB: 1XLR.^{75a}

A secondary objective was to develop a reliable strategy to prepare a library of hairpin structures. Our design allowed for this desired utility. To address the unknown solubility of our model, a methyl ester was incorporated on the upper ring. Ester hydrolysis could provide increased hydrophilicity to improve solubility in aqueous media for NMR experiments. Aware of the problematic self-assembly of sheet mimics to form intermolecular hydrogen-bonded cross structures, we planned to acetylate the terminal amine to form an N-acetyl amide, and, amidate the terminal carboxylate to form an N-methyl amide to avoid intermolecular association. These

termini modifications have been shown in interleukin-8 (IL-8) to adopt the *trans* amide conformation required for β -sheet formation and to prevent dimerization.⁷⁹

Structural assignment of the torsion balance derivatives is required to validate our design and accurately determine the effects of amino acid changes on β -turn configuration and stability.⁸⁰ Initial synthetic work and NMR experiments were described by Liberatore.⁸¹ ¹H NMR and EXSY experiments were described by Dr. Melissa Liberatore were used to calculate the torsion balance rotational barriers, which we discuss in Chapter 3.⁸¹ NMR data indicate the unfolded and folded states of the torsion balance are related as atropisomers in the biaryl template. Although the modeled scaffold has the overall shape necessary to match with the ends of an anti-parallel β -sheet, further investigation of the torsion balance structure was necessary to probe hydrogen bond formation.

In the current study, we aimed to conformationally control the balance through incorporation of bromines *ortho* to the side chains, with the goal of investigating alignment of the *o*-methylene ether side chains on the top half of the balance to promote interchain hydrogen bonding. Modeling suggests that 90° (relative to the plane of the aromatic ring) is the best angle to provide alignment (Figure 18). To achieve this conformation, we introduced bromine atoms *ortho* to the aryl ethers to enforce intramolecular interchain hydrogen bonding. This strategy would allow us to minimize the conformational entropy at the site of nucleation by imposing a noncovalent steric constrain between the bromine and ether methylenes. This technique was recently reported by Chatterjee et al. to induce a pseudoallylic strain between atoms of *i*+1 and *i*+2 residues in the reverse turn. Computational models indicated the radius of bromine was the correct size to provide a steric effect on the ether side chains and impose the desired conformational bias

in our template. 1D and 2D NMR experiments were carried out to investigate preferential folding and stability of the β -turn sequence.

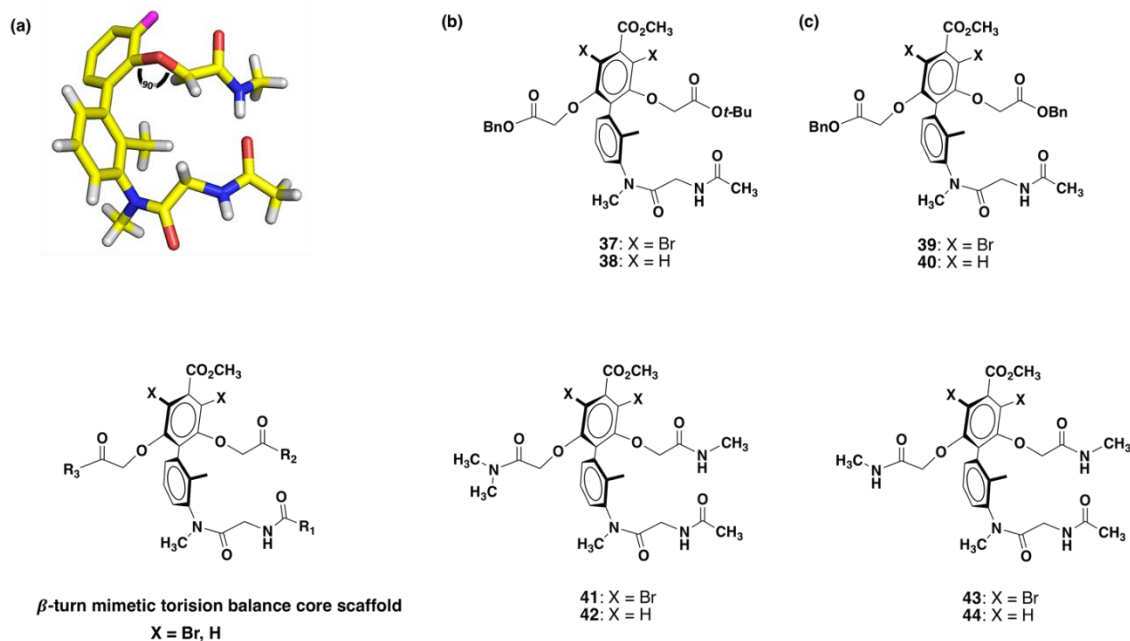


Figure 18. Conformationally controlled β -turn mimetic torsion balance core targets and control analogs. (a) 90° (relative to the plane of the aromatic ring) is the best angle to provide alignment for interchain hydrogen bonding in an antiparallel β -sheet motif. (b) Thermodynamic β -turn mimetic torsion balance core target **37** and control **38**. Ac-Gly-N(H)Me-N(Me)₂ Target **41** and control **42**. (c) Kinetic β -turn mimetic torsion balance core target **39** and control **40**. Ac-Gly-(N(H)Me)₂ Target **43** and control **44**.

2.2.2.2 β -Turn Mimetic Template

Core scaffolds of the thermodynamic (**37**) and kinetic (**39**) conformationally controlled β -turn mimetic torsion balances are shown in Figure 18. These structures differ from controls **38** and **40** by the presence of bromines on the top ring of **37** and **39**. We determined the control structures would be best to evaluate conformational effects from the bromines alone. We hypothesized **41** and **43** would form a stronger hydrogen bond than **42** and **44**. This study describes the synthesis toward targets **41** and **42**.

2.3 SYNTHESIS OF A CONFORMATIONALLY CONTROLLED β -TURN MIMETIC TORSION BALANCE CORE

In this project, two alternate routes to core targets were examined. Our first experiments were directed toward the thermodynamic, or asymmetric, torsion balance, which has orthogonally protected side chains at positions *a*, *b*, and *c*. The pathway was based on installment of two different upper side chains before the aryl coupling to give an asymmetrical balance (Scheme 1). In contrast, the second set of experiments discussed features addition of the upper side chains after the aryl coupling to form the kinetic, or symmetrical, biaryl core.

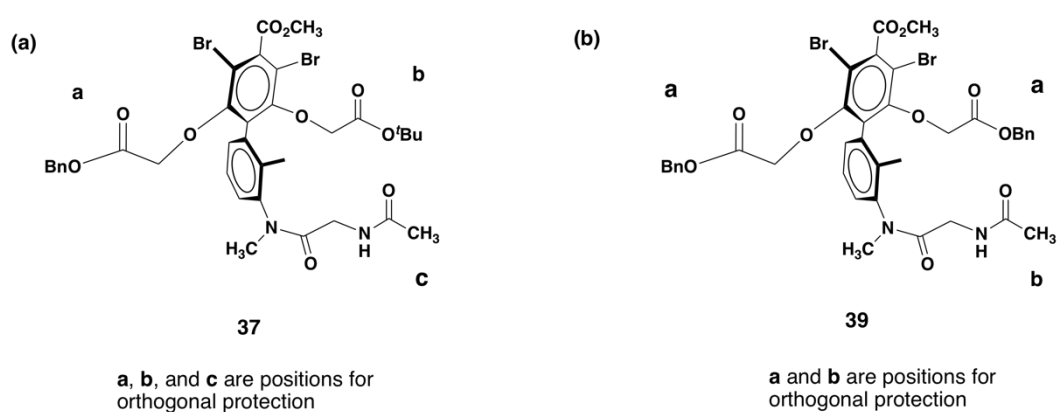


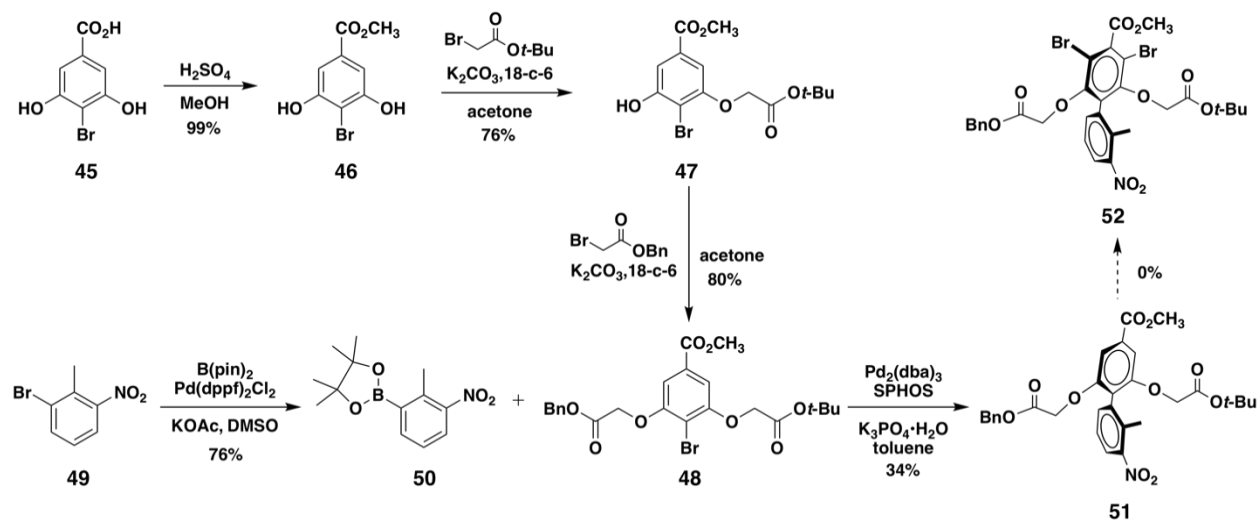
Figure 19. Orthogonal protection sites of conformationally controlled asymmetrical (**37**) and symmetrical (**39**) β -turn mimetic torsion balance core scaffolds.

2.3.1 Asymmetrical Synthesis

2.3.1.1 Method I

Following Liberatore's synthesis of the asymmetrical desbromo balance, we individually prepared the asymmetrical top and bottom halves of the balance for Suzuki coupling (Scheme 1.)⁸¹ Fischer esterification of commercially available 4-bromo-3,5-dihydroxybenzoic acid **45** afforded the methyl benzoate **46** in 99% yield. Alkylation of **46** with commercially available *t*-butyl bromoacetate gave **47** in 35% yield.⁸² Asymmetrical product was separated from its symmetrical ether via flash chromatography and subjected to the alkylation protocol using commercially available benzyl bromoacetate to form asymmetrical coupling fragment **48** in 80% yield.⁸² The bottom half of the balance **50** was provided in 70% yield by subjecting commercially available 2-bromo-6-nitrotoluene **49** to Miyaura boration conditions⁸⁹ with bis(pinacolato)diboron ((Bpin)₂) as the boron nucleophile. Suzuki Miyaura cross-coupling reaction^x of **48** and **50** provided biaryl **51**, which could then be brominated to afford the dibromo derivative **52**.

Scheme 1. Synthesis toward asymmetrical β -turn mimetic torsion balance **37**.

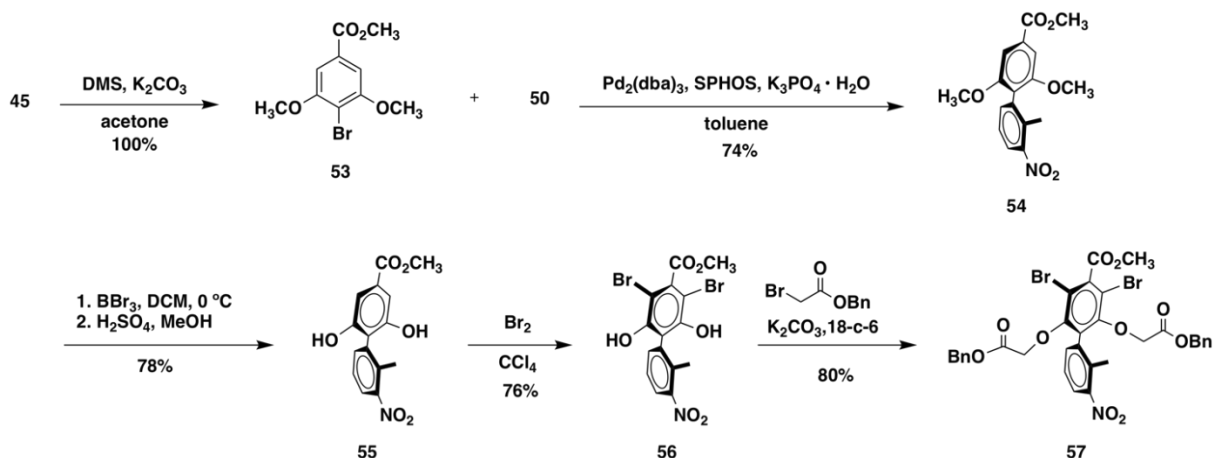


We anticipated the coupling step should be done before bromination because of the coupling fragments exhibiting a total of three *ortho*-substituents and a *meta*-substituent; dibromination of **48** would not only increase the difficulty of the coupling reaction due to the presence of two additional *meta*-substituents but also decrease the yield because of competing cross-couplings reactions. Treatment of fragments **47** and **48** with tris(dibenzylideneacetone)dipalladium(0) (Pd₂(dba)₃) in toluene, accompanied by Buchwald's phosphine ligand⁸⁸ afforded the Suzuki-Miyaura cross-coupled product **48** with a yield of 34%. Methods attempted to achieve dibromination *ortho* to the side chains to produce **51** from **52** were unsuccessful.

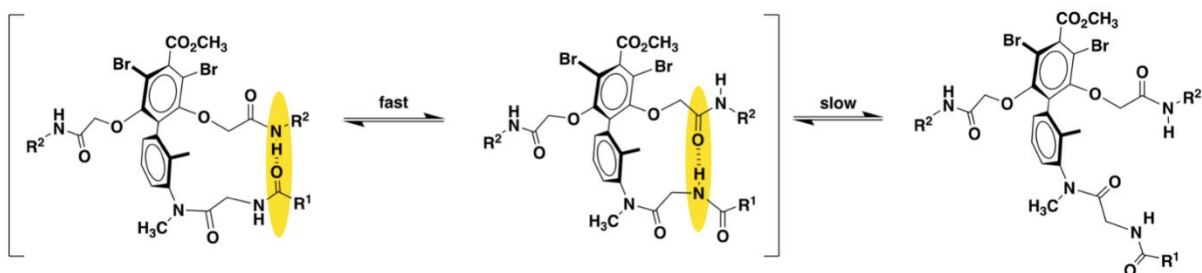
2.3.1.2 Method II

A modified synthetic route was developed (Scheme 2). The pathway featured the addition of the upper side chains after the aryl coupling and after bromination. Bromination on the phenol substrate before side chain attachment was readily achieved because of the enhanced activation and diminished steric hindrance of the phenol substrate in comparison with **51**. The alkylation step led to a symmetrical ether. Although this synthesis does not include the attachment of orthogonally protected side chains, our central question regarding the effect of dibromination on conformation could be answered using the symmetrical balance (Figure 19; Scheme 3) as discussed in Chapter 4.

Scheme 2. Synthesis of the torsion balance biaryl **57**.



Scheme 3. Three conformers of torsion balance **44** and control **43** (enantiomers not shown).



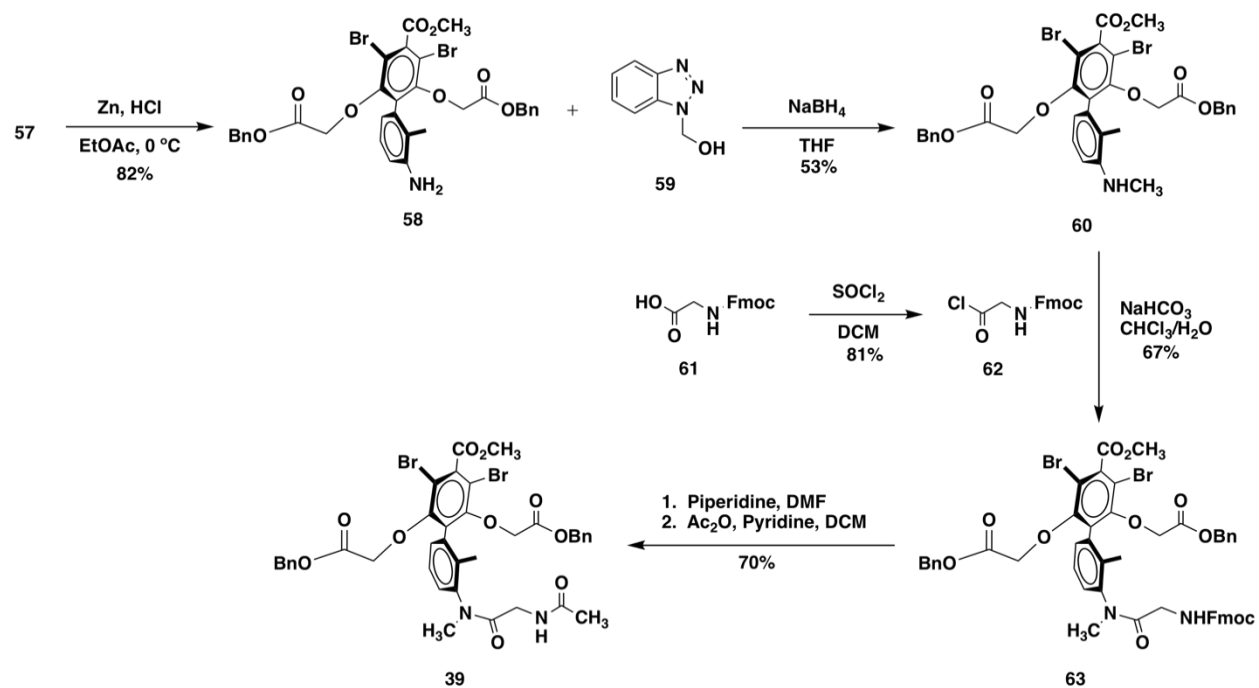
The synthesis of coupling fragment **53** was readily achieved with dimethylsulfate (DMS) to methylate commercially available 4-bromo-3,5-dihydroxybenzoic acid **45** in quantitative yield following recrystallization.⁸⁶ Cross-coupling of bromide **53** with boronic ester **50** using the same conditions for the Suzuki-Miyaura reaction as before afforded **51** with an exceptional yield of 74%. The increase in percent yield compared to formation of **52** (a yield of 34% in Scheme 2) is most likely due to the less sterically hindered nature of **51**. We employed a two-step reaction sequence of non-selective demethylation and subsequent Fischer re-esterification to afford dihydroxy-biaryl ester **55** in 78% overall yield. Biaryl **56** was subjected to 6 equivalents of BBr_3 in dichloromethane (DCM) followed by immediate esterification of the acid. Biaryl **54** was considered to be an

improved substrate for dibromination due to the more strongly electron-donating hydroxyl groups that replaced the inductively less activating α -benzyloxycarbonyl ether groups and due to diminished steric hindrance compared to substrate **48**. Treatment of **54** with 2.5 equivalents of Br₂ in carbon tetrachloride (CCl₄) afforded dibromination product **56** in 76% yield.⁴⁰ The symmetrical intermediate **57** was isolated in 80% yield after side chain attachment.

2.3.2 Symmetrical Synthesis

The bottom half of the balance was functionalized using the following protocol (Scheme 4). Reduction of biaryl **14** by Zn/HCl gave an 80% yield of **19**.⁵⁰ Treatment of **19** with **20**, followed by reduction with NaBH₄ afforded the methylated biaryl **60** in 53% yield. Commercially available 9-fluorenylmethoxycarbonyl-glycine (Fmoc-Gly) was converted to its corresponding acid chloride **62** with thionyl chloride, which was immediately coupled with biaryl **60**. Amide **63** was isolated in 67% yield. The final step to synthesize torsion balance core **39** involved treatment of **63** with piperidine in DMF to deprotect the amino acid, followed by immediate acylation with acetic anhydride (Ac₂O) and pyridine (76% yield).

Scheme 4. Successful completion of the symmetrical glycine core **39**.³⁹



3.0 EVALUATION AND VALIDATION OF THE WILCOX β -TURN MIMETIC TORSION BALANCE DESIGN

The results in Section 3.1 have been published in:

Liberatore, M. A. Synthesis and NMR Studies of a β -Turn Mimetic Molecular Torsion Balance. Ph.D. Dissertation, University of Pittsburgh, Pittsburgh, PA, 2012.⁸¹

In order to establish the peptide-hybrid molecular torsion balance scaffold as a viable β -turn mimic for the anti-parallel β -sheet motif, it was essential to first validate the novel design as a molecular torsion balance. Generally, a molecular torsion balance connects two functional groups (the top and bottom halves) by a gently restricted bond rotatable at room temperature ($\Delta G^\ddagger = 14$ kcal/mol) for detection of intramolecular folding preferences between the top and bottom halves by ^1H NMR. Liberatore evaluated rotational restriction of the desbromo torsion balance scaffold to meet the general criteria, which provides a foundation for our study of the dibromo torsion balance.

3.1 CONFORMATIONAL ANALYSIS OF CORE STRUCTURE

Model systems were used to gain insight into the folding preferences of advanced torsion balance derivatives (Figure 20). Carbamates **64** and **65** and amides **66** and **67** were analyzed by dynamic line shape analyses and EXSY experiments to determine torsion balance rotational barriers about

the aryl amide and N-aryl bonds, respectively.¹⁹ Biaryl amine **68** was studied by HPLC kinetic equilibrium methods to determine the torsion balance aryl-aryl barrier to rotation.¹⁷

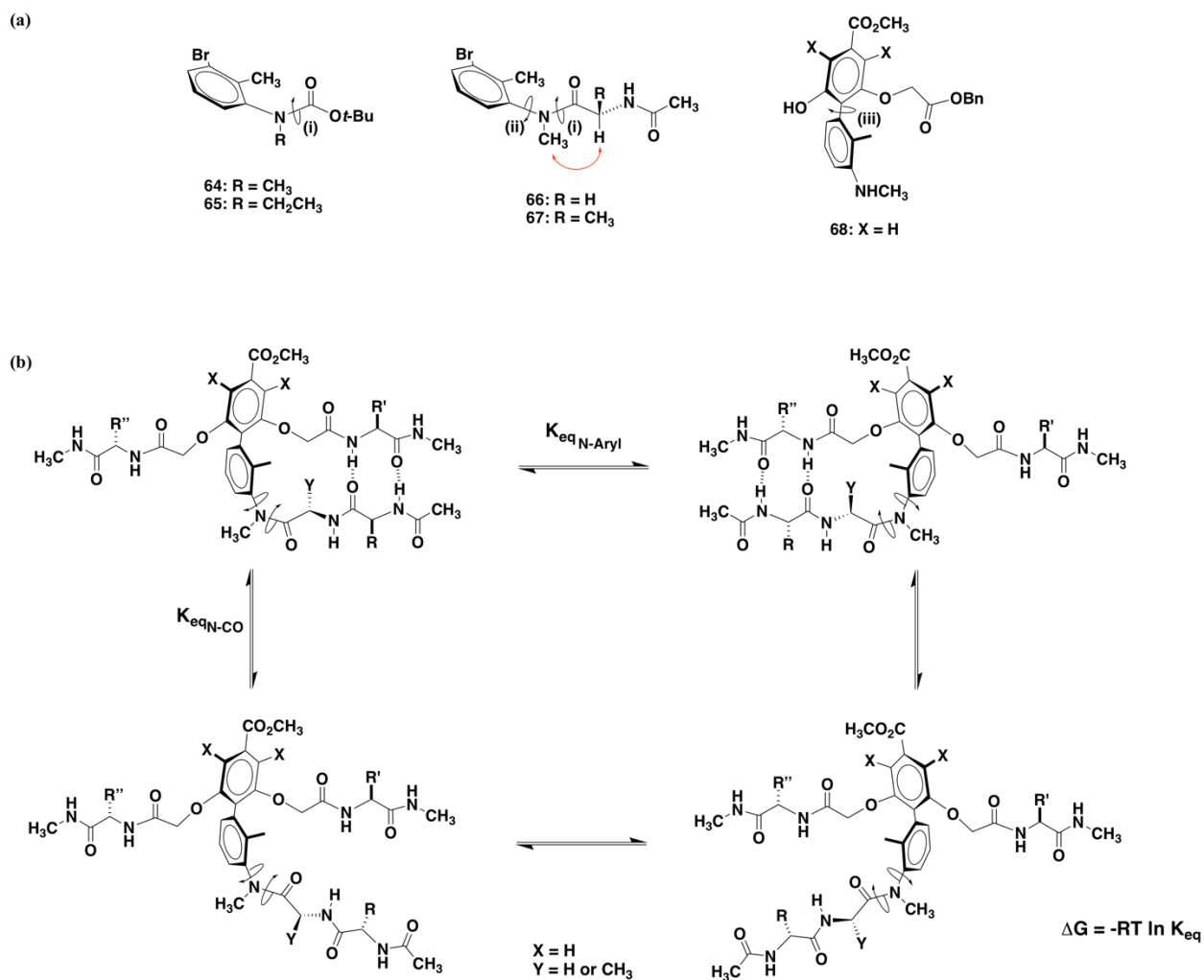
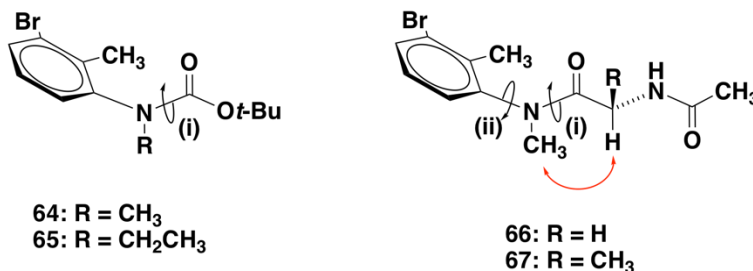


Figure 20. Systems studied to determine folding preferences of the β -turn mimetic torsion balance scaffold.⁸¹ (a) Models for quantifying aryl amide, N-aryl and aryl-aryl bond rotational barriers. (b) Example β -turn mimetic torsion balance derivative and possible rotations around N-aryl and aryl amide bonds. The R groups are different and each represents an amino acid.

Liberatore's results quantify restricted rotation around the aryl amide N-C(O), N-aryl and aryl-aryl bonds.⁸¹ Results of conformational analyses of **64-7** are reported in Table 6. The R groups studied were determined to have no effect on bond rotation, and therefore data reported for carbamates **64-65** and amides **66-67** are the same for each pair of model systems. The methyl substituent *ortho* to the carbamate led to a larger aryl amide N-C(O) rotational barrier ($\Delta G^\ddagger = 17$ kcal·mol⁻¹ at 298 K in CDCl₃) for *syn/anti* rotamers of **64-65** compared to Smith's 2-methyl-2-propanylmethyl(phenyl)carbamates.¹⁰²

Smith reported a rotational barrier of 12.5 kcal·mol⁻¹ around the aryl amide N-C(O) axis in a series of *para*-substituted *t*-butyl *N*-methyl-*N*-aryl carbamates that unlike **64** and **65**, lack a substituent *ortho* to the carbamate. The aryl amide N-C(O) rotational barrier in **66** and **67** was approximated to be the same as that in **64** and **65**. The higher barrier to rotation about the N-aryl bond in **66** and **67** ($\Delta G^\ddagger = 21$ kcal·mol⁻¹ at 343 K in toluene-*d*₈) compared to that of the aryl amide N-C(O) bond, suggested that the N-aryl bond was responsible for the major conformer while the aryl N-C(O) bond rotation was responsible for the minor conformer in ¹H NMR spectra at 298 K. This ratio of conformers was 93:7 in **66** and **67**. The aryl-aryl barrier to rotation in **68** ($\Delta G^\ddagger = 36$ kcal·mol⁻¹ at 418 K in hexanes with a $t_{1/2} = 2.2$ days at 418 K or $t_{1/2} = 2.8 \times 10^6$ years at 298 K) is so high that it is essentially a locked system at room temperature. We expect the rotational barriers in these systems to provide a good estimate of those in advanced desbromo and dibromo torsion balance targets (Figure 20).

Table 6. N-Aryl and aryl amide N-C(O) rotational barriers in **64-67**.^{81,108}



Compound	Bond	$\Delta G^{\ddagger a,b}$ (kcal/mol)	T (K)	$t_{1/2}$ (298 K) ^c (s)	$t_{1/2}$ (312 K) ^c (s)
64	N-C(O) (i)	17	298	0.2	0.04
65	N-C(O) (i)	17	298	0.2	0.04
66^d	N-C (ii)	21	343	140	30
67^d	N-C (ii)	21	343	140	30

^a Calculated from line shape analysis of the ¹H NMR spectra acquired on a 500 MHz NMR. ^b ± 0.5 kcal/mol. ^c Calculated using ΔG^{\ddagger} , assuming $\Delta S^{\ddagger} = 0$. ^d For ΔG^{\ddagger} of N-C(O) (i), see ΔG^{\ddagger} of N-C(O) (i) in **64** and **65**.

3.2 INVESTIGATION OF CONFORMATIONAL CONSTRAINT IN THE DIBROMO TORSION BALANCE

In the desbromo torsion balance scaffold, there was no substituent *ortho* to the aryl ether bonds to restrict rotation about the aryl C-O axis. We anticipated the incorporation of bromines *ortho* to the ether side chains would raise the aryl C-O rotational barrier. Biaryl benzyloxycarbonyl diether **58** was studied to realize the effects of bromines on the aryl C-O rotational axis.

3.2.1 Evaluation of Biaryl Benzyloxycarbonyl Diether **58** and Aryl Ether Bond Rotation

At 298 K, no evidence of restricted rotation was observed for biaryl benzyloxycarbonyl diether **58** by ^1H NMR analysis in CDCl_3 and CD_2Cl_2 . This led us to examine **58** by ^1H NMR experiments in CD_2Cl_2 over a temperature range from 178 to 273 K to look for evidence of restricted rotation around the aryl C-O bond (Figure 21). If aryl C-O rotation was restricted in biaryl **58**, we would expect to see diastereotopic α -methylene protons, “A” and “B”, by ^1H NMR.

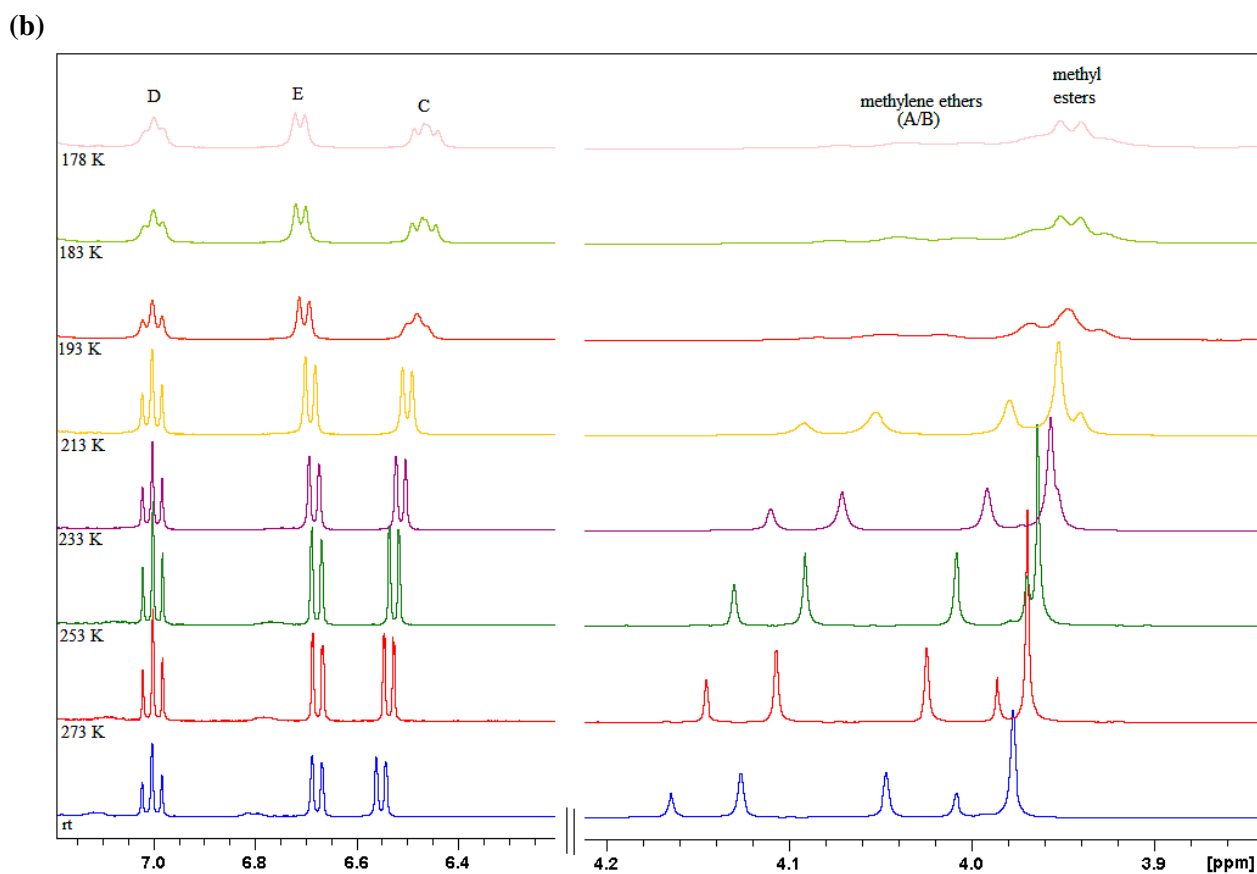
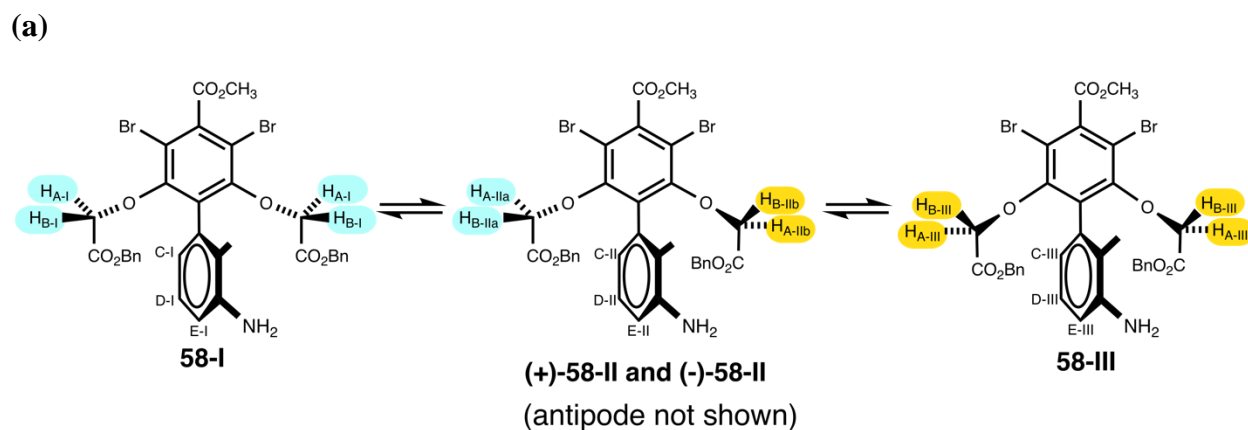


Figure 21. Conformational analysis of biaryl benzyloxycarbonyl diether **58**. (a) Conformations **I**, **II**, and **III**. The methylene protons *syn* and *anti* to the aryl methyl are shown in gold and blue, respectively. (b) Effect of temperature on the ^1H NMR spectra in CD_2Cl_2 (400 MHz) from 178 K to 298 K.

Results of low temperature ^1H NMR studies of **58** revealed evidence of conformational restriction about the aryl C-O axis. The AB quartet of diastereotopic α -methylene protons, “A” and “B”, broadens as temperature decreases and begins to separate into two AB quartets at 183 K.

Our hypothesis is one AB quartet is due to α -methylene protons that are *syn* to the amine, and the other is due to α -methylene protons that are *anti* to the amine. These *syn* and *anti* conformations are highlighted in Figure 21 in gold and blue, respectively. We expect very similar chemical shifts between protons highlighted in blue in **58-I** and **58-II**, and between protons highlighted in gold in **58-II** and **58-III**. The methyl ester's methyl proton signal "F" also broadens with decreasing temperature and splits into two signals at 183 K, overlapping with the AB quartet of the methylene protons. Additionally, the ^1H NMR spectra show the broadening of aromatic protons "C", "D" and "E". The doublet of the aromatic proton "C", *ortho* to the top aryl group, splits into two doublets at 183 K. This behavior of proton "C" provides further evidence to support our hypothesis. Altogether these observations are consistent with restricted bond rotation around the aryl C-O bonds.

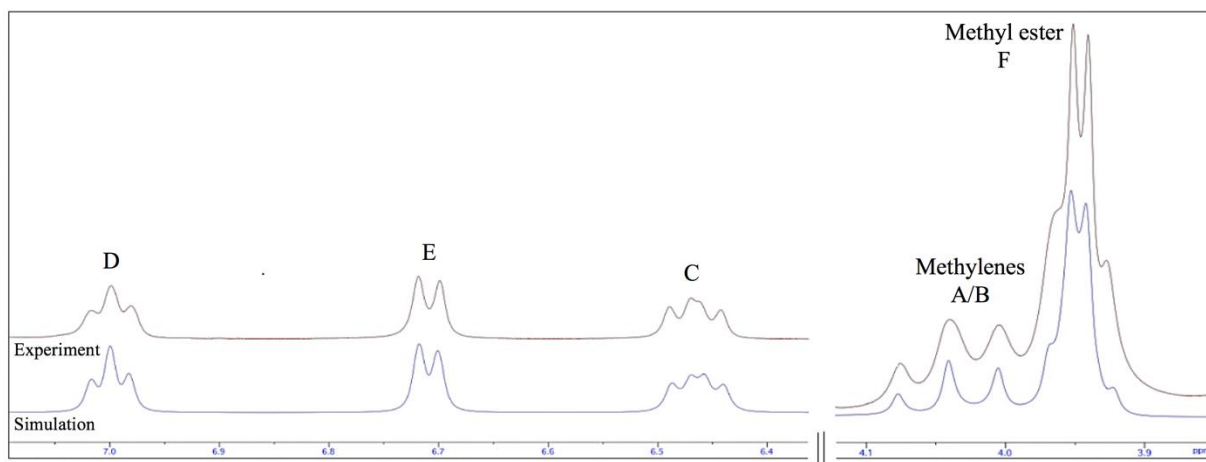


Figure 22. Simulated and experimental ^1H NMR data of biaryl benzyloxycarbonyl diether **58** in CD_2Cl_2 (400 MHz) at 183 K.

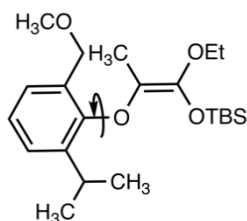
Dynamic NMR simulations of these data at 183 K were created using iNMR and agreed well with our above hypothesis (Figure 22). The simulation used a simplified model in that we assumed all *syn* methylene chemical shifts would be the same, and all *anti* methylene chemical

shifts would be the same, as mentioned above; however, it is expected there will be small differences amongst proton chemical shifts in those sets. We propose that the slightly different chemical shifts of each rotamer contribute to the broader appearance of methylene protons observed in the experimental spectrum compared to simulated data; yet, signal overlap of the two methyl ester's methyl proton shifts may also contribute to this effect. Because we did not know the exact chemical shifts of the AB quartet signals in the experimental ^1H NMR spectrum due to signal overlap of the methyl ester and methylene protons, the value of the shifts and coupling constant used for the simulation of *syn/anti* protons of "A" were estimated.

^1H	A	B	C	D	E	F
N	1	1	1	1	1	3
Multiplicity	d	d	d	dd	d	s
$^1\delta$ (PPM)	3.96 ^b	4.02	6.48	7.00	6.70	3.94
$^2\delta$ (PPM)	3.94 ^b	4.06	6.45	6.99	6.71	3.95
J (Hz)	14.4 ^b	14.4	8.0	8.0, 8.0	8.0	-

^a ΔG^\ddagger was determined from $k = 5.0$ s $^{-1}$ using the Eyring equation. ^b Estimated values.

The simulation best fit experimental data at an exchange rate of 5.0 s $^{-1}$. NMR line shape analysis provided the rotational barrier of biaryl benzyloxycarbonyl diether **58** of 9.9 ± 0.5 kcal·mol $^{-1}$ at 183 K in CD $_2$ Cl $_2$ (Table 7). In a similar case, Yoshimura reported a barrier to rotation for silyl ketene acetal **70** to be 11.5 kcal·mol $^{-1}$ at 231 K (Figure 23).¹⁰¹ However, his molecule contains a methyl group at the branched α -carbon to the aryl C-O bond as well as methylmethoxy and isopropyl groups *ortho* to the ether. The lower rotational barrier in **58** compared to **70** is most likely due to our structure being less bulky at the α -carbon.



11.5 kcal·mol⁻¹ at 231 K in CD₂Cl₂

Figure 23. Aryl ether rotational barrier of Yoshimura's silyl ketene acetal **70**.¹⁰¹

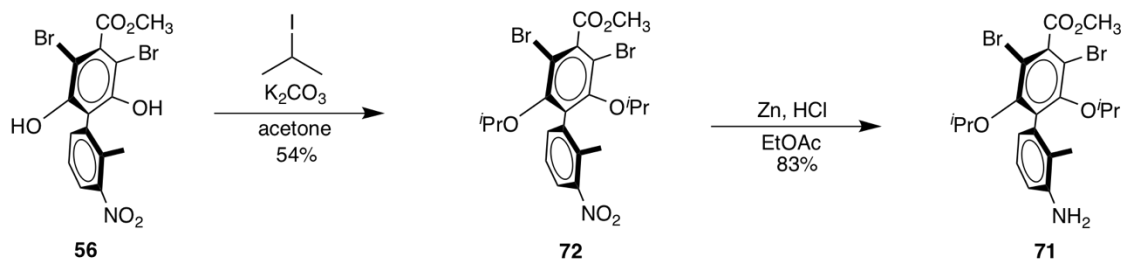
3.2.2 Synthesis and Analysis of Biaryl Isopropyl Diether **71**

We further examined the rotational restriction about the aryl C-O bonds by investigating effects of alkyl group size on hindered C-O rotation. We prepared biaryl isopropyl diether **71** for variable temperature ¹H NMR data collection to reevaluate the rotational barrier using line shape analysis. In the isopropyl case, we would be able to observe the behavior of the diastereotopic methyl doublets. This would eliminate ¹H NMR signal overlap with the ester and ether side chains.

3.2.2.1 Synthesis of biaryl isopropyl diether **71**

Biaryl isopropyl diether **71** was prepared over a straightforward two-step sequence (Scheme 5). Alkylation of **56** with iodopropane and K₂CO₃ in acetone gave **72** in 54% yield. Intermediate **72** was subjected to nitro group reduction using Zn/HCl from 0 °C to 298 K for 13 hours to produce **71** in 83% yield.

Scheme 5. Synthesis of biaryl isopropyl diether **71**.



3.2.2.2 Analysis of biaryl isopropyl diether **71**

We subjected **71** to variable temperature ^1H NMR experiments from 183 K to 298 K in CD_2Cl_2 to examine the restricted rotational barrier about the aryl C-O bond (Figure 24). The ^1H NMR spectrum of isopropyl diether biaryl **71** at 298 K revealed only one set of peaks. If the rate was lower than 0.017 s^{-1} and if α -methyl protons, “A” and “B”, have different chemical shifts, we would expect aryl C-O rotation to be sufficiently restricted in **71** and to permit observation of diastereotopic α -methyl protons, “A” and “B”, in the ^1H NMR spectrum.

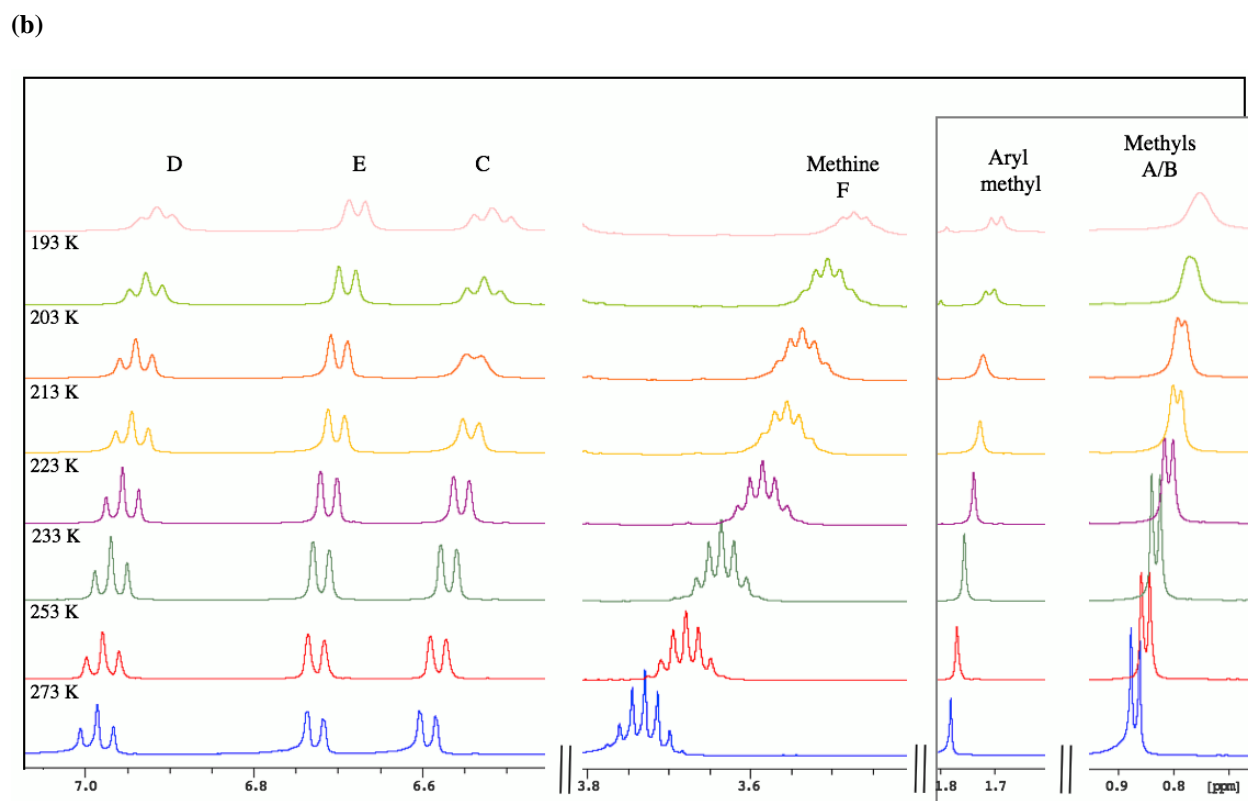
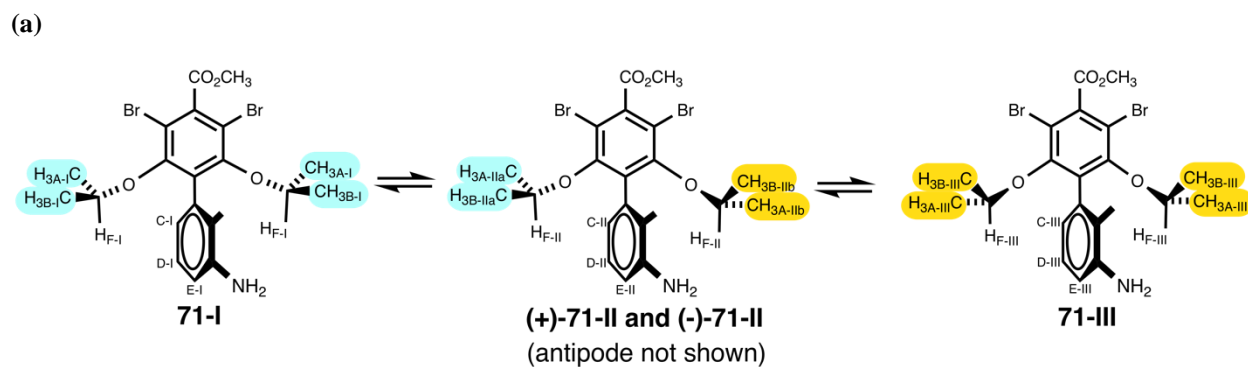


Figure 24. Conformational analysis of biaryl isopropyl diether **71**. (a) Conformations **I**, **II**, and **III**. The methyls *syn* and *anti* to the aryl methyl are shown in gold and blue, respectively. (b) Effect of temperature on the ^1H NMR spectra in CD_2Cl_2 (400 MHz) from 193 K to 298 K. The block on the right shows the aryl methyl protons and diastereotopic methyl protons of the isopropyls (A/B) at a decreased intensity, relative to that of the downfield aromatic and methine proton signals.

The ^1H NMR spectra of **71** provided evidence of conformational dynamics without the signal overlap that complicated the spectrum of **58** (Figure 24). The methyl doublets of the diastereotopic isopropyl protons, “A” and “B”, broaden as temperature decreases but never resolve into four peaks. The aromatic protons “C”, “D” and “E” behave similarly to those of **58**, in that

signals broaden with decreasing temperature. Because we were unable to recover meaningful data at temperatures lower than 193 K, the splitting of aromatic proton “C” and methine proton “F” into two separate signals was not observed; however, the aryl methyl protons on the lower ring broaden as temperature decreases and split into two signals at 193 K. We hypothesize this is due to the *syn* and *anti* conformations of the diastereotopic methyl protons, highlighted in gold and blue, respectively, in Figure 24. This observation is consistent with restricted bond rotation around the aryl C-O bonds.

The rotational barrier of biaryl isopropyl diether **58** was determined to be 10.7 ± 0.5 kcal·mol⁻¹ at 193 K in CD₂Cl₂ by dynamic line shape analysis ($k = 3.2$ s⁻¹; Figure 25). This barrier for **71** is higher than that of **58**. Their difference ($\Delta\Delta G^\ddagger = 0.5$ kcal·mol⁻¹ at 193 K) is most likely due to the increased steric hindrance at the α -carbon. The bulkiness of the isopropyl methyls (“A” and “B”) create additional steric crowding over the α -benzyloxycarbonyls of **71**. In this simulation, as in the simulation of **58**, expected small differences in chemical shifts of methyl protons are not incorporated. This may be the reason for the simulated peaks being slightly more narrow than the experimental result.

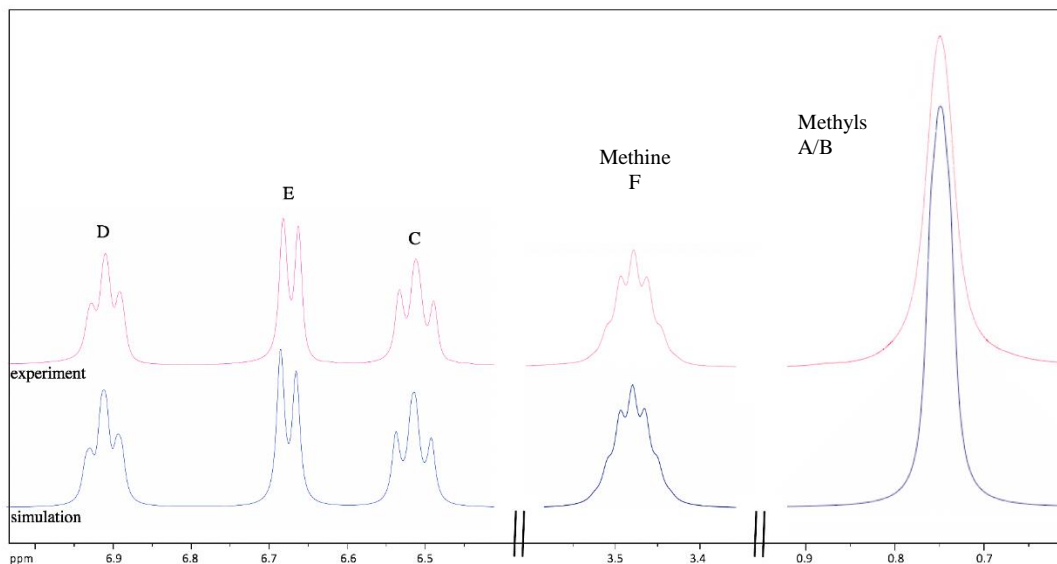
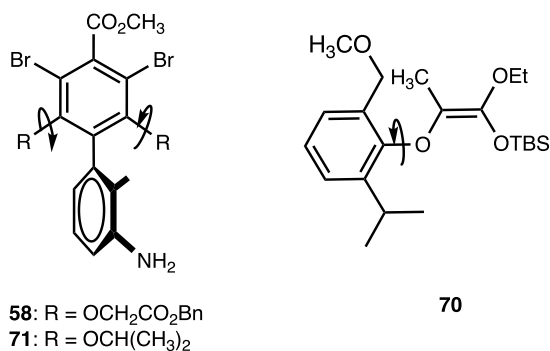


Figure 25. Experimental (top) and simulated (bottom) ^1H NMR spectra of biaryl isopropyl diether **71** in CD_2Cl_2 (400 MHz) at 193 K using iNMR.

These results quantify restricted rotation about the aryl ether bond in the dibromo β -turn mimetic torsion balance (Table 8). The aryl C-O barrier to rotation calculated for C-O bonds in biaryl isopropyl diether **71** and Yoshimura's silyl ketene acetal **70** ($10.7 \pm 0.5 \text{ kcal}\cdot\text{mol}^{-1}$ at 193 K in CD_2Cl_2 and $11.5 \text{ kcal}\cdot\text{mol}^{-1}$ at 231 K in toluene- d_8 , respectively) are in close agreement; however the slightly greater barrier observed for **70** is most likely due to steric crowding from the additional bulk at the α - and β -carbons and aryl C2 and C6 positions.

Table 8. Aryl C-O rotational barriers in **58**, **70**¹⁰¹ and **71**.

Compound	k^a (s ⁻¹)	$\Delta G^{\ddagger b,c}$ (kcal/mol)	T (K)	$t_{1/2}$ (193 K) ^d (s)	$t_{1/2}$ (213 K) ^d (s)
58	10.3	10	193	0.067	0.0056
70	3.2	11	193	0.22	0.017
71		11.5	231	-	-

^a Exchange rates that best matched the simulation to the experimental data. ^b Calculated from line shape analysis of the ¹H NMR spectra acquired on a 400 MHz NMR. ^c ±0.5 kcal/mol. ^d Calculated using given ΔG^{\ddagger} assuming $\Delta S^{\ddagger} = 0$.

3.3 CONFORMATIONAL ANALYSIS OF THE DIBROMO β -TURN MIMETIC TORSION BALANCE CORE

Because we hypothesized bromine incorporation *ortho* to the aryl ether bonds would provide steric control of upper side chain conformation to improve the structure of our peptide-torsion balance for β -turn mimicry and interchain hydrogen bonding in an antiparallel β -sheet configuration, the effects of bromine incorporation on the core conformation were assessed for evidence of improvement.

When both side chains of the dibromo β -turn mimetic torsion balance core are the same and have only achiral elements, rotation around the N-aryl bonds leads only to enantiomers; rotation around the aryl amide N-C(O) bond leads to diastereomers. Of these diastereomers, only

the *E* isomer has the potential to form an interchain hydrogen bond. Thus, a conformational study was carried out on the core structure (Gly target **13**) to preliminarily evaluate the propensity of the dibromo torsion balance to mimic a β -turn and participate in interchain hydrogen bonding. Gly target **39** was subjected to ^1H NMR and ROESY experiments in CDCl_3 and CD_2Cl_2 at 298 K (Figures 26- 27).

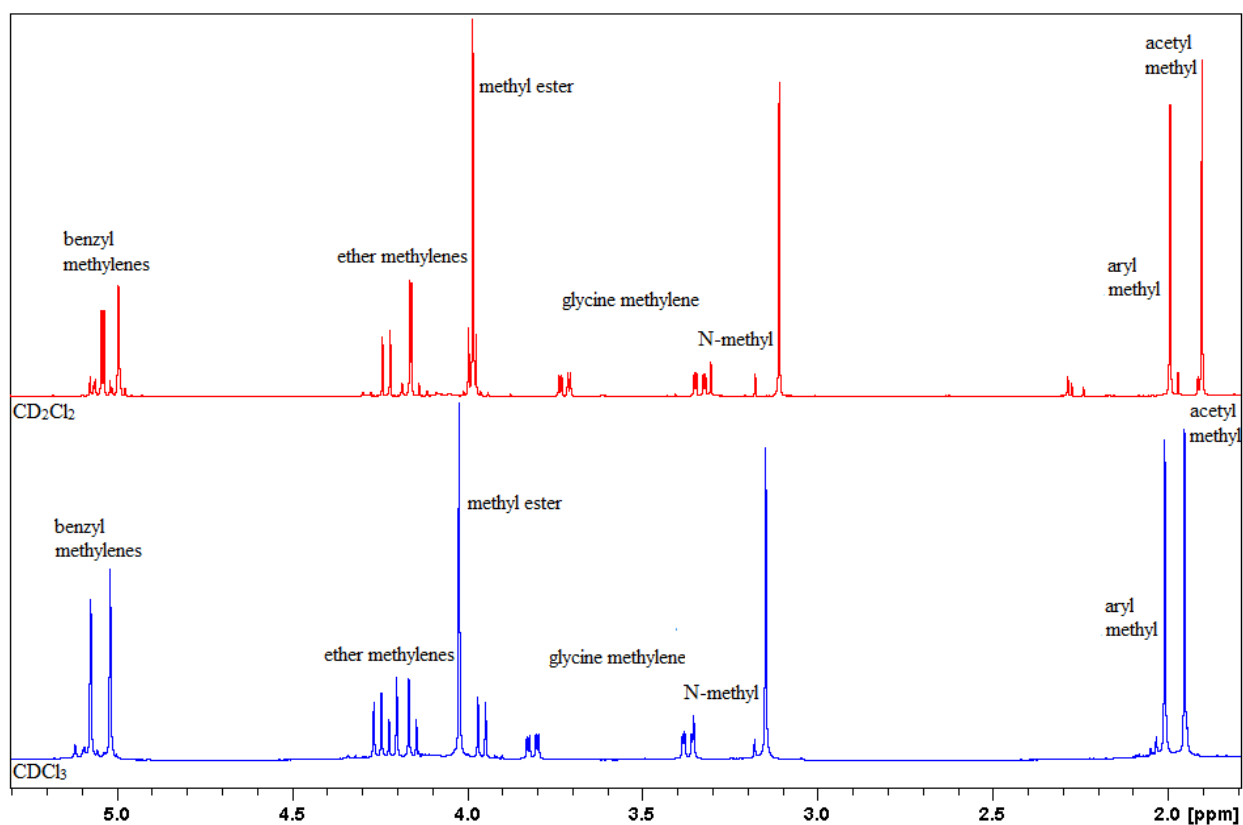


Figure 26. ^1H NMR spectra of Gly target **39** in CDCl_3 (bottom) and CD_2Cl_2 (top) at 298 K on a 700 MHz NMR. The chemical shift in CDCl_3 is slightly more downfield ($\delta = 3.25$ ppm) than in CD_2Cl_2 ($\delta = 3.21$ ppm).

Because rotation around the N-aryl bond leads only to enantiomers in **39**, we expected a simple NMR spectrum with only the two conformers that arise from rotation around the aryl amide N-C(O) bond. Two aryl N-methyl group singlets are observed in ^1H NMR spectra of **39** at 298 K

in both CDCl_3 and CD_2Cl_2 (Figure 26). ROESY and EXSY data support our hypothesis that restricted rotation around the aryl amide N-C(O) bond is responsible for the two conformers observed (Figure 27). The $E:Z$ ratio of **39** was found to be 94:6. This ratio confirms an isomeric preference in the dibromo core that is necessary to achieve intramolecular hydrogen bond formation within our peptide-torsion balance scaffold. This work is significant because it will inform our later studies in folding preferences and hydrogen bond selectivity of advanced dibromo β -turn mimetic derivatives.

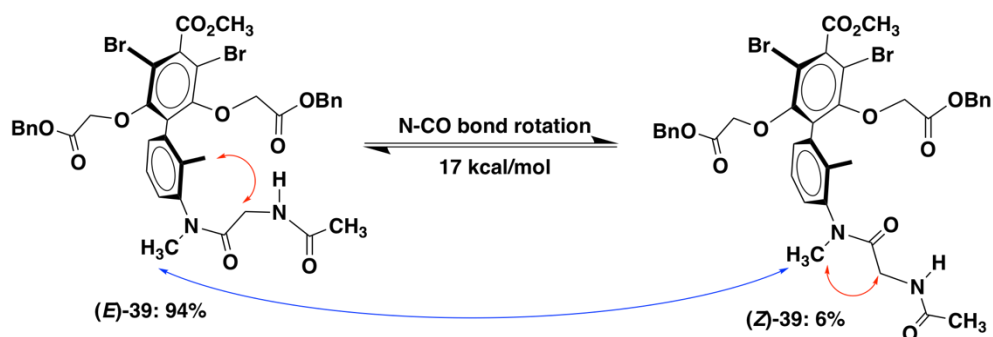


Figure 27. Two conformers of Gly target **39** by rotation around the aryl amide N-C(O) bond. ROESY and EXSY data are highlighted for glycine methylene and N-methyl protons in CDCl_3 at 298 K.

4.0 SYNTHESIS AND NMR STUDIES OF MONOMETHYLAMIDE TARGET 43 AND CONTROL 44

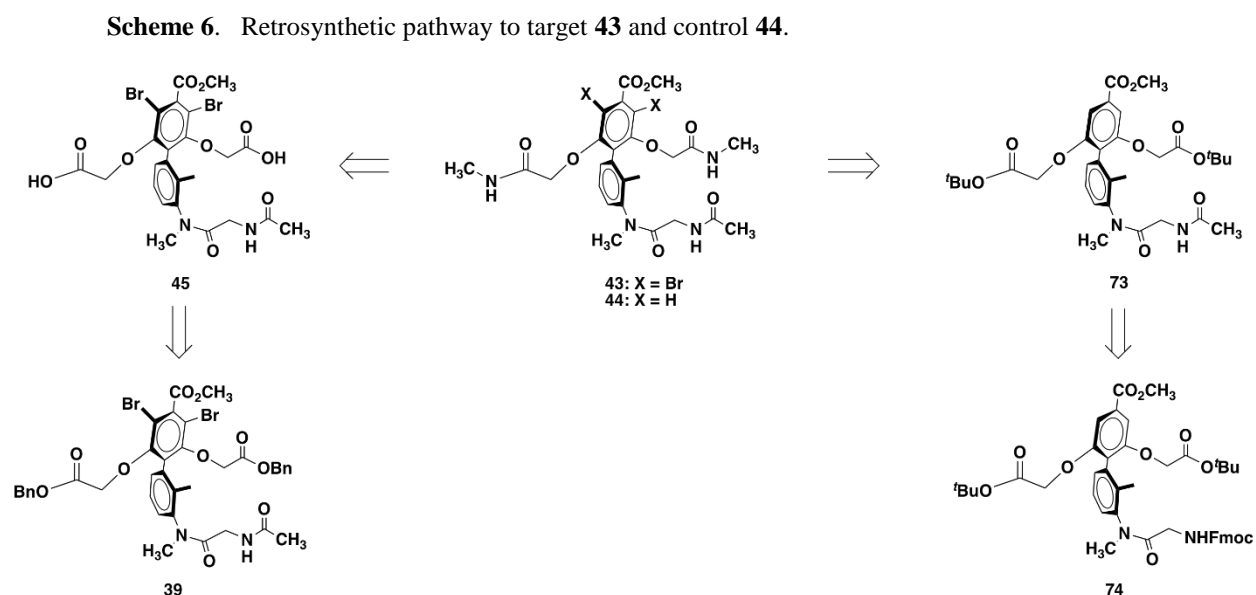
The results in this chapter have been published in:

Lypson, A.B. Wilcox, C.S. "Synthesis and NMR Analysis of a Conformationally Controlled β - Turn Mimetic Torsion Balance." *Journal of Organic Chemistry*, **2017**, 82, 898-909.

We extended our study of the torsion balance to further evaluate the effects of the bromines on folding when the ether side chains possess both a proton donor and acceptor. Therefore, we changed the side chain esters to amides to enhance hydrogen bond formation. Our goal was to detect any selectivity in the pattern for hydrogen bond formation, such as the glycine acetamide proton or the amide proton showing any preference to act as the hydrogen bond donor. The priority targets (dibromo target **43** and desbromo control **44**) share the same symmetrical structure, variable only at the *ortho*-substituent of the ether side chains. This would test the preference of an amino acid chain to hydrogen bond when the side chain is conformationally restricted.

4.1 RETROSYNTHETIC ANALYSIS OF MONOMETHYLAMIDE TARGET 43 AND CONTROL 44

We envisioned the synthesis of **43** to proceed by amide coupling of acid precursor **45**, after debenzoylation of **39**. Control amide **44** could be formed by deprotection and amidation reactions of **73**. Biaryl **73** would be formed by Fmoc-deprotection and acylation of biaryl amine **74**.

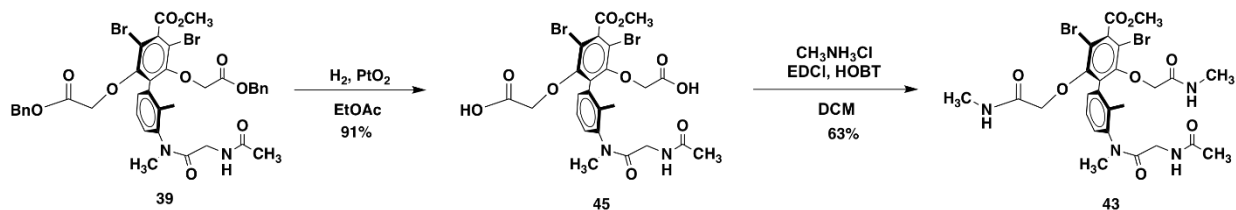


4.2 SYNTHESIS OF MONOMETHYLAMIDE TARGET 43 AND CONTROL 44

The synthesis of target **44** is shown in Scheme 7. Debzoylation of amide **39** by H_2/PtO_2 reduction generated diacid **45** in an excellent yield of 95% without any debromination product observed.¹⁰³ Amide coupling of diacid **32** by hydroxybenzotriazole (HOBt) with methylamine hydrochloride,

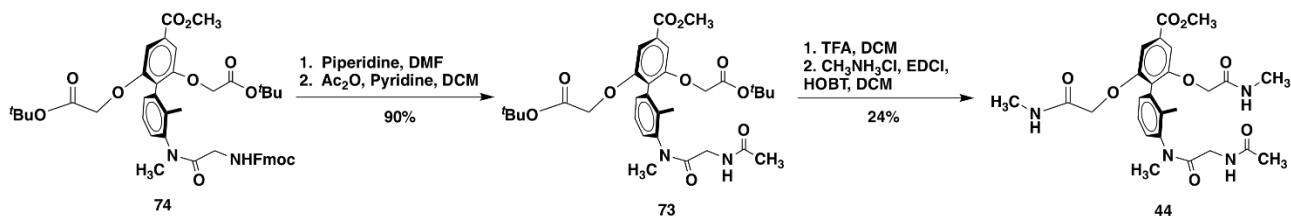
1-Ethyl-3-(3-dimethylaminopropyl)carbodiimide hydrochloride (EDCI), and diisopropylethylamine (DIEA) afforded the priority target **44** 63% yield.

Scheme 7. Synthesis of symmetrical torsion balance derivative **43**.



Synthesis of control **44** is shown in Scheme 8. Starting material **74** was supplied by Liberatore.⁸¹ Amide **73** was afforded in 70% yield by Fmoc deprotection by piperidine in DMF and subsequent acylation by treatment with acetic anhydride and pyridine. The *t*-butyl ester was cleaved with TFA and the same conditions as employed for previous amide couplings afforded the control amide **44** in 24% yield.

Scheme 8. Synthetic steps to control **44**.

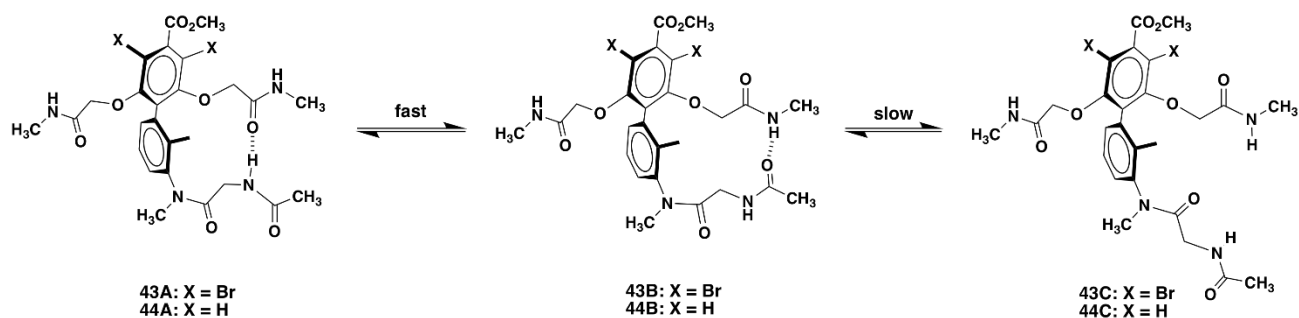


4.3 NMR ASSIGNMENTS AND COMPARISON OF MONOMETHYLAMIDE

TARGET 43 AND CONTROL 44

Core target **44** was designed to conformationally control the ether side chains in order to improve the configuration of the β -sheet mimetic torsion balance by increasing amino acid hydrogen bonding. Evaluation of control amide **43** can provide insight into the degree of control the bromines contribute to the torsion balance structure and allow us to discover the preferred identity of the hydrogen bond donor/acceptor between the glycine amino acid and amide functionality. Conformers of **44** and **43** are shown in Scheme 9. Only one enantiomer each for these three chiral molecules is shown. Conformers **A** and **B** are conformational isomers of one another which present two alternative patterns of hydrogen bonding: In **A**, the top side chain is the hydrogen bond *acceptor* and the glycine acetamide acts as the hydrogen bond donor. In **B**, the top side chain is the hydrogen bond *donor* and the glycine acetamide acts an acceptor. Conformer **C** arises from rotation around the aryl amide N-C(O) amide bond. Note that conformers **A** and **B** will interconvert rapidly, so it will not be possible to observe these conformers as separate signals in an NMR spectrum. NMR analysis of the dibenzyl derivative **A** reveals, as expected, that **A** and/or **B** are the major conformers and **C** is a minor component in solution.

Scheme 9. Three conformers of gly target **43** and control **44** (enantiomers not shown).



In the assignment of NMR resonances observed in **44** and **43**, 2D NMR spectroscopy was utilized to identify the ^1H and ^{13}C peaks of each conformer. These include COSY, NOESY, ROESY, HMQC, and HMBC NMR experiments. The ROESY data was most useful in assigning the acetyl methyl and aryl methyl as well as the amide protons. Figure 28 and Table 9 include all of the ^1H and ^{13}C assignments for spectra in CD_2Cl_2 .

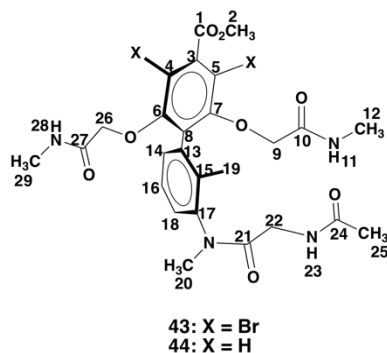


Figure 28. Representation of balances **44** and **43** with atom numbering (hydrogen or carbon) for spectroscopic assignment.

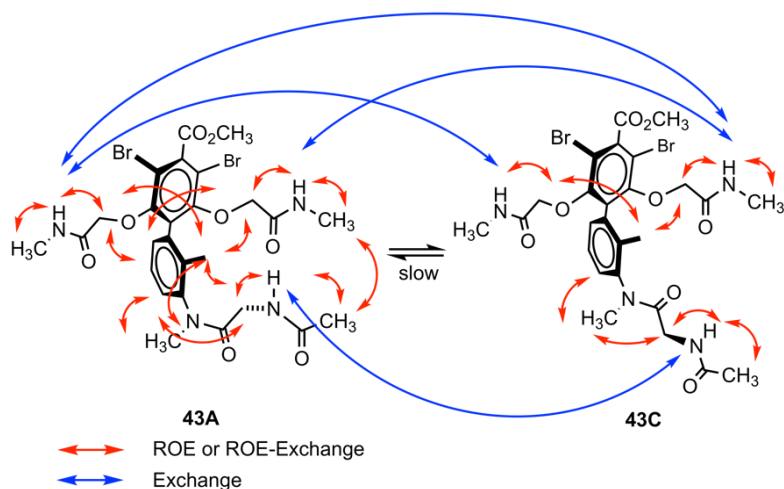


Figure 29. ROESY and EXSY (700 MHz, CD_2Cl_2) assignments data for **43**.

Table 9. Target **43** and control **44** ^1H (700 MHz, CD_2Cl_2) assignments and ^{13}C (600 MHz, CD_2Cl_2) assignments.

No.	Target 43		Control 44	
	^1H , ppm (major/minor)	^{13}C , ppm	^1H , ppm (major/minor)	^{13}C , ppm
1	--	167.4	--	168.0
2	4.00 (s, 3H)	41.8	3.93 (s, 3H)	42.0
3	--	131.0	--	131.1
4	--	111.1	7.38 (s, 1H)	108.2
5	--	111.4	7.39 (s, 1H)	108.7
6	--	153.2	--	155.5
7	--	153.5	--	155.9
8	--	140.0	--	136.1
9	4.18-4.00 (two AB q, 2H)	72.2	4.54, 4.34 (two ABq, 2H)	69.0
10	--	165.9	--	166.2
11	6.80, 6.03 (two broad s, 1H)	--	6.08, 6.23 (two broad s, 1H)	--
12	2.59, 2.47 (two d, 3H)	25.8	2.71, 2.64 (two s, 3H)	25.8
13	--	132.0	--	132.5
14	7.30, 7.17 (two d, 1H)	128.2	7.27, 7.17 (d, 1H)	127.7
15	--	135.8	--	135.9
16	7.43, 7.39 (two t, 1H)	129.3	7.44, 7.43 (t, 1H)	128.2
17	--	142.0	--	141.7
18	7.30, 7.26 (two d, 1H)	128.2	7.29, 7.22 (d, 1H)	123.7
19	2.02, 1.98 (two s, 3H)	15.2	1.95, 1.88 (two s, 3H)	14.7
20	3.36, 3.21 (two s, 3H)	36.5	3.37, 3.24 (two s, 3H)	36.5
21	--	165.9	--	166.2
22	4.30, 4.27 (qd, ABq, 2H)	41.8	4.25, 4.23 (qd, ABq, 2H)	42.0
23	6.46, 6.36 (two broad s, 1H)	--	6.38 (broad s, 1H)	--
24	--	168.7	--	168.7
25	2.00, 1.88 (two s, 3H)	23.2	2.10, 1.96 (two s, 3H)	23.1
26	4.10, 4.00 (two ABq, 2H)	72.0	4.46, 4.42 (two ABq, 2H)	68.5
27	--	165.9	--	166.2
28	6.26, 6.19 (two broad s, 1H)	--	5.72, 5.89 (two broad s, 1H)	--
29	2.65 (d, 3H)	25.8	2.63 (d, 3H)	25.8

The assignments of each ^1H signal (Table 9) to its major and minor conformer were aided by the ROESY data (Figures 29-31). The spectrum for control **44** is purposely displayed on the left. Reading the images from left to right will showcase the differences in the spectral data, observed when the bromines are present.

The three amide protons can be observed in Figure 30. The major and minor conformers of **44** and **43** are identifiable among the broad singlets appearing between 5.4 δ and 6.5 δ . The

spectra of the control exhibits apparent overlap of NH signals. Only five NH signals are observed, rather than the six possible for three amide NH protons and two observable conformers. Dynamic exchange and ROESY data for the three amide protons and their corresponding neighbors are depicted in Figure 30.

The most downfield amide proton signal “ii” of control **44** belongs to that of glycine. We have highlighted the ROESY cross peak for this proton and the glycine α -protons in Figure 30. Major and minor conformers appear to overlap for this proton (as shown by the dashed blue arrow). On the other hand, the data for dibromo balance **43** clearly show that it is the middle NH signal that corresponds to the major glycine conformer, while the most downfield major NH peak belongs to the methylamide proton “i”. The minor conformer NH signal for “iii” appears most upfield. We interpret the large difference in chemical shift found for proton “ii” as being due to a hydrogen bond that is present in **43** but not in **44**. Since the gly NH barely moves, we believe its environment has not changed. This also supports our conclusion that the top side chain is the hydrogen bond *donor* and the glycine acetamide is the hydrogen bond *acceptor*.

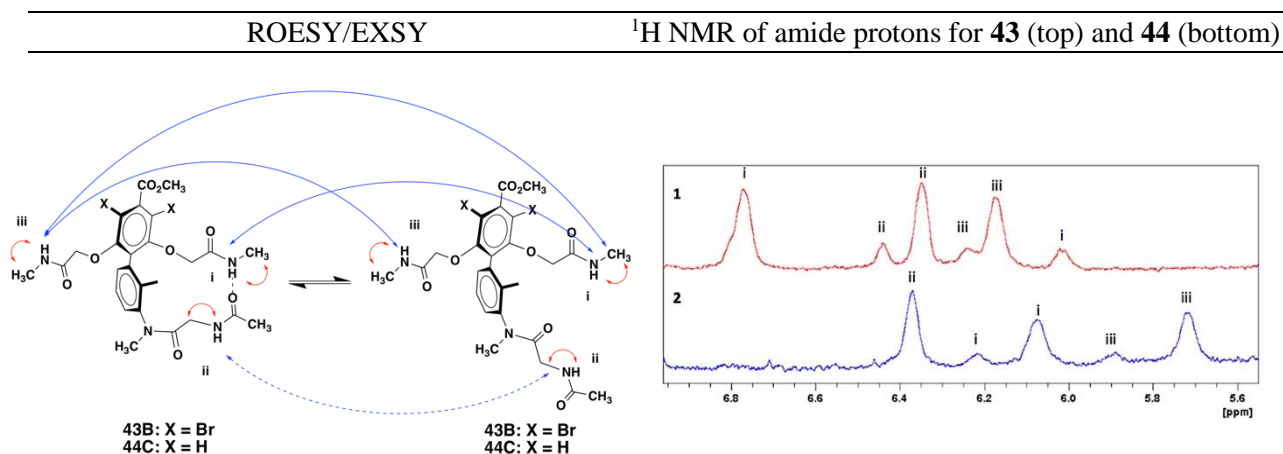


Figure 30. Summary of ROESY/EXSY data (left) and ^1H NMR spectra (right) of **43** and **44** in CD_2Cl_2 at 298 K for amide proton ^1H NMR assignment of the major (**B**) and minor (**C**) conformers.

ROESY data were also helpful in assigning the acetyl and aryl methyl protons (Figure 31). These two signals are very close in chemical shift. The data provide important clues. In **43**, it is the more upfield methyl signal that shows a strong ROESY effect due to the ether methylenes on the upper side chains (I). At the same time, in **43**, the more upfield methyl signal shows a ROESY effect due to the glycine methylenes (II). This establishes that the upfield methyl is the aryl methyl and the downfield methyl is the acetyl methyl. The opposite is observed in the dibromo case. Figure 31 also shows a ROESY effect due to the aryl N-methyl (III) that further supports our conclusion for ^1H assignment of the methyl protons.

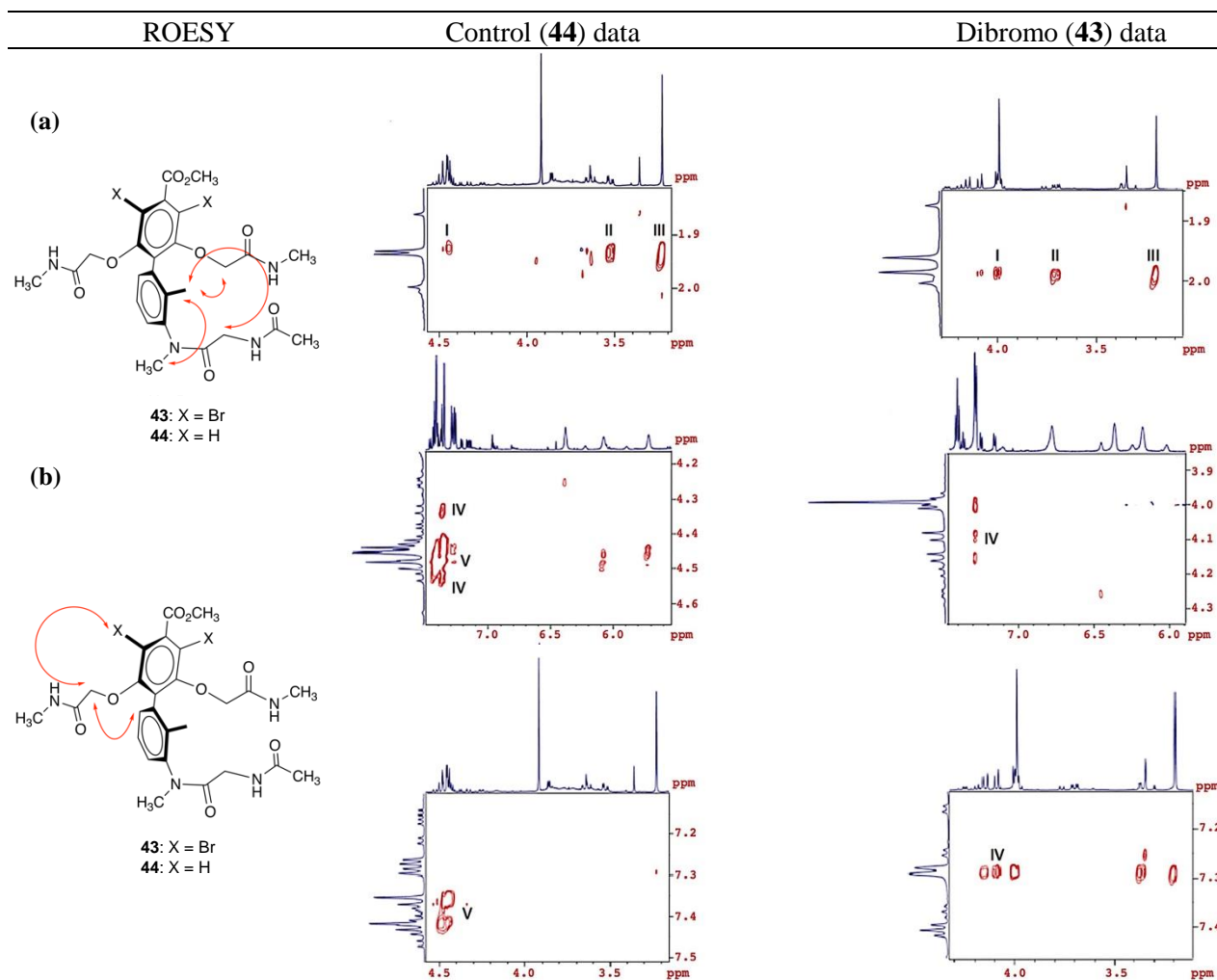


Figure 31. Selected ROESY data of control **44** (left) versus dibromo gly target **43** (right) in CD_2Cl_2 at 298 K for ^1H assignment of (a) aryl methyl protons and of (b) upper side chain methylene protons.

Several other prominent observations were used to evaluate conformational change between the target balance and the control. As expected, 2D-ROESY data for dibromo biaryl **43** show a significant off diagonal peak between the methylene protons on the upper side chains and the aromatic proton 14 *ortho* to the top aryl group (IV; Figure 31). In contrast, the side chain methylenes in **44** have a much stronger cross peak with the upper ring protons 4 and 5 compared to proton 14 (V). The side chains of **44** appear to be coplanar or close to coplanar with the upper aromatic ring (Figures 32-33). CPK models show an interchain H-bond is possible in **43**.

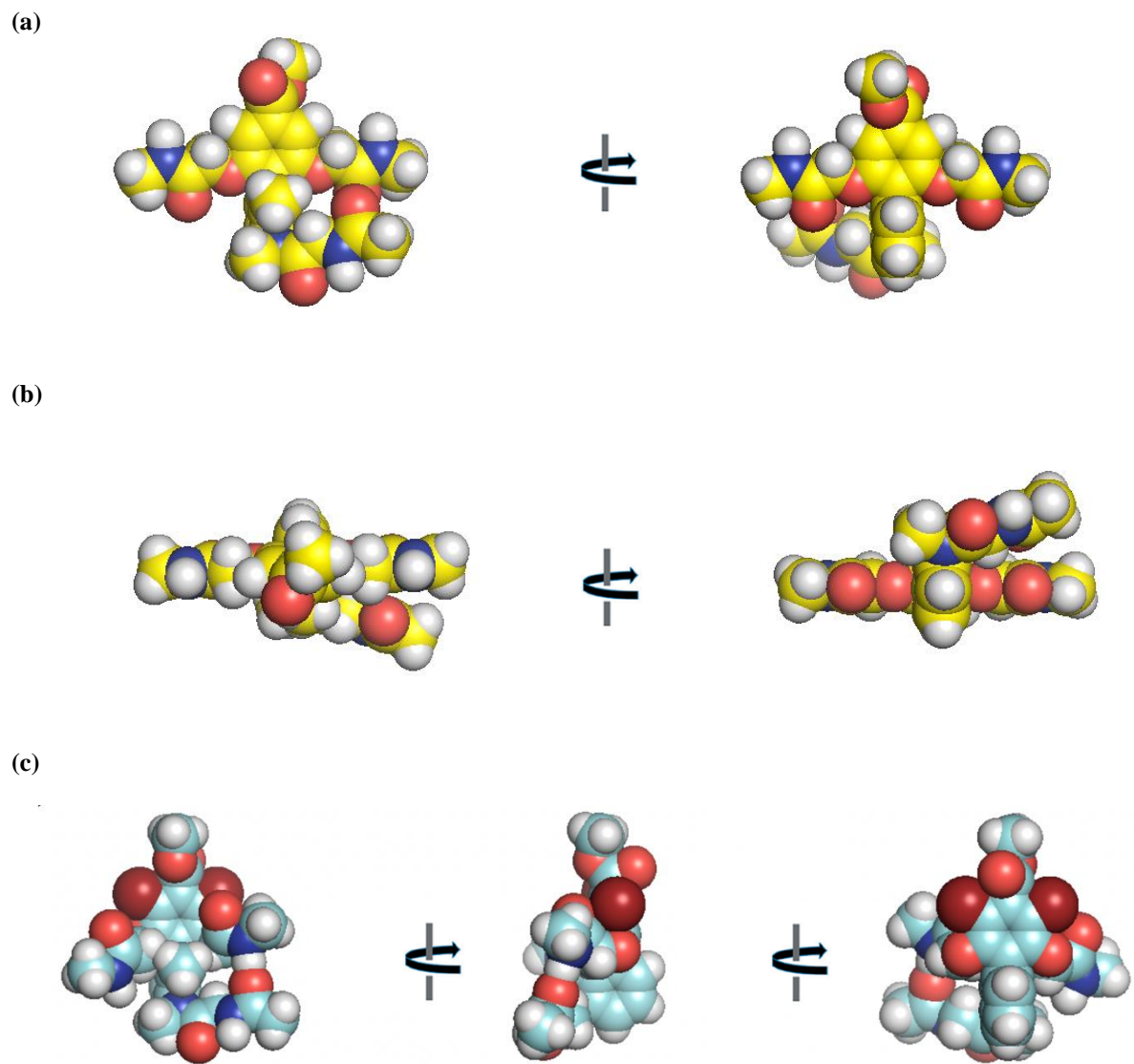


Figure 32. CPK models of **43** and **44**. (a) Control **44** from front and back view; (b) control **44** from top and bottom view; (c) Gly target **43** from front, side and back view.

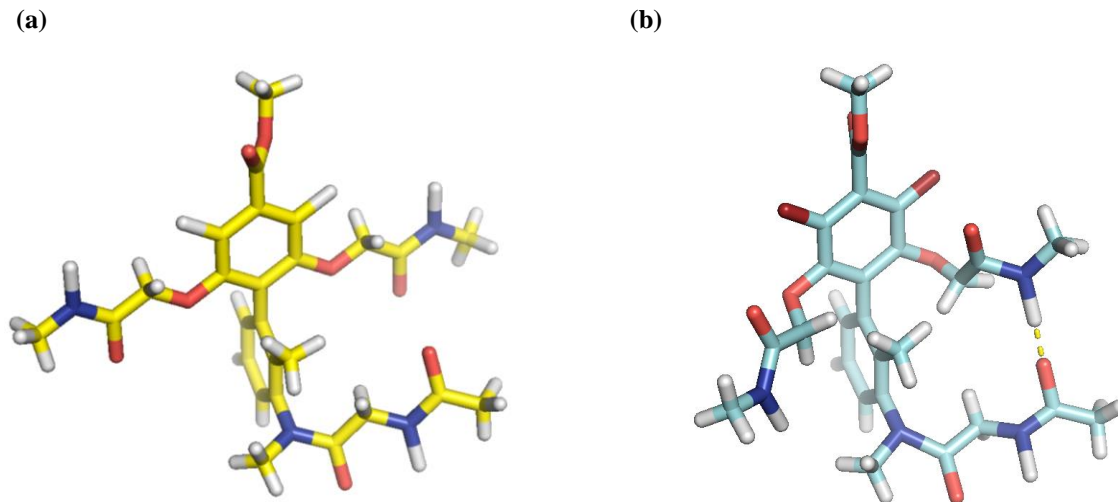


Figure 33. Models of Gly target **43** and control **44**. (a) Gly control **44** model. Side chains do not show the necessary conformation to achieve interchain hydrogen bonding between the upper and lower side chains. (b) Example hydrogen-bonded confirmation of Gly target **43**. The amide proton of the upper half is the hydrogen bond donor to the glycine acetamide hydrogen bond acceptor of the lower half.

4.4 ANALYSIS OF MONOMETHYLAMIDE TARGET 43

4.4.1 Folding Preference of Monomethylamide Target 43

^1H NMR and ROESY experiments were performed to evaluate solvation and concentration effects on torsion balance folding. NMR data collected at concentrations of 1 and 10 mM in CDCl_3 , C_7D_8 , and CD_2Cl_2 , did not have an impact on the chemical shift or folding ratio. There were some solvation effects noted. Figure 34 shows a comparison of an expanded region of the ^1H NMR data of **43** in three solvents. The chemical shifts in CDCl_3 and CD_2Cl_2 were similar but different in C_7D_8 . This was expected since hydrogen bonding is known to be promoted in C_7D_8 .¹⁰⁶ Deuterated chloroform and dichloromethane are known to compete for hydrogen bonding sites in comparison with toluene-d8 because it is acidic in comparison to its relatively low polarity. Therefore, the

degree of hydrogen bonding between the upper amide chain and lower glycine chain appear to be influenced by solvation. However, the ^1H NMR data was assigned in CD_2Cl_2 since its solvent peak did not interfere with any proton signals of the torsion balance. This is unlike CDCl_3 and C_7D_8 , which obscured the aromatic, aryl methyl, and acetyl methyl regions (Figure 34; aromatic region not shown).

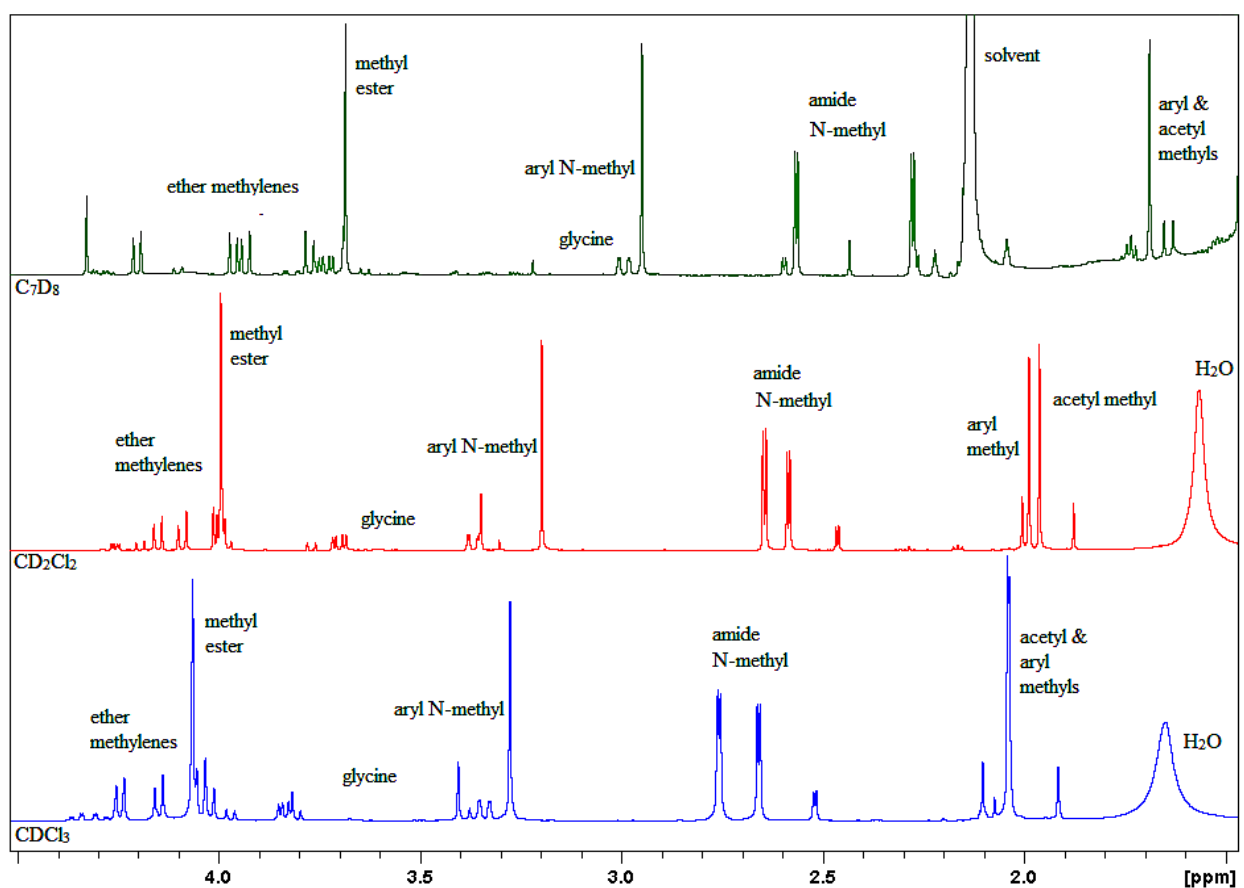


Figure 34. ^1H NMR spectra of **43** (700 MHz) in CDCl_3 (bottom), CD_2Cl_2 (middle) and C_7D_8 (top) at 298 K.

4.4.2 Evaluation of Hydrogen Bond Formation in Monomethylamide Target 43

Our next goal was to measure the effect of the dibromo balance core on the expected hydrogen bond formation by ^1H NMR experiments from 213 to 273 K. Gellman et al. has reported on low temperature NMR studies to indicate hydrogen bond formation.⁷⁶ Due to the presence of neighboring atoms competing in intramolecular hydrogen bonds, our findings from low temperature ^1H NMR studies were inconclusive.

^1H NMR studies were performed on **43** in C_7D_8 over a temperature range of 298 K to 338 K. Interesting behavior was observed for the *N*-methyl protons (Figure 35). ^1H peaks for the major (“**B-iv**”) and minor (“**C-iv**”) *N*-methyl protons of the methylamide are distinguishable at 298 K (2.54 δ and 2.58 δ , respectively). The signals broaden and coalesce into one broad singlet at 323 K. Note only one distinct doublet signal for protons 12 at 338 K. This observed behavior suggests fast rotation occurring around the *N*-methyl bonds above 333 K. This observation is in agreement with intramolecular hydrogen bond weakening or breaking in toluene- d_8 amide methyl protons.¹¹¹ is suggestive that is in identifies supports ROESY data used to determine hydrogen bonding the amide participating in hydrogen bonding, and thus supports our conclusion of hydrogen bond formation in the major conformer.

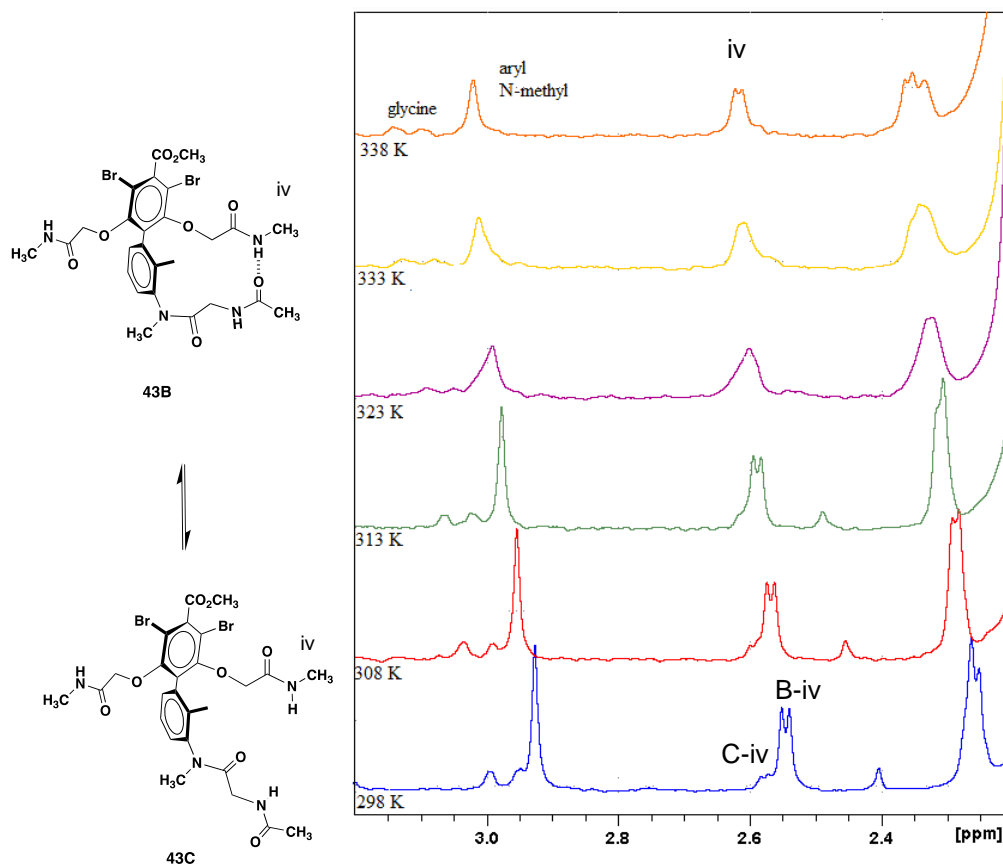


Figure 35. The effect of temperature on the ^1H NMR of N-methyl protons in **43** in C_7D_8 from 298 K to 338 K.

4.5 SUMMARY OF STUDIES OF MONOMETHYL TARGET **43** AND CONTROL **44**

In conclusion, a new conformationally controlled torsion balance can be applied toward quantitative comparison of side chain interactions in the antiparallel β -sheet motif. The design has previously shown a restricted N-aryl bond rotation to impose a two-state folding manifold to mimic the potential folding dynamics of a β -turn. However, the dibromo design features an additional degree of conformational control by the incorporation of the bromo substituents *ortho* to the upper side chains.

Through ^1H and 2D ROESY NMR analyses of **43** and **44**, we have determined the dibromo scaffold has improved the balance's shape to mimic the ends of an anti-parallel β -sheet. The side chains participating in hydrogen bond formation have the correct configuration and appear to display the required distance in interchain hydrogen-bonded amino acids. Furthermore, we have identified the NH amide proton of the top side chain to be the hydrogen bond *donor* and the glycine acetamide as the hydrogen bond *acceptor*.

5.0 ADVANCED β -TURN MIMETIC TARGETS 76-78

5.1 DESIGN AND RETROSYNTHETIC ANALYSIS OF ADVANCED β -TURN MIMETIC TARGETS 76-78

5.1.1 Polypeptide Derivatives

We next focused on developing more advanced analogs of the symmetrical scaffold of the dibromo β -turn mimetic torsion balance (Figure 36). Derivatives **75** and **76** were chosen to continue our investigation into the conformational control present in the dibromo scaffold. Specifically, we planned to search for evidence to study the formation of two interchain hydrogen bonds. Verifying the presence of two hydrogen bonds by 1D and 2D NMR could further validate a structural match between the antiparallel β -sheet motif and our β -turn mimetic torsion balance scaffold. Alanine was selected as the amino acid in **75** to simplify interpretation of NMR data and provide a good basis for comparison in studying bulkier side chains like isoleucine in **76**. Further extension of the peptide chains would allow us to develop polypeptide targets, such as torsion balance **77**. The amino acid sequence in **78** was based upon the hydrophobic sequence of the β -sheet neighboring the CPL-VNL binding pocket, as described in Chapter 1. Conformational analysis of **77** would be paramount to validating the torsion balance configuration to mirror the interactions in the bioactive antiparallel β -sheet motif.

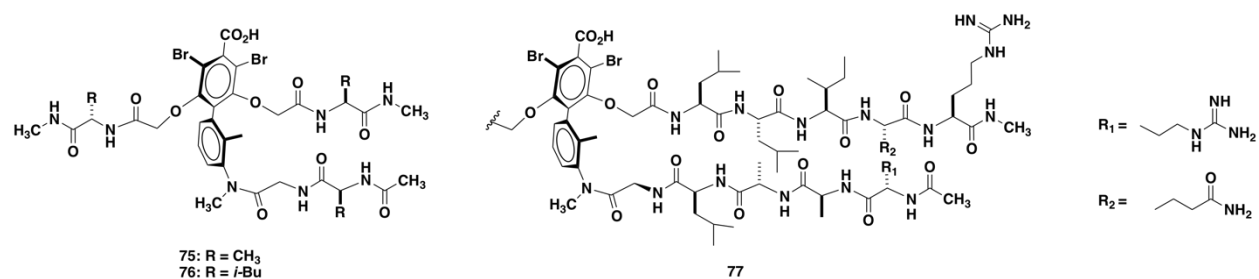


Figure 36. Advanced polypeptides of the symmetrical dibromo β -turn mimetic torsion balance for detection of two (**75-76**) and five (**77**) interchain hydrogen bonds.

Synthesis of target **75** would require iterative peptide bond formation for extension of the lower side chain with protected amino acids. Many solution-phase synthetic strategies for the installation of amide bonds have been demonstrated to be useful to synthesize peptide chains;¹⁰⁵ however in our case, enhanced access to iterative peptide bond formations from solid-phase peptide synthesis (SPPS) was of interest, particularly for developing advanced targets, such as **77**. Since its advent in 1963,^{104a} SPPS has been well-improved due to microwave-assisted Fmoc-SPPS.^{104b,106-7} The value of SPPS has been proven in the synthesis of many natural and modified peptide sequences.⁶⁸ Advantages, such as high product yields by use of excess soluble reagents and simple purification from soluble reagents and byproducts, would allow access to a diverse library of the β -turn mimetic torsion balance.¹⁰⁸ Our interest in applying SPPS methods led to a collaboration with Horne and colleagues. Based on discussions with Dr. Horne about his work on backbone alteration of the B1 domain of *Streptococcal* protein G (GB1),¹⁰⁹ we identified hairpin torsion balance **78** and closed hairpin control **79** as additional targets (Figure 37).

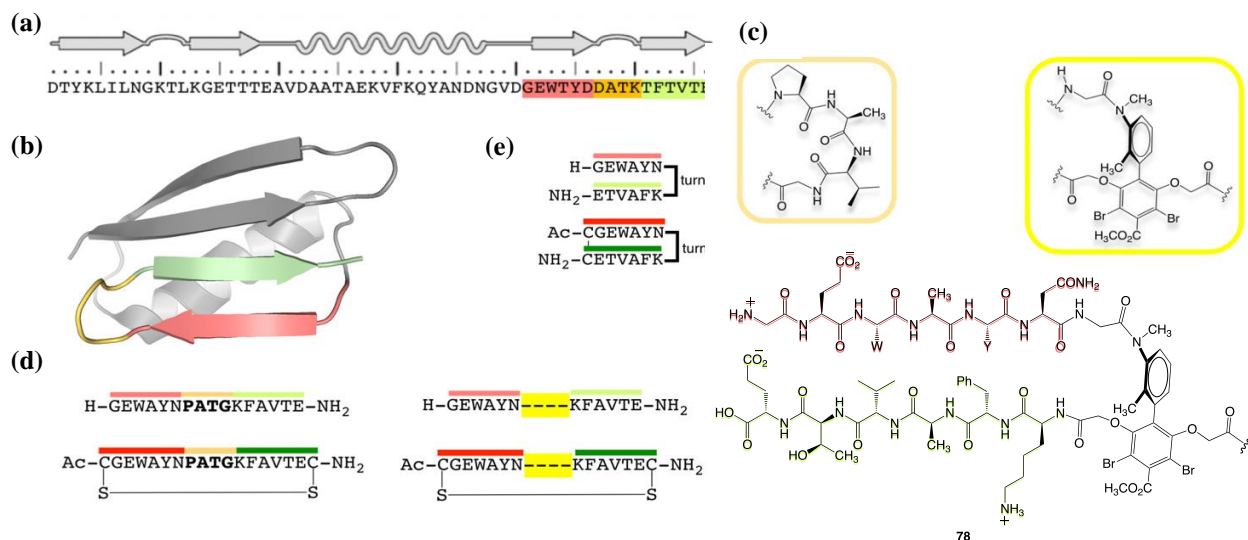


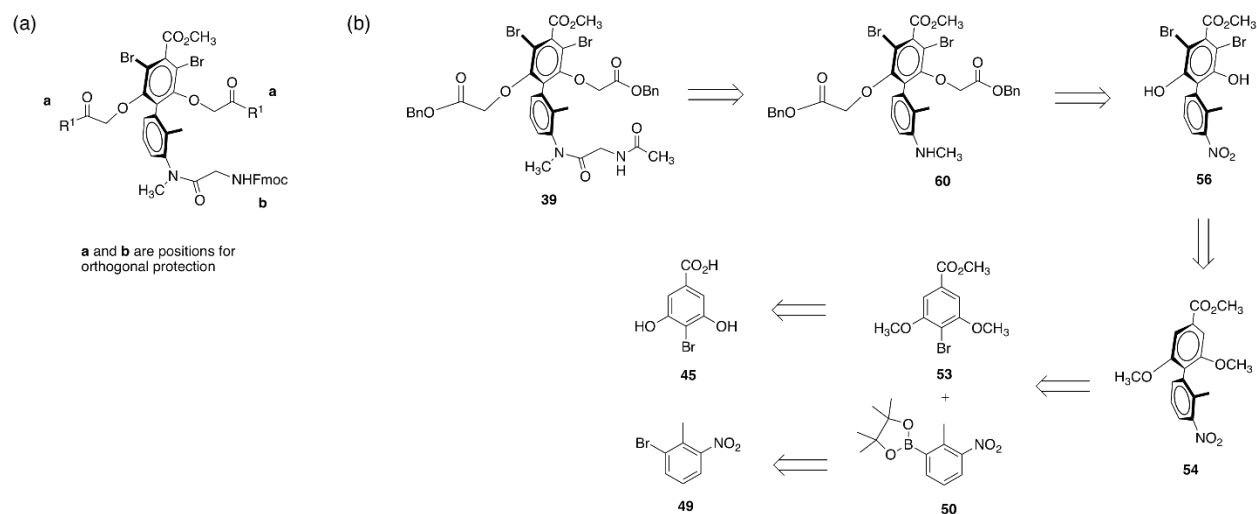
Figure 37. GB1 β -turn sequence modification for torsion balance derivatives **78** and **79**. (a) Sequence and structural map for GB1. (b) Structural analysis of GB1. PDB: 2QMT.^{115a} (c) Model β -hairpin system derived from GB1. (d) The peptide backbone structure of model β -turn for substitution by torsion balance scaffold, as shown in part (e). The disulfide linkages between cysteine residues for **79** (not shown) provide cyclic control hairpins.

GB1 is only 56 residues in length and contains four β -strands to form two β -sheets connected by an α -helix (Figure 37A; B). GB1 can be prepared by SPPS or by protein expression in bacteria and sixteen residue fragments of the C- and N-termina are known to form β -hairpins in aqueous solution, like those in Figure 37B.¹¹⁷ In addition to being well-describe by NMR and X-ray,¹¹⁵ GB1 has been shown that GB1 is amenable to backbone modification and side chain substitution. Introducing our β -turn mimetic torsion balance into GB1 anti-parallel β -sheet mimics (Figure 37C; D) would allow the effects of backbone modification on the formation of interchain hydrogen-bonded interactions in the antiparallel β -sheet motif to be studied. The long-term goal for this project would be to establish methodology for insertion of our β -turn mimetic torsion balance into a protein that has a tertiary folded structure. Furthermore, in using the GB1 domain, we can study modification effects on folding and function. Because the crystal for GB1 is known, crystals of GB1 mutants can be studied to compare mutation effects on peptide folding. In

addition, competitive binding assays with immunoglobulin G (IgG)¹¹⁶ using the selected GB1 segment are available to compare to our mutant GB1 to probe mutation effects on protein function.

Factors considered in planning the synthesis of advanced derivatives **75-79** included selection of solid support, choice of protection of side chains and amino acids as well as appropriate conditions for attachment and cleavage reactions. SPPS required the immobilization of the torsion balance substrate onto a solid support. Consequently, a resin attachment site was an additional design consideration for our torsion balance scaffold. Our molecular design of the precursor for SPPS was based on the torsion balance core that included a functional group suitable to attach to resin by SPPS. As in our synthetic strategy introduced in Chapter 2, chain extension demanded orthogonal protection of the top and bottom strands.

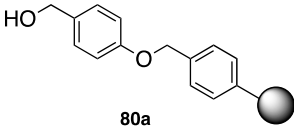
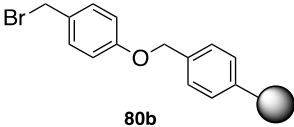
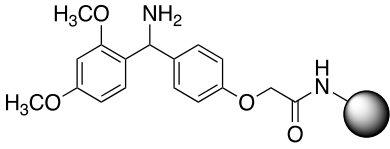
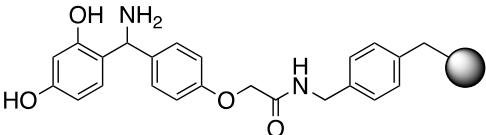
Scheme 10. (a) The symmetrical dibromo β -turn mimetic torsion balance scaffold. (b) Retrosynthetic analysis of the torsion balance core Gly target **39**.



The carboxyl group at the C3 position of the upper ring was exploited for resin attachment because the side chains would be free for amidation to produce symmetrical product. We reasoned that if the torsion balance methyl ester could be obtained as a free carboxylic acid, the latter could

be activated for nucleophilic resin attachment and desired targets **75-79** formed by SPPS. Hydrolysis could be incorporated into our established solution-phase synthesis of the torsion balance core, described in Chapter 1 and reproduced in Scheme 10.

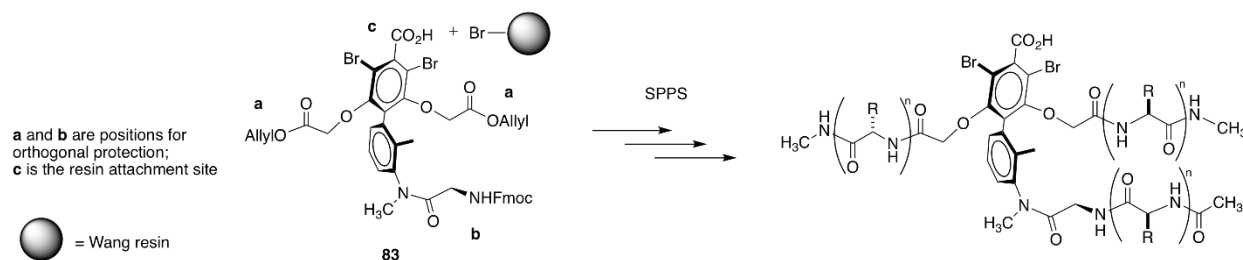
Polystyrene PHB Wang resins (**80**) were selected for resin attachment (Table 10). Specifically, the electrophilicity of bromo Wang resin **80b** was thought to be well-suited for nucleophilic resin attachment by the torsion balance carboxylic acid. The Wang resin is the most prevalent solid support used for carboxylic acid resin attachment in SPPS and employs moderate cleavage conditions with TFA.^{117,119} Perhaps most noteworthy is that Wang resin-bound material is known to survive a variety of transformations, such as Suzuki coupling following carbodiimide coupling to generate vinyl and iodobenzoic acids.¹²¹ Given the loading efficiency and versatility of the Wang resin, we planned to explore its utility for the solid-state synthetic route.

Table 10. Resins considered for SPPS.	
Resin Name	Structure
PEG/PS Wang resin	 <p style="text-align: center;">80a</p>
PEG/PS Bromo Wang resin	 <p style="text-align: center;">80b</p>
NOVAPeg Rink amide resin	 <p style="text-align: center;">81</p>
Rink amide AM resin	 <p style="text-align: center;">82</p>

For SPPS to be successful, it was necessary that conditions for orthogonal deprotection of the side chains and amino acid coupling not lead to premature substrate-resin cleavage. Protecting groups were selected based on these criteria. The allyl ester, commonly used in SPPS to protect carboxy groups,¹²¹ was selected for upper side chain protection. We reasoned that employment of the allyl ester protecting group would allow us to selectively deprotect the esters of the upper side chains under nonhydrolytic conditions and therefore would prevent undesired side reactions at the attachment/cleavage site and on the lower chain resin.

For lower side chain protection, Fmoc, the most common α -amino acid protecting group for SPPS, was selected.¹¹⁶⁻⁷ Using base labile α -amino Fmoc deprotection would prevent undesirable side reactions with the resin or the upper side chain. Thus, carboxylic acid **83** was determined to be the starting material for SPPS (Scheme 11).

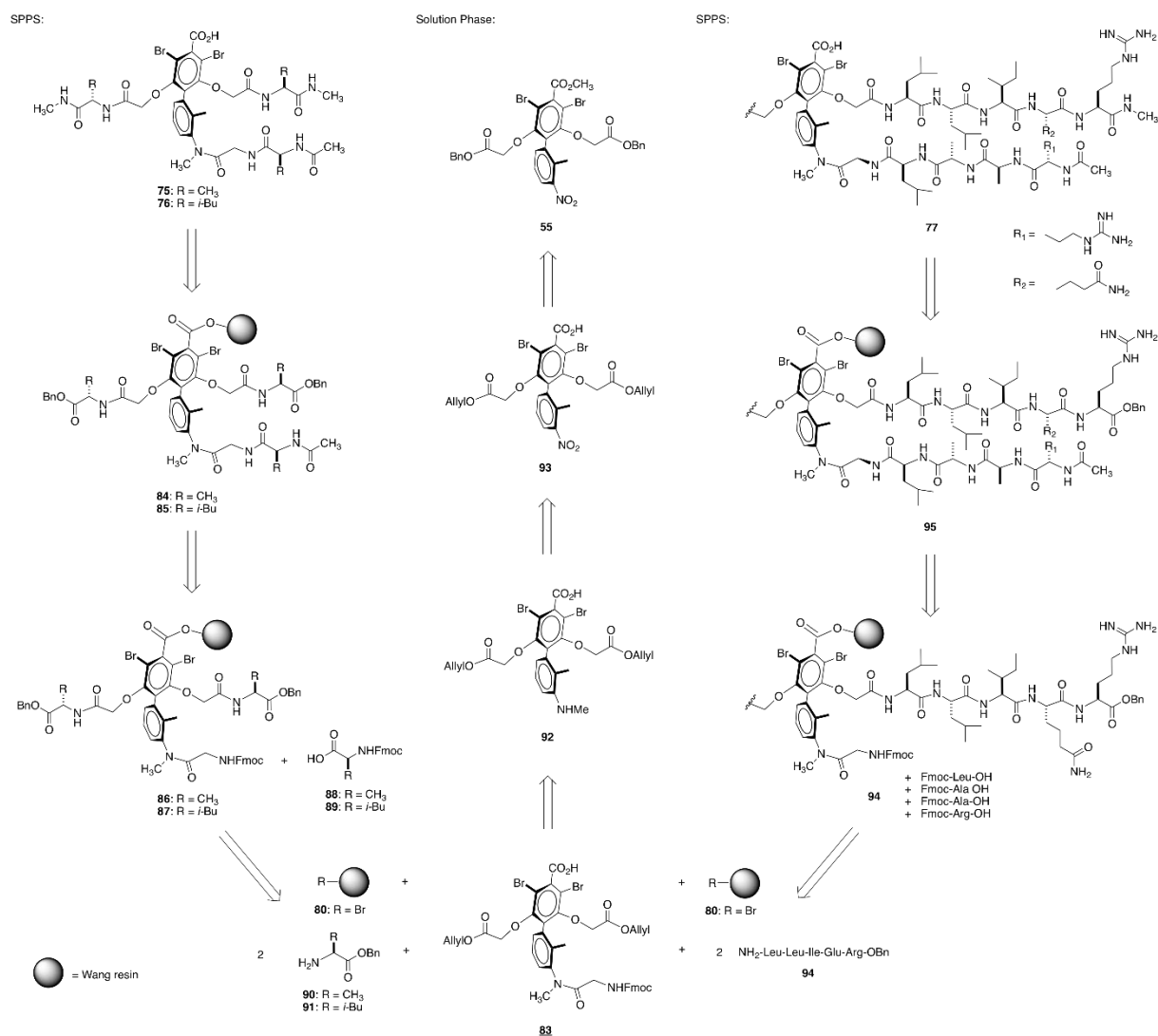
Scheme 11. Target SPPS precursor **83**.



Our synthesis relies on solid- and solution-phase routes (Scheme 12). These solid-phase syntheses require orthogonal deprotection and amidation to the upper and lower side chains following resin loading of substrate **83**. Targets **75** and **76** would be synthesized from **84** and **85**, respectively, by benzyl deprotection and amidation with N-methyl amine followed by resin cleavage with TFA. Extension of the lower chain to form Gly-Ala dipeptide **84** would include Fmoc deprotection of glycine in amide **86** and subsequent coupling with commercially available acetyl-L-alanine **88**. Gly-Leu dipeptide **85** would be synthesized using this same strategy, but with Gly biaryl **87** and acetyl-L-leucine **89**. A three-step sequence would construct amides **86** and **87**: resin loading of carboxylic acid biaryl **83** to Wang resin (**80**), deprotection of allyl esters and by segment condensation with benzyl protected amino acid (**90** or **91**).

The synthesis of **83** employed solution-phase methods. The retrosynthetic analysis suggested that **83** would arise from amine **92** by coupling Fmoc-protected L-glycine acid chloride to N-methyl amine **92** to install the lower glycine side chain. Carpino's conditions would be used to generate the requisite acid chloride for coupling. N-Methyl bond construction on the lower ring of **92** would be achieved by nitro group reduction of **93** and methylation of the resulting amine. We anticipated **93** would be synthesized through simultaneous hydrolysis of methyl and benzyl esters in **55** followed by esterification of the side chain acids.

Scheme 12. Retrosynthetic analysis of **75-77** using solid- and solution-phase methods.



The synthetic strategy for **75** and **76** was envisioned to be a feasible route to form hairpin derivatives **77-79**, as shown for **77** in Scheme 12. Extension of the upper side chains in **83** would be accomplished by symmetrical segment condensation using synthesized peptide segment **94** after allyl deprotection and before a series of iterative Fmoc deprotections and amino acid couplings to form resin-bound hairpin **96**. Cleavage of **96** from resin and amidation of upper side chain would provide **77**.

5.1.2 Zwitterion Derivatives

We were also interested in studying salt bridge formation and its effects on conformation in the dibromo torsion balance scaffold. Specifically, we wanted to examine salt bridge formation between an amino acid ammonium on the torsion balance lower half and amino acid carboxylate on the torsion balance upper half. Liberatore used EXSY analysis to determine effects of salt bridge stability on rates for a balance with a single alanine.⁸¹ The barriers were determined to be 19.7 kcal·mol⁻¹ at 343 K in CD₃CN and 22.6 kcal·mol⁻¹ at 373 K in deuterated buffer (pD 6.9), respectively. The higher rate in water shows that rotation in water is slower, most likely due to the capacity of water to form ion dipoles with electrostatic charges in the balance. Because of the improved alignment of our dibromo core scaffold, it would be of interest to study that same effect in the dibrominated balance.

Zwitterions **97** and **98** would test salt bridge effects on rates of rotation around the N-aryl bond (Figure 38). NMR analysis of glycine zwitterion **97** would provide data pertaining to salt bridge effects on the torsion balance core structure, while analysis of glycine-alanine zwitterion **98** would allow us to search for evidence of salt bridge effects after side chain extension. Control amides **99** and **100** were chosen because they eliminate any charge effect by replacing the amine with an N-acetyl amide group. Comparison of NMR data for **97** and **99** would help to reveal evidence of salt bridge effects on conformation of the torsion balance core, while comparison of **98** and **100** would provide insight into salt bridge effects on the formation of two interchain hydrogen bonds. After this assessment, we planned to further our study via preparation and analysis of a Gly-Leu zwitterion derivative.

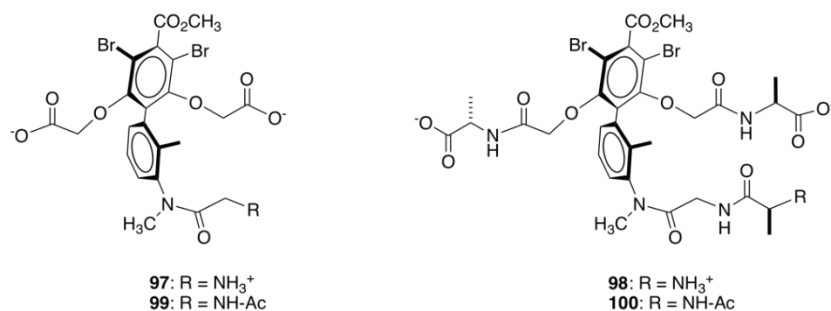
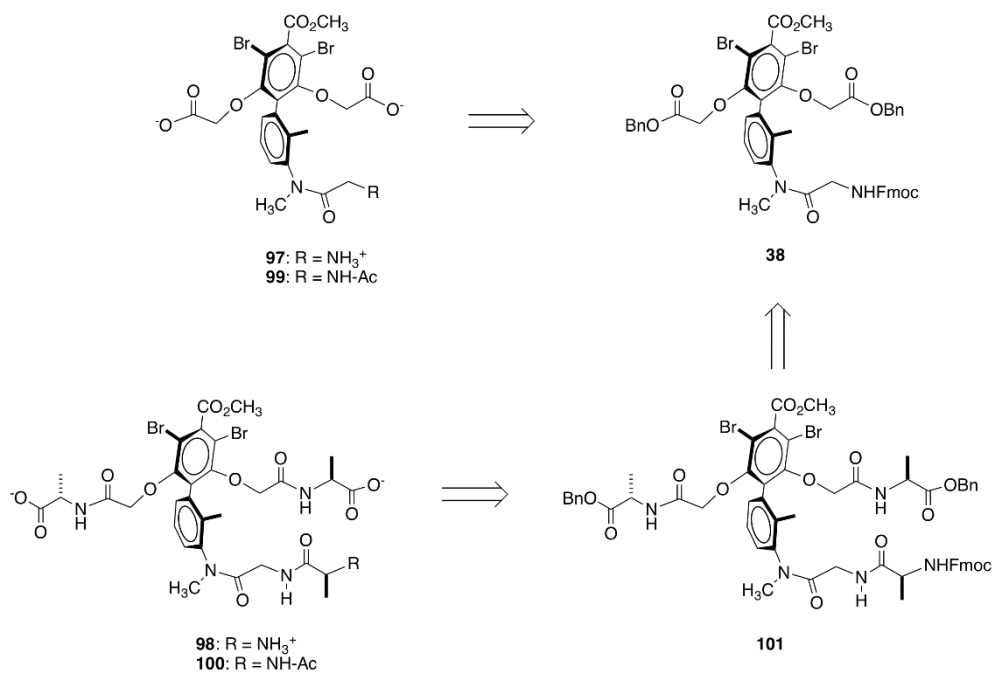


Figure 38. Zwitterions **97-98** and control amides **99-100** of the symmetrical dibromo β -turn mimetic to determine salt bridge effects on rates of N-aryl bond rotation.

Our proposed syntheses of zwitterions **97** and **98** and amides **59** and **60** were based on solution phase methods only. The desired zwitterions would be prepared by benzyl and Fmoc deprotections of Gly and Gly-Ala derivatives **38** and **101**, respectively (Scheme 13). In our proposed synthesis, control amides **99** and **100** would be prepared from amide acetylation, after benzyl and Fmoc deprotection of **38** and **101**, respectively. Protected Gly-Ala derivative **101** would be synthesized from **38** by deprotection and amidation reactions to the upper and lower side chains and acetylation of the lower chain amine.

Scheme 13. Retrosynthetic analysis of zwitterions **97-98** and control amides **59-60**.



5.2 UPPER SIDE CHAIN PROTECTION STRATEGIES

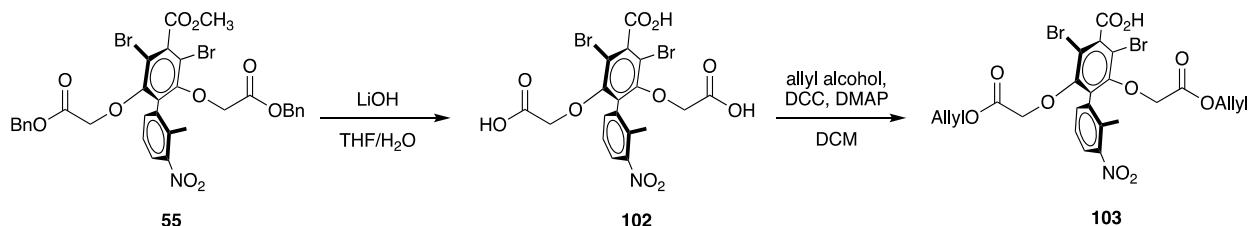
We were seeking conditions that would not require separate protection of the aromatic carboxylic acid to achieve protection of the hydroxycarbonyl ethers. Liberatore was unable to achieve selectivity in the desbromo analogue; however, the electronic effect of the bromines on the upper aromatic ring in the dibromo scaffold would alter the reactivity of the aromatic acid. We used model systems to test reaction conditions of two proposed methods.

5.2.1 Allyl Protection of Hydroxycarbonyl Ethers

To use the carboxylic acid of the upper half of the balance as the resin attachment site (Scheme 14), we needed to protect the side chains. We chose to use allyl groups. Our plan was to hydrolyze

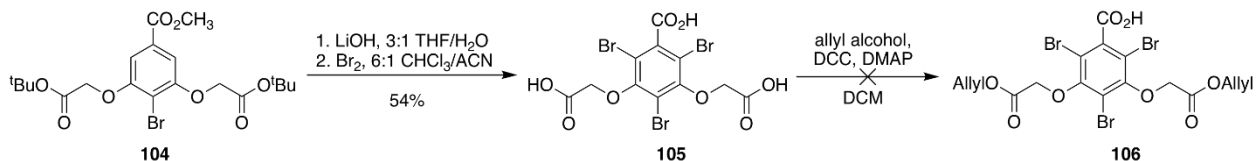
the methyl and benzyl esters in **55** and then attach the allyl groups to the carboxylic acids on the upper side chains by N,N'-dicyclohexylcarbodiimide (DCC) coupling with allyl alcohol.

Scheme 14. Reaction conditions for upper side chain protection.



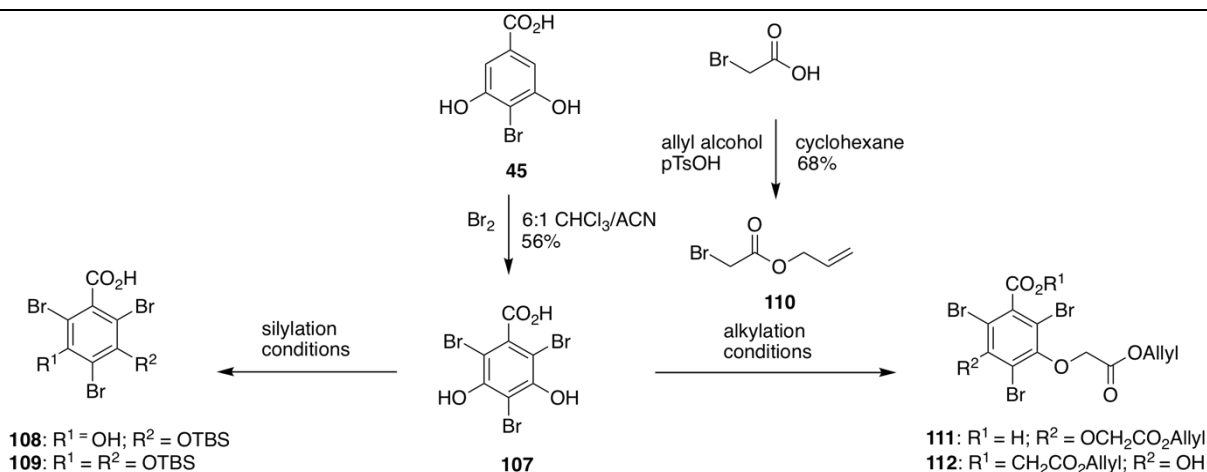
An important question to be answered was whether the allyl esterification method would be selective for the aliphatic carboxylic acids compared to the aromatic carboxylic acid. We reasoned that aliphatic carboxylic acids could be more reactive because they are less sterically hindered. To test this, we carried out reactions in Scheme 15. Test substrate **105** was made available by hydrolysis and subsequent bromination of **63**. Subjecting **105** to esterification conditions with DCC and allyl alcohol gave a mixture of products that arose from esterification of side chain and aromatic carboxylic acids. This observed lack of selectivity led us to consider alternate synthetic methods.

Scheme 15. Test reaction conditions for upper side chain protection.



5.2.2 Incorporation of Allyloxycarbonyl Ethers

Our new strategy was to introduce protected side chains, allyloxycarbonyl ethers, instead of adding protection to already attached hydroxycarbonyl ethers. We intended to find conditions that would not require a separate protecting group for the acid. Liberatore reported a lack of selectivity in the desbromo benzoic acid. We wondered if the bromines in our scaffold would alter this result. Model system **66** was studied to determine if a separate protecting group was needed for the carboxylic acid in order to allow for selective alkylation of the phenols enroute to our SPPS substrate, Fmoc-Gly target **83**. We investigated the relative reactivity of the hydroxyl groups and benzoic acid by silylation and by alkylation (Table 11). Reaction progress was monitored by TLC. If the acid was more reactive than the phenols by alkylation, our synthesis would require a separate protecting group for the acid, such as the silyl (if selective for the acid) or benzyl group. In that case, deprotection conditions would need to prevent side reactions with the upper and lower side chains.

Table 11. Phenol reactivity test and results of alkylation to form **111**.

Entry	Classification	Conditions ^a	Product ^b	Yield
1	silylation	TBSCl (1 equiv), TEA (1 equiv), DCM, rt, 13 h	111	52%
2	silylation	TBSCl (2 equiv), TEA (3 equiv), DCM, rt, 13 h	108	47%
3 ^c	silylation	TBSCl (1 equiv), TEA (2 equiv), DCM, rt, 13h	112	54%
4	alkylation	110 (2 equiv), TEA (3 equiv), DCM, rt, 13 h	111	43%
5	alkylation	110 (2 equiv), K ₂ CO ₃ (3.3 equiv), 18-c-6, acetone, reflux, 20 h	112	64%
6	alkylation	110 (2 equiv), TEA (2 equiv), DCM, rt, 13 h	111	48%
7	alkylation	110 (2 equiv), K ₂ CO ₃ (2.2 equiv), 18-c-6, acetone, reflux, 20 h	112	74%

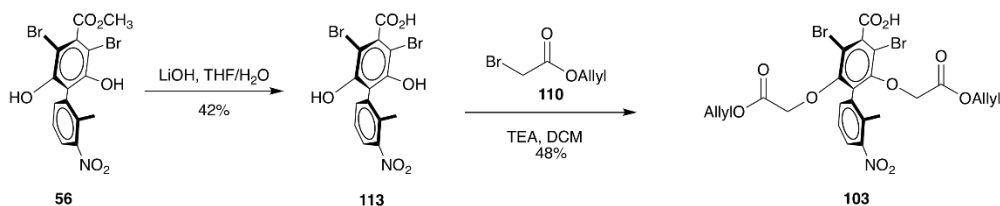
^a 0.13 mmol scale; ^b Major product observed. ^c Monoether **108** was used as starting material.

Model substrate **107** was prepared by treating commercially available 4-bromo-3,5-dihydroxybenzoic acid **45** with bromine. Dibromo **107** gave monosilyl ether upon treatment with 1 equivalent of TEA and 1 equivalent of TBSCl at room temperature. When monosilyl ether **108** was subjected to 2 equivalents of TEA and 1 equivalent of TBSCl, diether **109** was furnished in 54% yield. We attempted to alkylate **107** by similar chemical means without protecting the acid (Table 11). First, allyl bromoacetate (**110**) was formed by heating allyl alcohol and bromo acetic

acid in cyclohexane with catalytic *p*-toluenesulfonic acid (*p*TsOH) under Dean-Stark conditions.^[ref] Alkylation of dihydroxybenzoic acid **107** with **110** using 2 equivalents of TEA at room temperature afforded diether **111** in 43% yield. When the alkylation was carried out in refluxing acetone with K₂CO₃, **112** was identified as the major product. The chemoselectivity using K₂CO₃ method was poor compared to the selectivity observed in the TEA-mediated reaction. This may be due to the higher temperature needed for the reaction to proceed with K₂CO₃. The observed results suggested that a separate protecting group for the carboxylic acid would not be required before subjecting the biaryl complex to the TEA-mediated alkylation.

Hydrolysis of biaryl methyl ester **56** provided dihydroxy acid **113**, which was subjected to the aforementioned TEA etherification conditions with allyl bromoacetate **110** to accomplish the intended alkylation of the phenol groups (Scheme 16). In Chapter 5, we discuss methods to improve the yield of the hydrolysis step. The target biaryl carboxylic acid **103** was afforded in 48% yield.

Scheme 16. Synthesis of carboxylic acid **103** for upper side chain protection.

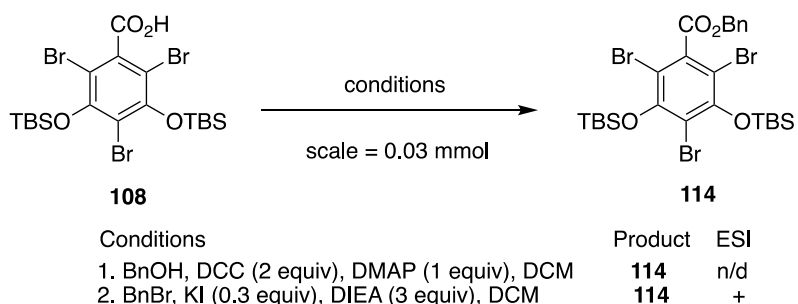


5.3 UPPER SIDE CHAIN EXTENSION STRATEGY

With acid **103** in hand, we focused on testing upper side chain extension on-resin. Our objective was to measure the efficiency of resin coupling to aromatic acid and of amino acid coupling to the

aliphatic acids. We intended to use the PEG/PS (TentaGel) bromo Wang resin, which would require the conversion of commercially available Wang resin **80a** to its bromo derivative (**80b**). To assess methods for resin loading, we subjected benzoic acid **109** to standard loading conditions using commercially available benzyl alcohol and benzyl bromide, which were reasoned to be fair models to test resin reactivity. Like in the resin-loading step, substrate would be in excess to drive the reaction to completion.

Scheme 17. Test reaction conditions for resin loading.



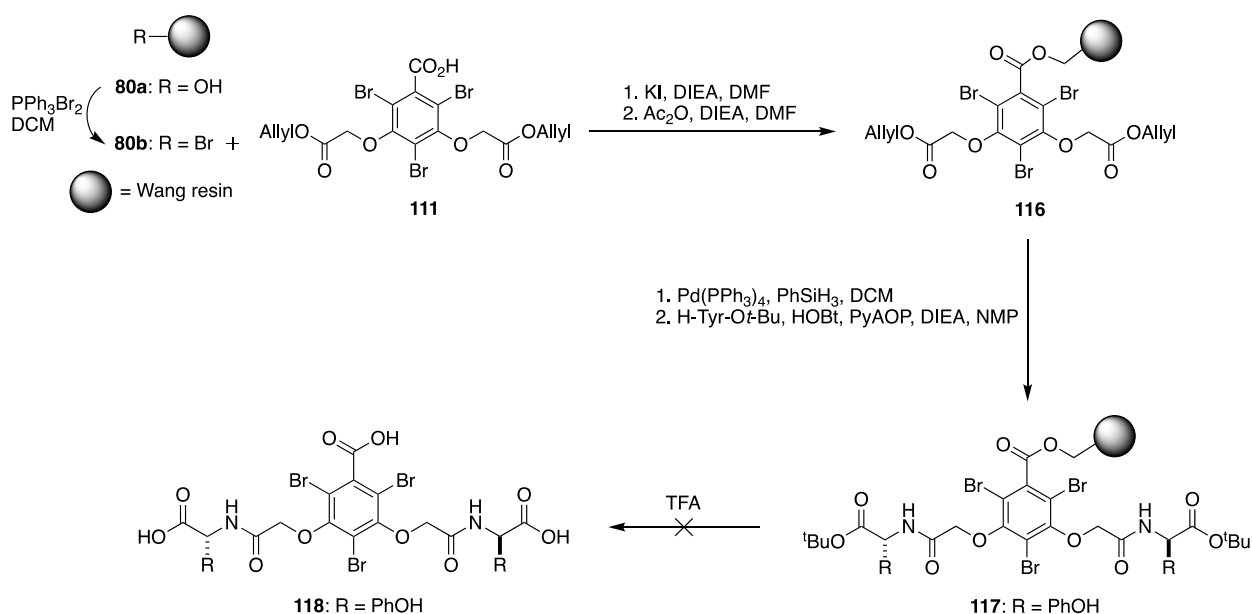
Coupling with benzyl alcohol using DCC and DMAP failed. When **108** and benzyl bromide were treated with DIEA and KI, the favored benzyl ester product **114** was detected by ESI-MS. This supported our hypothesis that the bromo Wang resin **80** would be more reactive with our substrate. Therefore, we investigated the resin loading efficiency on substrates **103** and **111**.

5.3.1 Initial Evaluation of SPPS Strategy

Commercially available Wang resin **80a** was converted to the bromo derivative (**80b**) using 3 equivalents of triphenyl phosphine dibromide (PPh_3Br_2) at room temperature (Scheme 18).¹²⁰

Benzoic acid **111** was loaded onto resin **80a** by treatment with DIEA and KI. The resin-bound material was capped using acetic anhydride (Ac₂O) and DIEA. Treatment of **product** with 3.2 equivalents of tetrakis(triphenylphosphine)palladium(0) (Pd(PPh₃)₄) followed by employment of commercially available 7-azabenzotriazol-1-yloxy)trispyrrolidinophosphonium hexafluorophosphate (PyAOP) and HOBT to activate the solid-supported acid *in situ* for amino acid coupling failed to provide diamide **75**. MALDI-TOF MS analysis of small scale TFA cleavage product revealed mono-deprotected allyl product and no tyrosine peptide **75**. Because our SPPS strategy for the upper side chain extension used C-terminal protected residues we could not employ simple tests, such as the Kaiser test, to measure amino acid coupling to our solid-supported substrate. A second attempt to deprotect remaining monoallyl product using 3.2 equivalents of Pd(PPh₃)₄ also failed. Faced with the result of unsuccessful allyl deprotection and amino acid coupling, we reexamined our SPPS protocol.

Scheme 18. Initial attempt of upper side chain extension using SPPS.

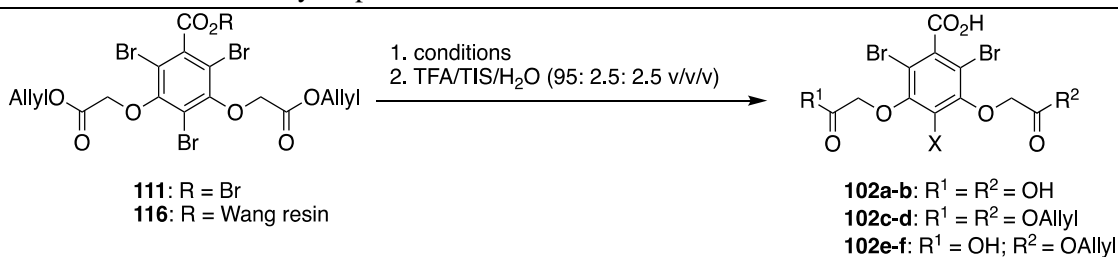


5.3.2 Evaluation of Upper Side Chain Deprotection

We needed more efficient analytical methods to monitor reaction progress. ESI-MS and reverse-phase HPLC methods were reasoned to be better techniques than MALDI-TOF MS to check the success of allyl group cleavage in our test substrate, therefore we explored reaction conditions off-resin. Results would indicate if the conditions were only producing monoallyl product or the desired symmetrical aliphatic acid on-resin, but also if the Pd(PPh₃)₄ was causing formation of bromine cleavage side product. If monoallyl product was isolated in addition to the desired triacid product, we would be able to determine the retention time of each by reverse-phase HPLC analysis. With retention times known, we could have had a simpler analytical method than the aforementioned MALDI-TOF MS.

5.3.3 Evaluation of Allyl Deprotection Conditions Off-Resin

In separate reaction vessels, **111** was subjected to 3.2 equivalents of Pd(PPh₃)₄ with 48 equivalents of PhSiH₃ in DCM and to 0.5 equivalent of Pd(PPh₃)₄ with 7.5 equivalents of PhSiH₃ in DCM. Analysis of the crude mixture by ESI-MS did not reveal monoallyl product alongside desired triacid; however, monodebromination product was observed. Reducing the amount of Pd(PPh₃)₄ used from 3.2 to 0.5 equivalents of Pd(PPh₃)₄ did not entirely eliminate but did significantly reduce the amount of debromination. Before developing HPLC methods for this system, we reexamined our SPPS protocol.

Table 12. Results of allyl deprotection to form **102**.

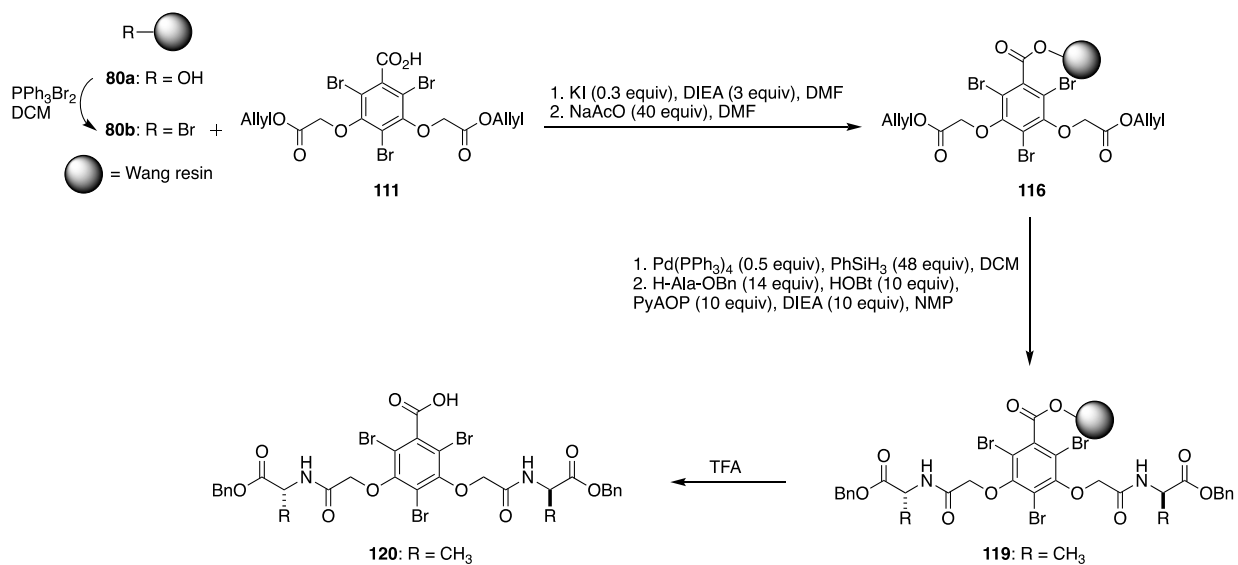
Entry	Substrate	Conditions ^a	Product	X	ESI	MALDI
1	116	Pd(PPh ₃) ₄ (3.2 equiv), PhSiH ₃ (48 equiv), DCM, rt, 30 min	102e	Br	-	+
2	116	Pd(PPh ₃) ₄ (3.2 equiv), PhSiH ₃ (48 equiv), DCM, rt, 30 min	102e	Br	-	+
3	102	Pd(PPh ₃) ₄ (3.2 equiv), PhSiH ₃ (48 equiv), DCM, rt, 30 min	102b	H	+	n/d
4	102	Pd(PPh ₃) ₄ (0.5 equiv), PhSiH ₃ (7.5 equiv), DCM, rt, 30 min	102a	Br	+	n/d
5	116	Pd(PPh ₃) ₄ (0.5 equiv), PhSiH ₃ (7.5 equiv), DCM, rt, 30 min	-			

^a Scale = 0.03 mmol, 0.09 g. Scale reported is based on scale of loading step.

5.3.4 Evaluation of Allyl Deprotection Conditions On-Resin

For our SPPS attempt using model substrate **111** (Scheme 19), reaction progress of the allyl deprotection step was monitored prior to the amino acid coupling step. If conditions used for resin coupling and allyl deprotection were successful, we would expect to observe triacid product **102** from exposing **116** to TFA. On the other hand, if starting material **111** was observed, then only conditions used for resin coupling would be demonstrated to be successful.

Scheme 19. SPPS test conditions for upper side chain extension.



Our attempt to detect the desired allyl deprotection product by MALDI-TOF MS analysis failed. Monoallyl product and starting material **65** were also undetected. Unsure if product formation was unsuccessful or if our analytical method was unsuccessful at detecting formed product, we proceeded to the amidation step.

5.3.5 Evaluation of Amino Acid Coupling

The solid-state material was activated and subjected to microwave (MW) irradiation with L-alanine benzyl ester. After TFA-mediated cleavage, the crude product was subjected to analysis by MALDI-TOF MS and ESI-MS (Entry 3 in Table 13).

Table 13. Results of solid-state amino acid coupling to upper side chains to form **102**.^a

1. **AA** (14 equiv), HOBT (11 equiv),
PyAOP (10 equiv), DIEA (10 equiv),
NMP, 70 °C, 4 min
2. TFA/TIS/H₂O (95: 2.5: 2.5 v/v/v)

116 **102a-b**: X = Br
121a-b: X = H

Entry	AA	Product	R ¹	R ²	ESI	MALDI-TOF
1	L-Tyr- <i>Or</i> -Bu	102a	OAllyl	OH	-	+
2	L-Tyr- <i>Or</i> -Bu	102a	OAllyl	OH	-	+
3	L-Ala-OBn	121a-b	Ala-OBn	Ala-OBn/ OAllyl	+	-

^a Scale = 0.03 mmol, 0.09 g. Scale reported is based on scale of loading step.

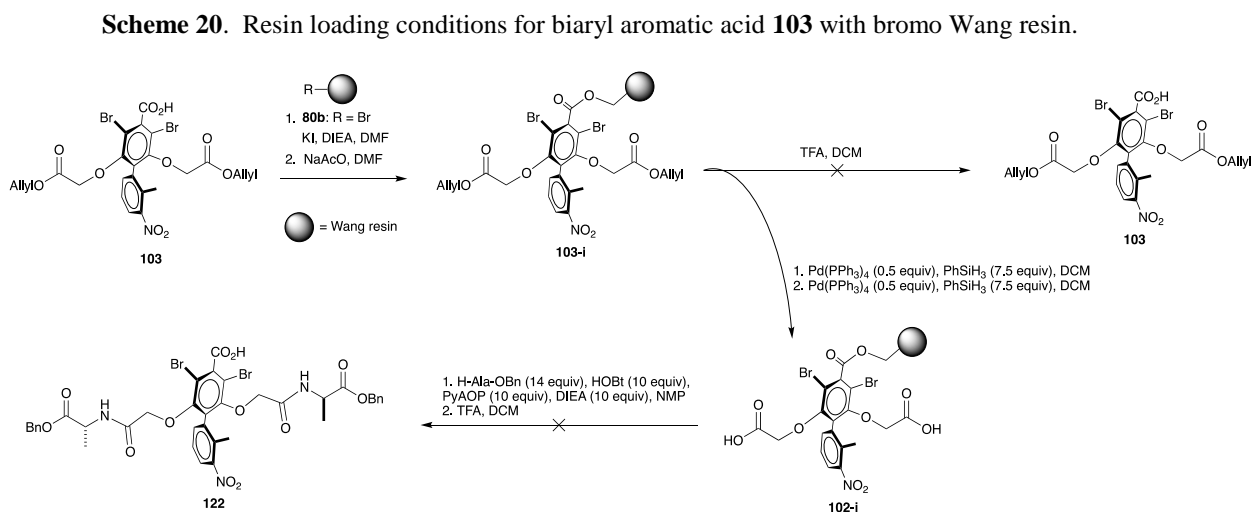
ESI-MS and MALDI-TOF MS data revealed products **121a** and **121b**. These findings validated the following conclusions: (i) resin loading conditions were successful; (ii) deallylation conditions produced deprotected and monodeprotected product; (iii) Pd(PPh₃)₄ was causing undesired monodebromination (either as a side product to the deallylation reaction or as a result of residual Pd(PPh₃)₄ remaining on resin after washing the deallylation product); (iv) PyAOP/HOBt acid activation and microwave-assisted coupling conditions were successful for upper side chain extension. Despite the accessibility of MALDI-TOF MS for product detection, it proved to be a poor analytical method to identify allyl deprotection product. In a control study, triacid **103**, synthesized by SPS, was undetected by MALDI-TOF; probably because the *m/z* ion was too small for effective detection upon ionization with MALDI-TOF MS, which is primarily used for peptide sequencing (≤ 500 ppm).¹¹⁷

MALDI-TOF MS was used for initial mass detection and compound identification because it requires less time for sample preparation and produces less ions than ESI-MS. Additionally, we reasoned that the method would offer less contamination than LCMS to allow for mass

determination with sufficient accuracy (≤ 500 ppm). Upon detection, the samples were then analyzed by ESI-MS for mass detection with higher accuracy (≤ 50 ppm). The matrix and deposition technique are both known to influence the quality of MALDI-TOF MS data. In our case, the most common organic matrix for peptide mass detection, α -cyano-4-hydroxycinnamic acid (α -CHCA), was used to prepare samples via the dried droplet deposition method. Yet, challenges such as sample inhomogeneity or analyte delocalization experienced in MALDI-TOF MS may have also contributed to variability in our results.

5.3.6 Evaluation of Resin Loading Efficiency

Certain that conditions for resin loading worked, we turned to biaryl substrate **103** to evaluate loading efficiency using improved analytical methods.



The elution time of substrate **103** was determined by HPLC-DAD analysis to compare to the result of SPSS resin-cleaved products. Because the biaryl torsion balance substrate is UV

active at a wavelength higher than that of peptide bonds, we planned to exploit this intrinsic property of our structure in order to quantify the yield of the resin loading step. With the extinction coefficient of **103** known, UV/Vis absorbance data of resin-cleaved product would provide the information necessary to calculate product concentration. The extinction coefficient was found to be $6100 \text{ L} \cdot \text{mol}^{-1} \text{ cm}^{-1}$ at 298 nm (Figure 39). In the end, we chose not to monitor progress by UV spectroscopy due to formation of other UV active products detected at 298 nm, as later discussed in Chapter 5.

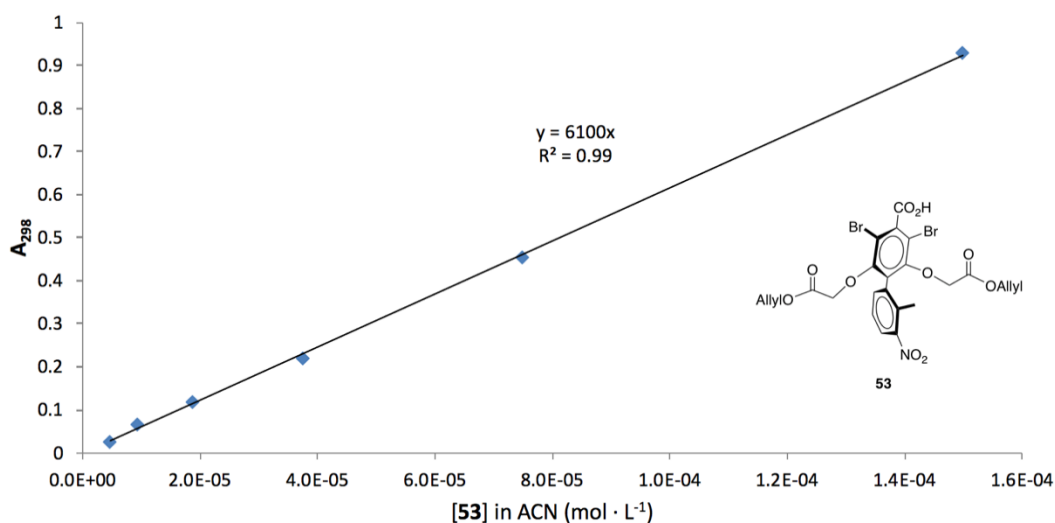
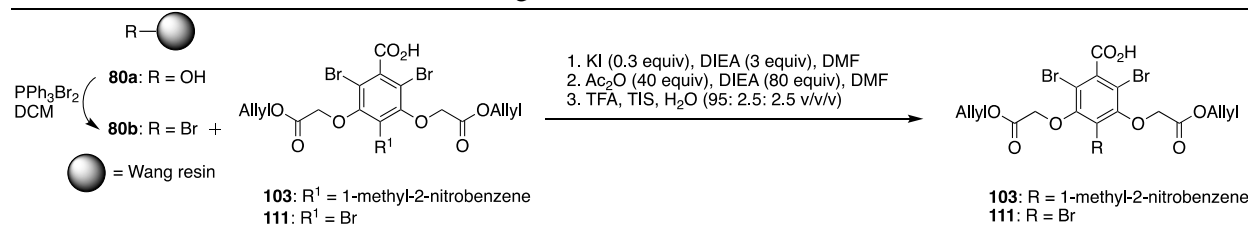


Figure 39. Beer-Lambert plot of **103** in ACN at $\lambda = 298 \text{ nm}$.

The bromo Wang resin (**80b**) was generated from its hydroxy precursor **80a** with PPh_3Br_2 . Carboxylic acid **103** was subjected to standard resin-coupling conditions and treated with Ac_2O and DIEA. MALDI-TOF and ESI-MS and HPLC data of TFA-mediated cleavage product showed no expected product. Furthermore, the mass balance of the resulting filtrate from solvent used to wash the solid-support material after the resin loading step was indicative of poor resin loading.

Table 14. Results of resin loading to form **111**.

Entry	Substrate	Product	ESI	MALDI
1	103	103	+	+
2	103	103	+	+
3	111	111	n/d	n/d

n/d = not detected. ^a Scale = 0.03 mmol, 0.09 g. Resin loading was carried out at rt for 16 h.

5.4 SUMMARY AND CONCLUSION OF PROGRESS TOWARD ADVANCED DERIVATIVES 77-79

Advanced torsion balance derivatives were designed to detect multiple interchain hydrogen bonds to further assess the dibromo scaffold for mimicry of the antiparallel β -sheet. Our method for solution-phase protection of the upper side chains of the torsion balance was successful (Section 5.2); however, difficulties arose from solid-phase deprotection and resin loading.

Standard solid-state methods for deallylation using benzoic acid **111** resulted in incomplete deprotection and undesired monodebromination product. Despite optimization of reaction conditions off-resin to achieve deprotection and minimize formation of monodebromination product, MALDI-TOF MS was unsuccessful to detect evidence of the desired result when optimized conditions were applied on-resin. Because of the lower *m/z* ion value of allyl-deprotected derivatives of benzoic acid **65**, ESI-MS was determined to be an improved method to

monitor reaction progress. Additionally, amino acid coupling to the upper side chain did provide an ion detectable by MALDI-TOF MS.

The unsuccessful SPPS result observed when using biaryl carboxylate **103** was attributed to poor resin loading. We had good prior results of model resin-coupling reactions with benzoates **107** and **111**, but the lack of product formation when employing biaryl carboxylate **103** suggests poor loading of the aromatic acid. Sterically these are very similar substrates; however, there could be an electronic effect or solubility effect from the methyl-nitrobenzene ring in **103** that is not present in **107** or **111**. We directed our attention to redesigning our SPPS approach for improved resin loading.

6.0 ADVANCED β -TURN MIMETIC TARGETS 122-125

Verification of the presence of interchain hydrogen bonds by 1D and 2D NMR was necessary to further validate a structural match between our β -turn mimetic torsion balance scaffold and the antiparallel β -sheet motif. If our scaffold was proven to match, we envisioned its potential broad range application in backbone modification of known tertiary folded peptides. SPPS methods would be integral at that juncture. Thus, rather than turning to SPS, next steps to generate advanced derivatives were still directed toward SPPS methods. To develop our approach, we focused on the challenges from our initial attempt.

6.1 DESIGN AND RETROSYNTHETIC ANALYSIS OF ADVANCED β -TURN MIMETIC TARGETS 122-126

6.1.1 Polypeptide Derivatives

To continue our investigation into the conformational control present in the dibromo scaffold and to study the formation of two interchain hydrogen bonds, derivatives **122-123** were identified using the same rationale for derivatives **75-76** (Figure 40). Like **77**, the extension of the peptide chains in **124** would allow us to develop polypeptide targets for conformational analysis to validate the torsion balance scaffold as a β -turn mimetic to match the interchain bonding patterns within an antiparallel β -sheet motif. Incorporation of the β -turn mimetic torsion balance into GB1 mimetic

sequence (hairpin **125** and control **126**) would allow us to determine the effects of backbone modification within the antiparallel β -sheet in GB1.

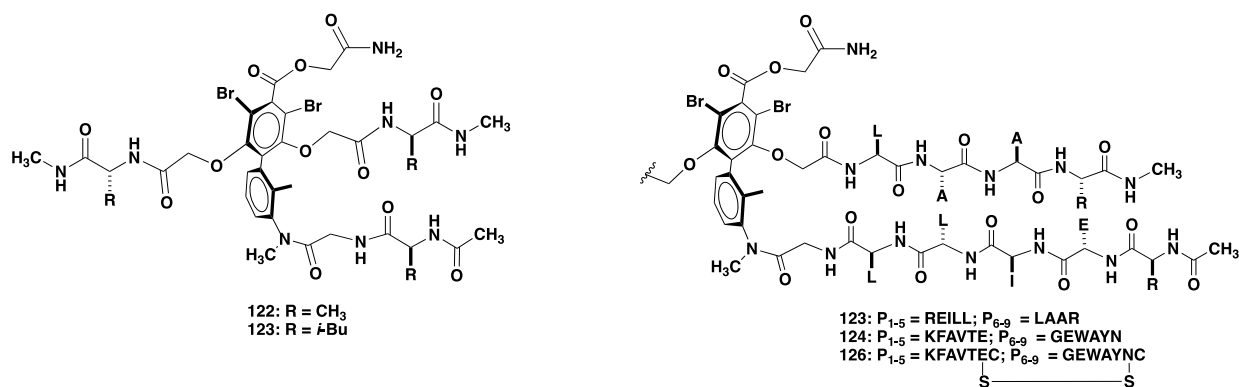
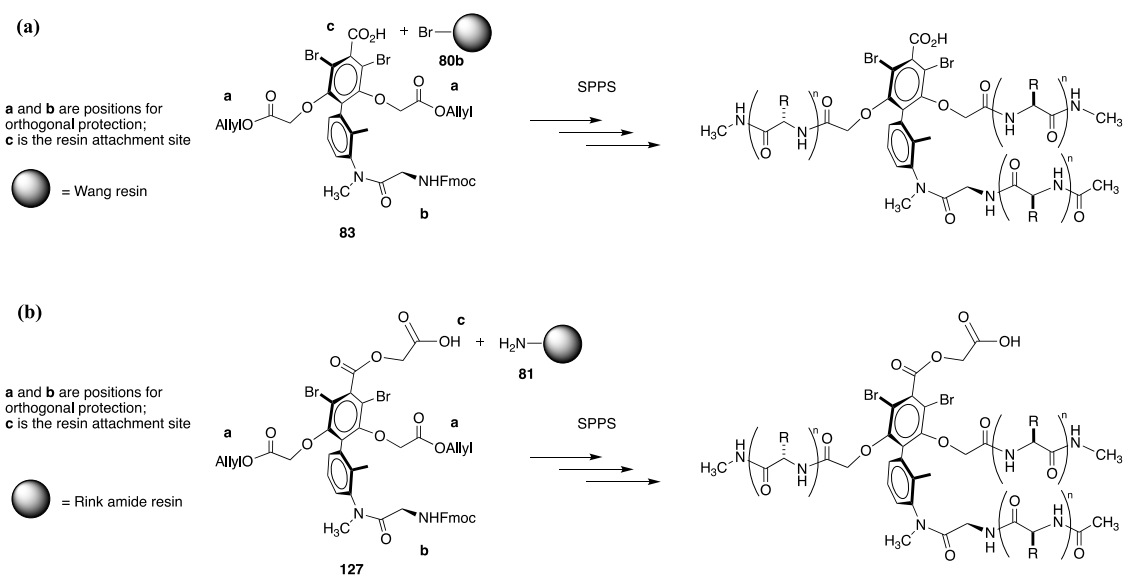


Figure 40. Advanced polypeptides of the symmetrical dibromo β -turn mimetics for detection of two (**121-122**) and five (**124-126**) interchain hydrogen bonds.

In the original strategy, results of SPPS experiments revealed poor reactivity of the biaryl carboxylate toward the bromo Wang resin. To improve the outcome of the attachment step, we needed to improve the reactivity of the torsion balance substrate. Our approach was to activate the acid using aminium coupling reagent 2-(6-Chloro-1H-benzotriazol-1-yl)-*N,N,N,N'*-tetramethylaminium hexafluoro-phosphate (HCTU) and replace the resin with NovaPEG Rink amide resin **81**. Because the 2-(4-(amino(2,4-dimethoxyphenyl)methyl)phenoxy)acetamide linker of the Rink amide resin is not sterically hindered, nor is it inductively deactivated, the nucleophilicity of the linker's amine would be sufficient to anchor the HCTU-activated biaryl acid via amidation to achieve resin loading. Secondary to this change, the biaryl carboxylate (**103**) was modified to afford a less sterically hindered attachment site for activation and amide coupling. Extension of the attachment functionality led to a new solid-phase precursor target (**127**; Scheme 21). It was reasoned that moving the carboxylate further from the aromatic ring would remove

steric hindrance from the neighboring *ortho* bromine atoms. The orientation of ether side chains on the top half of the balance needed to achieve interchain hydrogen bonding with the bottom side chain would not be disturbed by this change. Extension of the biaryl carboxylic acid resin attachment site demanded orthogonal protection in addition to that of the upper and lower side chains. The *t*-butyl group was selected for its mild deprotection conditions that would prevent side reactions with upper and lower side chains.

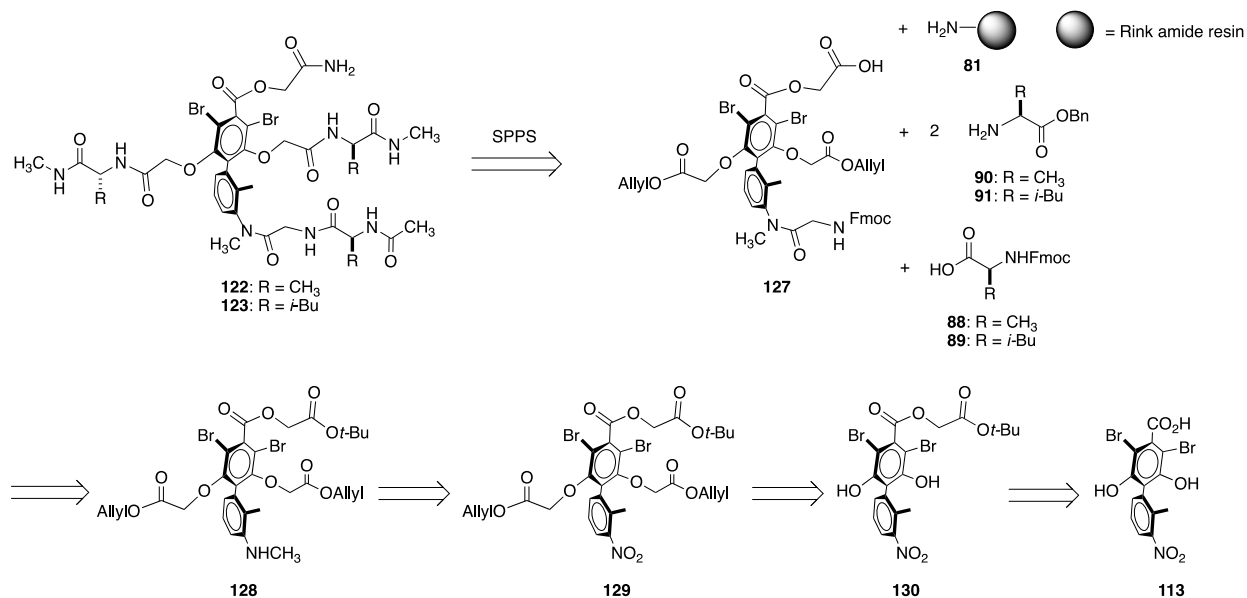
Scheme 21. Target SPPS acid precursors **83** and **127**. (a) Initial SPPS strategy using biaryl acid **83** and bromo Wang resin (**80b**). (b) Alternate SPPS strategy using biaryl carbonyloxy acetic acid **127** and Rink amide resin **81**.



Before exploring alternate options for upper side chain protection, such as propargyl or 3,5-dimethoxy benzyl, to eliminate debromination, we planned to continue to use the allyl group. If resin loading were improved in our new approach, we reasoned that the deallylation conditions on-resin could provide the desired allyl group deprotection and minimize formation of debromination side product. Additionally, the allyl group would not be susceptible to side

reactions with the TFA-mediated *t*-butyl deprotection of the resin attachment site. This modification led us to identify Gly-Ala and Gly-Leu analogs **122** and **123** as our new torsion balance targets (Scheme 22).

Scheme 22. Retrosynthetic analysis of **122-123** using solid- and solution-phase methods.



Our retrosynthetic analysis is based on three important objectives, chain extension along the upper and lower halves of the balance and the resin attachment site. The major disconnections in Gly-Ala and Gly-Leu torsion balances **122** and **123** are across the amide bonds in the upper and lower side chains. Targets **122** and **123** would be prepared via attachment of upper and lower side chains using SPPS methods. The amide bond construction for the lower glycine side chain in **127** would be formed by amidation of **128** with Fmoc-protected *L*-glycine acid chloride, generated under Carpino's conditions. Deprotection of the *t*-butyl ester would provide carboxylic acid **127** for resin attachment. The N-methyl bond of biaryl methyl amine **128** would be prepared by nitro group reduction of **129**, followed by methylation of the primary amine. We anticipated **129** would

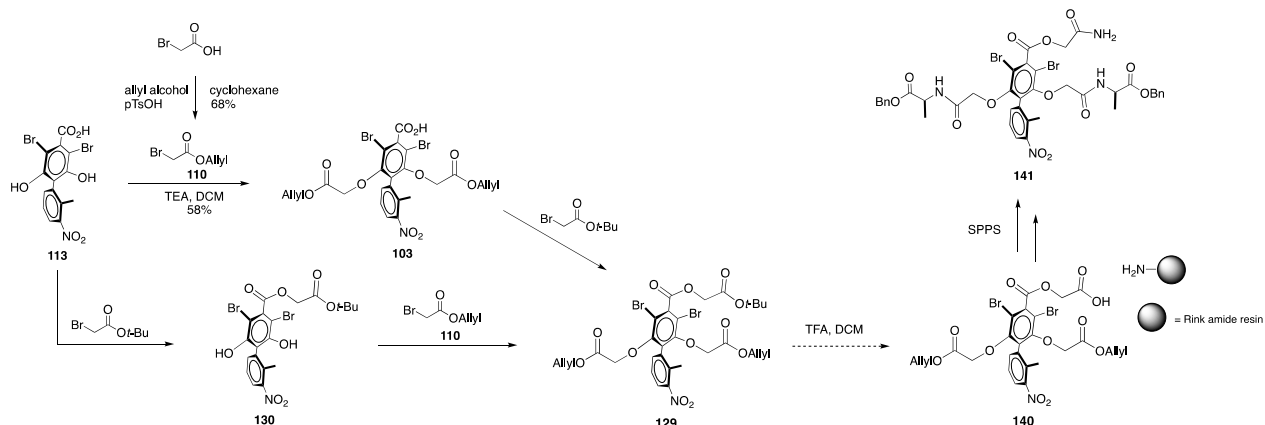
be synthesized by etherification of phenol groups in **130** with allyl bromoacetate to install the C-O bonds of the upper side chains. Extension of the resin attachment site in intermediate **130** was straightforward by esterification of acid **113**.

6.2 SYNTHESIS OF BIARYL ACID **140**

6.2.1 Synthetic Strategies for Extension of Resin Attachment Site

We examined two approaches to synthesize **129** from dihydroxybiaryl acid **113** enroute to **140** (Scheme 23). One approach to **129** was to introduce allyloxycarbonyl side chains (using our known protocol to synthesize **103**) followed by esterification of the aromatic acid. Because the aromatic acid **103** showed poor reactivity toward the bromo Wang resin in the resin loading step (Chapter 4.3), we hypothesized the esterification of **103** with *t*-butylbromoacetate would also be challenging. A second approach to **129** was pursued. Esterification of the aromatic acid in **113** prior to etherification could improve the carboxylic acid reactivity. In this way, acid **113** would be more electronically activated than **103** and increase the yield of product **130** enroute to **129**.

Scheme 23. Synthetic strategies to *t*-butyloxycarbonyl ester **129** enroute to biaryl acid **140**.



6.2.1.1 Incorporation of *t*-butyloxycarbonyl ester in biaryl acid **103**

Prior experiments for upper side chain protection revealed etherification of **113** was possible without separate protection of the hydroxyl groups (Scheme 24). Yet, we were unsure if esterification of **103** was feasible. Because the observed preference in model substrate **111** at refluxing temperatures was ester formation (Table 15), we subjected **103** to refluxing alkylation conditions to reveal product in 31% yield. Increasing the reaction time from 4 to 8 hours resulted in a mixture of products. Exposure to DIEA at room temperature failed to produce **129**. Subjecting **103** to esterification conditions with DCC and allyl alcohol gave **129** in 26% yield. An alternate synthesis to **129** was examined to improve yield.

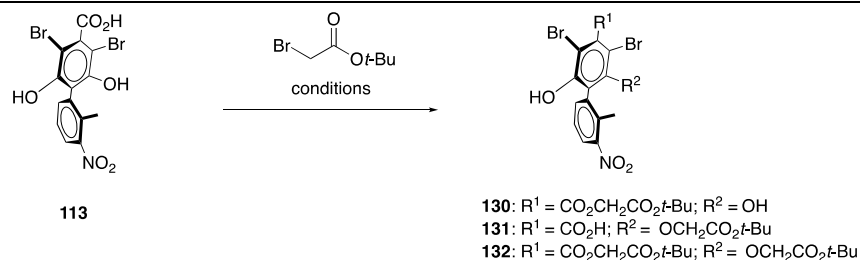
6.2.1.2 Incorporation of *t*-butyloxycarbonyl ester in **113**

The second synthetic route to **129** was to form **130** from esterification of acid **113** followed by incorporation of allyloxycarbonyl ether side chains. An important question to be answered was

whether the conditions would be selective for the acid in the presence of exposed hydroxyl groups.

Conditions used to test the feasibility of esterification **113** are reported in Table 15.

Table 15. Reactivity of biaryl carboxylic acid **113** and results of alkylation to form **130**.



Entry	Conditions ^a	Product ^b	Yield
1	TEA (1 equiv), DCM, rt, 13 h	132	44%
2	K ₂ CO ₃ (1.1 equiv), 18-c-6, acetone, reflux, 4 h	131	41%
3	2,6-dimethylpyridine (1 equiv), DCM, rt, 14 h	130 ^c	12%
4	KHCO ₃ (1.1 equiv), 18-c-6, acetone, reflux, 3 h	130 ^c	36%
5	KHCO ₃ (1.1 equiv), 18-c-6, acetone, reflux, 6 h	130	80%
6	KHCO ₃ (1.1 equiv), 18-c-6, acetone, reflux, 7 h	130	81%
7 ^d	KHCO ₃ (1.1 equiv), 18-c-6, acetone, reflux, 6 h	130	78%

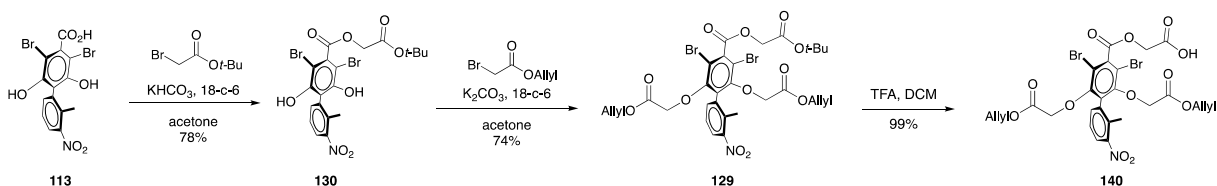
^a 0.1 mmol scale. ^b Major product observed. ^c Starting material recovered. ^d 0.35 mmol scale.

Esterification product **130** was found to be the major product in all entries with the exception of 1 and 2. As expected, subjecting **113** to TEA at room temperature produced the ether product **132**. The desired reaction product was achieved by subjecting carboxylic acid **113** to one equivalent of *t*-butyl bromoacetate in the presence of potassium bicarbonate, furnishing **129** in 78% yield. Small amounts of side products, arising from alkylation of the phenol groups, were observed.

6.2.1.3 Incorporation of allyloxycarbonyl ethers in **130**

Etherification of hydroxyl groups in **130** with allyl bromoacetate in the presence of K_2CO_3 gave biaryl **129** in 74% yield (Scheme 24). Subjecting **130** to TEA in the presence of allyl bromoacetate at room temperature also afforded **129** but in slightly lower yield. Deprotection of **129** with TFA afforded test substrate **140**, the component to be coupled to the resin, in quantitative yield.

Scheme 24. Synthesis of symmetrical ether **129** and acid **140**.



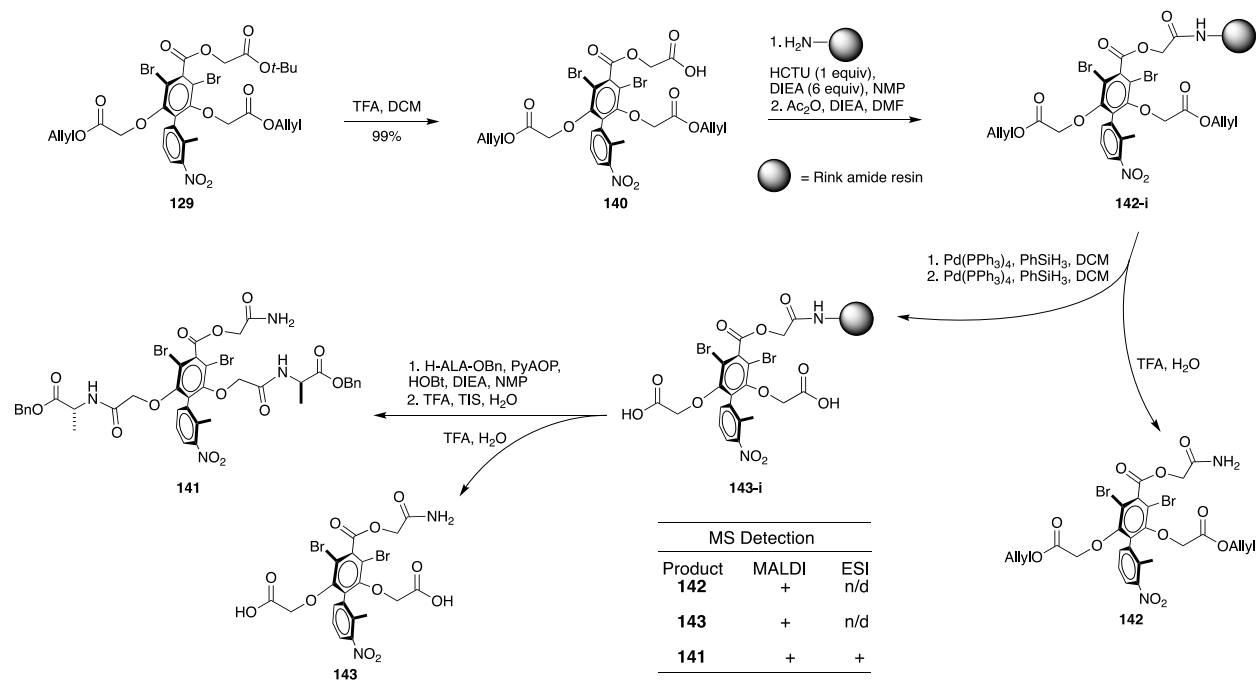
6.3 SYNTHESIS OF **141**

6.3.1 Solid-Phase Synthesis

For the following SPPS (0.01 mmol; Scheme 25), we monitored reaction progress via small scale cleavage products; product identity was established by MALDI-TOF MS before purification and by ESI-MS after purification. HPLC data for **140** was collected to serve as a baseline indication for identification of cleaved products. Substrate **140** was activated by HCTU to couple **140** to Rink amide resin **81**. HCTU was selected over more common reagents, such as BOP, PyBOP, and HBTU, to transform acid **140** to an activated ester because its lower pKa offers increased reactivity in comparison to many HOBt counterparts. Next, the resin-bound substrate was capped using acetic anhydride in the presence of DIEA. The solid phase was exposed to two deallylation

reactions. This two-step approach was necessary to avoid the debromination side reaction. The product was subjected to microwave-assisted amino acid coupling using HCTU to couple L-alanine benzyl ester to the upper side chain. MALDI-TOF MS analysis of small-scale cleavages showed product **142** and **143**. Failure to detect ions **142** and **143** by ESI-MS upon chromatographic separation was most likely due to high dilution caused by the separation process. We did an extraction to increase the concentration for detection of **141** by ESI-MS. Analysis of TFA-mediated cleavage product showed evidence of **141** by MALDI-TOF MS and ESI-MS. Due to small scale cleavages diminishing the crude yield of **141**, we do not report a yield for this sequence.

Scheme 25. Preparation of symmetrical Ala derivative **141**.



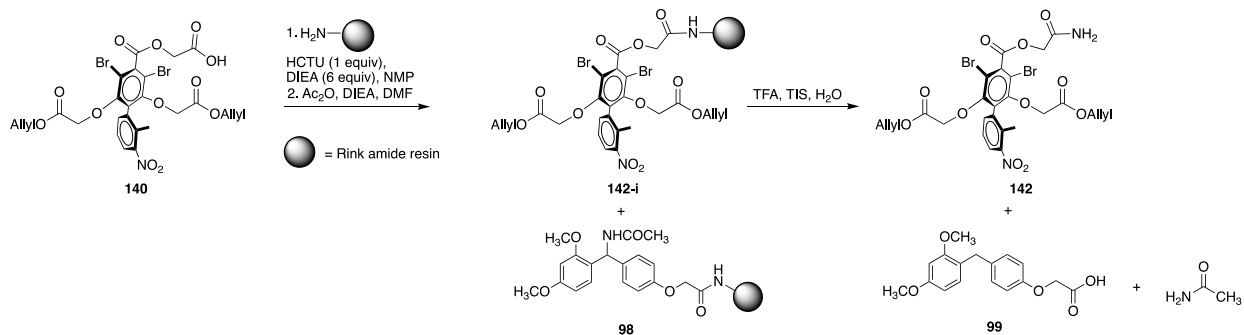
To determine reproducibility of our solid-phase protocol for upper side chain extension and resolve the NMR data of **141**, the sequence was repeated using the conditions detailed above (Scheme 25) without monitoring reaction progress. The result was a complex reaction mixture in which desired product **141** was detected in low concentration by ESI-MS. Efforts to isolate pure

product for NMR analysis were unsuccessful. Unsure if the low yield of **141** observed in the crude product was a result of incomplete resin loading or a result of substrate degradation from side reactions on-resin, our attention turned to evaluating the resin loading step.

6.3.2 Resin Loading

The HCTU-activated acid of **140** was loaded onto resin **81** with microwave-assistance, and the resin-bound product was subjected to capping with acetic anhydride and DIEA to form **142** (Scheme 26). Resin-bound product was freed by resin cleavage with TFA in the presence of triisopropyl silane (TIS) and H₂O. Product **142** was confirmed by ESI-MS data. NMR revealed acetamide and a complex mixture of products. Failure to efficiently load substrate **140** to resin would result in resin-bound amide **153-i** aside **142-i** following the capping step. We also observed a mixture of UV active products by HPLC. The UV active side product formation was probably due to linker cleavage or substrate side reaction on-resin. It is well-known that acid cleavage causes side reactions at the amide bond used to anchor the linker to the solid support.¹⁰⁹ A simple HPLC experiment was executed comparing the elution times of our impurity and dimethoxybenzene. The elution times were the same. We searched for evidence of cleaved linker side product **153** to establish that the observed outcome was a result of linker cleavage and not a result of a substrate side reaction. This was necessary because we planned to use photometric methods to determine resin loading efficiency.

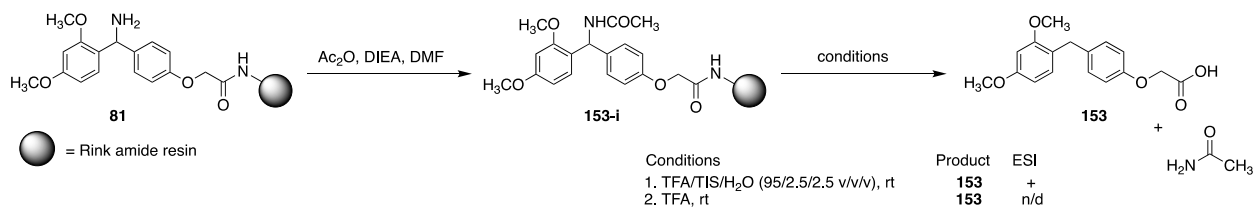
Scheme 26. Solid-phase synthesis of amide **142**.



6.3.3 Resin Cleavage

In our attempt to identify formation of side product, we carried out a control study on resin **81**. By subjecting resin **81** to the capping and cleavage protocol, a baseline purity level for the crude cleavage product was established (Scheme 27). NMR and ESI-MS analysis from the control study led us to identify resin-linker cleaved product **153**. Comparison of HPLC and NMR data of the resin loading test (Scheme 26) and control experiment (Scheme 27) confirmed the identical UV active impurity as side product **153**. Thus, the observed outcomes from the resin-loading test (Scheme 25) were a result of linker cleavage and not a result of a substrate side reaction. Acetamide was used as a standard to estimate purity of the crude product by ^1H NMR and resolve an approximate 12% yield of **142**. At this point it was evident a more efficient method was needed to load our substrate. We investigated if removing scavengers from the cleavage step would eliminate side product formation. When **81** was subjected to TFA cleavage without H_2O or TIS, only acetamide product was detected. The lack of formation of linker cleaved product **153**, led us to examine the application of scavengers in our SPPS protocol.

Scheme 27. Control test for formation of resin-linker cleavage product **153**.



6.3.4 Optimization of Resin Loading and Cleavage Steps

Optimization of the resin substitution and cleavage conditions was our next priority. We needed to improve resin loading efficiency and the purity of liberated crude product for accurate quantification and characterization of SPPS intermediates. Since our biaryl substrate was ideal for photometric resin loading measurement, it was necessary to prevent formation of UV-active linker product to accurately quantify substitution. The elimination of additional purification steps was also necessary for waste minimization practices.

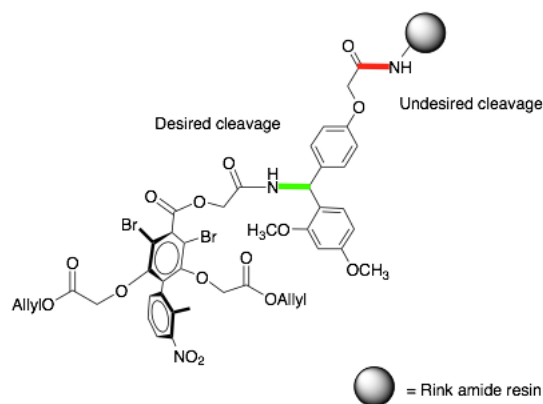


Figure 41. Cleavage sites in resin-bound substrate **142-i**.

Our approach to improve resin coupling was to activate acid **140** with PyAOP in the presence of HOBt instead of HCTU (Figure 42). PyAOP was expected to improve loading efficiency because the pyridine nitrogen provides anchimeric assistance during coupling.¹⁰⁶ The cleavage protocol was examined to determine if H₂O and TIS were necessary during liberation of our substrate from resin. These scavengers as well as ethane dithiol (EDT) are commonly used in SPPS to minimize undesired peptide modifications that may occur from reactions with TFA-liberated reactive species.¹¹³ Because the elimination of scavengers decreased the production of undesired linker product **153** in our control study (Scheme 27), we examined the effects of those on substrate-resin cleavage. NMR and HPLC-DAD analysis were used to determine purity of product with dimethoxybenzene standardized samples.

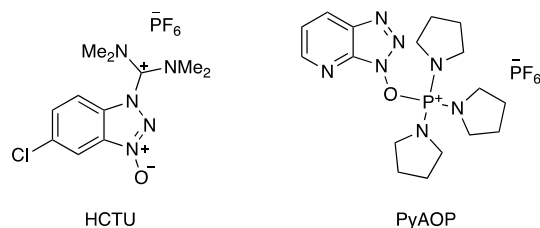


Figure 42. Resin coupling reagents for activation of acid **140**.

We applied the new activation protocol on acid **140** followed by resin substitution using MW irradiation. The product was treated with capping conditions and subsequent cleavage by TFA alone. Amide **142** was observed in an estimated 14% yield without detection of acetamide or **153**. The absence of acetamide was unlikely a result of quantitative loading in the coupling step, but rather due to reattachment to the linker in the cleavage step. The solid-supported material was subjected to two additional cleavage reactions using the TFA/TIS/H₂O cocktail. HPLC and NMR analysis revealed additional amide **142**, but with a 30% decrease in purity. The combined

results of repetitive cleavages gave amide **142** in approximately 27% yield, a significant improvement from the estimated 12% yield of the HCTU-mediated loading conditions.

Efforts were made to improve purity of reaction product. We hypothesized that the presence of H₂O was causing amide bond hydrolysis at the linker-resin attachment point and that removal of H₂O would decrease production of undesired linker-cleaved product **153**. Treatment of our solid-supported substrate with two repetitive TFA/TIS (95/5 v/v) cleavage cocktails revealed product **142** in 31% yield and in 90% purity. These results support our hypothesis that H₂O was causing hydrolysis of the linker at the resin attachment site. In summary, these data indicate increased resin loading efficiency and crude product purity. PyAOP and HOBt are improved coupling reagents compared to HCTU. Elimination of H₂O from the cleavage step, significantly minimizes undesired linker cleavage product. Despite our improvements, we chose not to utilize photometric measurement to determine resin loading efficiency as planned (Chapter 4.3.5). NMR and HPLC-DAD analysis were used for our study due to UV active side product formation.

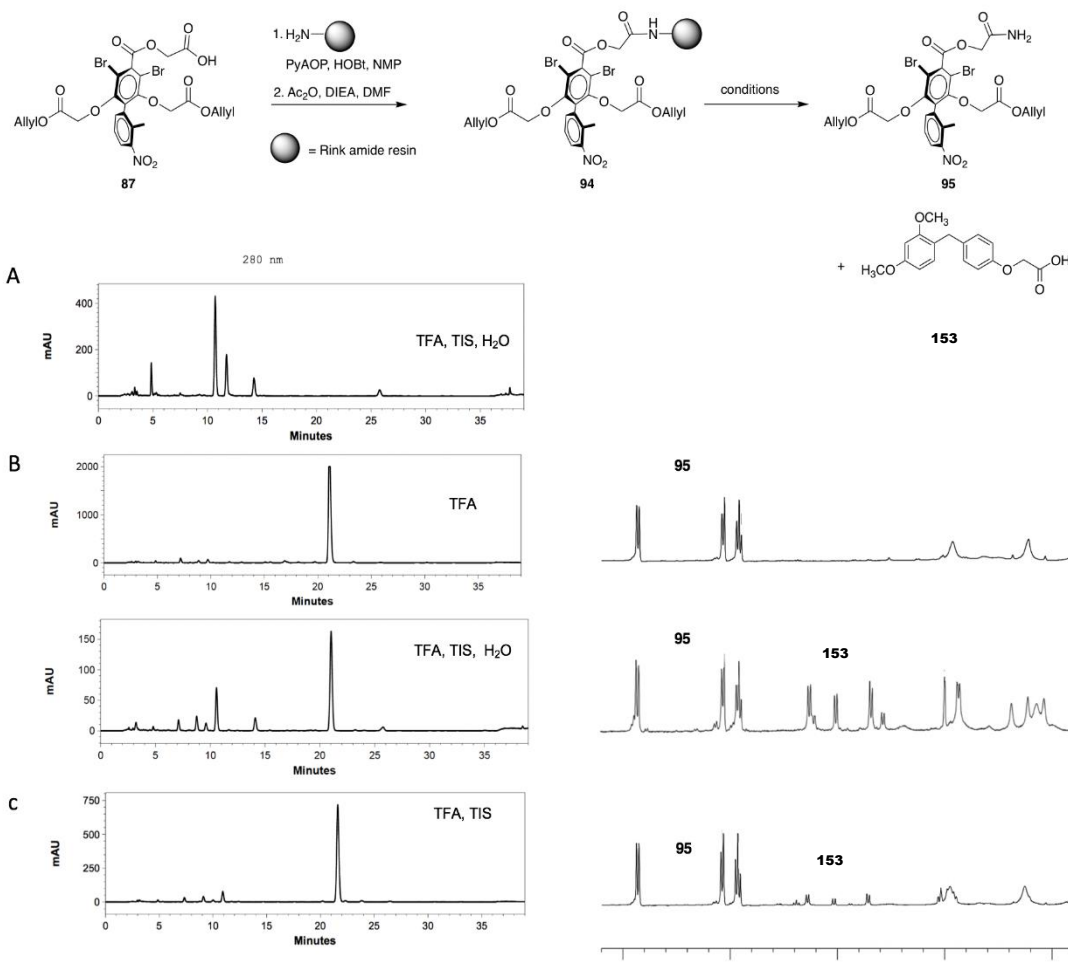


Figure 43. Analytical HPLC-DAD chromatograms (280 nm) and NMR data (700 MHz, CD₃CN) at room temperature of Rink amide resin cleavage experiments. Product **153** was observed at A₂₂₀ and A₂₉₈. (a) Baseline purity of Rink amide cleavage control experiment (TFA/TIS/H₂O (95/2.5/2.5 v/v/v)). HPLC and NMR results of treatment of **142-i** with (b) TFA, (c) TFA/TIS (95:5 v/v), and (d) TFA/H₂O/TIS after 2 hours.

6.3.5 Optimized Synthesis of **141**

Activated acid **140** was anchored onto resin **81**, and resin-bound product was capped using Ac₂O and DIEA (Scheme 28). Formed product was treated with two consecutive aliquots of 0.5 equivalents of Pd(PPh₃)₄. Finally, the microwave-assisted coupling of alanine benzyl ester to the aliphatic carboxylic acids in **143-i** was carried out and followed by resin cleavage with TFA/TIS only. In this way, target **141** was prepared in six steps and 29% overall yield with an approximate

95% purity by HPLC (Figure 44). In an attempt to further optimize our new cleavage conditions, reaction time of the cleavage step was reduced from 3 hours to 1.5 hours. Cleaved linker **153** still remained a minor contaminant. 2D NMR experiments of **141**, including ROESY and HMBC, were performed at 1 and 10 mM in CD₃CN at 298 K on a 700 MHz NMR. We searched for evidence of upper side chain interaction. Since our preliminary data confirm that the side chains are perpendicular to the plane of the aromatic ring, it is of interest to determine the cavity size between upper peptide strands of *n* residues *syn* to one another (discussed in Chapter 3.2.). Extending the length of the upper side chains in derivatives of **141** would provide important data for solvation effects and upper strand interchain aggregation.

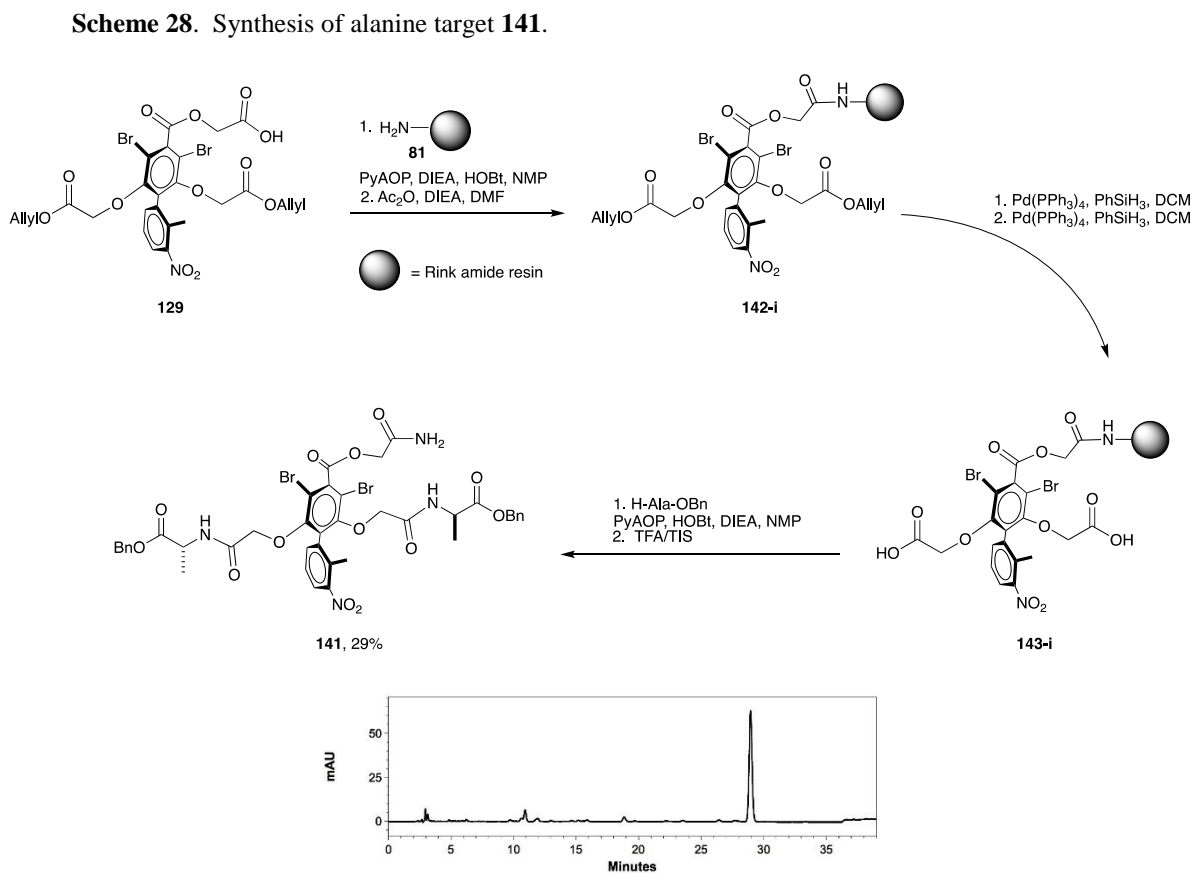
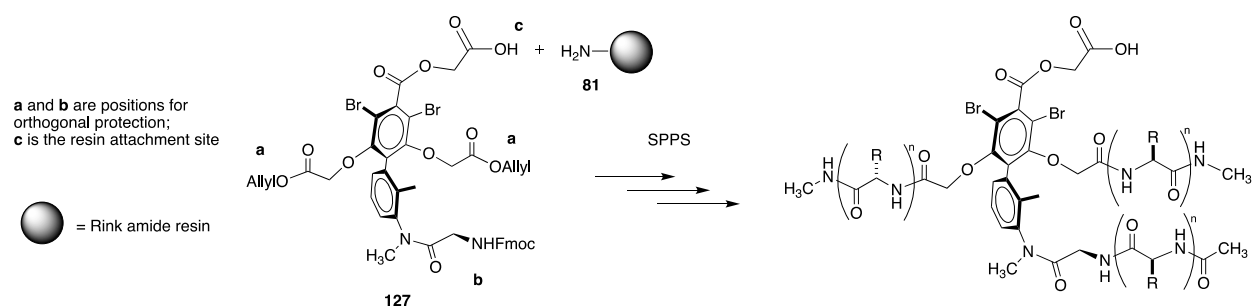


Figure 44. HPLC chromatogram of crude alanine product **141** (A₂₈₀) from SPPS protocol in Scheme 28.

6.4 SYNTHESIS OF SPPS PRECURSOR BIARYL ACID **127**

With an acceptable route to **141** in hand, we directed our attention to functionalizing the bottom half of the balance to generate SPPS precursor **127** for resin attachment. The synthesis of **127** proceeded by functionalizing the top half of the balance before the lower half of the balance.

Scheme 29. SPPS precursor **127**.



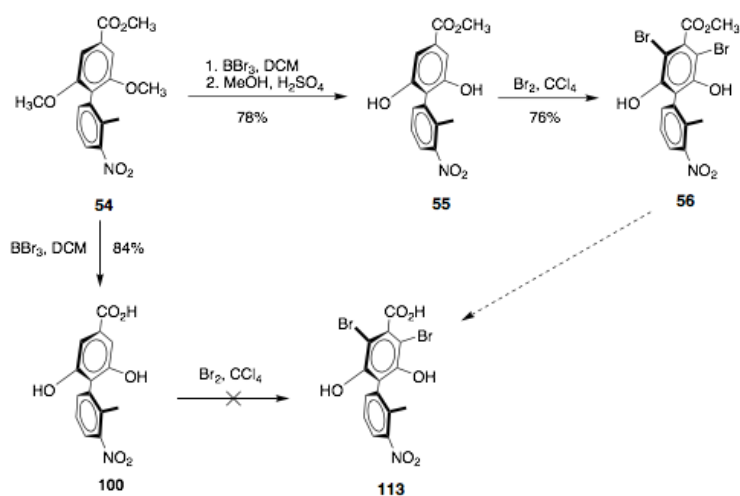
During our attempt to prepare a library of peptides from solid-phase syntheses, low yields were obtained when scaling up the hydrolysis of **54** beyond 1 mmol. The LiOH-promoted hydrolysis of the methyl ester was complicated by inconsistent yields of **113** and complex mixtures of products. At this point we sought a more efficient synthesis of **113**.

6.4.1 Synthesis of Acid **113**

Our inefficient synthesis of **113** relied upon the one-pot synthesis of **54** by cleavage of dimethyl ethers and methyl ester by BBr_3 , followed by immediate Fischer esterification prior to dibromination *ortho* to the phenols and methyl ester; however, dibromination of carboxylic acid **100** would lead directly to **113** and avoid the additional esterification before dibromination and methyl ester cleavage step after debromination (Scheme 30). Biaryl **54** was subjected to treatment

with BBr_3 to give **100** but attempts to dibrominate **100** were unsuccessful. We failed to detect **113**, the dibrominated product. Efforts were taken to optimize reaction conditions, such as changing solvent, but no positive result was obtained. Experiments employing additional equivalents of Br_2 were not pursued because prior experience showed the lower ring was susceptible to bromination under forcing conditions. We expect our results are due to the carboxylic acid being less inductively deactivated than the methyl ester derivative. The three-step sequence shown in Scheme 30 was revisited using different conditions for the crucial step.

Scheme 30. Attempted synthetic strategies of acid **154**.

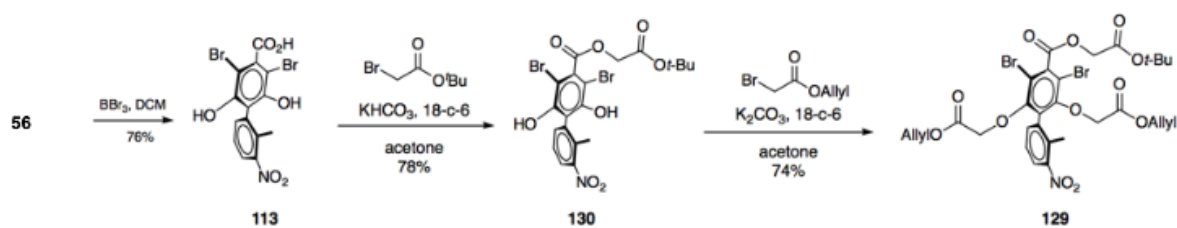


6.4.1.1 Optimization of biaryl methyl ester cleavage

We examined conditions for the less efficient strategy of methyl ester cleavage of **56**. Despite sufficient yields of initial saponification experiments, large scale saponification of **56** using traditional basic hydrolytic methods was complicated by inconsistent yields of **113** and complex mixtures of products. These conditions were initially pursued because of Liberatore's success with similar substrates as well as the inexpensive cost of reagents. In light of work by Nicolau and

coworkers on mild hydrolysis of methyl esters using trimethyltin hydroxide (Me_3SnOH),¹²² we tested such conditions with our substrate. Model reactions with trimethyltin hydroxide on commercially available 5-methyl-2-methylbenzoate in DCE afforded the acid derivative in 90% yield; however, application of the conditions to biaryl methyl ester **56** failed to produce hydrolyzed product **113**, even with forcing conditions. The low-yielding and failed reactions may have been due to inefficient aqueous workup or base-promoted decomposition of material. The use of BBr_3 provided carboxylic acid **113** in 76% yield without incident. The successful route was not considered sooner because of expense. From this point forward, we used the pathway shown in Scheme 31. With **113** in hand, we converted the acid to **129** via alkylations with *t*-butyl and allyl bromoacetate, respectively.

Scheme 31. Improved synthesis of acid **113** enroute to **129**.

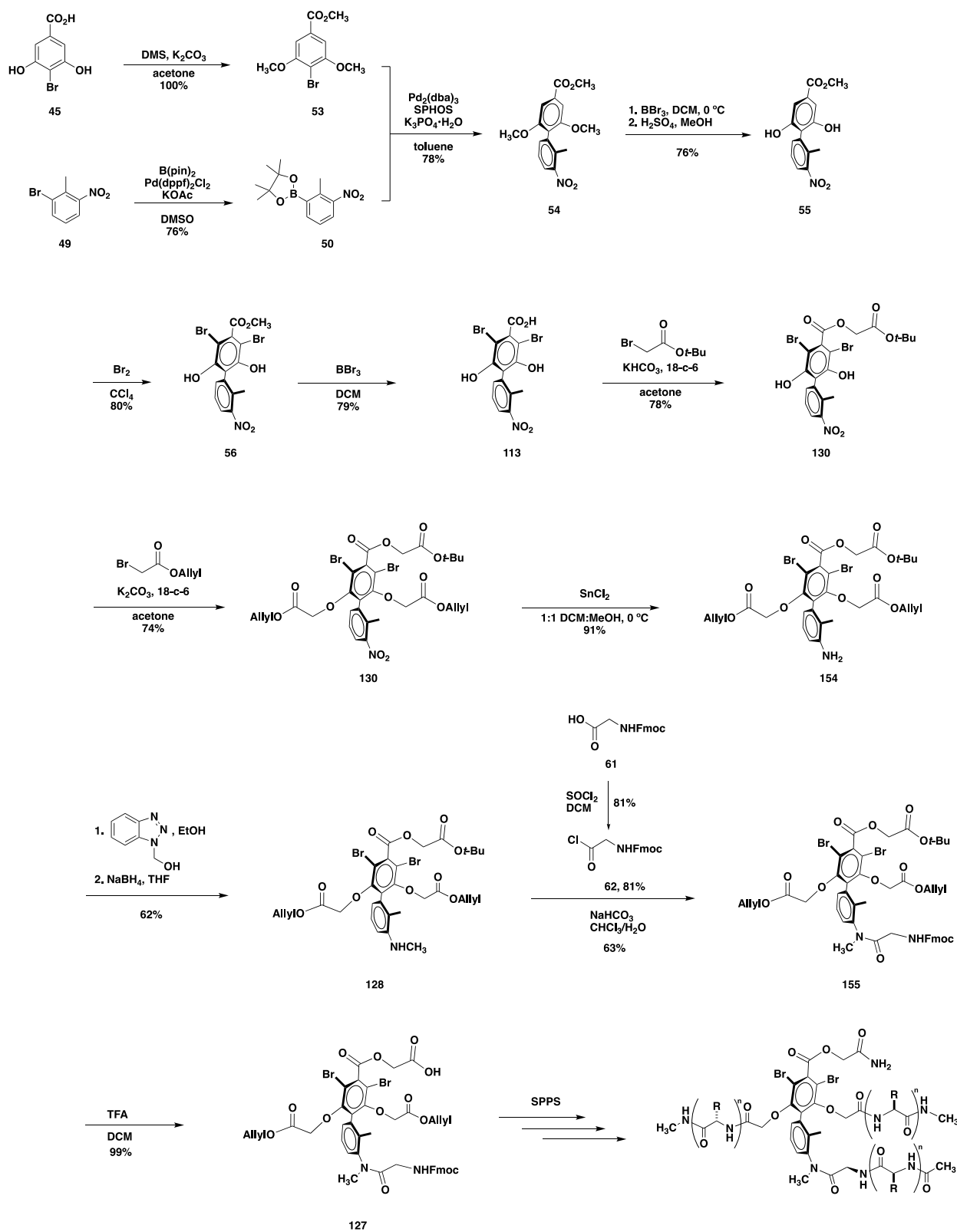


6.4.2 Incorporation of Lower Peptide Chain

Less acidic methods for nitro reduction were necessary to prevent cleavage of the *t*-butyl group under acidic conditions. In a model reaction, *t*-butyl 3,5-bis(allyloxy)-4-bromobenzoate was subjected to SnCl_2 in DCM and MeOH at 0 °C and warmed to room temperature to stir for 13 hours. There was no evidence of *t*-butyl ester cleavage. Following this success, we found treating **89** with SnCl_2 at 0 °C gave **155** in 91% yield.¹²¹ N-Methylation using our modified Katritzky route afforded derivative **128** (Scheme 32). This was followed by coupling Fmoc-glycine chloride **62**

to furnish biaryl **127**. Treatment of **155** with **20**, followed by reduction with NaBH₄ afforded the methylated biaryl **128** in 62% yield. Commercially available 9-fluorenylmethyloxycarbonyl-glycine (Fmoc-gly) was converted to its corresponding acid chloride **62** with thionyl chloride, which was immediately coupled with biaryl **128**. Biaryl amide **156** was isolated in 67% yield. The final step to synthesize torsion balance core **127** involved treatment of **156** with TFA in DCM to deprotect the acid (99% yield). Finally, cleavage of the *t*-butyl ester with TFA could provide product **86** over 14 steps for upper and lower chain extension on-resin.

Scheme 32. Synthesis toward advanced derivatives **81-85**.



6.5 SUMMARY OF PROGRESS TOWARD ADVANCED DERIVATIVES 122-126

Progress toward the synthesis of advanced derivatives of the β -turn mimetic torsion balance using solid-phase synthetic methods has been achieved. We have overcome many setbacks from the resin loading step, which is well-known to be the most demanding transformation in SPPS. In conclusion: (i) derivative **140** is an improved substrate to achieve resin loading in comparison to **103**; (ii) the Rink amide resin is superior to the bromo Wang resin to anchor the torsion balance substrate; and (iii) PyAOP activation improves loading efficiency compared to HCTU. Additionally, we have established the solid-phase synthetic route is feasible for upper side chain extension. The core structure was successfully coupled to protected amino acid esters on-resin. Furthermore, we have significantly improved the purity of our crude samples for quantification, characterization and waste minimization. 2D NMR data did not reveal upper interchain ROEs. The synthetic route to SPPS precursor **127** was established by attachment and extension of the lower peptide chain.

7.0 EXPERIMENTAL

7.1 GENERAL

Dry solvents were obtained prior to use by distilling the solvents from the appropriate drying agent under nitrogen atmosphere. DCM was distilled from CaH_2 , toluene was distilled from CaCl_2 , DMF was vacuum distilled from 4 Å molecular sieves, and diethyl ether and THF were distilled from sodium metal and benzophenone. Dry CCl_4 and DMSO were purchased from Aldrich and used as supplied. “Removal of volatile components under reduced pressure” refers to rotary evaporation of the sample at 21-65 °C at a pressure of 18-25 mm Hg followed by treatment under high vacuum (0.1 mm Hg) at room temperature. All other reagents and solvents were purchased from Aldrich, Baker, EMD, or Fisher and used without further purification. NovaPEG Rink Amide resin, Wang resin, HCTU and Fmoc-protected α -amino acids were purchased from Novabiochem. HOBt was purchased from Anaspec Inc. Microcleavages were taken for SPPS intermediates.

Bruker Avance 300, 400, 500, 600 and 700 MHz spectrometers were used to find proton and carbon nuclear magnetic resonance spectra (^1H and ^{13}C NMR). TMS (^1H) or residual solvent (^1H ; ^{13}C) peak were set as the reference value to report chemical shifts in parts per million (PPM; δ). 1D and 2D NMR experiments were performed at room temperature (21 – 27 °C) unless indicated otherwise. NMR Data are reported using the following list of abbreviations: s = singlet; d = doublet; t = triplet; q = quartet; dd = doublet of doublets; m = multiplet; quin = quintet; ABq = AB quartet; quartet of doublets = qd; doublet of quintets = dquin. NMR samples were prepared by dissolving peptide in 750–850 μL of degassed 50 mM phosphate, 9:1 $\text{H}_2\text{O}:\text{D}_2\text{O}$, pH 6.3

(uncorrected for the presence of D₂O) to a final concentration of 0.8–3 mM. 3-(Trimethylsilyl)-1-propanesulfonic acid sodium salt (DSS, 50 mM in water) was added to a final concentration of 0.2 mM. The NMR tube headspace was purged with a stream of nitrogen prior to capping.

Thin layer chromatography (TLC) was performed on E. Merck 60F 254 (0.25 mm) analytical glass plates. A Thomas Hoover capillary melting point apparatus was used to obtain melting points and are uncorrected. A Nicolet Avatar 360 FT-IR was utilized to determine infrared (IR) spectra. High resolution mass spectra were recorded on a VG 7070 spectrometer. Percent yields are for material of >95% purity as indicated by ¹H NMR spectra and/or HPLC data.

7.1.1 General information for SPPS protocols

Two SPPS protocols were applied in our synthesis. For all syntheses, after the final deprotection reaction, the resin was washed three times with 3 mL of dichloromethane followed by three 3 mL washes of methanol. After drying in a vacuum desiccator, the resin was cleaved.

Compounds were synthesized using microwave-assisted Fmoc solid-phase synthesis techniques on a MARS microwave reactor (CEM) using NovaPEG Rink Amide resin. Couplings were carried out in NMP at 70 °C for 4 min using 4 equiv. of Fmoc-protected amino acid, 4 equiv. of HCTU, and 6 equiv. DIEA. PyAOP was used in place of HCTU for the coupling of N-methylated residues and residues immediately following them. Deprotections were performed using an excess of 20% 4-methylpiperidine in DMF at 80 °C for 2 min. After each coupling or deprotection cycle, the resin was washed three times with DMF. Double couplings were performed at sequence positions following proline or N-methylated residues. Prior to cleavage, the resin was washed three times each with DMF, dichloromethane, and methanol, and then dried. Intermediates were cleaved from resin by suspension in a solution of 95% trifluoroacetic acid (TFA), 2.5%

triisopropylsilane (TIS), and 2.5% water or 95% trifluoroacetic acid (TFA), 5% triisopropylsilane (TIS). This solution was then subjected to purification protocol outlined below.

7.1.1.1 Purification and Characterization

Compounds generated by SPPS were purified by preparative C18 reverse-phase HPLC using gradients between 0.1% TFA in water and 0.1% TFA in acetonitrile. The identity of each was confirmed by MS analysis on a Voyager DE Pro MALDI-TOF instrument or VG 7070 spectrometer. Following HPLC purification, each was subjected to extraction with H₂O and ACN. Final samples were $\geq 95\%$ pure by analytical reverse-phase HPLC.

7.1.2 Monte Carlo Simulations and Dynamics

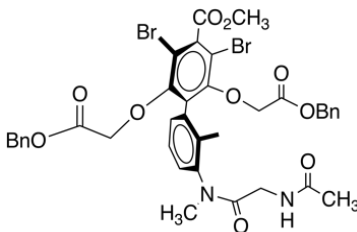
Monte Carlo simulations were completed by Craig S. Wilcox.

Line shape analysis was performed using iNMR. Bond rotational barriers were calculated using the Eyring equation.

$$\left| k = \frac{k_B T}{h} e^{-\left(\frac{\Delta G^\ddagger}{RT}\right)} \right|_{\Delta S^\ddagger = 0}$$

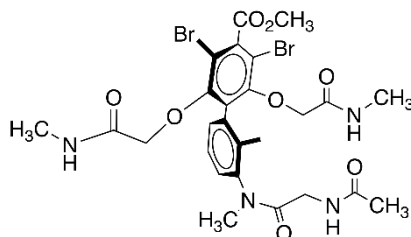
7.2 EXPERIMENTAL PROCEDURES

Representative Procedures: A solution of the requisite carboxylic acid and DIEA in DMF or DCM was added to a stirred solution of requisite bromide and KI in DMF. The reaction mixture was stirred at room temperature for 16 hours. For SPPS: The solid-phase was filtered and washed with DMF x 3. For SPS: The reaction was concentrated and subjected to purification by flash chromatography. Derivatives were synthesized using microwave-assisted Fmoc solid-phase synthesis techniques oMARS microwave reactor (CEM) using NovaPEG Rink Amide resin. Couplings were carried out in NMP at 70 °C for 4 min using 4 equiv. of Fmoc-protected amino acid, 4 equiv. of HCTU, and 6 equiv. DIEA. PyAOP was used in place of HCTU for the coupling of N-methylated residues and residues immediately following them. Deprotections were performed using an excess of 20% 4-methylpiperidine in DMF at 80 °C for 2 min. After each coupling or deprotection cycle, the resin was washed three times with DMF. Prior to cleavage, the resin was washed three times each with DMF, dichloromethane, and methanol, and then dried. The filtrate was saved and extracted.



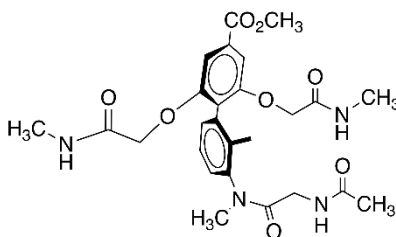
Dibenzyloxycarbonyl 2,2'-((3'-(2-acetamido-N-methylacetamido)-3,5-dibromo-4-(methoxycarbonyl)-2'-methyl-[1,1'-biphenyl]-2,6-diyl)bis(oxy))diacetate (39). To 0.01 g (0.01 mmol) of **63** in a round-bottom flask was added 0.045 mL of a 20% piperidine/DMF solution, and the reaction mixture was stirred at room temperature for 20 min. Then 0.24 mL (mmol) of acetic anhydride

and 0.71 mL (mmol) of pyridine were added, and the solution was stirred at room temperature for 30 min. The volatile components were removed from the filtrate under reduced pressure to give a yellow oil. The oil was purified by flash chromatography (SiO₂, hexanes/ethyl acetate/methanol elution gradient 1:1:0/2:3:0/0:1:0/0:9:1) to give 0.007 g (76%) of **39** as a white foam: *R_f* 0.34 (100% ethyl acetate); IR (thin film, cm⁻¹) 3338, 2932, 1751, 1723, 1655, 1580, 1423, 1393, 1369, 1329, 1235, 1193, 1135, 1029, 996, 844, 806, 733; ¹H NMR (700 MHz, CDCl₃) δ 7.34-7.27 (m, 8H), 7.22-7.19 (m, 4H), 7.14-7.13 (m, 1H), 6.26 (broad s, 1H), 5.07 (s, 2H), 5.02 (s, 2H), four protons of conformers: [4.25, 3.96 (qAB, *J* = 15 Hz), 4.20, 4.15 (qAB, *J* = 15 Hz)], 4.02 (s, 3H), two protons of conformers: [3.65 (qd, *J* = 4.9 Hz), 3.35 (s)], 3.15 (s, 3H), 2.01 (s, 3H), 1.95 (s, 3H); ¹³C NMR (500 MHz, CDCl₃) δ 170.0, 169.0, 167.2, 167.1, 166.1, 153.5, 141.6, 139.6, 136.4, 135.6, 135.3, 133.9, 131.4, 131.3, 127.8, 111.7, 111.3, 69.5, 67.4, 67.1, 53.7, 42.2, 36.3, 23.4, 15.3; HRMS (ESI-TOF) *m/z*: [M+CHO₂]⁻ calcd for C₃₉H₃₇O₁₂N₂Br₂ 885.0700, found 885.0709.



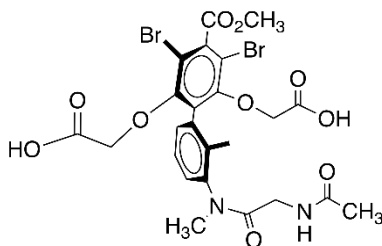
Methyl 3'-(2-acetamido-N-methylacetamido)-3,5-dibromo-2'-methyl-2,6-bis(2-(methylamino) -2-oxoethoxy)-[1,1'-biphenyl]-4-carboxylate (43). To a round-bottom flask equipped with a condenser and nitrogen gas inlet were added 0.015 g (0.023 mmol) of diacid **45**, 0.006 g (0.068 mmol) of methylamine hydrochloride, 0.013 g (0.17 mmol) of EDCI, 0.010 g (0.068 mmol) of HOBT, 0.015 mL (0.084 mmol) of DIEA, and 0.46 mL of DCM. The reaction mixture was stirred at room temperature for 16 h and diluted with EtOAc (10 mL) and washed with 1.0 M NaOH (5 mL), water (10 mL), and then brine (10 mL). The organic layers were combined, dried over MgSO₄ and filtered, and the volatile components were removed from the filtrate under

reduced pressure to give a crude brown oil. The oil was purified twice by flash chromatography (SiO₂, (first column: hexanes/EtOAc/MeOH elution gradient 1:1:0/2:3:0/0:1:0/0:9:1); (second column: DCM/MeOH elution gradient 1:0/49:1/19:1)) to give 0.009 g (63%) of **43** as a white foam: *R_f* 0.15 (100% EtOAc); ¹H NMR (700 MHz, CD₂Cl₂) δ One proton of conformers: [7.43 (t, *J* = 15.4 Hz), 7.39 (t, *J* = 15.4 Hz)], one proton of conformers: [7.30 (d, *J* = 7.7 Hz), 7.17 (d, *J* = 7.7 Hz)], one proton of conformers: [7.30 (d, *J* = 7.7 Hz), 7.26 (d, *J* = 7.7 Hz)], one proton of conformers: [6.80 (broad s), 6.03 (broad s)], one proton of conformers: [6.36 (broad s), 6.46 (broad s)], one proton of conformers: [6.19 (broad s), 6.26 (broad s)], two protons of conformers: [4.30, 4.27 (qd, *J* = 18.2, 6.3 Hz), 3.72, 3.36 (ABq, *J* = 6.3 Hz)], two protons of conformers: [4.18-4.00 (ABq, *J* = 6.3 Hz), 4.56-3.79 (ABq, *J* = 14.7 Hz)], two protons of conformers: [4.10, 4.00 (ABq, *J* = 10.5 Hz), 4.20, 4.00 (ABq, *J* = 10.5 Hz)], 4.00 (s, 3H), three protons of conformers: [3.36 (s), 3.21 (s)], 2.65 (d, *J* = 4.9 Hz, 3H), three protons of conformers: [2.59 (d, *J* = 4.9 Hz), 2.47 (d, *J* = 4.9 Hz)], three protons of conformers: [2.02 (s), 1.98 (s)], three protons of conformers: [2.00 (s), 1.88 (s)]; ¹³C NMR (700 MHz, CD₂Cl₂) δ 168.7, 167.4, 165.9, 153.5, 153.2, 143.4, 142.0, 140.0, 135.8, 135.3, 134.4, 133.6, 132.1, 132.0, 131.0, 129.3, 128.2, 127.8, 111.4, 111.1, 72.2, 72.0, 42.0, 41.8, 36.5, 30.0, 26.2, 25.8, 23.2, 15.7, 15.2; HRMS (ESI-TOF) *m/z*: [M+H]⁺ calcd for C₂₆H₃₁N₄O₈Br₂ 687.0488, found 687.0477.

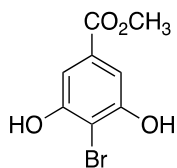


Methyl 3'-(2-acetamido-N-methylacetamido)-2'-methyl-2,6-bis(2-(methylamino)-2-oxoethoxy)-[1,1'-biphenyl]-4-carboxylate (44). To a solution of 0.015 g (0.028 mmol) of **73** in DCM (0.045 mL) at room temperature was added 0.009 ml (0.111 mmol) of TFA and the reaction

mixture was stirred for 2 h. The volatile components were removed under reduced pressure to give a brown crude oil. To this crude oil, in a vial equipped with a condenser and nitrogen gas inlet were added 0.007 g (0.108 mmol) of methylamine hydrochloride, 0.021 g (0.108 mmol) of EDCI, 0.016 g (0.108 mmol) of HOBT, 0.023 mL (0.132 mmol) of DIEA, and 0.72 mL of DCM. The reaction mixture was stirred at room temperature for 80 h, and the volatile components were removed under reduced pressure to give a crude brown oil. The oil was purified by flash chromatography (SiO₂, (first column: hexanes/EtOAc/MeOH elution gradient 1:1:0/2:3:0/0:1:0/0:9:1); (second column: DCM/MeOH elution gradient 1:0/49:1/19:1)) to give 0.004 g (24%) of **44** as a white foam: *R_f* 0.1 (100% EtOAc); ¹H NMR (700 MHz, CD₂Cl₂) δ one proton of conformers: [7.44 (t, *J* = 7.7 Hz), 7.43 (t, *J* = 7.7 Hz)], 7.39 (d, *J* = 0.7 Hz), 7.38 (d, *J* = 0.7 Hz, 1H), one proton of conformers: [7.29 (d, *J* = 7.7 Hz), 7.22 (d, *J* = 7.7 Hz)], one proton of conformers: [7.27 (d, *J* = 7.7 Hz), 7.17 (d, *J* = 7.7 Hz)], 6.38 (broad s, 1H), one proton of conformers: [6.08 (broad s), 6.23 (broad s)], one proton of conformers: [5.89 (broad s), 5.72 (broad s)], two protons of conformers: [4.54, 4.34 (ABq, *J* = 14.0 Hz), 4.45, 4.44 (qAB, *J* = 4.9, 3.5 Hz)], two protons of conformers: [4.46, 4.42 (ABq, *J* = 14.7 Hz), 4.39, 4.37 (ABq, *J* = 7.0 Hz)], two protons of conformers: [4.25, 4.23 (qd, *J* = 18.2, 4.2 Hz), 3.66, 3.54 (ABq, *J* = 17.5, 4.2 Hz)], 3.93 (s, 3H), three protons of conformers [3.37 (s), 3.24 (s)], three protons of conformers: [2.71 (d, *J* = 4.9 Hz), 2.66 (d, *J* = 4.9 Hz)], 2.63 (d, *J* = 4.9 Hz, 3H), three protons of conformers: [2.1 (s), 1.96 (s)], three protons of conformers: [1.95 (s), 1.88 (s)]; ¹³C NMR (700 MHz, CD₂Cl₂) δ 168.7, 168.0, 166.2, 155.9, 155.5, 141.7, 136.1, 135.9, 132.5, 131.1, 128.2, 127.7, 123.7, 108.7, 108.2, 69.0, 68.5, 42.0, 36.5, 30.1, 25.8, 23.1, 14.7; HRMS (ESI-TOF) *m/z*: [M+H]⁺ calcd for C₂₆H₃₃N₄O₈ 529.2298, found 529.2289.

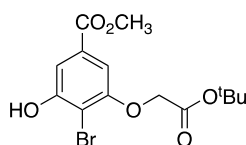


2,2'-((3'-(2-Acetamido-*N*-methylacetamido)-3,5-dibromo-4-(methoxycarbonyl)-2'-methyl-[1,1'-biphenyl]-2,6-diyl)bis(oxy))diacetic acid (45). To a nitrogen charged flask, 0.01 g (0.01 mmol) of **39** and 0.01 g (0.01 mmol) of PtO₂ were added and dried under reduced pressure for 5 minutes and backfilled with nitrogen twice. Under hydrogen atmosphere, ethyl acetate (0.2 mL) was added and stirred for 13 hours. The reaction mixture was passed through a Celite plug and washed with ethyl acetate (2 ml). Volatile components were removed from the filtrate under reduced pressure to obtain 0.01 g (91%) of **45** as a glass-like foam. *R_f* 0.18 (9:1 ethyl acetate:MeOH); ¹H NMR (400 MHz, CDCl₃) δ 7.31 (t, *J* = 8 Hz, 1H) 7.22 (d, *J* = 8 Hz, 1H), 7.11 (d, *J* = 8 Hz, 1H), 6.89 (broad s, 2H), 4.33, 4.03 (ABq, *J* = 16, 15 Hz, 2H), 4.17-3.97 (m, 2H), 3.68, 3.58 (ABq, *J* = 18, 4 Hz, 2H), 3.74 (s, 3H), 3.16 (s, 3H), 2.00 (s, 3H), 1.99 (s, 3H); ¹³C NMR (400 MHz, CDCl₃) δ 172.2, 169.8, 169.4, 168.7, 168.0, 166.0, 154.3, 153.4, 141.0, 139.7 135.9, 134.2, 132.3, 131.8, 129.2, 128.3, 112.1, 111.4, 70.5, 69.3, 53.8, 47.9, 43.1, 43.0, 36.6, 32.3, 30.0, 29.7, 26.7, 25.8, 24.7, 23.2, 23.0, 21.5, 15.1; HRMS (ESI-TOF) *m/z*: [M+H]⁺ calcd for C₂₄H₂₃Br₂N₂O₁₀ 656.9714, found 656.9732.



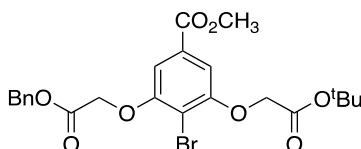
Methyl 4-bromo-3,5-dihydroxybenzoate (46). To 1.0 g (4.4 mmol) of carboxylic acid **45** in 6.8 mL of methanol was added .41 mL (7.6 mmol) of H₂SO₄ dropwise, and the reaction mixture was refluxed for 16 h. The reaction was quenched by addition of NaHCO₃ (1.2 g, 14.8 mmol) and the

volatile components were removed under reduced pressure. The residue was diluted with ethyl acetate (25 mL) and water (25 mL); the organic layer was extracted, and the aqueous layer was washed with additional ethyl acetate (3 x 25 mL). The organic layers were dried over MgSO₄ and filtered, and the volatile components were removed from the filtrate under reduced pressure to give 1.05 g (99%) of **46** as a white solid: R_f 0.34 (hexanes/ethyl acetate 3:2); mp 225-227 °C; IR (thin film, cm⁻¹) 3416, 3329, 1701, 1594, 1421, 1353, 1270, 1233, 1118, 1033, 990, 907, 857, 760, 705; ¹H NMR (300 MHz, MeOD) δ 7.03 (s, 2H), 4.85 (broad s, 2H), 3.85 (s, 3H); ¹³C NMR (600 MHz, MeOD) δ 168.1, 156.7, 131.0, 108.6, 105.1, 52.7; HRMS (EI) *m/z* calcd for C₈H₇O₄Br 245.9528, found 245.9519.



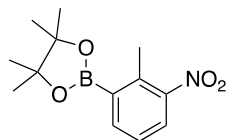
Methyl 4-bromo-3-(2-*t*-butoxy-2-oxoethoxy)-5-hydroxybenzoate (47). In a round-bottom flask, 1.0 g (4.2 mmol) of benzoate **46**, 0.62 mL (4.2 mmol) of *t*-butyl bromoacetate, 1.2 g (8.8 mmol) of K₂CO₃, and 0.05 g (0.2 mmol) of 18-crown-6 were dissolved in acetone (21.0 mL), and the reaction mixture was refluxed for 24 h. The volatile components were removed under reduced pressure, and the residue was diluted with ethyl acetate (50 mL) and water (50 mL); the organic layer was extracted, and the aqueous layer was washed with additional ethyl acetate (2 x 50 mL). The organic layers were dried over MgSO₄ and filtered, and the volatile components were removed from the filtrate under reduced pressure to give a crude yellow oil. The oil was purified by flash chromatography (SiO₂, hexanes/ethyl acetate, elution gradient 5:1/3:2/0:1) to give 0.49 g (32.4%) of **47** as a white solid: R_f 0.44 (hexanes/ethyl acetate 3:2); mp 117-118 °C; IR (thin film, cm⁻¹) 3393, 2923, 2852, 1724, 1590, 1497, 1438, 1354, 1247, 1158, 1117, 1011, 904, 870, 843, 767; ¹H NMR (400 MHz, CDCl₃) δ 7.24 (s, 1H), 6.92 (s, 1H), 6.41 (s, 1H), 4.57 (s, 2H), 3.81 (s, 3H), 1.18

(s, 9H); ^{13}C NMR (500 MHz, CDCl_3) δ 166.9, 166.0, 154.9, 153.7, 130.6, 110.4, 105.8, 105.2, 82.9, 66.4, 52.5, 28.0; HRMS (EI) m/z calculated for $\text{C}_{14}\text{H}_{17}\text{BrO}_6$ 360.0209, found 360.0205.

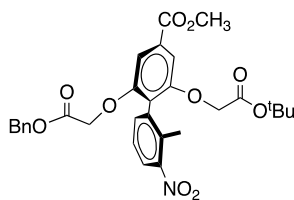


Methyl 3-(2-(benzyloxy)-2-oxoethoxy)-4-bromo-5-(2-*t*-butoxy-2-oxoethoxy) benzoate (48).

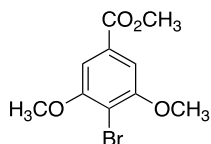
In a round bottom flask, 0.49 g (1.36 mmol) of benzoate **47**, 0.26 mL (1.63 mmol) of benzyl bromoacetate, 0.22 g (1.63 mmol) of K_2CO_3 , and 0.08 g (0.33 mmol) of 18-crown-6 were dissolved in acetone (35.4 mL), and the reaction mixture was refluxed for 24 h. The volatile components were removed under reduced pressure, and the residue was diluted with DCM (25 mL) and water (25 mL); the organic layer was extracted, and the aqueous layer was washed with additional DCM (3 x 25 mL). The combined organic layers were dried over MgSO_4 and filtered, and the volatile components were removed from the filtrate under reduced pressure to give a crude yellow oil. The oil was purified by flash chromatography (SiO_2 , hexanes/ethyl acetate, elution gradient 7:1/6:1/3:1) to yield 0.55 g (80.2%) of **48** as a white solid: R_f 0.48 (hexanes/ethyl acetate 3:2); mp 68-70 $^\circ\text{C}$; IR (thin film, cm^{-1}) 2978, 1753, 1724, 1587, 1423, 1369, 1337, 1241, 1194, 1133, 1029, 1000, 844, 763; ^1H NMR (400 MHz, CDCl_3) δ 7.24 (s, 5H), 7.04 (d, $J = 4$ Hz, 2H), 5.14 (s, 2H), 4.70 (s, 2H), 4.56 (s, 2H), 3.77 (s, 3H), 1.40 (s, 9H); ^{13}C NMR (500 MHz, CDCl_3) δ 167.8, 166.9, 165.9, 155.8, 155.7, 149.9, 149.1, 143.4, 141.7, 140.0, 135.0, 130.5, 130.0, 128.7, 128.6, 128.6, 128.5, 128.5, 108.2, 107.4, 107.2, 82.9, 67.3, 67.2, 66.6, 66.3, 60.7, 52.5, 28.0; HRMS (ESI-TOF) m/z : $[\text{M}+\text{Na}]^+$ calcd for $\text{C}_{23}\text{H}_{25}\text{O}_8\text{NaBr}$ 531.0630, found 531.0663.



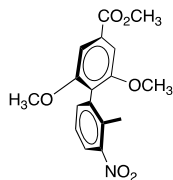
4, 4, 5, 5-tetramethyl-2-(2-methyl-3-nitrophenyl)-1,3,2-dioxaborolane (50). To a third flame-dried 200 ml round-bottom flask, 3.00 g (13.9 mmol) of **49**, 5.29 g (20.8 mmol) of (Bpin)₂, 4.09 g (41.7 mmol) of KOAc, and 0.45 g of [1,1'-bis(diphenylphosphino)ferrocene]dichloropalladium(II), complex with DCM (Pd(dppf)Cl₂•DCM; 0.56 mmol) were added. The reaction flask was then placed on vacuum line for 5 minutes and backfilled with nitrogen and repeated. DMSO (83.2 mL) was then added and the solution degassed using the freeze-pump-thaw method three times under a nitrogen atmosphere. The flask was sealed; the reaction mixture was stirred at 90 °C for 20 hours and then cooled to room temperature. The reaction mixture was then diluted with DCM (100 mL) and H₂O (100 mL). The organic layer was extracted and washed with H₂O (3 x 100 mL). The aqueous layer was washed with additional DCM (2 x 100 mL). Organic extracts were combined, and the volatile components were removed from the filtrate under reduced pressure to give a brown crude oil. The oil was purified twice by flash column chromatography (SiO₂, hexanes/ethyl acetate, elution gradient (2 columns) 10:1/6:1; then 30:1) to give 2.7 g (76%) of **50** as a pale yellow solid: R_f 0.89 (hexanes/ethyl acetate, 4:1); mp 52-53 °C; IR (thin film, cm⁻¹) 3055, 2982, 2933, 1603, 1569, 1527, 1474, 1439, 1344, 1267, 1214, 1144, 1109, 1026, 1078, 963, 786, 739, 669, 579. 463; ¹H NMR (300 MHz, CDCl₃) δ 7.94 (d, *J* = 7 Hz, 1H), 7.77 (d, *J* = 8 Hz, 1H), 7.27 (t, *J* = 8 Hz, 1H), 2.67 (s, 3H), 1.36 (s, 12H); ¹³C NMR (300 MHz, CDCl₃) δ 151.3, 139.9, 138.2, 126.3, 126.0, 84.4, 25.0, 18.0; HRMS (ESI-TOF) *m/z*: [M+H]⁺ calcd for C₁₃H₁₉BNO₄ 264.1407, found 264.1405.



Methyl 2,6-dimethoxy-2'-methyl-3'-nitro-[1,1'-biphenyl]-4-carboxylate (51). In a round-bottom flask, 0.17 g (0.34 mmol) of benzoate **48**, 0.14 g (0.55 mmol) of boronic ester **50**, 0.013 g (0.014 mmol) of Pd₂(dba)₃, 0.022 g (0.055 mmol) of 2-dicyclohexylphosphino-2',6'-dimethoxybiphenyl (SPhos), and 0.24 g (1.03 mmol) of KPO₄•H₂O (ground) were added and dried under reduced pressure for 5 minutes and backfilled with nitrogen two times. Toluene (3 ml) was added, and the solution was degassed using the freeze-pump-thaw method three times under a nitrogen atmosphere. The flask was sealed; the reaction mixture was stirred at 90 °C for 18 h, and cooled to room temperature. The mixture was diluted with DCM (30 mL) and H₂O (30 mL); the organic layer was extracted, and the aqueous layer was washed with additional DCM (3 x 30 mL). The combined organic layers were dried over MgSO₄ and filtered, and volatile components were removed from the filtrate under reduced pressure to give a brown crude oil. The oil was purified by flash chromatography (SiO₂, hexanes/ethyl acetate, 5:1) to afford 0.13 g (67.6%) of **51** as a white foam: R_f 0.36 (hexanes/ethyl acetate, 4:1); IR (thin film, cm⁻¹) 3442, 2979, 1751, 1725, 1581, 1528, 1437, 1422, 1354, 1330, 1236, 1194, 1136; 1082, 1029, 999, 867, 844, 810, 771, 741, 698; ¹H NMR (400 MHz, CDCl₃) δ 7.83 (d, *J* = 8 Hz, 1H), 7.42 (d, *J* = 7 Hz, 1H), 7.33 (broad s, 4H), 7.27 (broad s, 2H), 7.19 (s, 2H), 5.16 (s, 2H), 4.67 (s, 2H), 4.49 (s, 2H), 3.91 (s, 3H), 2.27 (s, 3H), 1.44 (s, 9H); ¹³C NMR (400 MHz, CDCl₃) δ 168.2, 167.4, 166.2, 156.2, 155.9, 150.8, 136.2, 135.3, 135.1, 132.8, 131.5, 128.8, 128.6, 126.0, 123.9, 122.5, 106.5, 106.0, 82.9, 67.3, 66.0, 65.4, 52.6, 28.2, 16.5; HRMS (ESI-TOF) *m/z*: [M+Na]⁺ calcd for C₃₀H₃₁NO₁₀Na 588.1840, found 588.1854.

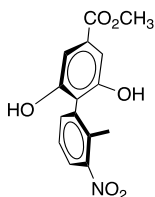


Methyl 4-bromo-3,5-dimethoxybenzoate (53). To a stirred solution of 2.50 g (10.7 mmol) of carboxylic acid **45** and 6.2 g (45.1 mmol) of K_2CO_3 in acetone (67.0 mL), 3.46 mL (36.5 mmol) of dimethyl sulfate was added. The mixture was stirred at reflux for 4.5 h and cooled to room temperature. Volatile components were removed under reduced pressure. The residue was then diluted with ethyl acetate (75 mL) and H_2O (75 mL); the organic layer was extracted, and the aqueous layer was washed with additional ethyl acetate (2 x 75 mL). The combined organic layers were washed with brine (200 mL), dried over $MgSO_4$ and filtered, and the volatile components were removed under reduced pressure to yield a white solid. The solid was purified by recrystallization to give 2.9 g (100%) of benzoate **53** as white crystals: R_f 0.45 (hexanes/ethyl acetate, 4:1); mp 121-122°C ; 1H NMR (300 MHz, $CDCl_3$) δ 7.23 (s, 2H), 3.95 (s, 6H), 3.93 (s, 3H); ^{13}C NMR (300 MHz, $CDCl_3$) 166.7, 157.3, 130.4, 106.9, 105.8, 56.9, 52.7; HRMS (ESI-TOF) m/z calc for $C_{10}H_{11}BrO_4$ 273.9827, found 273.9829.



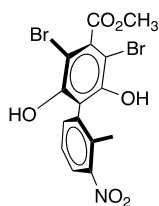
Methyl 2,6-dimethoxy-2'-methyl-3'-nitro-[1,1'-biphenyl]-4-carboxylate (54). In a round-bottom flask, 1.45 g (5.29 mmol) of benzoate **53**, 2.08 g (7.94 mmol) of boronic ester **50**, 0.19 g (0.21 mmol) of $Pd_2(dba)_3$, 0.35 g (0.85 mmol) of SPhos, and 3.66 g (15.87 mmol) of $K_3PO_4 \cdot H_2O$ (ground) were added and dried under reduced pressure for 5 minutes and backfilled with nitrogen two times. Toluene (30 ml) was added, and the solution was degassed using the freeze-pump-thaw method three times under a nitrogen atmosphere. The flask was sealed; the reaction mixture was

stirred at 90 °C for 18 h and cooled to room temperature. The mixture was diluted with DCM (150 mL) and H₂O (150 mL); the organic layer was extracted, and the aqueous layer was washed with additional DCM (3 x 150 mL). The combined organic layers were washed with brine (200 mL), dried over MgSO₄ and filtered. Volatile components were removed from the filtrate under reduced pressure to give a reddish brown crude oil. The oil was purified by flash chromatography (SiO₂, hexanes/ethyl acetate, elution gradient, 8:1/6:1) to give 1.19 g (74%) of **54** as a pale yellow solid: *R_f* 0.28 (hexanes/ethyl acetate, 4:1); mp 119-120 °C; IR (thin film, cm⁻¹) 3436, 2919, 2881, 1721, 1580, 1527, 1456, 1434, 1409, 1351, 1326, 1242, 1126, 997, 770; ¹H NMR (400 MHz, CDCl₃) δ 7.84 (dd, *J* = 6, 3 Hz, 1H), 7.36-7.34 (m; 4H), 3.97 (s, 3H), 3.78 (s, 6H), 2.20 (s, 3H); ¹³C NMR (400 MHz, CDCl₃) δ 167.0, 157.7, 150.9, 137.0, 135.4, 132.6, 131.8, 126.1, 123.8, 121.8, 105.4, 56.3, 52.7, 16.4; HRMS (ESI-TOF) *m/z*: [M+H]⁺ calcd for C₁₇H₁₈NO₆ 332.1134, found 332.1124.



Methyl 2,6-dihydroxy-2'-methyl-3'-nitro-[1,1'-biphenyl]-4-carboxylate (55). In a third-flame dried round-bottom flask, 5.35 g (21.36 mmol) of a 1.0 M solution of BBr₃ in DCM was added dropwise over 30 minutes to a stirred solution of 1.18 g (3.56 mmol) of **54** in DCM (8 mL) at 0 °C. The reaction mixture was stirred at 0 °C for 3 hours and gradually warmed to room temperature and stirred for an additional 21 h. The volatile components were removed under reduced pressure. The residue was charged with nitrogen and slowly diluted with MeOH (7 mL). 0.33 mL (6.14 mmol) of H₂SO₄ was added dropwise at 0 °C. The reaction mixture was then heated to reflux for 20 h. After cooling to room temperature, the reaction was quenched by addition of NaHCO₃ (1.03 g, 12.3 mmol) and the volatile components were removed under reduced pressure. The residue was

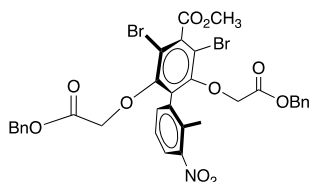
diluted with ethyl acetate (75 mL) and H₂O (75 mL); the organic layer was extracted, and the aqueous layer was washed with additional ethyl acetate (2 x 75 mL). The combined organic layers were washed with brine (200 mL), dried over MgSO₄ and filtered. Volatile components were removed from the filtrate under reduced pressure to yield a brown oil. The oil was purified by flash column chromatography (SiO₂, hexanes/ethyl acetate, elution gradient, 2:1) to give 0.84 g (78%) of **55** as a white solid: R_f 0.22 (hexanes/ethyl acetate, 2:1); mp 160-161 °C; IR (thin film, cm⁻¹) 3310, 2524, 2219, 2043, 1653, 1451, 1113, 1034; ¹H NMR (300 MHz, CDCl₃) δ 7.92 (d, J = 6 Hz, 1H), 7.49-7.47 (m, 2H), 7.31 (s, 2H), 5.71 (broad s, 2H), 3.92 (s, 3H), 2.31 (s, 3H); ¹³C NMR (400 MHz, CDCl₃) δ 154.4, 151.7, 135.53, 134.6, 133.7, 131.9, 127.5, 125.2, 118.6, 109.5, 53.0, 16.4; HRMS (ESI-TOF) m/z: [M+H]⁺ calcd for C₁₅H₁₄NO₆ 304.0821, found 304.0837.



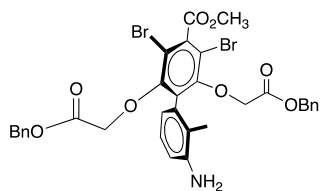
Methyl 3,5-dibromo-2,6-dihydroxy-2'-methyl-3'-nitro-[1,1'-biphenyl]-4-carboxylate (56).

In an oven-dried round-bottom flask, 0.26 ml (4.12 mmol) of Br₂ in CCl₄ (2.9 mL) was added dropwise over 30 min to a stirred solution of 0.52 g (1.72 mmol) of **55** in CCl₄ (7 mL) in the dark. The reaction mixture was stirred for 1 h. Saturated NaHSO₃ was then added until red color dissipated. Mixture was diluted with ether (30 mL) and organic layer was extracted. The aqueous layer was washed with additional ether (2 x 30 mL). The combined organic layers were washed with brine (75 mL), dried over MgSO₄ and filtered, and the volatile components were removed from the filtrate under reduced pressure to yield a brown oil. The oil was purified by flash column chromatography to give 0.60 g (76%) of **56** as an off-white foam: R_f 0.36 (hexanes/ethyl acetate, 4:1); mp 158-159 °C; IR (thin film, cm⁻¹) 3431, 2101, 1642, 1264, 790; ¹H NMR (400 MHz,

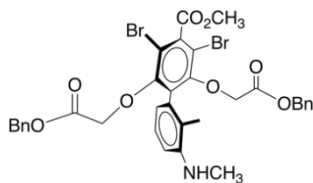
CDCl₃) δ 7.90 (dd, *J* = 7, 2 Hz, 1H), 7.44-7.39 (m, 2H), 5.91 (broad s, 2H), 4.02 (s, 3H), 2.28 (s, 3H); ¹³C NMR (600 MHz, CDCl₃) δ 166.0, 151.1, 150.5, 137.0, 135.0, 134.6, 132.9, 126.8, 124.9, 115.7, 99.3, 53.7, 16.4; HRMS (ESI-TOF) *m/z*: calcd for C₁₅H₁₁NO₆Br₂ 461.8900, found 461.8882.



Dibenzyl 2,2'-((3,5-dibromo-4-(methoxycarbonyl)-2'-methyl-3'-nitro-[1,1'-biphenyl]-2,6-diyl)bis(oxy))diacetate (57). In an oven-dried round bottom flask, 0.46 g (1.0 mmol) of **56**, 0.38 mL (2.4 mmol) of benzyl bromoacetate, 0.42 g (3.0 mmol) of K₂CO₃, and 0.10 g (0.40 mmol) of 18-crown-6 were dissolved in acetone (11.1 mL), and the reaction mixture was refluxed for 24 h. The volatile components were removed from the filtrate under reduced pressure, and the residue was diluted with DCM (30 mL) and water (30 mL); the organic layer was extracted, and the aqueous layer was washed with additional DCM (3 x 30 mL). The combined organic layers were washed with brine (90 mL), dried over MgSO₄ and filtered, and the volatile components were removed from the filtrate under reduced pressure to give a crude yellow oil. The oil was purified by flash chromatography (SiO₂, hexanes/ethyl acetate, elution gradient 6:1) to yield 0.60 g (80%) of **57** as a light yellow foam: *R_f* 0.48 (hexanes/ethyl acetate 2:1); ¹H NMR (400 MHz, CD₂Cl₂) δ 7.82 (d, *J* = 8 Hz, 1H), 7.43 (d, *J* = 8 Hz, 1H), 7.36-7.34 (m, 6H), 7.30 – 7.24 (m, 5H), 5.02 (q, *J* = 4 Hz, 4H), 4.22, 4.10 (ABq, *J*_{AB} = 15 Hz, 4H), 2.30 (s, 3H); ¹³C NMR (400 MHz, CD₂Cl₂) δ 167.2, 166.1, 154.0, 151.3, 140.4, 135.8, 135.5, 134.5, 133.1, 131.0, 129.1, 129.0, 128.9, 127.1, 125.5, 111.7, 70.0, 67.4, 17.2; HRMS (ESI-TOF) *m/z*: [M+H]⁺ calcd for C₃₃H₂₈NO₁₀Br₂ 758.01052, found 758.0080.

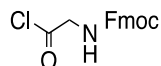


Dibenzyl 2,2'-((3'-amino-3,5-dibromo-4-(methoxycarbonyl)-2'-methyl-[1, 1'-biphenyl]-2,6-diyl)bis(oxy))diacetate (58). 0.5 g (0.67 mmol) of **57** were dissolved in ethyl acetate (11 ml) and concentrated HCl (0.33 ml). The solution was cooled to 0 °C and Zn powder (.21 g, 3.3 mmol) was added in portions over 20 min with stirring. The mixture was gradually warmed to room temperature and stirred for 15 h. The reaction mixture was passed through a Celite plug and washed with ethyl acetate (5 ml). The filtrate was washed with saturated NaHCO₃ solution (1 x 5 ml), water (1 x 5 ml), and brine (1 x 10 ml). The organic layer was dried over anhydrous MgSO₄, filtered, and volatile components were removed from the filtrate under reduced pressure to give a crude yellow oil. The oil was purified by flash chromatography (SiO₂, hexanes/ethyl acetate, elution gradient 3:1/2:1) to yield 0.41 g (82%) of **58** as a light yellow foam: *R_f* 0.21 (hexanes/ethyl acetate 2:1); mp 58-59 °C; ¹H NMR (400 MHz, CDCl₃) δ 7.34-7.30 (m, 5H), 7.28-7.25 (m, 5H), 6.99 (t, *J* = 8 Hz, 1H), 6.64 (d, *J* = 8 Hz, 1H), 6.58 (d, *J* = 7 Hz, 1H), 5.05 (s, 4H), 4.17, 4.00 (ABq, *J*_{AB} = 15 Hz, 4H), 4.01 (s, 3H), 3.61 (broad s, 2H), 1.90 (s, 3H); ¹³C NMR (400 MHz, CDCl₃) δ 167.6, 166.4, 153.6, 145.6, 138.7, 135.4, 132.1, 131.6, 128.9, 128.8, 128.7, 126.9, 121.9, 120.9, 115.9, 111.0, 69.4, 67.0, 53.6, 30.0, 14.8; HRMS (ESI-TOF) *m/z*: [M+H]⁺ calcd for C₃₃H₃₀NO₈Br₂ 728.02395, found 728.02593.

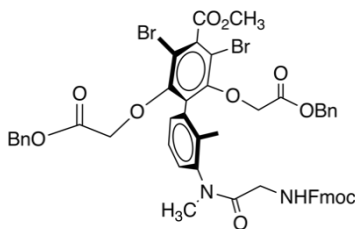


Dibenzyl 2,2'-((3,5-dibromo-4-(methoxycarbonyl)-2'-methyl-3'-(methylamino)-[1,1'-biphenyl]-2,6-diyl)bis(oxy))diacetate (60). To biaryl-methylamide (0.1 g, 0.14 mmol) of **58** 0.025 g (0.17 mmol) of **59** in THF (0.1 mL) were sonicated for 5 minutes to give a homogenous solution. The mixture was then diluted with EtOH (0.16 mL) and stirred at room temperature for 12 h. Volatile components were removed under reduced pressure, and reaction vial was cooled to 0 °C for 10 minutes. The residue was rinsed with chilled, dry DCM followed by hexanes to produce an off-white solid. The precipitate was isolated and taken up into DCM, dried over K₂CO₃, filtered, and volatile components were removed under reduced pressure to give an off-white solid. The dry intermediate was dissolved in THF (0.3 mL), and 0.01 g (0.18 mmol) of NaBH₄ were added and stirred for 14 h. The reaction mixture was concentrated under reduced pressure and the residue was diluted with ice, cold H₂O, and DCM; the organic layer was extracted and aqueous layer washed with additional DCM (2 x 4 mL). The combined organic layers were washed with additional H₂O (5 mL) and then brine (5 mL); the organic layer was dried over MgSO₄, filtered, and volatile components were removed from the filtrate under reduced pressure to give a yellow foam. The foam was purified by flash chromatography (SiO₂, hexanes/ethyl acetate, elution gradient 7:1/6:1) to yield 0.040 g (41%) of **60** as a white foam: R_f 0.38 (hexanes/ethyl acetate 2:1; IR (thin film, cm⁻¹) 3432, 3059, 2978, 2303, 2053, 1648, 1420, 1375, 1241, 1122, 892, 743; ¹H NMR (400 MHz, CDCl₃) δ 7.33 (broad s, 5H), 7.26 (broad s, 5H), 7.12 (t, *J* = 8 Hz, 1H), 6.59 (d, *J* = 8 Hz, 1H), 6.53 (d, *J* = 8 Hz, 1H), 5.04 (s, 4H), 4.12, 4.00 (ABq, *J* = 15 Hz, 4H) 4.01 (s, 3H), 3.66 (broad s, 2H), 2.87 (s, 3H), 1.86 (s, 3H); ¹³C NMR (500 MHz,

CDCl₃) δ 167.7, 166.4, 153.7, 147.9, 138.7, 135.5, 132.3, 131.1, 128.9, 128.8, 128.6, 127.2, 121.4, 119.2, 111.0, 109.9, 69.4, 67.0, 53.6, 31.2, 30.1, 28.7, 14.6, 14.5; HRMS (ESI-TOF) *m/z*: [M+H]⁺ calcd for C₃₄H₃₂Br₂NO₈ 742.0495, found 742.0496.

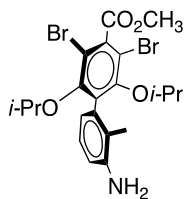


(9H-Fluoren-9-yl)methyl (2-chloro-2-oxoethyl)carbamate (62). To a solution of 0.030 g (0.1 mmol) of commercially available Fmoc-gly (61) in DCM (0.5 mL) was added 0.07 ml (1.0 mmol) of thionyl chloride (SOCl₂) and the reaction mixture was refluxed for 30-45 min. The solution was cooled to room temperature and the volatile components were removed under reduced pressure. The residue was dissolved in minimal DCM followed by hexanes to produce an off-white precipitate. The solid was filtered and dried in vacuo to afford 0.025 g (81%) of 62 as an off-white solid. Only an IR spectra was obtained to confirm this highly reactive intermediate: (thin film, cm⁻¹) 3315, 3066, 2967, 2947, 1811, 1702, 1540, 1477, 1448, 1395, 1349, 1271, 1182, 1104, 1087, 1051, 991, 955, 919, 780, 758, 742.



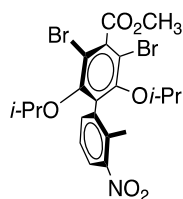
Dibenzyl 2, 2'-((3'-((2-(((9H-fluoren-9-yl)methoxy)carbonyl)amino)-N-methylacetamido)-3,5-dibromo-4-(methoxycarbonyl)-2;-methyl-[1,1'-biphenyl]-2,6-diyl)bis(oxy))diacetate (63). To 0.05 g (0.07 mmol) of 60 in 0.62 mL of CHCl₃ was added 0.03 g (0.09 mmol) of Fmoc-gly acid chloride 61 (generated according to above procedure and used immediately thereafter) in 0.37 mL of CHCl₃ followed by 0.62 mL of saturated NaHCO₃ solution, and the reaction mixture was stirred at room temperature for 20 min. The solution was diluted with DCM (10 mL) and

saturated NaHCO₃ solution (10 mL), the organic layer was extracted, and the aqueous layer was washed with DCM (3 × 10 mL). The organics were dried over MgSO₄, filtered and the volatile components were removed from the filtrate under reduced pressure to give a light brown crude oil. The oil was purified by flash chromatography (SiO₂, hexanes/ethyl acetate, elution gradient 5:1/3:1/2:1) to give 0.046 g (67%) of **63** as a white foam: R_f 0.31 (hexanes/ethyl acetate, 1:1); IR (thin film, cm⁻¹) 3392, 2926, 2855, 1751, 1722, 1660, 1581, 1421, 1369, 1329, 1299, 1234, 1193, 1134, 1028, 998, 864, 845, 806, 735; ¹H NMR (400 MHz, CDCl₃) δ 7.66 (d, *J* = 7 Hz, 2H), 7.48 (d, *J* = 7 Hz, 2H), 7.32-7.25 (m, 5H), 7.22-7.18 (m, 5H), 7.14-7.06 (m, 7H), 5.49 (broad s, 1H), 4.94 (s, 4H), 4.23-4.14 (m, 4H), 4.10-4.01 (m, 4H), 3.94 (s, 3H), 3.88 (d, *J* = 15 Hz, 2H), 3.65, 3.32 (qd, *J* = 4, 17 Hz, 2H), 3.08 (s, 3H), 1.95 (s, 3H); ¹³C NMR (400 MHz, CDCl₃) δ 168.6, 166.8, 165.8, 156.1, 153.1, 144.0, 143.9, 141.3, 141.3, 139.3, 136.2, 135.1, 135.0, 133.6, 131.0, 128.7, 128.6, 128.5, 128.4, 128.3, 127.7, 127.4, 127.1, 125.2, 120.0, 111.3, 111.0, 69.2, 69.1, 67.0, 66.8, 53.4, 47.1, 43.2, 36.3, 15.3; HRMS (ESI-TOF) *m/z*: [M+H]⁺ calcd for C₅₁H₄₅N₂O₁₁Br₂ 1019.1384, found 1019.1366.



Methyl 3'-amino-3,5-dibromo-2,6-diisopropoxy-2'-methyl-[1,1'-biphenyl]-4-carboxylate (71). Diisopropyl biaryl **72** (0.10 g, 0.18 mmol) were dissolved in ethyl acetate (4 ml) and concentrated HCl (0.08 ml). The solution was cooled to 0 °C and Zn powder (.08 g, 3.3 mmol) was added in portions over 20 min with stirring. The mixture was gradually warmed to room temperature and stirred for 15 h. The reaction mixture was passed through a Celite plug and washed with ethyl acetate (5 ml). The filtrate was washed with saturated NaHCO₃ solution (1 x

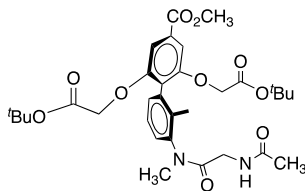
2.5 ml), water (1 x 5 ml), and brine (1 x 10 ml). The organic layer was dried over anhydrous MgSO₄ and filtered, and volatile components were removed from the filtrate under reduced pressure to give a crude yellow oil. The oil was purified by flash chromatography (SiO₂, hexanes/ethyl acetate, elution gradient 3:1) to yield 0.077 g (83%) of **71** as a light yellow solid: *R_f* 0.37 (hexanes/ethyl acetate 2:1); mp 141-3 °C; ¹H NMR (400 MHz, CD₂Cl₂) δ 6.99 (t, *J* = 4 Hz, 1H), 6.73 (d, *J* = 8 Hz, 1H), 6.59 (d, *J* = 8 Hz, 1H), 4.45 (broad s, 2H), 3.90 (s, 3H), 3.73 (sext, *J* = 6 Hz, 2H), 1.88 (s, 3H), 0.87 (d, *J* = 6 Hz, 12 H); ¹³C NMR (400 MHz, CD₂Cl₂) 167.6, 154.1, 145.9, 138.5, 134.4, 133.9, 126.6, 122.6, 122.1, 115.8, 110.9, 77.2, 49.6, 49.4, 49.2, 49.0, 48.8, 48.5, 48.3, 22.39, 14.73; HRMS (ESI-TOF) *m/z*: [M+H]⁺ calcd for C₂₁H₂₆NO₄Br₂ 514.0223, found 514.0204.



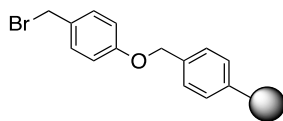
Methyl 3,5-dibromo-2,6-diisopropoxy-2'-methyl-3'-nitro-[1,1'-biphenyl]-4-carboxylate (72**).**

Dihydroxy biaryl **56** (0.30 g, 0.78 mmol) was dissolved in 4 mL of DMF, followed by addition of potassium carbonate (0.2 g, 1.7 mmol), and then the solution was heated to 60 °C. After approximately fifteen minutes, 2-iodopropane (1.6 mL, 1.7 mmol) was added dropwise to the mixture and the solution stirred at 60 °C for three hours under an argon atmosphere. After cooling to room temperature, the reaction mixture was partitioned between ethyl acetate and water. The aqueous layer was extracted with ethyl acetate (3 x 10 mL) and the combined organic layers were dried over MgSO₄ and filtered, and volatile components removed under reduced pressure to give a crude product. The crude was purified by flash chromatography (SiO₂, hexanes/ethyl acetate, 20:1) to afford 0.23 g (54%) of **72** as a pale yellow solid: *R_f* 0.34 (hexanes/ethyl acetate, 5:1); mp

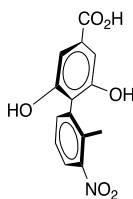
109 °C ; ¹H NMR (400 MHz, CDCl₃) δ 7.82 (d, *J* = 8 Hz, 1H), 7.43 (d, *J* = 8 Hz, 1H), 7.32 (t, *J* = 8 Hz, 1H), 3.95 (s, 3H), 3.79 (sext, *J* = 6 Hz, 2H), 2.25 (s, 3H), 0.86 (d, *J* = 9.2 Hz, 12H); ¹³C NMR (400 MHz, CDCl₃) δ 166.6, 153.5, 151.1, 139.6, 136.8, 136.3, 132.8, 131.6, 126.1, 124.3, 111.0, 53.5, 22.4, 22.4, 17.0; HRMS (ESI-TOF) *m/z* calcd for [M+H]⁺ C₂₁H₂₄Br₂NO₆ 543.9970, found 543.9923.



Di-*t*-butyl 2,2'-((3'-(2-acetamido-*N*-methylacetamido)-4-methoxycarbonyl)-2'-methyl-[1,1'-biphenyl]-2,6-dilyl)bis(oxy))diacetate (73). To 0.02 g (0.03 mmol) of carboxylate **74** in a vial was added a 0.11 mL of a 20% piperidine/DMF solution, and the reaction mixture was stirred at room temperature for 30 min. Then 0.35 mL (4.06 mmol) of acetic anhydride and 1.16 mL (15.4 mmol) of pyridine were added, and the solution was stirred at room temperature for 30 min. The volatile components were removed from the filtrate under reduced pressure to give a crude brown oil. The oil was purified by flash chromatography (SiO₂, hexanes/ethyl acetate/methanol elution gradient 1:5/1:20) to give 0.02 g (90%) of **73** as a white foam: *R_f* 0.22 (100% ethyl acetate); ¹H NMR (400 MHz, CDCl₃) δ 7.31-7.27 (m, 2H), 7.19-7.12 (m, 3H), 6.47 (broad s, 1H), four protons of conformers [4.64, 4.53 (ABq, *J*_{AB} = 16 Hz), 4.55, 4.50 (ABq *J*_{AB} = 15 Hz)], 3.91 (s, 3H), 3.70 (qd, *J* = 18, 4 Hz, 2H), 3.29 (s, 3H), 2.03, (s, 3H), 1.98 (s, 3H), 1.45 (s, 18H); ¹³C NMR (500 MHz, CDCl₃) δ 169.7, 168.9, 167.7, 166.3, 155.9, 155.7, 140.1, 135.8, 135.7, 131.3, 130.7, 127.0, 126.8, 123.1, 106.1, 105.98, 82.5, 82.2 65.9. 65.6, 52.3, 42.2, 36.3, 28.0, 23.1, 14.6; HRMS (ESI-TOF) *m/z*: [M+Na]⁺ calcd for C₃₂H₄₂N₂O₁₀Na 637.2737, found 637.2761.

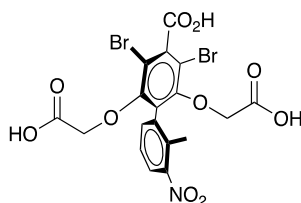


Bromo Wang resin (80b). A suspension of PPh_3Br (0.03 g, 0.08 mmol) in DCM (0.33 mL) was slowly added to a stirred suspension of Wang resin **80a** (0.09 g, 0.03 mmol) in DCM (0.67 mL) at room temperature. After stirring for 3 hours, the reaction mixture was filtered and the resin was washed with DCM (4 x 0.7 mL) and used immediately for SPPS.

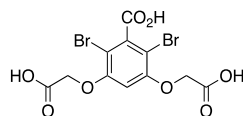


Methyl 2,6-dihydroxy-2'-methyl-3'-nitro-[1,1'-biphenyl]-4-carboxylate (100). In a third-flame dried round-bottom flask, 98.1 mL (98.1 mmol) of a 1.0 M solution of BBr_3 in DCM was added dropwise over 45 minutes to a stirred solution of 5.01 g (15.1 mmol) of **56** in DCM (50.3 mL) at 0 °C. The reaction mixture was stirred at 0 °C for 3 hours and gradually warmed to room temperature and stirred for an additional 13 h. After cooling to 0 °C, the reaction mixture was slowly poured over chilled H_2O (40 mL) and diluted with Et_2O (30 mL); the organic layer was extracted, and the aqueous layer was washed with additional ether (3 x 30 mL). The combined organic layers were washed with 0.5 N NaHCO_3 ; the basic layer was extracted and acidified to pH = 1. The acidified aqueous layer was diluted with Et_2O ; the organic layer was extracted, and the aqueous layer was washed with additional ether (2 x 30 mL). The combined organic layers were washed with brine, dried over MgSO_4 and filtered, and the volatile components were removed under reduced pressure to yield a brown oil. The oil was purified by flash column chromatography (SiO_2 , hexanes/ethyl acetate, elution gradient, 1:3) to give 3.73 g (86%) of **100** as a pale yellow solid: R_f 0.34 (hexanes/ethyl acetate, 1:6); mp 160-161 °C; IR (thin film, cm^{-1}) 3310, 2524, 2219,

2043, 1653, 1451, 1113, 1034; ^1H NMR (300 MHz, CD_3OD) δ 7.81 (d, $J = 7$ Hz, 1H), 7.44-7.7.37 (m, 2H), 7.14 (s, 2H), 4.93 (broad s, 2H), 2.25 (s, 3H); ^{13}C NMR (400 MHz, CDCl_3) δ 154.4, 151.7, 135.53, 134.6, 133.7, 131.9, 127.5, 125.2, 118.6, 109.5, 53.0, 16.4; HRMS (ESI-TOF) m/z : $[\text{M}-\text{H}]^-$ calcd for $\text{C}_{14}\text{H}_{10}\text{NO}_6$ 288.0502 found 288.0519.

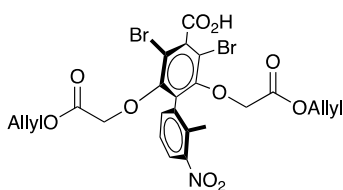


2,2'-((3,5-Dibromo-4-carboxy-2'-methyl-3'-nitro-[1,1'-biphenyl]-2,6-diyl)bis(oxy))diacetic acid (102). Biaryl (0.02 g, 0.03 mmol) as a suspension in 3 ml of THF:H₂O (2:1), was stirred at reflux with 0.3 ml of LiOH/H₂O (5 M) overnight. The reaction mixture was cooled in an ice bath and acidified with HCl until pH = 1. The mixture was diluted with EtOAc (10 mL) and H₂O (10 mL); the organic layer was extracted, and the aqueous layer was washed with additional EtOAc (3 x 10 mL). The combined organic layers were dried over MgSO₄ and filtered. Volatile components were removed under reduced pressure, and the crude solid was purified by flash chromatography (SiO₂, ethyl acetate, methanol 80:1) to afford 0.87 g (90.8%) of **102** as a white crystal: R_f 0.16 (ethyl acetate/methanol, 20:1); mp 69 °C; ^1H NMR (400 MHz, CD_3OD) δ 7.94 (d, $J = 8$ Hz, 1H), 7.59 (d, $J = 7$ Hz, 1H), 7.47 (t, $J = 8$ Hz, 1H), 4.86 (broad s, 2H) 4.26, 4.12 (ABq, $J_{AB} = 16$ Hz, 4H), 2.31 (s, 3H); ^{13}C NMR (MHz, CDCl_3) δ 170.7, 154.8, 152.4, 136.4 135.8, 133.6, 132.6, 131.6, 127.7, 125.9, 111.4, 70.2, 61.6, 30.92, 17.1, 14.6; HRMS (ESI-TOF) m/z calcd for $[\text{M}-\text{H}]^-$ $\text{C}_{18}\text{H}_{12}\text{Br}_2\text{NO}_8$ 561.8910, found 561.8918.



2,2'-((4,6-Dibromo-5-carboxy-1,3-phenylene)bis(oxy))diacetic acid (102). Pd(PPh₃)₄ (0.01 g,

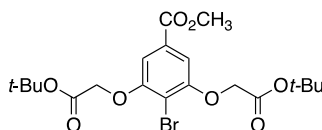
0.05 mmol) in 1.2 mL DCM was transferred to a stirred solution of **111** (0.01 g, 0.02 mmol) and PhSiH₃ (0.10 mL, 0.03 mmol) in DCM (0.66 mL) under argon atmosphere. The reaction mixture was stirred at room temperature for 30 min and filtered. The reaction mixture was filtered through a Celite plug and rinsed with DCM. Volatile components were removed by a stream of nitrogen and product dried *in vacuo* to give 0.39 g (89%) of product as a white solid with identical spectroscopic properties to those described above. MS (MALDI-TOF) *m/z* calc for [M+Na]⁺ C₁₄H₁₁Br₃O₈Na 426.8459, found 426.8479.



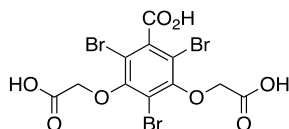
2,6-Bis(2-(allyloxy)-2-oxoethoxy)-3,5-dibromo-2'-methyl-3'-nitro-[1,1'-biphenyl]-4-carboxylic acid (103). Biaryl **102** (0.15 g, 0.33 mmol) and TEA (0.14 mL, 0.65 mmol) in DCM (3 mL) were added to a stirred solution of allyl-2-bromoacetate **110** (0.08 mL, 0.98 mmol) in 0.5 mL DCM and stirred for 13 h at room temperature. The mixture was diluted with Et₂O (10 mL) and H₂O (10 mL); the organic layer was extracted, and the aqueous layer was washed with additional Et₂O (3 x 10 mL). The combined organic layers were dried over MgSO₄ and filtered. The volatile components were removed under reduced pressure, and the crude oil was purified by flash chromatography (SiO₂, hexanes/ethyl acetate elution gradient 3:1) to afford 0.87 g () of **103** as a white crystal: *R_f* 0.29 (hexanes/ethyl acetate, 1:1); ¹H NMR (300 MHz, CDCl₃) δ 7.16 (s, 2H), 3.89 (s, 3H), 1.05 (s, 18H), 0.26 (s, 12H); ¹³C NMR (400 MHz, CDCl₃) δ 166.7, 157.3, 130.4, 106.9, 105.8, 56.9, 53.2, 29.3, 17.1, 4.3; HRMS (ESI-TOF) *m/z* calc for [M-H]⁻ C₂₄H₂₀Br₂NO₁₀ 639.9448, found 639.9446.

Diallyl 2,2'-((4-((2-(allyloxy)-2-oxoethoxy)carbonyl)-3,5-dibromo-2'-methyl-3'-nitro-[1,1'-

biphenyl]-2,6-diyl)bis(oxy))diacetate. ^1H NMR (400 MHz, CDCl_3) δ 7.93,7.91 (dd, $J = 8, 2$ Hz, 2H), 7.91-7.41 (m, 2H), 6.01-5.90 (m, 1H), 5.82-5.75 (m, 2H), 5.41,5.37 (dd, $J = 15,2$ Hz, 1H), 5.32,5.29 (dd, $J = 9,1$ Hz, 1H), 5.24-5.23 (m, 2H), 5.21-5.20 (m, 2H), 4.96 (s, 2H), 4.76-4.74 (m, 2H), 4.51-4.48 (m, 4H), 4.18, 4.06 (qAB, $J = 15$ Hz, 4H), 2.35 (s, 3H); ^{13}C NMR (500 MHz, CDCl_3) δ 166.6, 166.5, 164.5, 153.6, 150.9, 138.8, 135.1, 134.1, 132.8, 131.4, 131.3, 131.2, 126.7, 125.2, 119.6, 119.5, 111.9, 69.6, 66.4, 66.1, 62.3, 17.1; HRMS (ESI-TOF) m/z calc for $[\text{M}+\text{H}]^+$ $\text{C}_{29}\text{H}_{28}\text{Br}_2\text{NO}_{12}$ 739.9972, found 739.9966.



Methyl 4-bromo-3,5-bis(2-*t*-butoxy-2-oxoethoxy)benzoate (104). In a round-bottom flask, 0.25 g (1.0 mmol) of benzoate 122, 0.45 mL (3.0 mmol) of *t*-butyl bromoacetate, 0.41 g (3.0 mmol) of K_2CO_3 , and 0.26 g (1.0 mmol) of 18-crown-6 were dissolved in acetone (25.0 mL), and the reaction *mixture* was refluxed for 16 h. The volatile components were removed under reduced pressure, and the residue was diluted with DCM (50 mL) and water (50 mL); the organic layer was extracted, and the aqueous layer was washed with additional DCM (3 x 50 mL). The organic layers were dried over MgSO_4 and filtered, and the volatile components were removed under reduced pressure to give a crude yellow oil. The oil was purified by flash chromatography (SiO_2 , hexanes/ethyl acetate elution gradient 3:1) to give 0.39 g (89%) of **104** as a white solid: R_f 0.47 (hexanes/ethyl acetate, 7:3); mp 103-105 $^\circ\text{C}$; IR (thin film, cm^{-1}) 3090, 2980, 1753, 1725, 1588, 1423, 1394, 1369, 1339, 1304, 1239, 1161, 1132, 1030, 1000, 951, 900, 844, 763; ^1H NMR (400 MHz, CDCl_3) δ 7.16 (s, 2H), 4.67 (s, 4H), 3.92 (s, 3H), 1.51 (s, 18H); ^{13}C NMR (400 MHz, CDCl_3) δ 167.0, 166.0, 155.8, 129.9, 108.0, 107.1, 82.8, 66.6, 52.5, 28.0; HRMS (Q-TOF) m/z calcd for $[\text{M}+\text{Na}]^+$ $\text{C}_{20}\text{H}_{27}\text{O}_8\text{BrNa}$ 497.0787, found 497.0819.

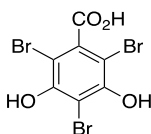


2,2'-((2,4,6-Tribromo-5-carboxy-1,3-phenylene)bis(oxy))diacetic acid (105).

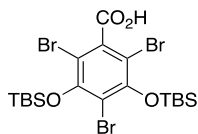
Method A: Benzoic acid **104** (0.11 g, 0.21 mmol), as a suspension in 5 ml of THF:H₂O (2:1), was stirred at reflux with 0.5 ml of LiOH/H₂O (5 M) overnight. The reaction mixture was cooled in an ice bath and acidified with HCl until pH = 1. The precipitate was filtered and washed with chilled water. The solid was taken up into ethyl acetate and diluted with H₂O; the organic layer was extracted, and the aqueous layer was washed with additional EtOAc (10 mL). The combined organic layers were dried with brine (15 mL) and filtered over MgSO₄. Volatile components were removed under reduced pressure, and the crude solid was subjected to bromination conditions without further purification. To a stirred solution of 0.07 g (0.30 mmol) of **105** in CCl₄ (2.2 mL) in the dark, 0.04 ml (0.6 mmol) Br₂ in CCl₄ (0.6 mL) was added dropwise over 15 min. The reaction mixture was stirred for 5 h. The reaction mixture was then cooled in an ice bath and 30% NaHSO₃ was added until red color dissipated. The precipitate was isolated and washed with ice water. The crude solid was purified by flash column chromatography (SiO₂, ethyl acetate/hexanes, 50:1) to afford 0.06 g (54%) of **105** as a white solid: R_f 0.21 (ethyl acetate/methanol, 20:1); mp 70 °C ; ¹H NMR (300 MHz, CDCl₃) δ 6.83 (broad s, 3H), 3.89 (qAB, J = , 4H); ¹³C NMR (400 MHz, CDCl₃); HRMS (ESI-TOF) *m/z* calcd for [M+Na]⁺ C₁₁H₆O₈Br₃ 502.7607, found 502.7616.

Method B: Bromo Wang resin (g, mmol) was suspended in (ml) and left to swell for 15 minutes. A solution of benzoic acid **111** (0.09 g, 0.12 mmol), PyAOP (0.06 g, 0.12 mmol), HOBt (0.02 g, 0.12 mmol) and DIEA (0.02 g, 0.18 mmol) in NMP was vortexed and left to activate for 2 minutes. DMF was filtered and the activated acid solution added to swelled resin. The stirred solution was heated at 70 °C for 4 min using microwave irradiation. The solution was then stirred at room

temperature for 5 min, filtered and resin washed with additional DMF (3 x 3 mL). The following protocol was repeated twice for allyl deprotection. The resin was suspended in DMF (0.73 ml), treated with DIEA (0.45 mL) and Ac₂O (0.22 mL) and stirred at room temperature for 20 min. After filtration and washing with DMF (3 x 3 mL) and DCM (2 x 3 mL), the resin was suspended in DCM (0.76 mL) under Argon atmosphere and PhSiH₃ (28 ul, 0.23 mmol) added. Pd(PPh₃)₄ (2.6 mg, 15 umol) in 1.37 mL of DCM was transferred to the stirred solution. The reaction mixture was stirred at room temperature for 30 min and filtered. The resin was rinsed and filtered with THF (3 x 3 mL), DMF (3 x 3 mL), DCM (3 x 3 mL), 5% DIEA in DCM (3 x 3 mL), and 0.02 M sodium diethyldithiocarbamate (NaDDTC) (3 x 3 mL).

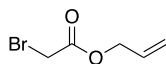


3,5-Bis(2-(allyloxy)-2-oxoethoxy)-2,4,6-tribromobenzoic acid (107). In a round-bottom flask, 0.8 ml (12.8 mmol) of Br₂ in CCl₄ (5 mL) was added dropwise over 30 min to a stirred solution of 1.0 g (4.29 mmol) of **45** in CCl₄ (10 mL) in the dark. The reaction mixture was stirred for 4.5 h. The reaction mixture was cooled in an ice bath, and 30% NaHSO₃ was added until red color dissipated. The precipitate was isolated and washed with ice water. The crude solid was purified by flash column chromatography (SiO₂, hexanes/ethyl acetate, 1:5) to give 0.92 g (56%) of **107** as a yellow solid: R_f 0.19 (hexanes/ethyl acetate, 1:10); ¹H NMR (300 MHz, CD₃OD) δ 4.92 (s, 3H); ¹³C NMR (400 MHz, CD₃OD) δ 169.19, 152.95, 139.70, 102.40, 98.3; HRMS (ESI-TOF) *m/z* calcd [M-H]⁻ for C₇H₂Br₃O₄ 388.7651, found 388.7687.



2,4,6-Tribromo-3,5-bis((t-butyltrimethylsilyloxy)benzoic acid (108). To a stirred solution of 0.08 g (0.5 mmol) of t-butylchlorodimethylsilane in 0.75 mL of DCM, 0.10 g (0.26 mmol) of **107** and 0.1 mL (0.76 mmol) TEA in DCM (1.50 mL) was added and stirred for 15 h at room temperature. The mixture was diluted with DCM (5 mL) and H₂O (5 mL); the organic layer was extracted, and the aqueous layer was washed with additional Et₂O (3 x 10 mL). The combined organic layers were dried over MgSO₄ and filtered, and volatile components removed under reduced pressure to give a crude white solid. The powder was purified by flash chromatography (SiO₂, ethyl acetate/hexanes, 1:50) to afford 0.08 g (90.8%) of **108** as a white crystal: *R_f* 0.34 (hexanes/ethyl acetate, 2:1); ¹H NMR (500 MHz, CDCl₃) δ 4.44 (s, 1H), 1.04 (s, 18H), 0.34 (s, 12H); ¹³C NMR (600 MHz, CDCl₃) δ 167.4, 152.0, 138.7, 112.5, 105.5, 27.0, 19.9, 0.98; HRMS (ESI-TOF) *m/z* calcd for C₁₉H₃₁Br₃O₄Si₂ 617.93, found 617.932.

2,4,6-Tribromo-3-((t-butyltrimethylsilyloxy)-5-hydroxybenzoic acid (109). ¹H NMR (400 MHz, CDCl₃) δ 6.04 (broad s, 1H), 1.05 (s, 9H), 0.36 (s, 6H); ¹³C NMR (400 MHz, CDCl₃) δ 166.9, 151.7, 150.8, 138.3, 106.1, 104.2, 99.5, 29.9, 26.9, 19.7; HRMS (ESI-TOF) *m/z* calcd for C₁₃H₁₇Br₃O₄Si 503.84, found 503.8457.

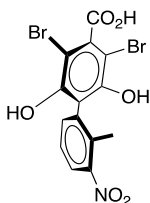


Allyl-2-bromoacetate (110). To 5.0 g of bromoacetic acid (35.98 mmol) and 2.45 ml of allyl alcohol (35.98 mmol) in cyclohexane (36 mL) was added 0.01 g *p*TsOH and the resulting reaction mixture was heated at reflux for 3 hours with azeotropic removal of the formed water employing a Dean and Stark apparatus. The reaction mixture was neutralized by washing with dil. Na₂CO₃. After washing with brine and drying (MgSO₄) the volatile components were removed under

reduced pressure to give 4.33 g (68%) of **110** as a colorless very irritating liquid (bp = 73 °C/15 mmHg). R_f 0.47 (hexanes/ethyl acetate, 7:3); mp 103-105 °C; ^1H NMR (400 MHz, CDCl_3) δ 5.93 (dquin, $J = 17, 6$ Hz, 1H), 5.39,5.35 (dd, $J = 17,1$ Hz, 2H), 4.67 (d, $J = 6$ Hz, 2H), 3.87 (s, 2H); ^{13}C NMR (300 MHz, CDCl_3) δ 170.9, 132.1, 117.6, 65.6, 48.3.

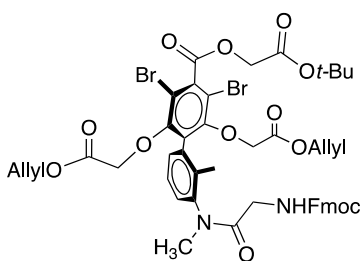


3,5-Bis(2-(allyloxy)-2-oxoethoxy)-2,4,6-tribromobenzoic acid (111). Benzoic acid **107** (0.16 g, 0.41 mmol) and TEA (0.17 mL, 1.24 mmol) in DCM (3 mL) were added to a stirred solution of allyl-2-bromoacetate **x** (0.10 mL, 0.98 mmol) in 0.6 mL DCM and stirred for 13 h at room temperature. The mixture was diluted with Et_2O (10 mL) and H_2O (10 mL); the organic layer was extracted, and the aqueous layer was washed with additional Et_2O (3 x 10 mL). The combined organic layers were dried over MgSO_4 and filtered. The volatile components were removed under reduced pressure, and the crude oil was purified by flash chromatography (SiO_2 , hexanes/ethyl acetate, elution gradient 2:1) to afford 0.11 g (48%) of **111** as a white crystal: R_f 0.29 (hexanes/ethyl acetate, 1:2); ^1H NMR (300 MHz, CDCl_3) δ 5.95 (dquin, $J = 17,6$ Hz, 2H), 5.40,5.32 (dABq, $J = 10,1$ Hz, 2H), (dABq, $J_{AB} = 10,1$ Hz, 2H), 4.76,4.74 (dt, $J = 6,1$ Hz, 4H), 4.63 (s, 4H); ^{13}C NMR (400 MHz, CDCl_3) δ 167.1, 153.4, 131.6, 119.6, 111.8, 69.3, 66.4; HRMS (ESI-TOF) m/z calcd for $\text{C}_{17}\text{H}_{15}\text{Br}_3\text{O}_8$ 581.7524, found 581.7545.



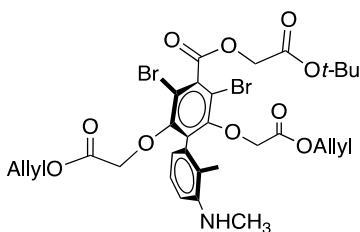
3,5-Dibromo-2,6-dihydroxy-2'-methyl-3'-nitro-[1,1'-biphenyl]-4-carboxylic acid (113). In a third-flame dried round-bottom flask, 1.0 mL of a 1.0 M solution of BBr_3 in DCM was added

dropwise over 30 minutes to a stirred solution of 0.35 g (0.76 mmol) of **15** in DCM (4 mL) at 0 °C. The reaction mixture was stirred at 0 °C for 3 hours and gradually warmed to room temperature and stirred for an additional 13 h. After cooling to 0 °C, the reaction mixture was quenched by the slow addition of chilled H₂O (15 mL) and diluted with Et₂O (30 mL); the organic layer was extracted, and the aqueous layer was washed with additional ether (3 x 30 mL). The combined organic layers were washed with 1 N NaOH (50 mL); the basic layer was extracted and acidified to pH = 1. The acidified aqueous layer was diluted with Et₂O; the organic layer was extracted, and the aqueous layer was washed with additional ether (3 x 30 mL). The combined organic layers were washed with brine, dried over MgSO₄ and filtered, and the volatile components were removed under reduced pressure to yield a brown oil. The oil was purified by flash column chromatography (SiO₂, hexanes/ethyl acetate, elution gradient, 1:2) to give 0.27 g (76%) of **72** as a pale yellow solid: *R_f* 0.22 (hexanes/ethyl acetate, 1:4); ¹H NMR (300 MHz, CD₃OD) δ 7.88, 7.85 (dd, *J* = 8, 2 Hz, 1H), 7.47-7.39 (m, 2H), 5.03 (broad s, 2H), 2.24 (s, 3H); ¹³C NMR (400 MHz, CD₃OD) δ 210.7, 169.5, 152.7, 152.1, 140.6, 137.2, 136.3, 133.3, 127.6, 124.8, 118.7, 98.9, 30.7, 24.0, 16.1; HRMS (ESI-TOF) *m/z* calc for [M-H]⁻ C₁₄H₈Br₂NO₆ 443.8716, found 443.8712.



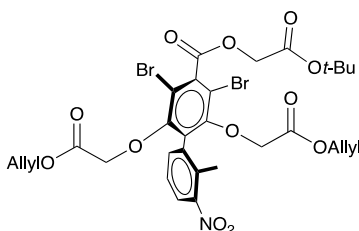
Diallyl 2,2'-((3'-(2-(((9H-fluoren-9-yl)methoxy)carbonyl)amino)-N-methylacetamido)-3,5-dibromo-4-((2-(*t*-butoxy)-2-oxoethoxy)carbonyl)-2'-methyl-[1,1'-biphenyl]-2,6-diyl)bis(oxy))diacetate (127**).** To 0.06 g (0.08 mmol) of **155** in 0.75 mL of CHCl₃ was added 0.03 g (0.11 mmol) of Fmoc-gly acid chloride **62** (generated according to above procedure and

used immediately thereafter) in 0.5 mL of CHCl₃ followed by 0.75 mL of saturated NaHCO₃ solution, and the reaction mixture was stirred at room temperature for 20 min. The solution was diluted with DCM (10 mL) and saturated NaHCO₃ solution (10 mL), the organic layer was extracted, and the aqueous layer was washed with DCM (3 × 10 mL). The organics were dried over MgSO₄, filtered and the volatile components were removed from the filtrate under reduced pressure to give a light brown crude oil. The oil was purified by flash chromatography (SiO₂, hexanes/ethyl acetate, elution gradient 4:1/3:1) to give 0.05 g (67%) of **127** as a white foam: R_f 0.39 (hexanes/ethyl acetate, 1:1); ¹H NMR (400 MHz, CDCl₃) δ 7.75 (d, *J* = 7 Hz, 2H), 7.58 (d, *J* = 7 Hz, 2H), 7.38 (t, *J* = 7 Hz, 2H), 7.36-7.24 (m, 4H), 7.22-7.18 (dqin, *J* = 7 Hz, 2H), 5.61 (broad s, 1H), 5.24,5.21 (dABq, *J* = 4,1 Hz, 2H), 5.18,5.12 (qAB, *J* = 23,10 Hz, 2H), 4.82 (s, 2H), 4.31 (d, *J* = 6 Hz, 2H), 4.19,4.13 (ABq, *J* = 7 Hz, 4H), 3.77,3.46 (qd, *J* = 4 Hz, 2H), 3.27 (s, 3H), 2.09 (s, 3H), 1.53 (s, 9H); ¹³C NMR (600 MHz, CDCl₃) δ 168.8, 166.7, 165.8, 164.6, 153.3, 153.3, 144.1, 144.0, 141.5, 141.4, 138.5, 136.3, 133.7, 131.6, 131.5, 131.3, 131.2, 128.9, 127.8, 127.5, 127.1, 125.3, 120.0, 119.1, 119.0, 111.8, 111.6, 83.1, 69.3, 69.2, 67.2, 66.0, 65.7, 62.8, 47.2, 43.2, 36.2, 28.2, 15.2; HRMS (ESI-TOF) *m/z* calcd for [M+H]⁺ C₄₄H₄₀Br₂N₂O₁₃ 962.5919, found 962.5928.



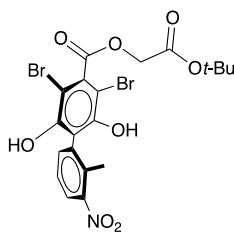
Dibenzyl 2,2'-((3,5-dibromo-4-(methoxycarbonyl)-2'-methyl-3'-(methylamino)-[1,1'-biphenyl]-2,6-diyl)bis(oxy))diacetate (128). Biaryl **126** (0.12 g, 0.17 mmol) and 0.027 g (0.18 mmol) of **69** in THF (0.12 mL) were sonicated for 5 minutes to give a homogenous solution. The mixture was then diluted with EtOH (0.16 mL) and stirred at room temperature for 12 h. Volatile

components were removed under reduced pressure and reaction vial was cooled to 0 °C for 10 minutes. The residue was rinsed with chilled dry DCM followed by hexanes to produce an off-white solid. The precipitate was isolated and taken up into DCM, dried over K₂CO₃, filtered, and volatile components were removed under reduced pressure to give an off-white solid. The dry intermediate was dissolved in THF (1.18 mL), and 0.013 g (0.33 mmol) of NaBH₄ were added and stirred for 6 h. The reaction mixture was concentrated under reduced pressure and the residue was diluted with ice, cold H₂O, and DCM; the organic layer was extracted and aqueous layer washed with additional DCM (2 x 5 mL). The combined organic layers were washed with additional H₂O (5 mL) and then brine (5 mL); the organic layer was dried over MgSO₄, filtered, and volatile components were removed under reduced pressure to give a yellow foam. The foam was purified by flash chromatography (SiO₂, hexanes/ethyl acetate, elution gradient 6:1) to yield 0.08 g (65%) of **128** as a white foam: R_f 0.32 (hexanes/ethyl acetate 3:1; ¹H NMR (400 MHz, CDCl₃) δ 7.19 (t, *J* = 8 Hz, 1H), 6.62 (d, *J* = 8 Hz, 1H), 6.56 (d, *J* = 8 Hz, 1H), 5.83,5.78 (dq, *J* = 20, 8 Hz, 2H), 5.23 (dd, *J* = 12 Hz, 2H), 5.20 (dd, *J* = 6 Hz, 4H), 4.81 (s, 2H), 4.50 (d, 2H), 4.12,3.99 (ABq, *J* = 15 Hz, 4H), 2.91 (s, 3H), 1.92 (s, 3H), 1.53 (9H); ¹³C NMR (500 MHz, CDCl₃) δ 167.7, 166.4, 153.7, 147.9, 138.7, 135.5, 132.3, 131.1, 128.9, 128.8, 128.6, 127.2, 121.4, 119.2, 111.0, 109.9, 69.4, 67.0, 53.6, 31.2, 30.1, 28.7, 14.6, 14.5; HRMS (Q-TOF) *m/z* calcd for [M+H]⁺ C₃₁H₃₆Br₂NO₁₀ 740.0700, found 740.0669.



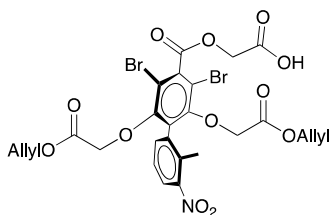
Diallyl 2,2'-((3,5-dibromo-4-((2-(*t*-butoxy)-2-oxoethoxy)carbonyl)-2'-methyl-3'-nitro-[1,1'-biphenyl]-2,6-diyl)bis(oxy))diacetate (129). In a round bottom flask, 0.18 g (0.33 mmol) of **89**,

0.09 mL (0.72 mmol) of allyl bromoacetate, 0.09 g (0.65 mmol) of K_2CO_3 , and 0.01 g (0.01 mmol) of 18-crown-6 were dissolved in acetone (3.3 mL), and the reaction mixture was refluxed for 14 h. The volatile components were removed under reduced pressure, and the residue was diluted with DCM (10 mL) and water (10 mL); the organic layer was extracted, and the aqueous layer was washed with additional DCM (3 x 10 mL). The combined organic layers were washed with brine, dried over $MgSO_4$ and filtered, and the volatile components were removed under reduced pressure to give a crude brown foam. The foam was purified by flash chromatography (SiO_2 , hexanes/ethyl acetate, elution gradient 2:1) to yield 0.18 g (74%) of **129** as a pale yellow foam: R_f 0. (hexanes/ethyl acetate 2:1); 1H NMR (400 MHz, $CDCl_3$) δ 7.92 (d, $J = 6$, 1H), 7.47-7.39 (m, 2H), 5.79 (dq, $J = 22$, 6 Hz 2H), 5.25 (dABq, $J_{AB} = 3$, 2 Hz, 2H) 5.20 (dABq, $J_{AB} = 9,8$ Hz, 2H), 4.82 (s, 2H), 4.49 (dt, $J = 6,1$ Hz, 4H) 4.20,4.09 (ABq, $J_{AB} = 35$, 15 Hz, 4H), 2.35 (s, 3H) 1.54 (s, 9H); ^{13}C NMR (600 MHz, $CDCl_3$) δ 166.6, 165.8, 164.5, 153.6, 150.9, 139.1, 135.1, 134.1, 132.8, 131.3, 131.1, 126.6, 125.2, 119.4, 111.9, 83.2, 69.5, 66.1, 62.9, 28.3, 17.0; HRMS (ESI-TOF) m/z calcd for $[M+Na]^+$ $C_{30}H_{31}Br_2NO_{12}Na$ 778.0105, found 778.0108.



2-(*T*-butoxy)-2-oxoethyl 3,5-dibromo-2,6-dihydroxy-2'-methyl-3'-nitro-[1,1'-biphenyl]-4-carboxylate (130). In an oven-dried round bottom flask, 0.25 g (0.56 mmol) of **113**, 0.091 mL (0.62 mmol) of *t*-butyl bromoacetate, 0.06 g (0.56 mmol) of $KHCO_3$, and 0.01 g (0.02 mmol) of 18-crown-6 were dissolved in acetone (5.5 mL), and the reaction mixture was refluxed for 4 h. The volatile components were removed under reduced pressure, and the residue was diluted with DCM (20 mL) and water (20 mL); the organic layer was extracted, and the aqueous layer was

washed with additional DCM (3 x 20 mL). The combined organic layers were washed with brine (50 mL), dried over MgSO₄ and filtered, and the volatile components were removed under reduced pressure to give a crude light brown foam. The foam was purified by flash chromatography (SiO₂, hexanes/ethyl acetate, elution gradient 6:1/5:1) to yield 0.24 g (78%) of **130** as a pale yellow foam: *R_f* 0.36 (hexanes/ethyl acetate 4:1); ¹H NMR (300 MHz, CDCl₃) δ 7.93 (d, *J* = 8 Hz, 1H), 7.46-7.38 (m, 2H), 5.73 (broad s, 2H), 4.81 (s, 2H), 2.29 (s, 3H), 1.54 (s, 9H); ¹³C NMR (400 MHz, CD₃OD) δ 169.5, 152.7, 152.1, 140.6, 137.2, 136.3, 133.3, 127.6, 124.8, 118.7, 98.9, 30.7, 16.1; HRMS (ESI-TOF) *m/z* calcd for [M-H]⁻ C₂₀H₁₈Br₂NO₈ 557.9393, found 557.9404.



2-((2,6-Bis(2-(allyloxy)-2-oxoethoxy)-3,5-dibromo-2'-methyl-3'-nitro-[1,1'-biphenyl]-4-carbonyloxy)acetic acid (140). To a solution of 0.17 g (0.23 mmol) of **129** in DCM (1.5 mL) at room temperature was added 0.5 mL (6.8 mmol) of TFA and the reaction mixture was stirred for 2 h. The reaction mixture was diluted with DCM (10 mL) and water (10 mL); the organic layer was extracted, and the aqueous layer was washed with additional DCM (2 x 10 mL). The combined organic layers were washed with brine (30 mL), dried over MgSO₄ and filtered, and the volatile components were removed under reduced pressure to yield 0.15 g (99%) of **140** as a white foam: *R_f* 0.32 (hexanes/ethyl acetate 1:1); ¹H NMR (400 MHz, CDCl₃) δ 7.84 (d, *J* = 8 Hz, 1H), 7.40-32 (m, 2H), 6.69 (broad s, 1H), 5.71 (dq, *J* = 12, 6 Hz, 2H), 5.18 (dABq, *J* = 9, 1 Hz, 2H), 5.16 (app dd, *J* = 9, 1 Hz, 2H), 4.92 (s, 2H), 4.44 (dt, *J* = 6, 1 Hz, 4H), 4.13, 4.02 (ABq, *J_{AB}* = 15 Hz, 4H), 2.28 (s, 3H); ¹³C NMR (400 MHz, CD₃CN) δ 168.3, 167.6, 165.5, 154.6, 151.7, 139.3,

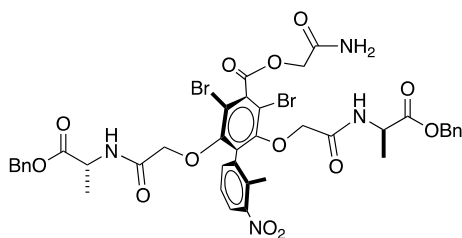
135.9, 135.0, 133.0, 132.8, 132.0, 127.6, 125.8, 118.8, 118.3, 111.9, 70.35, 66.21, 62.95, 17.00; HRMS (ESI-TOF) m/z calcd for $[M-H]^-$ $C_{26}H_{22}Br_2NO_{12}$ 697.95033, found 697.95150.

Diallyl-2,2'-((5-((2-(allyloxy)-2-oxoethoxy)carbonyl)-2,4,6-tribromo-1,3-

phenylene)bis(oxy))diacetate. 1H NMR (400 MHz, $CDCl_3$) δ 4.76 (s, 2H), 4.74 (s, 4H), 1.52 (s, 18H), 1.51 (s, 9H), 2.29 (s, 3H), 1.54 (s, 9H); ^{13}C NMR (500 MHz, $CDCl_3$) δ 166.2, 165.7, 164.3, 153.6, 137.7, 116.2, 111.6, 83.0, 82.7, 70.8, 69.6, 68.5, 63.9, 62.8, 61.6, 29.7, 28.7, 27.7, 26.7; HRMS (ESI-TOF) m/z calcd for $[M+H]^+$ $C_{21}H_{26}Br_3O_{10}$ 674.9872, found 674.9865.

2-(*T*-butoxy)-2-oxoethyl 2,4,6-tribromo-3-(2-(*t*-butoxy)-2-oxoethoxy)-5-hydroxybenzoate. 1H NMR (400 MHz, $CDCl_3$) δ 6.50 (broad s, 1H), 4.77 (s, 2H), 4.48 (s, 2H), 1.52 (s, 9H), 1.52 (s, 9H); ^{13}C NMR (500 MHz, $CDCl_3$) δ 166.4, 165.8, 164.5, 153.0, 150.7, 136.8, 108.0, 105.8, 103.5, 83.1, 82.8, 69.7, 62.8, 28.2; HRMS (ESI-TOF) m/z calcd for $[M-H]^-$ $C_{19}H_{22}Br_3O_8$ 614.8859, found 614.8881.

2,4,6-Tribromo-3,5-bis(2-(*t*-butoxy)-2-oxoethoxy)benzoic acid. 1H NMR (400 MHz, $CDCl_3$) δ 6.24 (broad s, 1H), 4.76 (s, 2H), 4.48 (s, 2H), 1.52 (d, 18H); ^{13}C NMR (500 MHz, $CDCl_3$) δ 166.4, 165.8, 164.6, 153.1, 150.6, 136.9, 107.9, 106.0, 103.4, 83.1, 82.8, 69.7, 62.8, 28.3; HRMS (ESI-TOF) m/z calcd for $[M-H]^-$ $C_{19}H_{22}Br_3O_8$ 614.8859, found 614.8860.

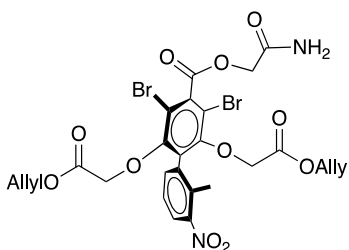


**Dibenzyl 2,2'-((2,2'-((4-((2-amino-2-oxoethoxy)carbonyl)-3,5-dibromo-2'-methyl-3'-nitro-
[1,1'-biphenyl]-2,6-diyl)bis(oxy))bis(acetyl))bis(azanediy)))(2*R*,2'*R*)-dipropionate (141).**

NovaPEG rink amide resin (0.07 g, approx. 0.03 mmol) was suspended in DMF (2.5 ml) and left to swell for 10 minutes. A solution of **140** (0.09 g, 0.12 mmol), PyAOP (0.06 g, 0.12 mmol),

HOBt (0.02 g, 0.12 mmol) and DIEA (0.02 g, 0.18 mmol) in NMP was vortexed and left to activate for 2 minutes. DMF was filtered and the activated acid solution added to swelled resin. The stirred solution was heated at 70 °C for 4 min using microwave irradiation. The solution was then stirred at room temperature for 5 min, filtered and resin washed with additional DMF (3 x 3 mL). The following protocol was repeated twice for allyl deprotection. The resin was suspended in DMF (0.73 ml), treated with DIEA (0.45 mL) and Ac₂O (0.22 mL) and stirred at room temperature for 20 min. After filtration and washing with DMF (3 x 3 mL) and DCM (2 x 3 mL), the resin was suspended in DCM (0.76 mL) under Argon atmosphere and PhSiH₃ (28 ul, 0.23 mmol) added. Pd(PPh₃)₄ (2.6 mg, 15 umol) in 1.37 mL of DCM was transferred to the stirred solution. The reaction mixture was stirred at room temperature for 30 min and filtered. The resin was rinsed and filtered with THF (3 x 3 mL), DMF (3 x 3 mL), DCM (3 x 3 mL), 5% DIEA in DCM (3 x 3 mL), and 0.02 M sodium diethyldithiocarbamate (NaDDTC) (3 x 3 mL). The resin was washed with DMF (2 x 3 mL) and suspended in NMP (2.1 mL). To the suspension, PyAOP (0.24 mmol, 0.13 g), HOBt (0.04 g, 0.24 mmol), and DIEA (0.06 mL, 0.36 mmol) were added and stirred for 3 min. Alanine benzyl ester (0.05 g, 0.24 mmol) was added to the activated acid and heated at 70 °C for 4 min using microwave irradiation. The solution was then stirred at room temperature for 5 min and filtered. After filtration with DMF (3 x 3 mL), DCM (3 x 3 mL) and MeOH (3 x 3 mL), the resin was dried in a vacuum dessicator for 30 min. TFA (2.19 mL, 28.64 mmol) and TIS (0.12 mL, 0.57 mmol) were added to the reaction and the vessel shaken for 3 hours. The reaction mixture was filtered and resin treated with additional TFA (2.0 mL, 27 mmol) and filtered. TFA was removed from the filtrate by a stream of nitrogen and product dried *in vacuo*. The crude product was purified using the preparative RP-HPLC standard protocol in Chapter 9.1 and freeze-dried to give **141** in >95% purity. ¹H NMR (700 MHz, CD₃CN) δ 7.90 (d, *J* = 8 Hz, 1H), 7.57 (d, *J* = 8 Hz,

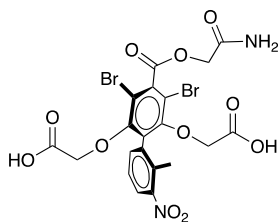
1H), 7.43 (t, $J = 8$ Hz, 1H), 7.36 (m, 10H), (q, $J =$ Hz, 2H), 6.49 (broad s, 1H), 6.15 (broad s, 1H), 5.13-5.08 (m, 4H), 4.80 (s, 2H), four protons of conformers [4.33,4.32 (ABq, $J_{AB} = 4$ Hz), 4.18,3.91 (ABq, $J_{AB} = 14$ Hz), 4.03 (s)], 2.39 (s, 3H), 1.28,1.25 (dd, $J = 20,8$ Hz, 6H); ^{13}C NMR (400 MHz, CDCl_3) δ 167.2, 166.1, 154.0, 151.3, 140.4, 135.8, 135.5, 134.5, 133.1, 131.0, 129.1, 129.0, 128.9, 127.1, 125.5, 111.7, 70.0, 67.4, 54.6, 54.3, 54.1, 53.9, 53.8, 17.2; HRMS (ESI-TOF) m/z calcd for $[\text{M}+\text{H}]^+$ $\text{C}_{40}\text{H}_{39}\text{Br}_2\text{N}_4\text{O}_{13}$ 941.08749, found 941.0873.



Diallyl 2,2'-((4-((2-amino-2-oxoethoxy)carbonyl)-3,5-dibromo-2'-methyl-3'-nitro-[1,1'-biphenyl]-2,6-diyl)bis(oxy))diacetate (142). NovaPEG rink amide resin (0.02 g, 0.01 mmol) was suspended in DMF (2.5 ml) and left to swell for 10 minutes. A solution of biaryl **124** (0.03 g, 0.04 mmol), PyAOP (0.02 g, 0.04 mmol), HOBT (0.01 g, 0.04 mmol) and DIEA (0.01 g, 0.06 mmol) in NMP (mL) was vortexed and left to activate for 2 minutes. DMF was filtered, and the activated acid solution was added to swelled resin **142**. The stirred solution was heated for 4 minutes at 70 °C by microwave irradiation. The solution was then stirred at room temperature for 5 minutes, filtered, and resin washed with additional DMF (3 x 3 mL). The resin was suspended in DMF (0.73 ml), treated with DIEA (mL, mmol) and Ac_2O (mL, mmol) and stirred at room temperature for 15 minutes. After filtration and washing with DMF (3 x 3 mL), DCM (3 x 3 mL) and MeOH (3 x 3 mL), the resin was dried *in vacuo* for 20 minutes. TFA (1.0 mL) was added to resin and reaction vessel shaken for 2.5 hours. The reaction mixture was filtered and resin treated with additional 0.6 ml TFA, shaken for 1 hour, and filtered. TFA was removed from the filtrate by a stream of nitrogen and product dried *in vacuo*. The resin was treated with additional cleavage

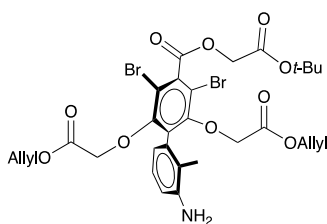
cocktail of TFA (95 μ L), H₂O (25 μ L) and TIS (25 μ L), shaken for 30 min, filtered and repeated. The crude product was purified using the preparative RP-HPLC standard protocol (see Chapter 9.1) and freeze-dried to give 0.84 g (78%). ¹H NMR (500 MHz, CD₃CN) δ 7.92 (d, *J* = 8 Hz, 1H), 7.53 (d, *J* = 8 Hz, 1H), 7.45 (t, *J* = 8 Hz, 1H), 6.49 (broad s, 1H), 6.13 (broad s, 1H), 5.80 (dq, *J* = 12, 6 Hz, 2H), 5.21, (dABq, *J* = 9,1 Hz, 2H), 5.18 (dABq, *J* = 9,1 Hz, 2H), 4.79 (s, 2H), 4.43 (qt, *J* = 9,5 Hz, 4H), 4.26,4.13 (ABq, *J*_{AB} = 16 Hz, 4H), 2.28 (s, 3H); ¹³C NMR (400 MHz, CDCl₃) δ 167.2, 166.1, 154.0, 151.3, 140.4, 135.8, 135.5, 134.5, 133.1, 131.0, 129.1, 129.0, 128.9, 127.1, 125.5, 111.7, 70.0, 67.4, 54.6, 54.3, 54.1, 53.9, 53.8, 17.2; HRMS (ESI-TOF) *m/z*: [M+H]⁺ calcd for C₂₆H₂₄Br₂N₂O₁₁ 699.96598, found 699.96778.

2-(4-(2,4-Dimethoxybenzyl)phenoxy)acetic acid (153). Product **154** was isolated as a side product of the above process when TIS was used in the cleavage step. ¹H NMR (300 MHz, CD₃CN) δ 7.12 (d, *J* = 5 Hz, 2H), 7.00 (d, *J* = 8, 1H), 6.84 (d, *J* = 5, 2H), 6.50 (d, *J* = 2, 1H), 6.44 (d, *J* = 9, 1H), 4.99 (broad s, 1H), 4.38 (s, 2H), 3.79 (s, 2H), 3.77 (s, 3H), 3.75 (s, 3H); ¹³C NMR (400 MHz, CDCl₃) δ 154.4, 151.7, 135.53, 134.6, 133.7, 131.9, 127.5, 125.2, 118.6, 109.5, 53.0, 16.4; HRMS (ESI-TOF) *m/z*: [M+H]⁺ calcd for C₁₇H₁₉O₅ 303.12270, found 303.12345.



2,2'-((4-((2-Amino-2-oxoethoxy)carbonyl)-3,5-dibromo-2'-methyl-3'-nitro-[1,1'-biphenyl]-2,6-diyl)bis(oxy))diacetic acid (143). NovaPEG rink amide resin (0.07 g, 0.03 mmol) was suspended in DMF (2.5 ml) and left to swell for 10 minutes. A solution of biaryl **143-i** (0.09 g, 0.12 mmol), HCTU (0.06 g, 0.12 mmol) and DIEA (0.02 g, 0.18 mmol) in NMP was vortexed and left to activate for 2 minutes. DMF was filtered and the activated acid solution added to **143-i**.

The stirred solution was heated at 70 °C for 4 min using microwave irradiation. The solution was then stirred at room temperature for 15 min, filtered and resin washed with additional DMF (3 x 3 mL). The resin was suspended in DMF (0.73 ml), treated with DIEA (0.45 mL) and Ac₂O (0.22 mL) and stirred at room temperature for 20 min. After filtration and washing with DMF (3 x 3 mL) and DCM (2 x 3 mL), the resin was suspended in DCM (0.76 mL) under Argon atmosphere. The following step was repeated twice for allyl deprotection. To the solution, PhSiH₃ (28 ul, 0.23 mmol) was added, followed by addition of Pd(PPh₃)₄ (2.6 mg, 15 umol) in DCM (1.37 mL). The reaction mixture was stirred at room temperature for 30 min and filtered. The resin was rinsed with THF (3 x 3 mL), DMF (3 x 3 mL), DCM (3 x 3 mL), 5% DIEA in DCM (3 x 3 mL), 0.02 M sodium diethyldithiocarbamate (NaDDTC) (3 x 3 mL) and DMF (2 x 3 mL). Solid supported material was separated (6 mg) and exposed to TFA (2.19 mL, 28.64 mmol) and TIS (0.12 mL, 0.57 mmol) were added to the reaction and the vessel shaken for 3 hours. The reaction mixture was filtered and resin treated with additional TFA (2.0 mL, 27 mmol) and filtered. TFA was removed from the filtrate by a stream of nitrogen and **143** dried *in vacuo*. MS (MALDI-TOF) *m/z*: [M+H]⁺ calcd for C₂₀H₁₇Br₂N₂O₁₁ 618.9156, found 618.9162.



Diallyl 2,2'-((3'-amino-3,5-dibromo-4-((2-(*t*-butoxy)-2-oxoethoxy)carbonyl)-2'-methyl-[1,1'-biphenyl]-2,6-diyl)bis(oxy))diacetate (154**)**. In a round bottom flask, 0.25 g (1.33 mmol) of SnCl₂ were dissolved in DCM (2.2 ml) and MeOH (2.2 ml) and the solution was cooled to 0 °C and added dropwise to 0.20 g (0.26 mmol) of **130**. The mixture was gradually warmed to room temperature and stirred for 16 h. The reaction mixture was passed through a Celite plug and

washed with DCM (10 ml). The filtrate was washed with saturated NaHCO₃ solution (5 ml) and H₂O (5 ml) and brine (2 x 10 ml). The organic layer was dried over anhydrous MgSO₄, filtered and volatile components removed under reduced pressure to give a crude yellow oil. The oil was purified by flash chromatography (SiO₂, hexanes/ethyl acetate, elution gradient 3:1) to yield 0.17 g (91%) of **154** as a light yellow foam: R_f 0.31 (hexanes/ethyl acetate 2:1); ¹H NMR (400 MHz, CDCl₃) δ 6.98 (t, *J* = 8 Hz, 1H), 6.64 (d, *J* = 8 Hz, 1H), 6.54 (d, *J* = 8 Hz, 1H), (dq_{in}, *J* = 23, 6 Hz, 2H), 5.18 (dABq, *J* = 15 Hz, 2H), 5.16 (app dd, *J* = 8, 1 Hz, 2H), 4.74 (s, 2H), 4.49 (d, *J* = 6 Hz, 4H), 3.95, 3.92 (ABq, *J*_{AB} = 15, 2 Hz, 4H), 1.89 (s, 3H), 1.46 (s, 9H); ¹³C NMR (400 MHz, CDCl₃) δ 167.4, 166.1, 165.1, 153.7, 145.5, 137.7, 132.6, 131.7, 131.6, 126.9, 121.9, 120.9, 119.2, 115.8, 111.4, 83.2, 69.3, 65.9, 62.9, 28.4, 14.8; HRMS (Q-TOF) *m/z* calcd for [M+H]⁺ C₃₀H₃₄Br₂NO₁₀ 726.0544, found 726.0517.

APPENDIX A

SUPPORTING INFORMATION

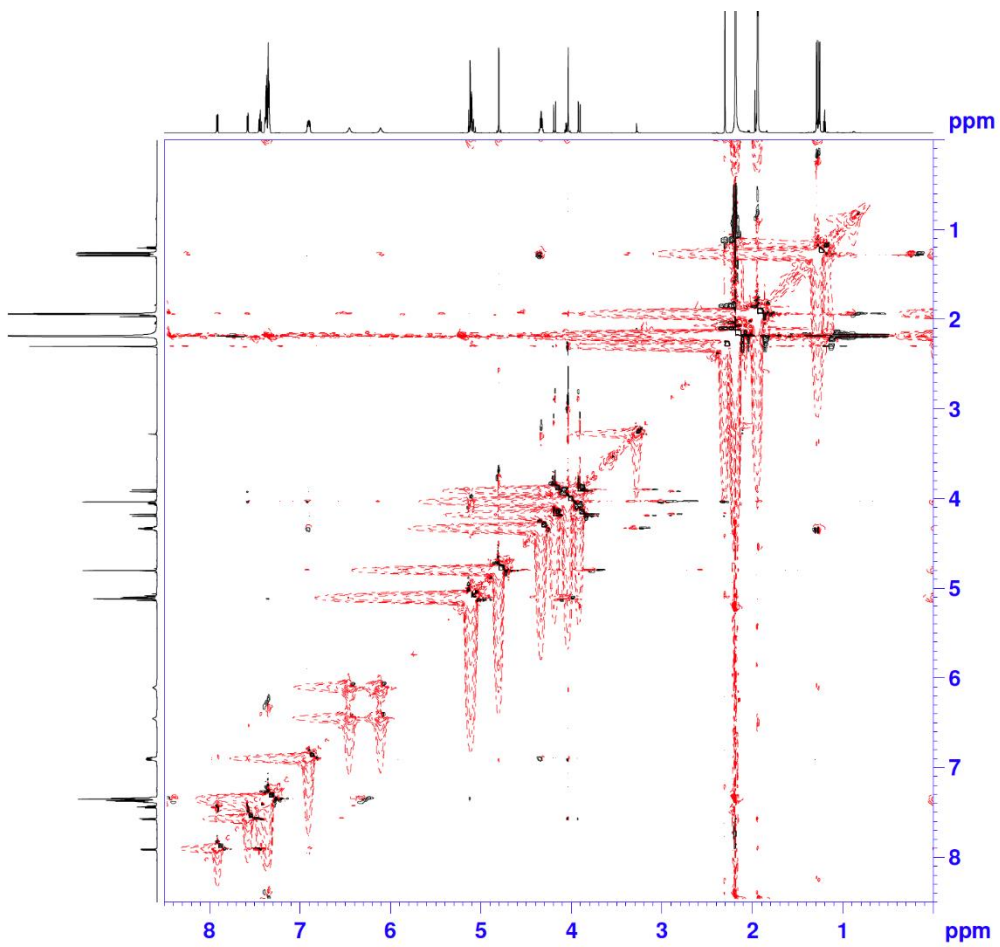
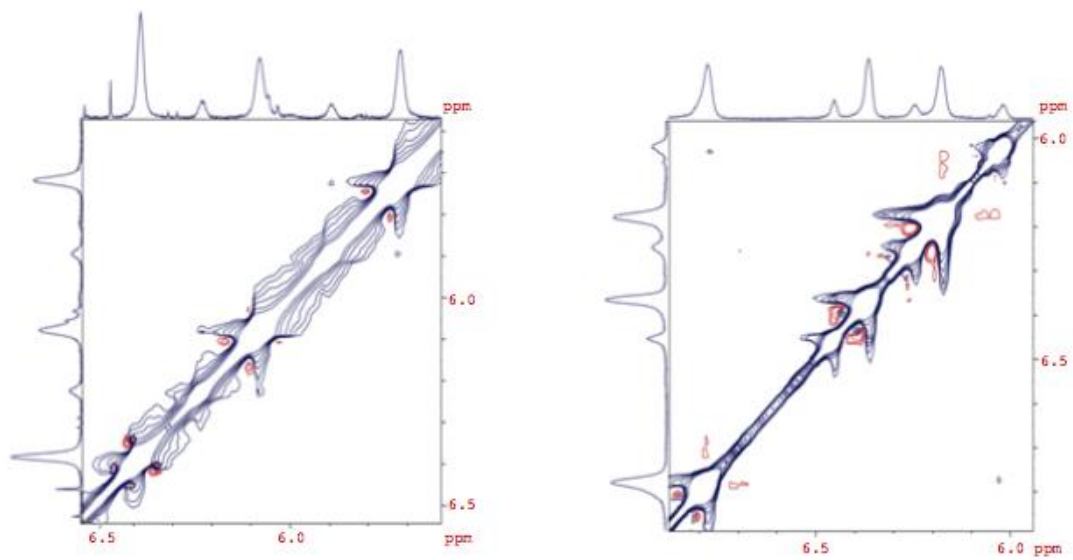


Figure SI-45. ROESY/EXSY data of **141** in CD₃CN (1.0 mM) at 298 K.

A



B

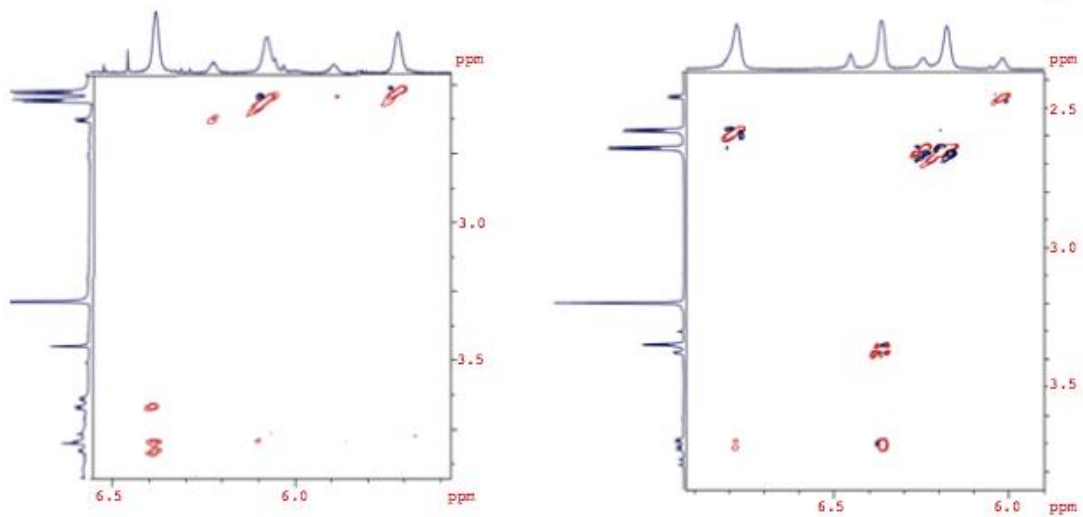


Figure SI-46. ROESY/EXSY data of **44** (left) and (right) **43** in CD₂Cl₂ (0.1 mM) at 298 K. (a) Amide proton ¹H NMR assignments of the major and minor conformers. (b) Amide protons and their correlation to glycine and N-methyl neighbors.

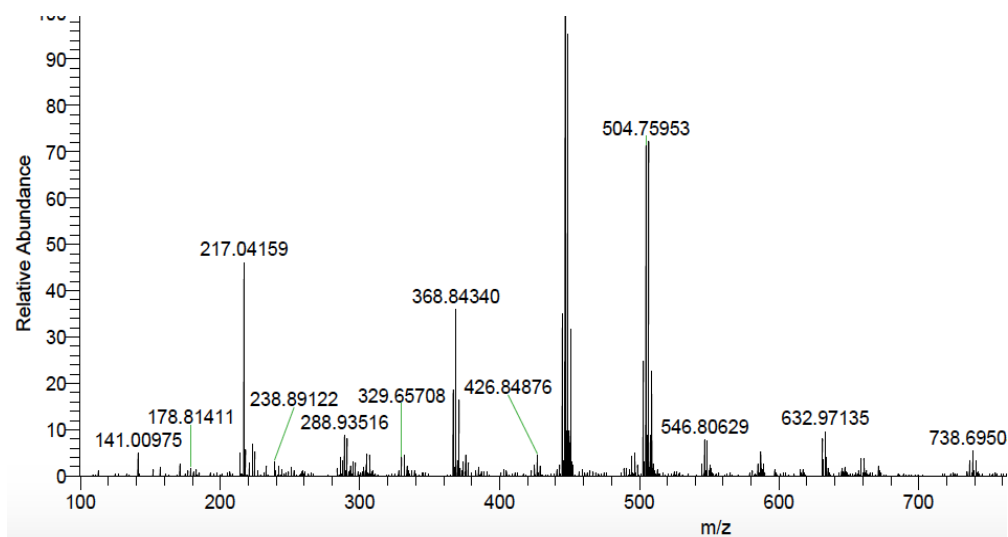
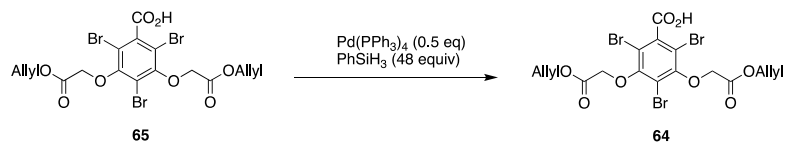
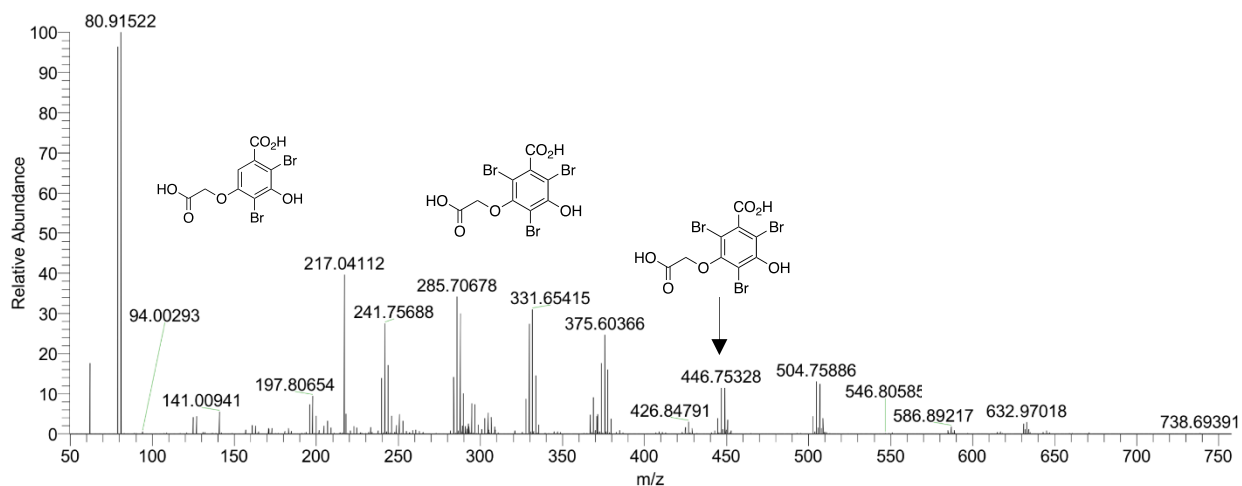
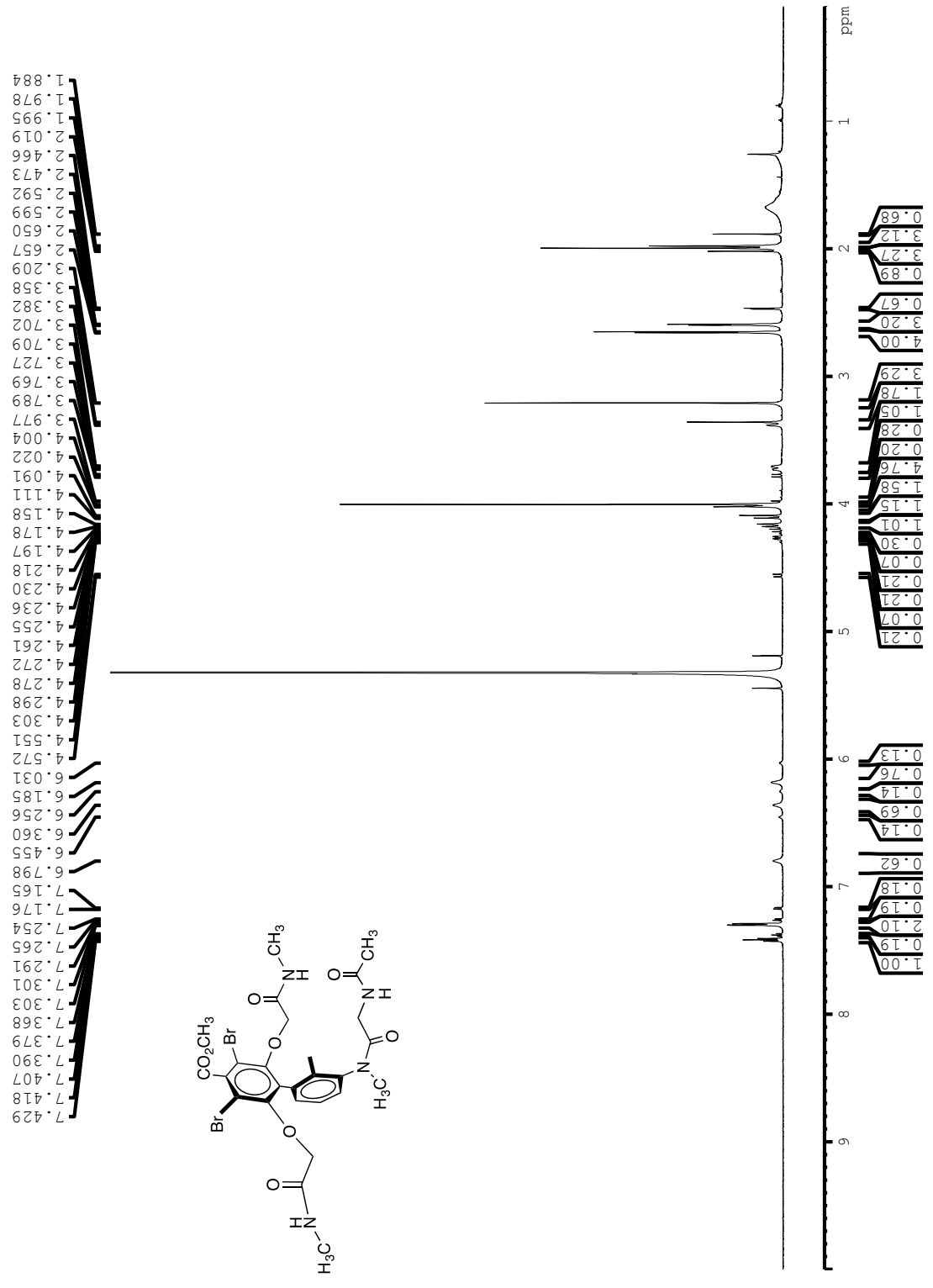
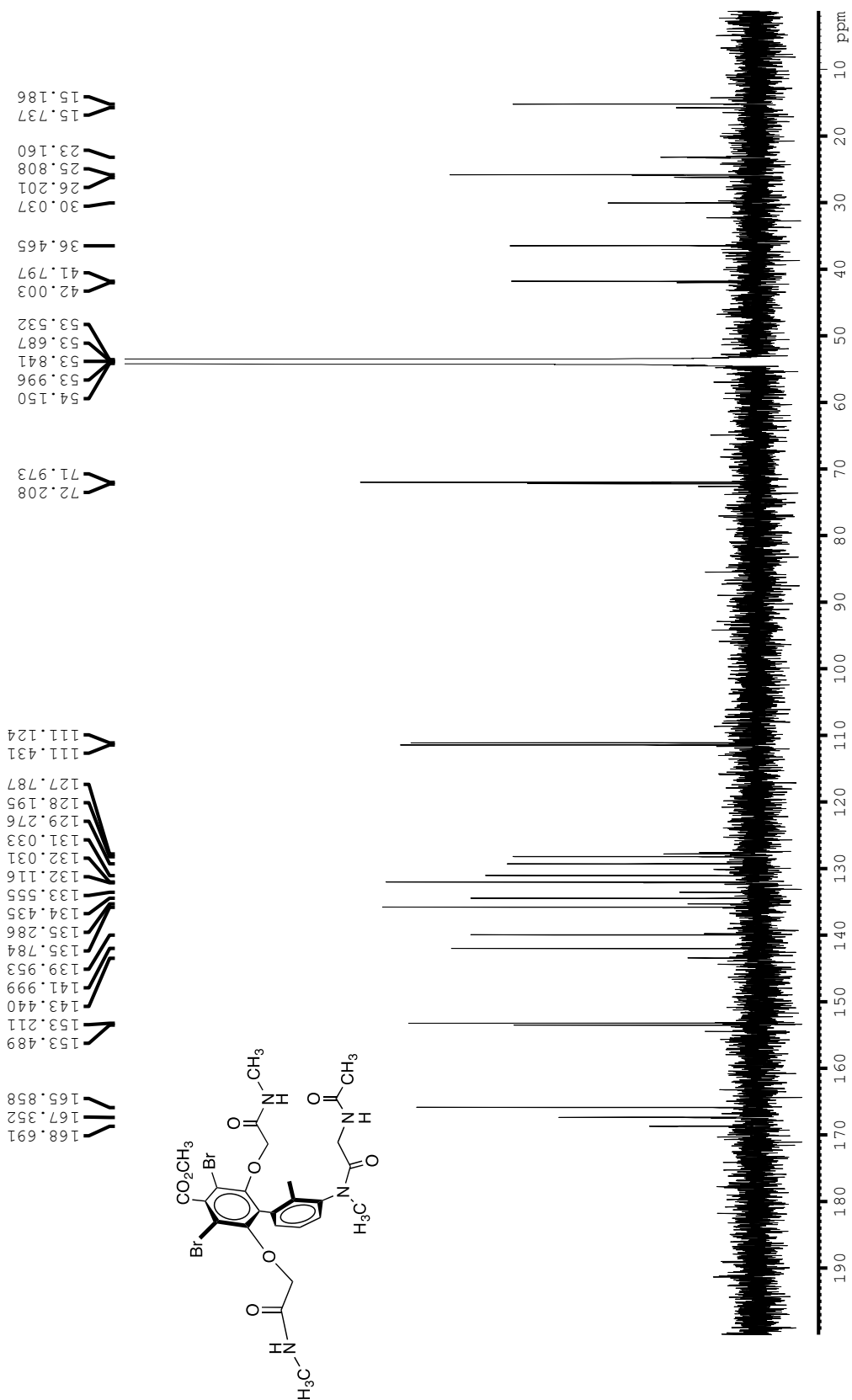


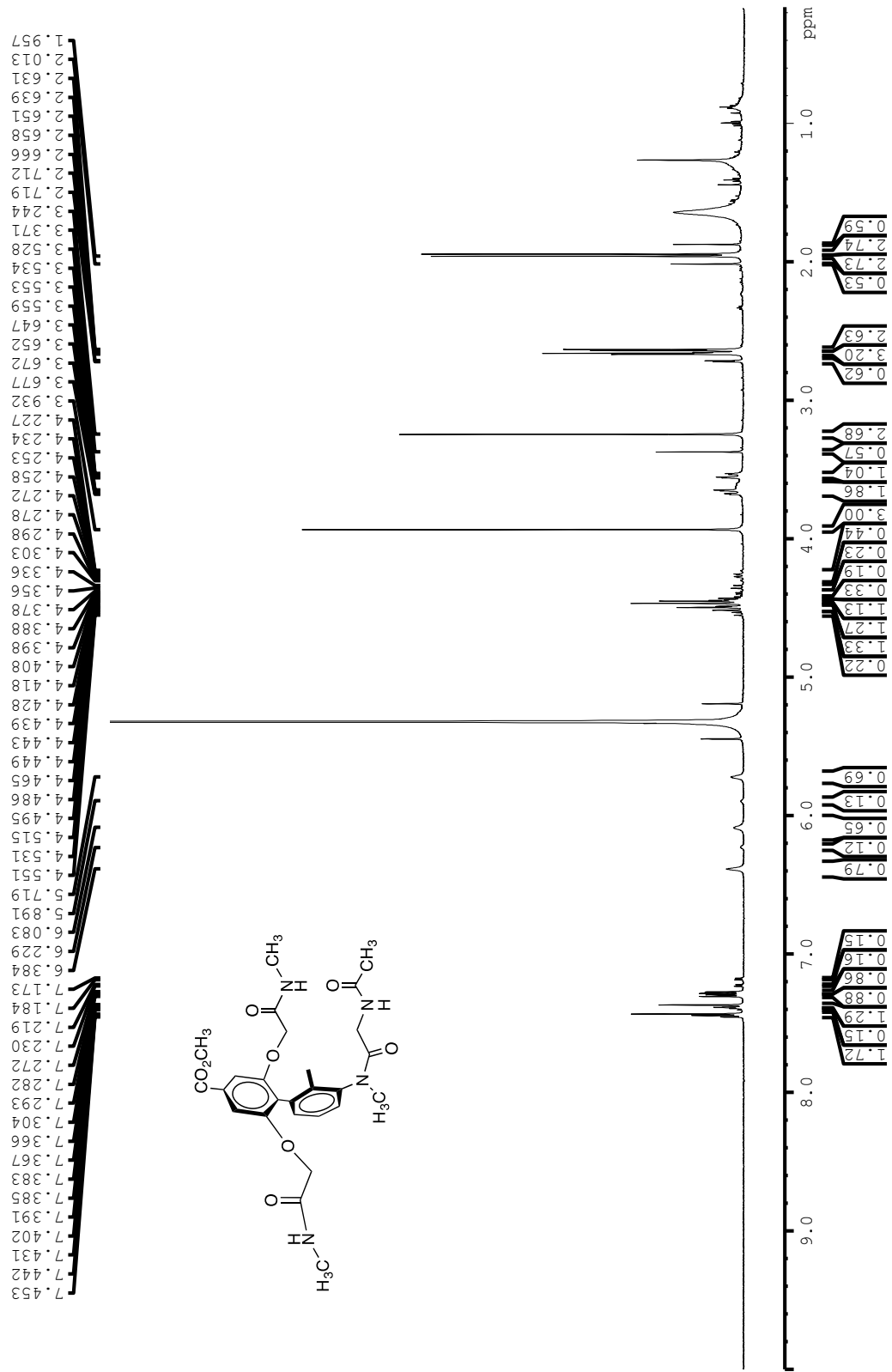
Figure SI-47. ESI-MS data for test allyl deprotection. Debromination product was observed in both cases. A decrease in $\text{Pd(PPh}_3)_4$ from 3.2 to 0.5 equivalents provided improved conditions to afford acid **105**.

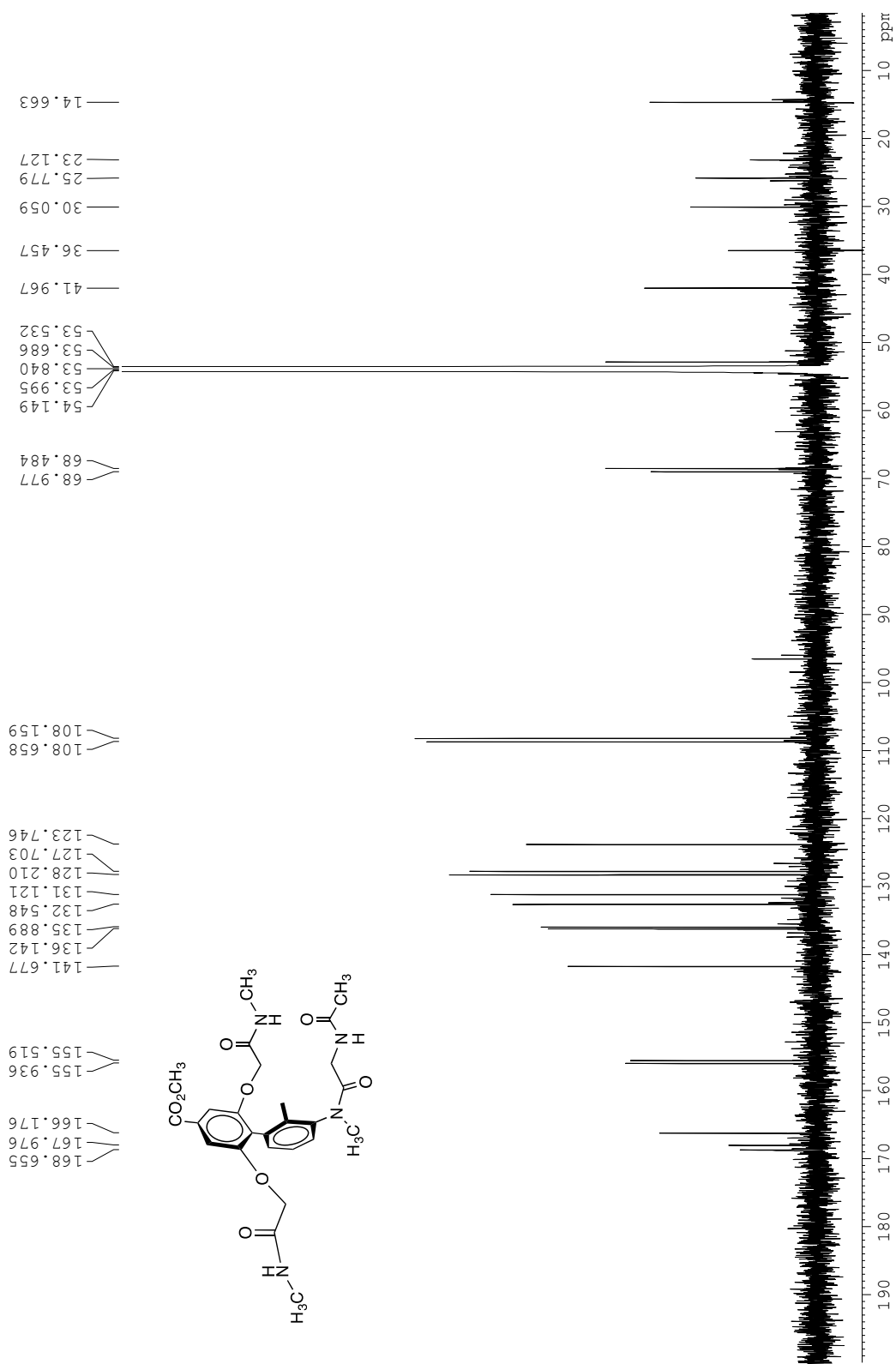
APPENDIX B

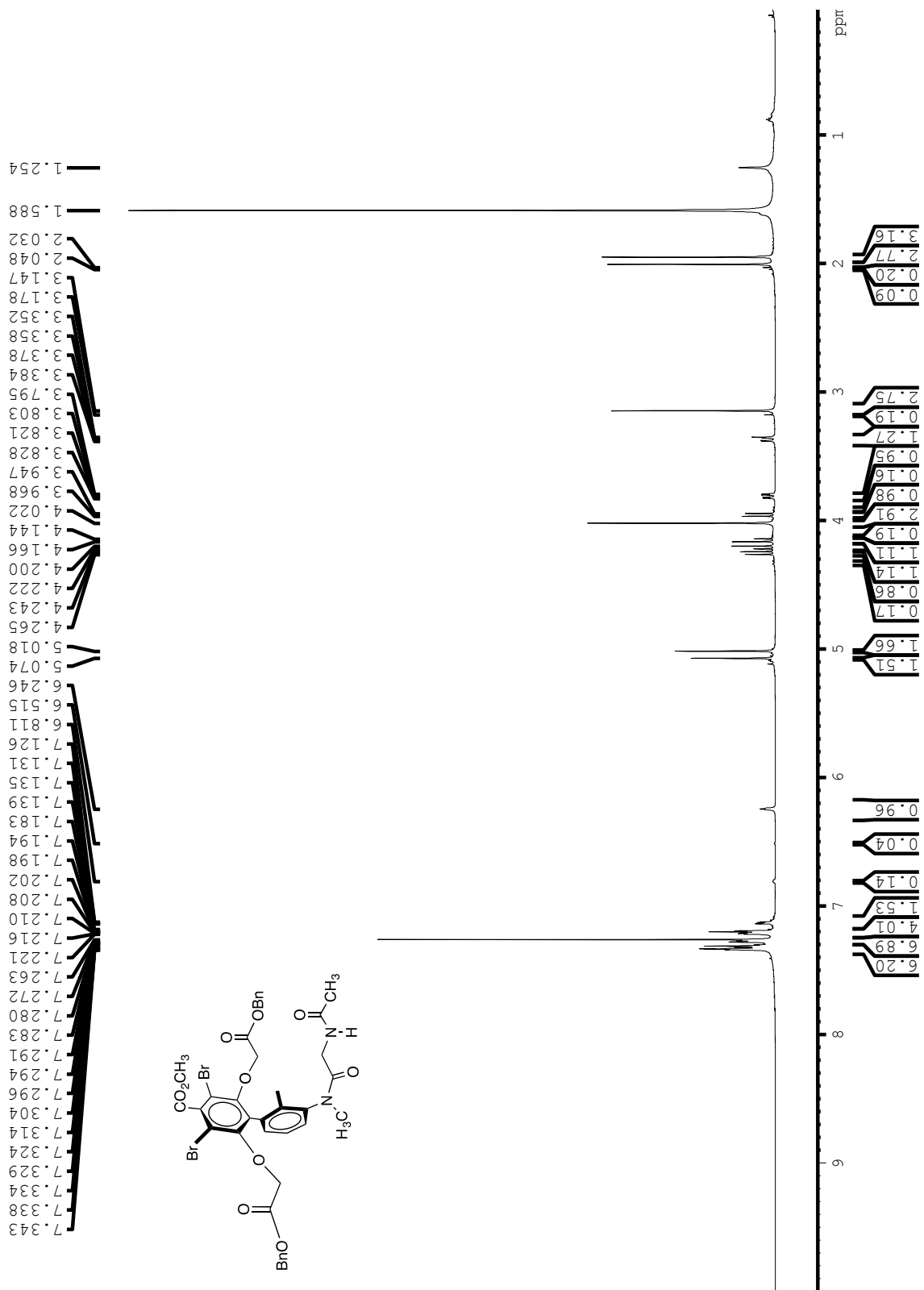
^1H AND ^{13}C NMR DATA

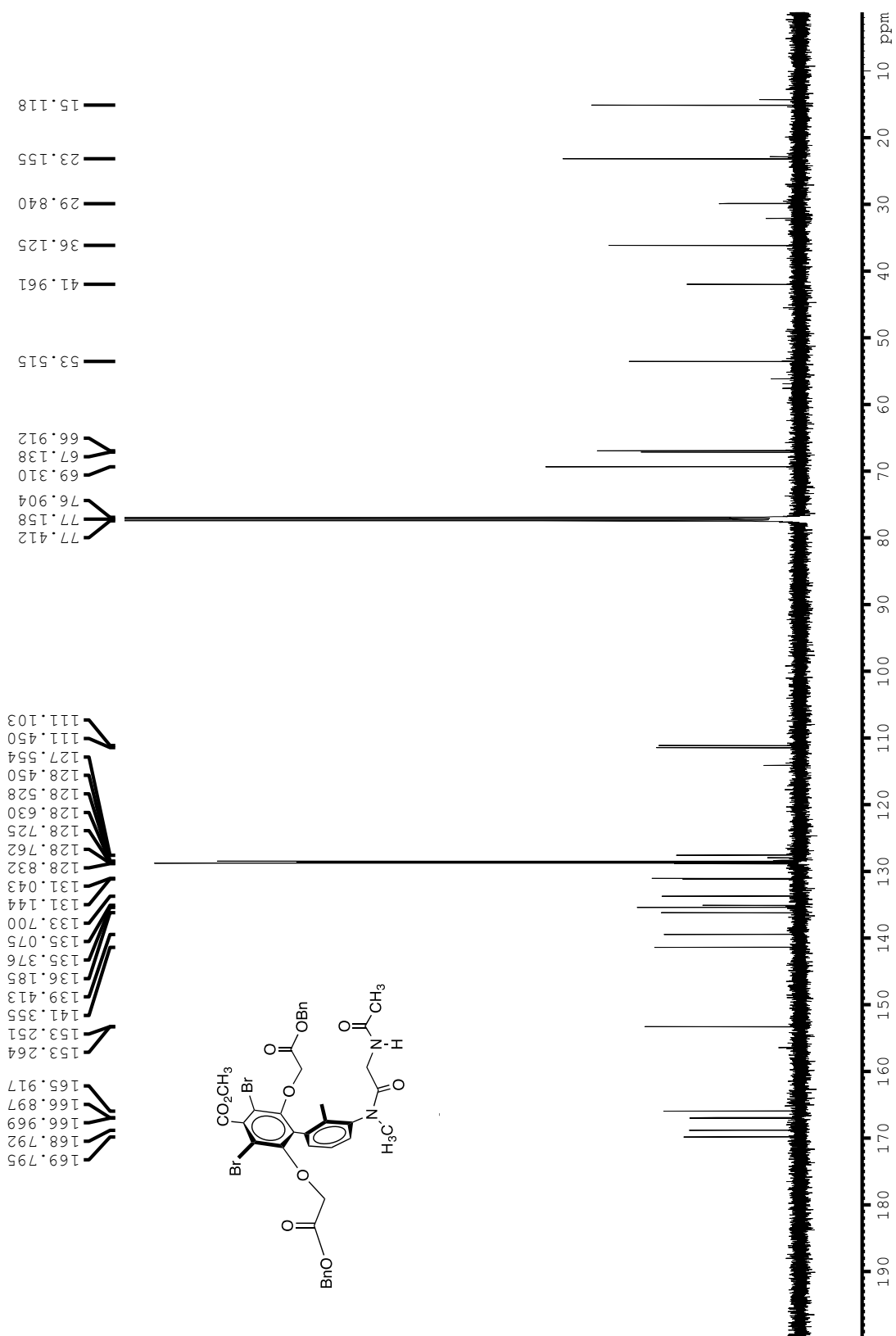


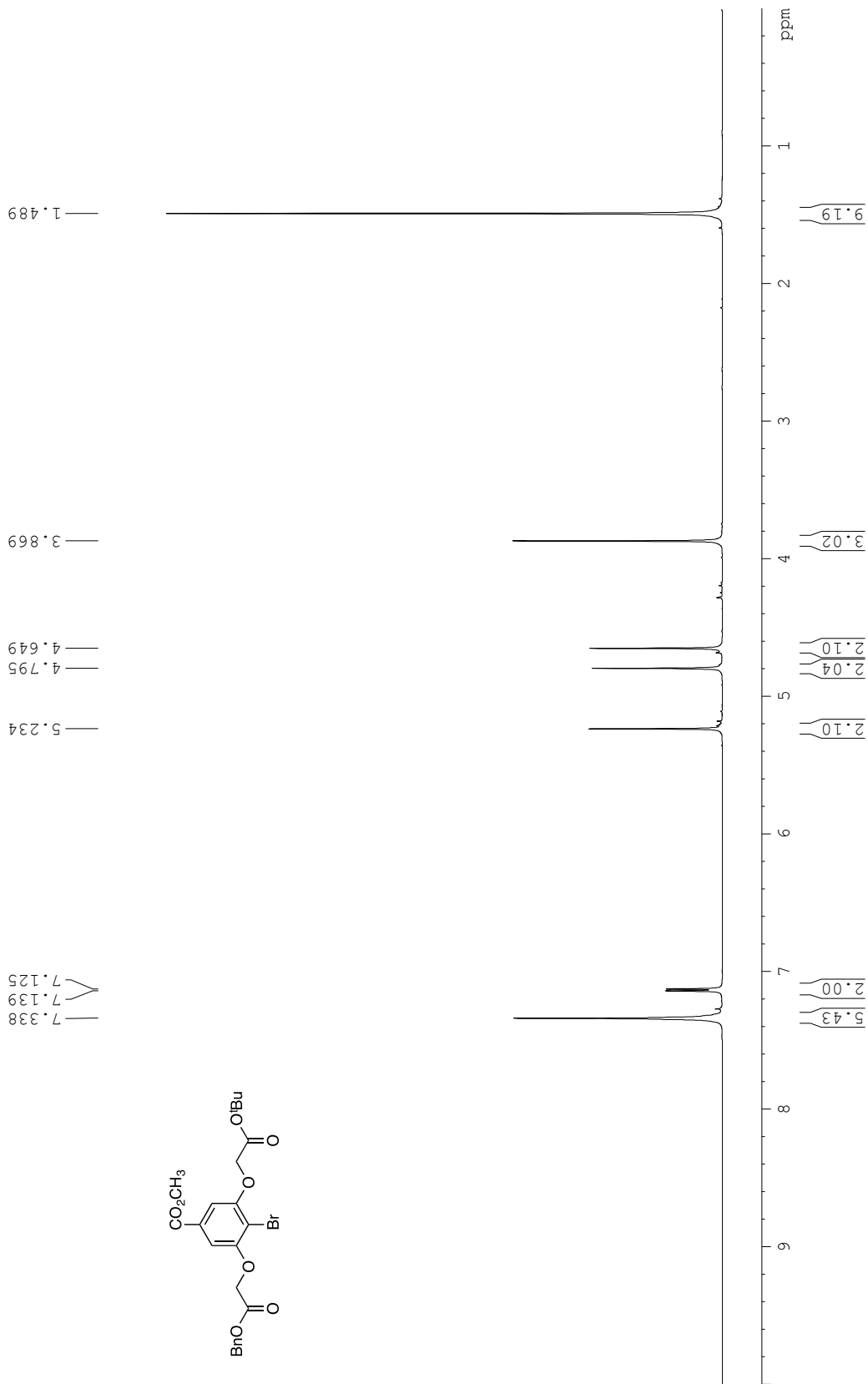


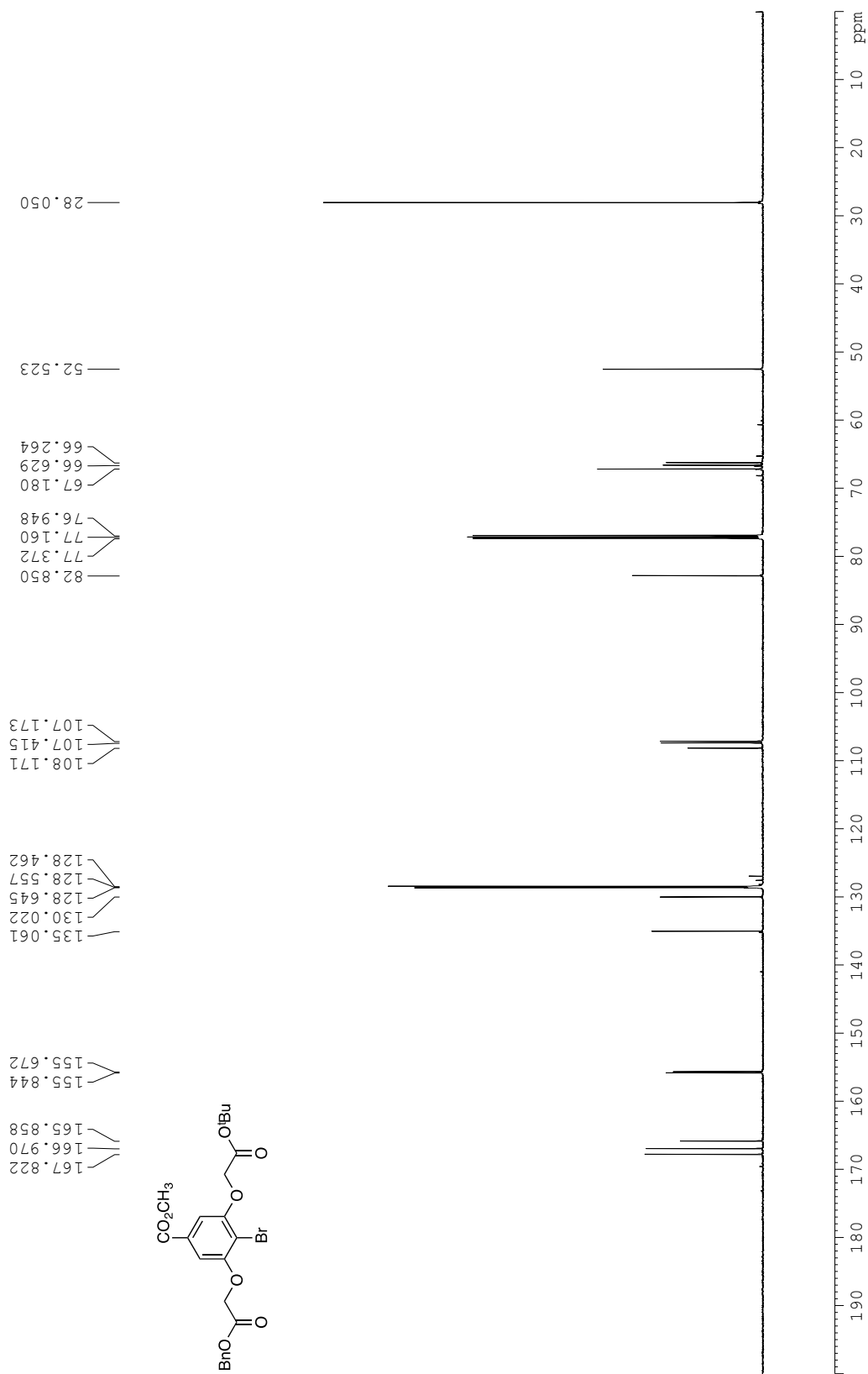


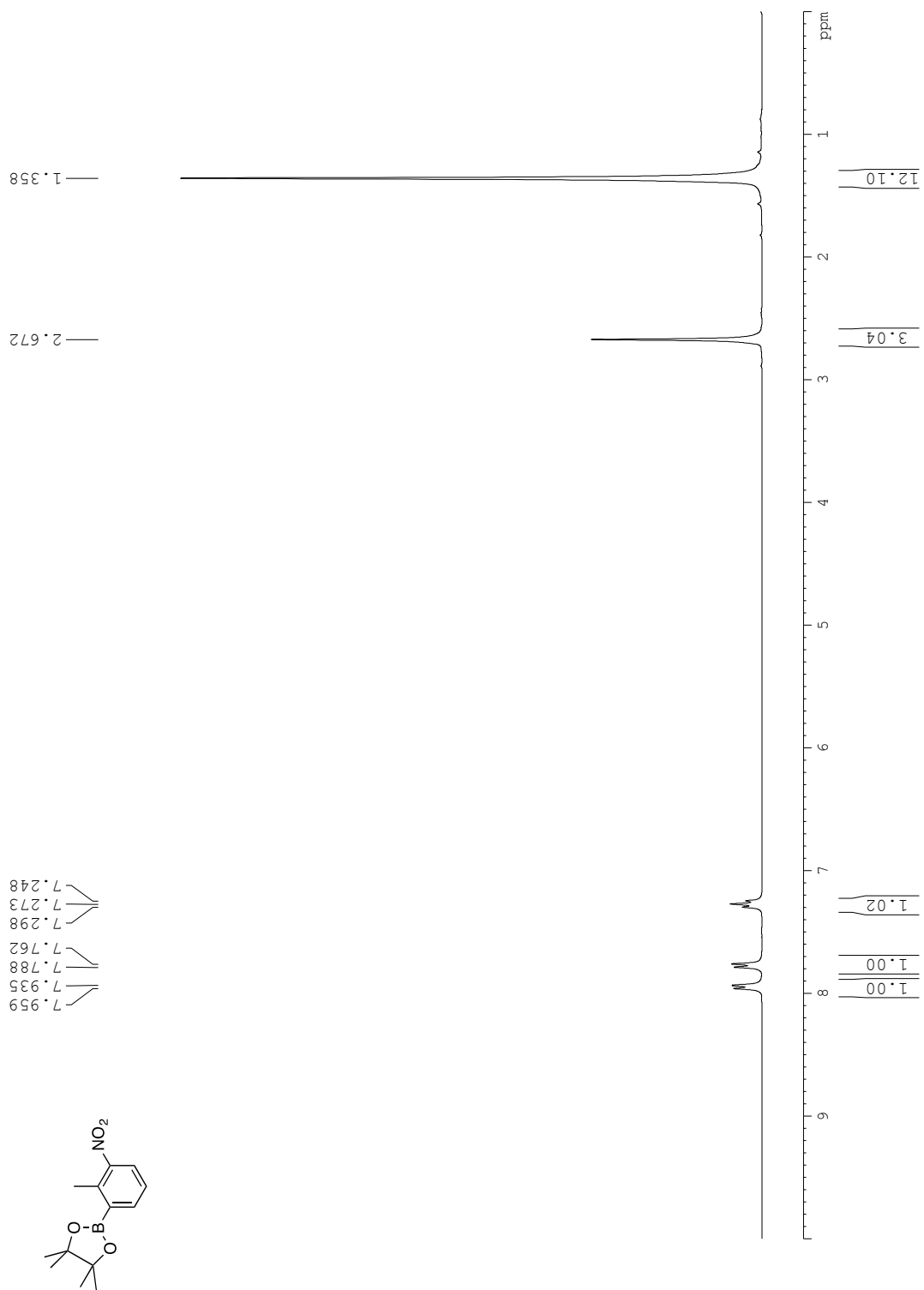


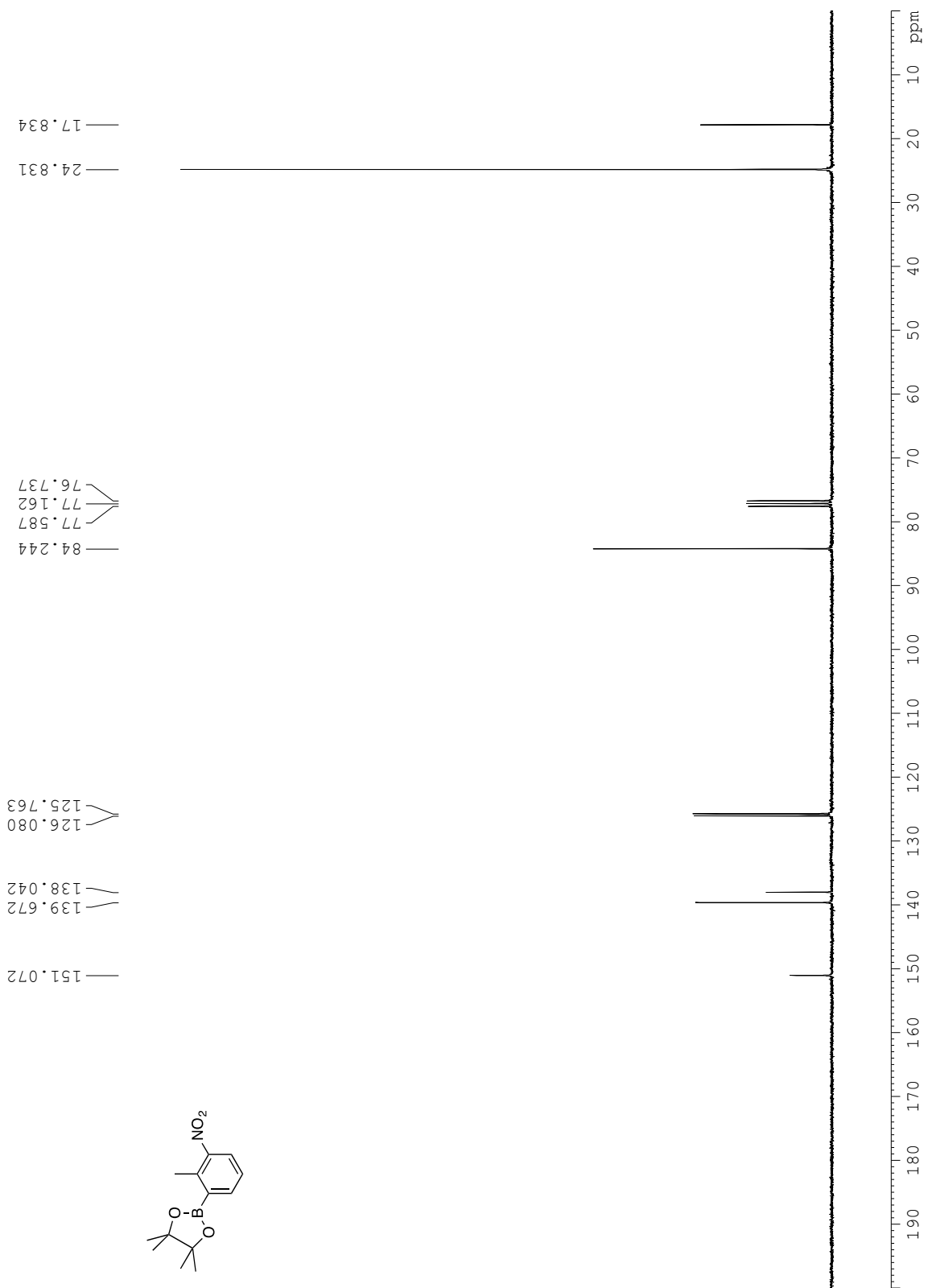


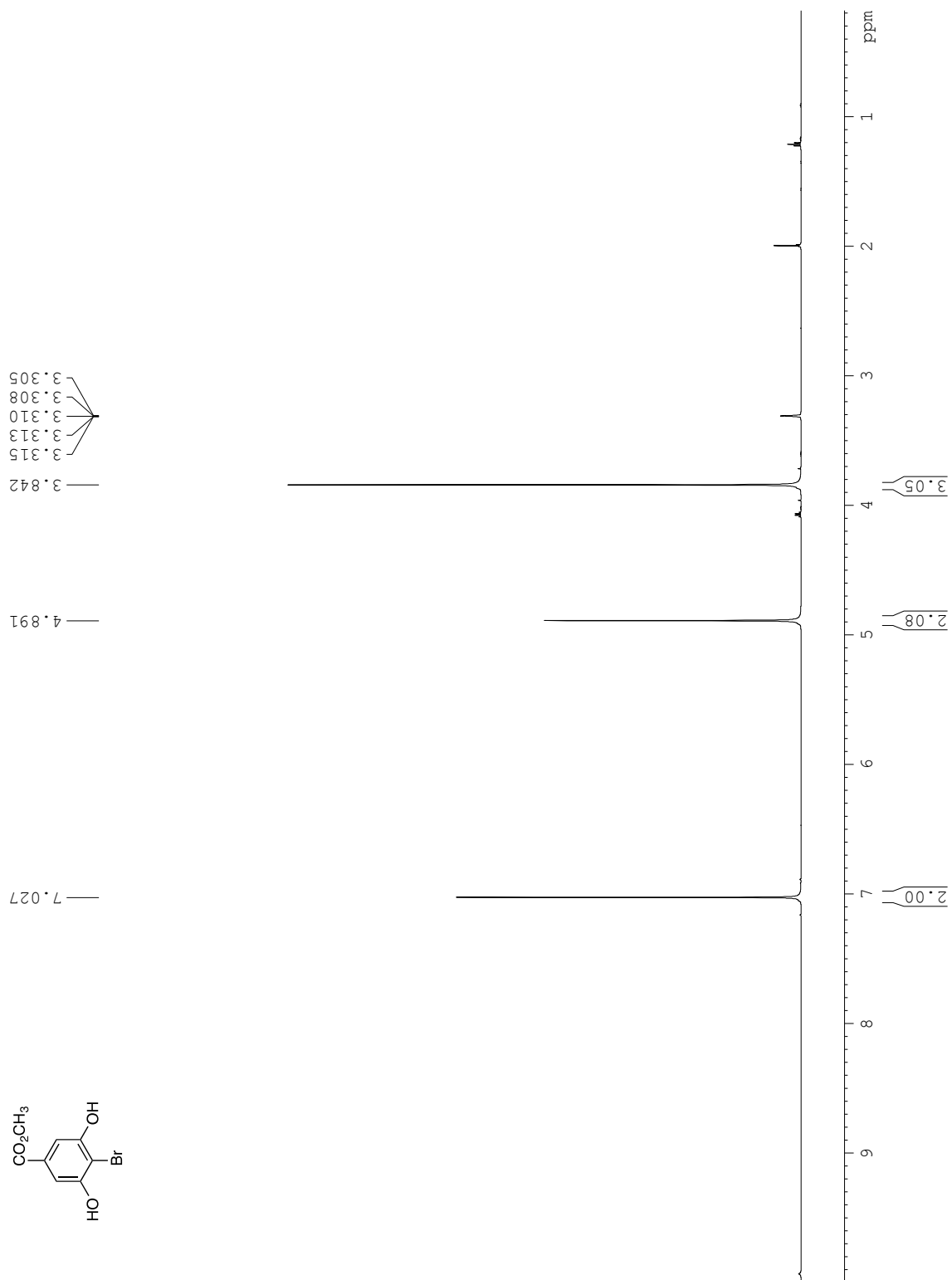


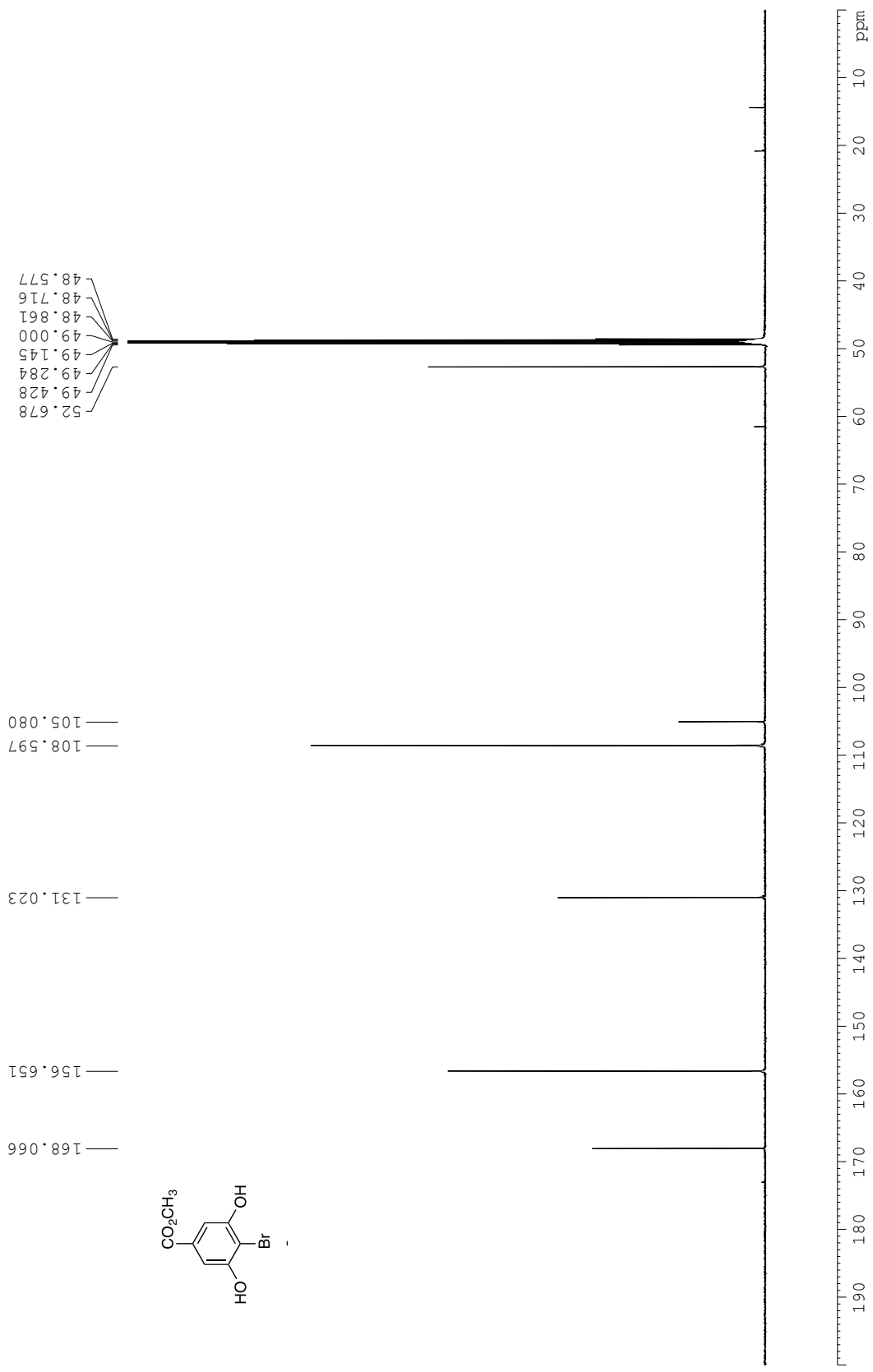


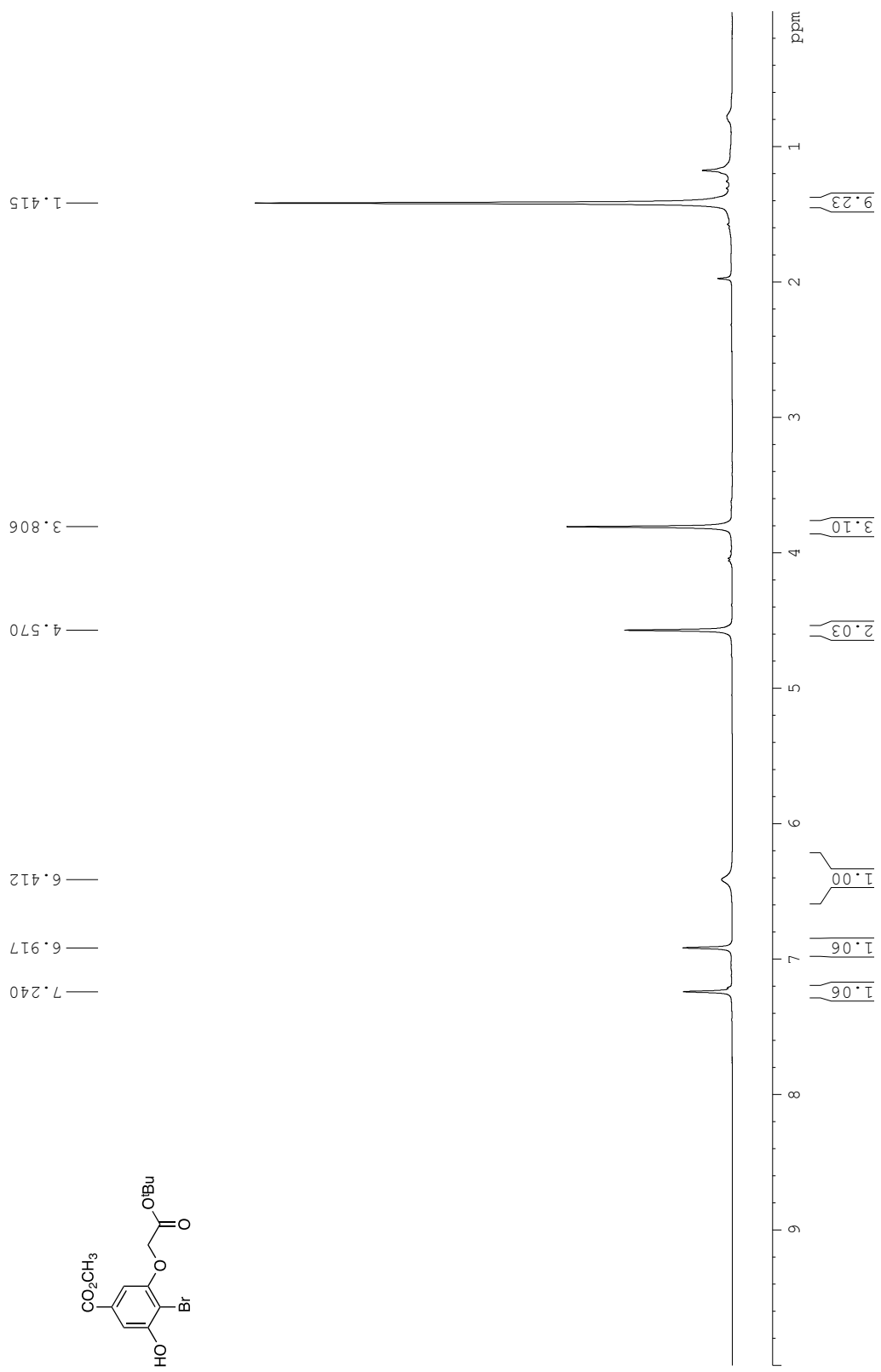
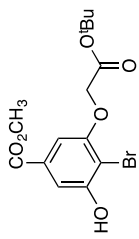


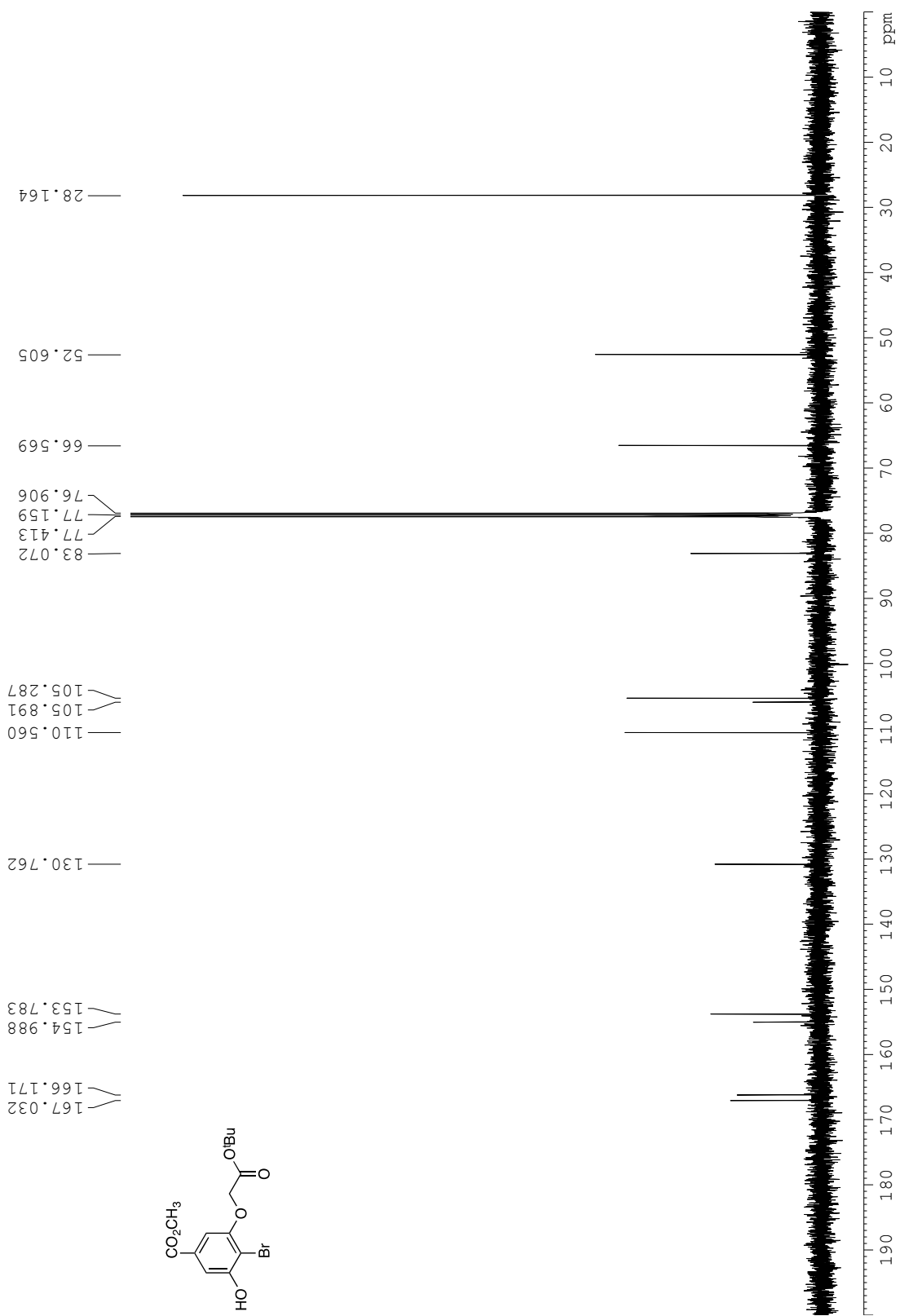


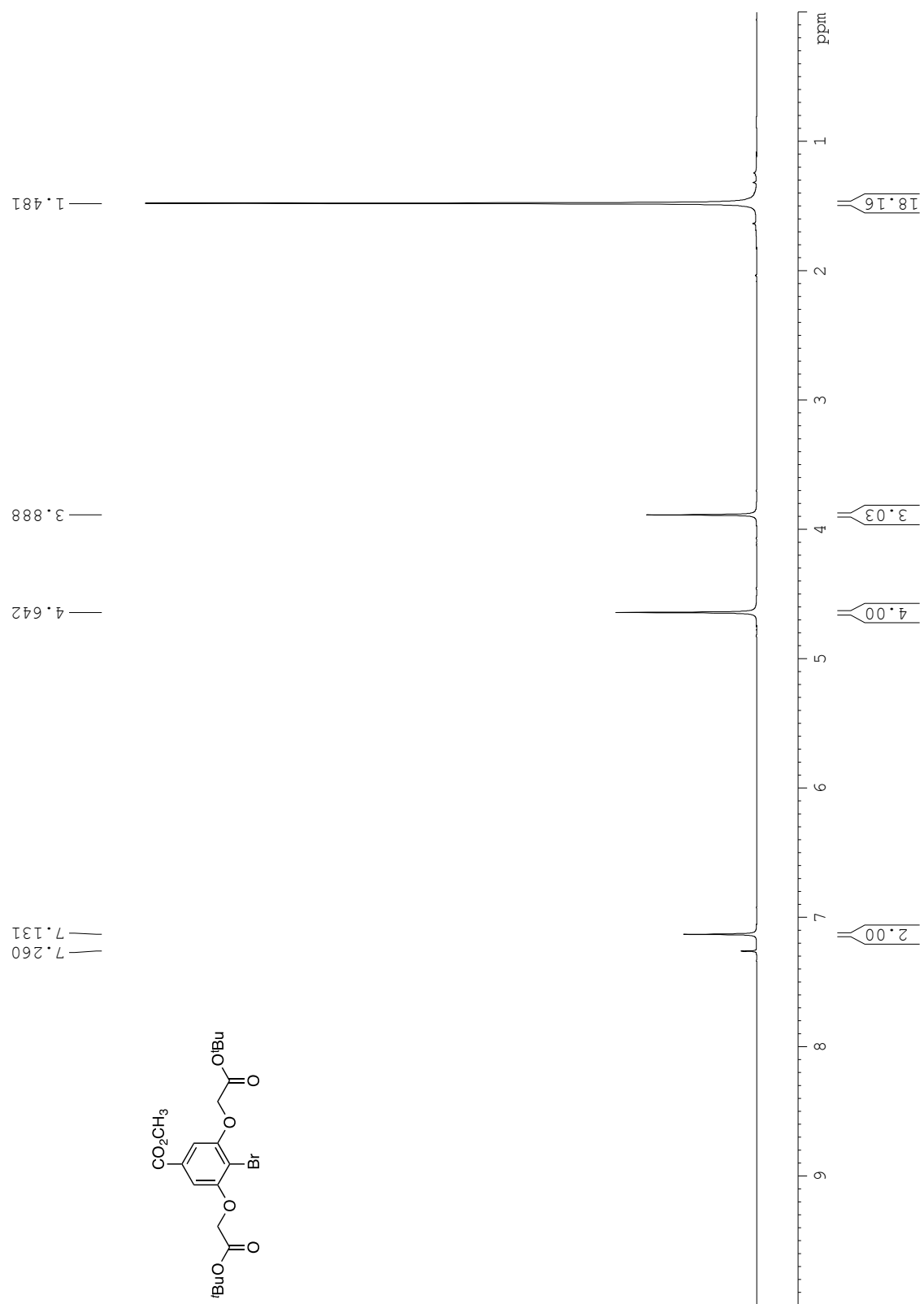


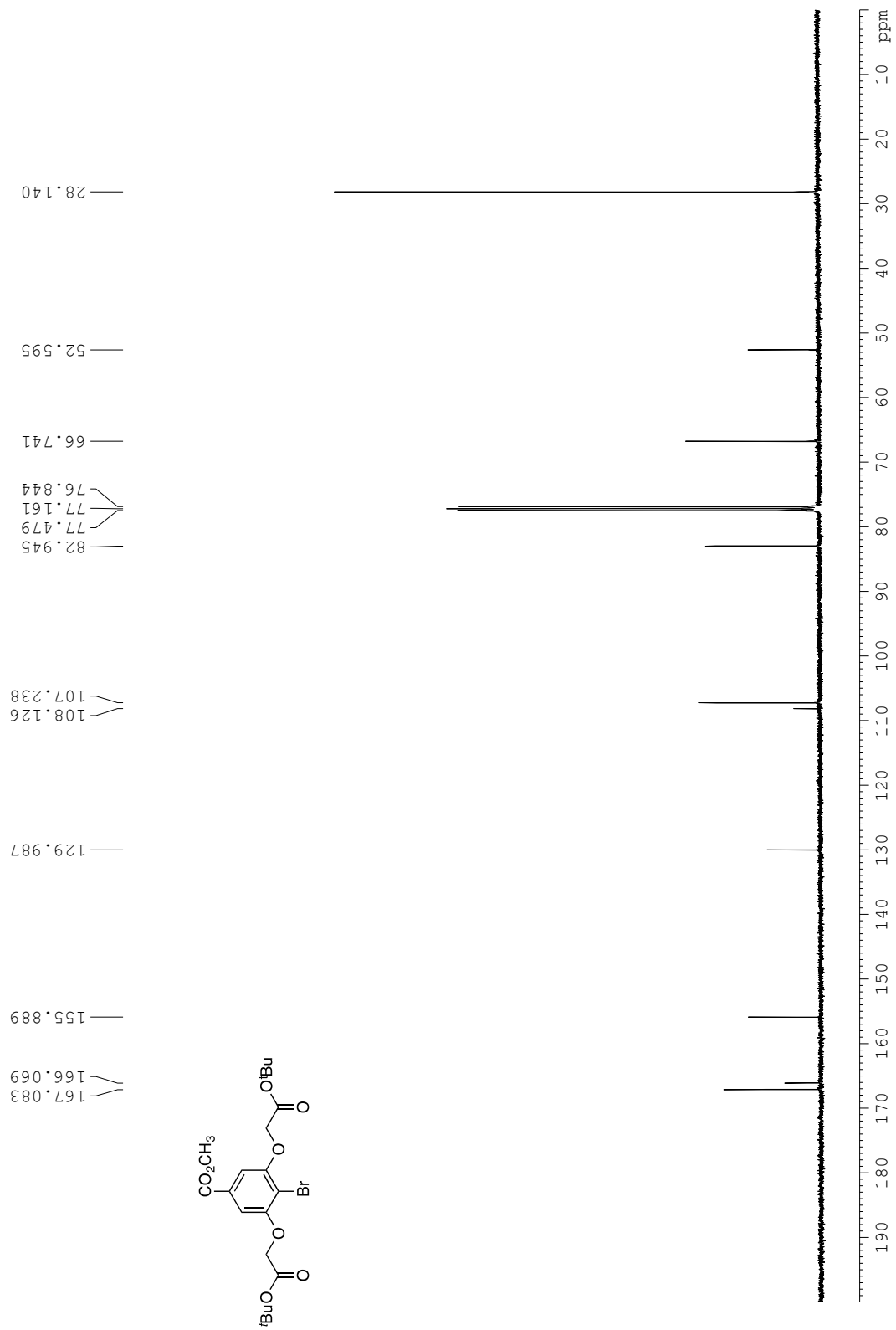


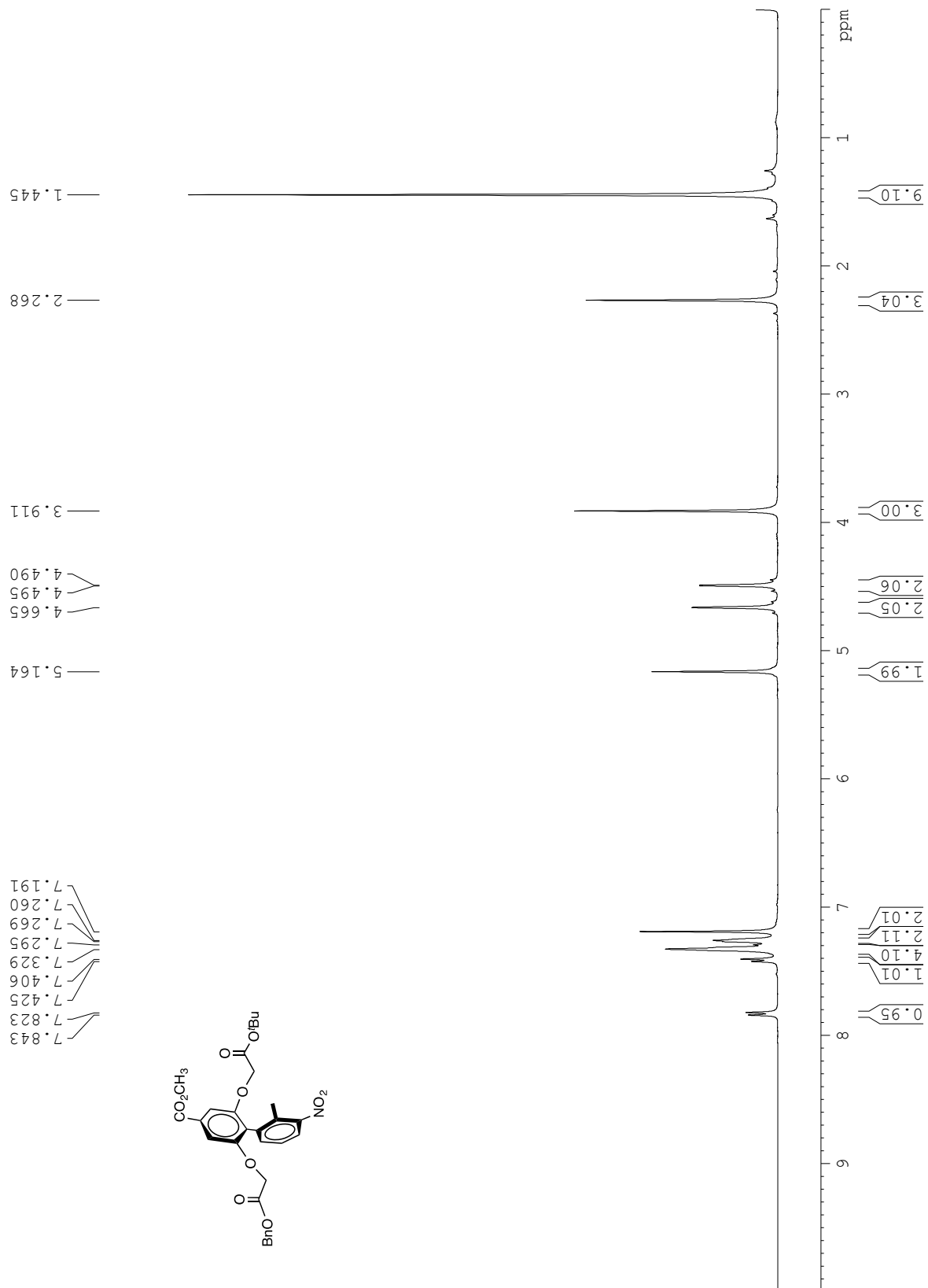


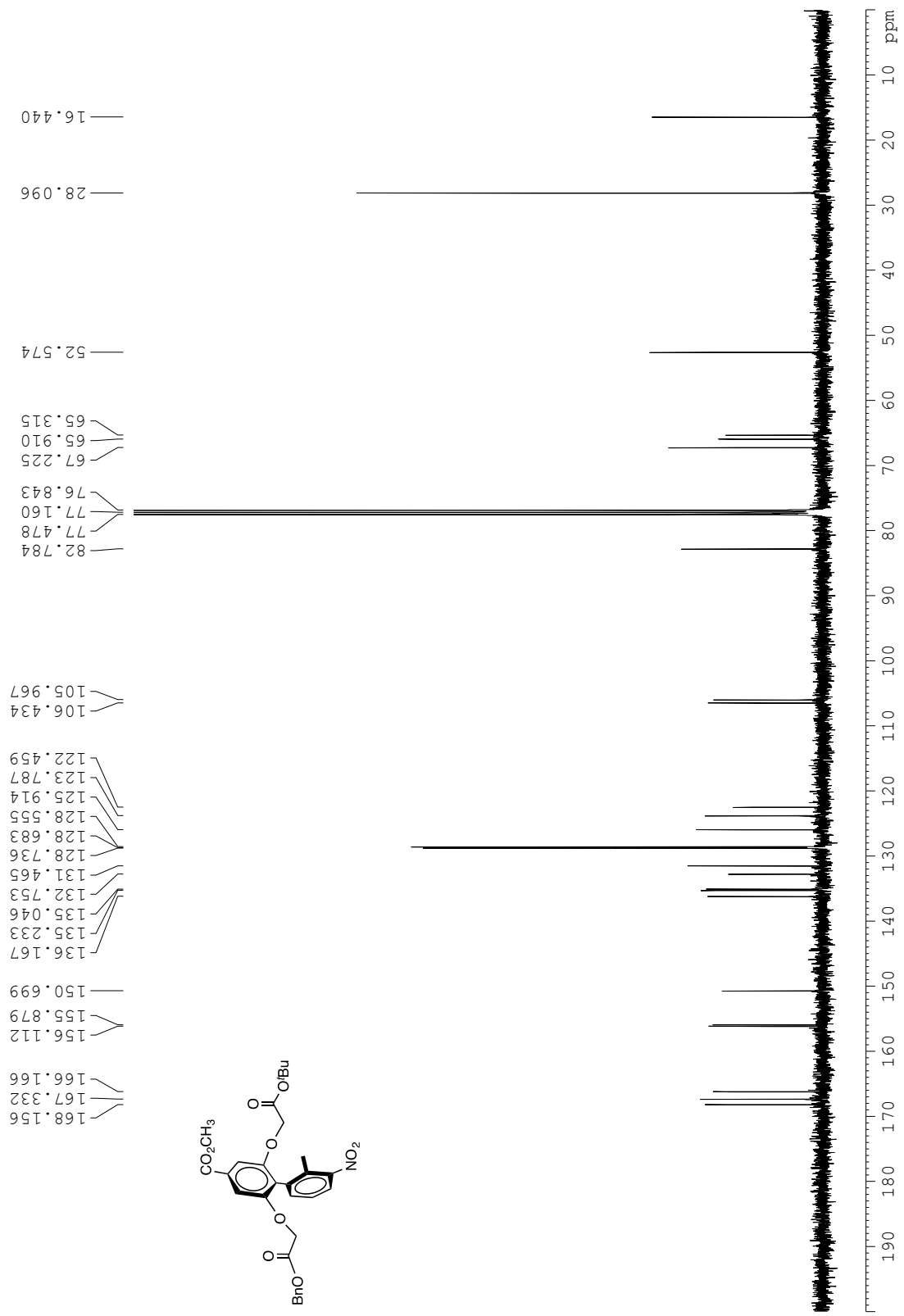


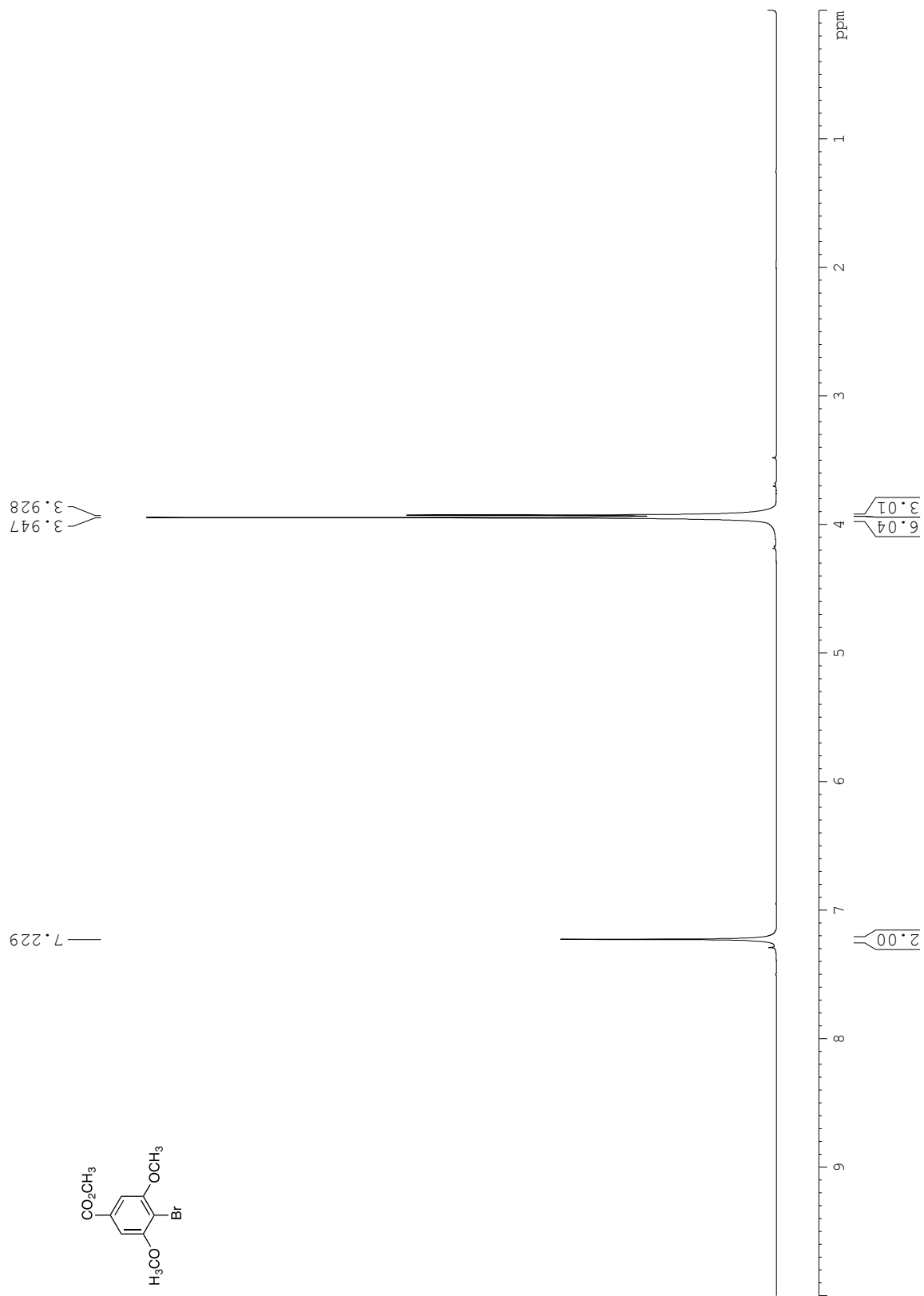


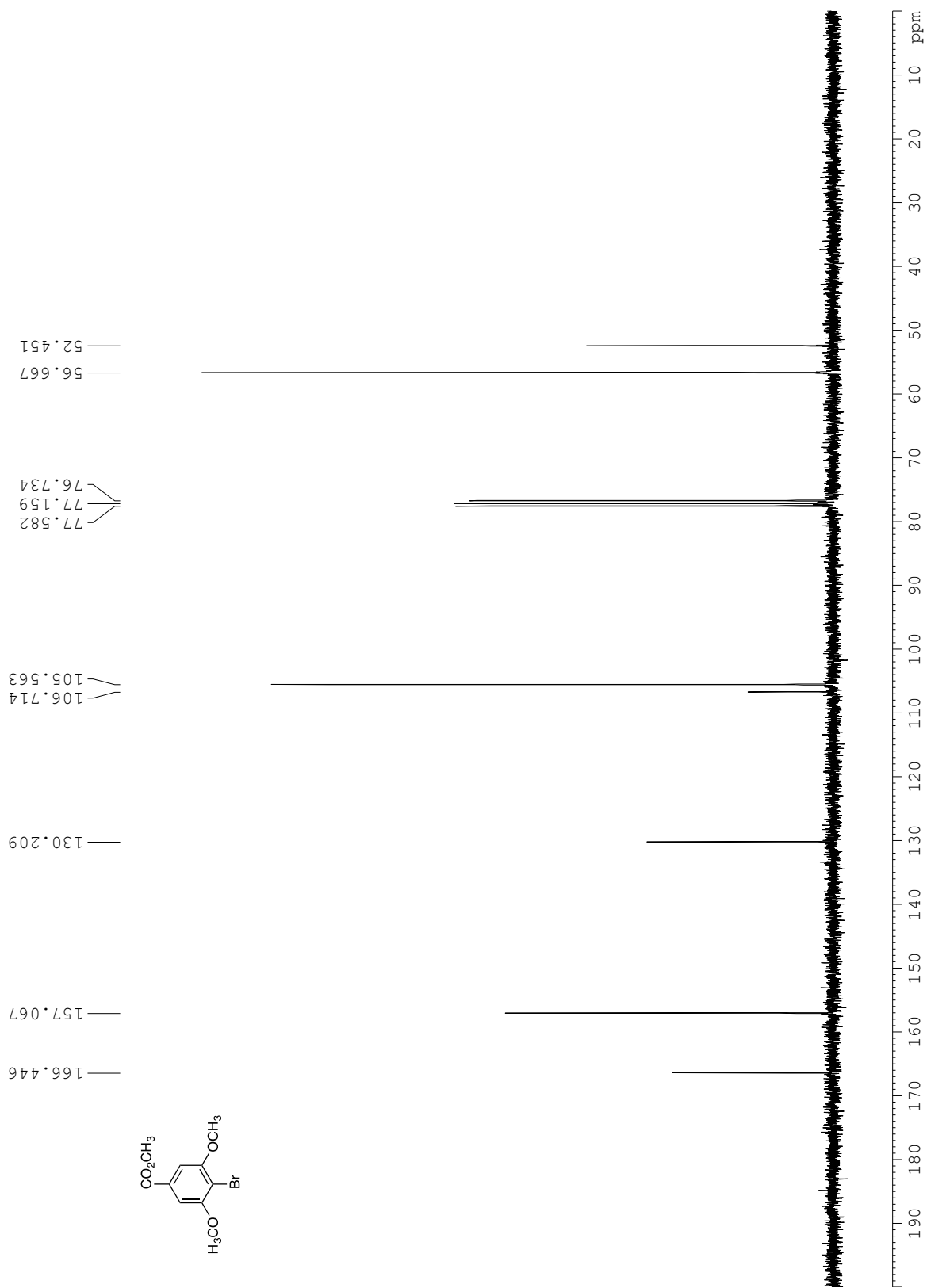


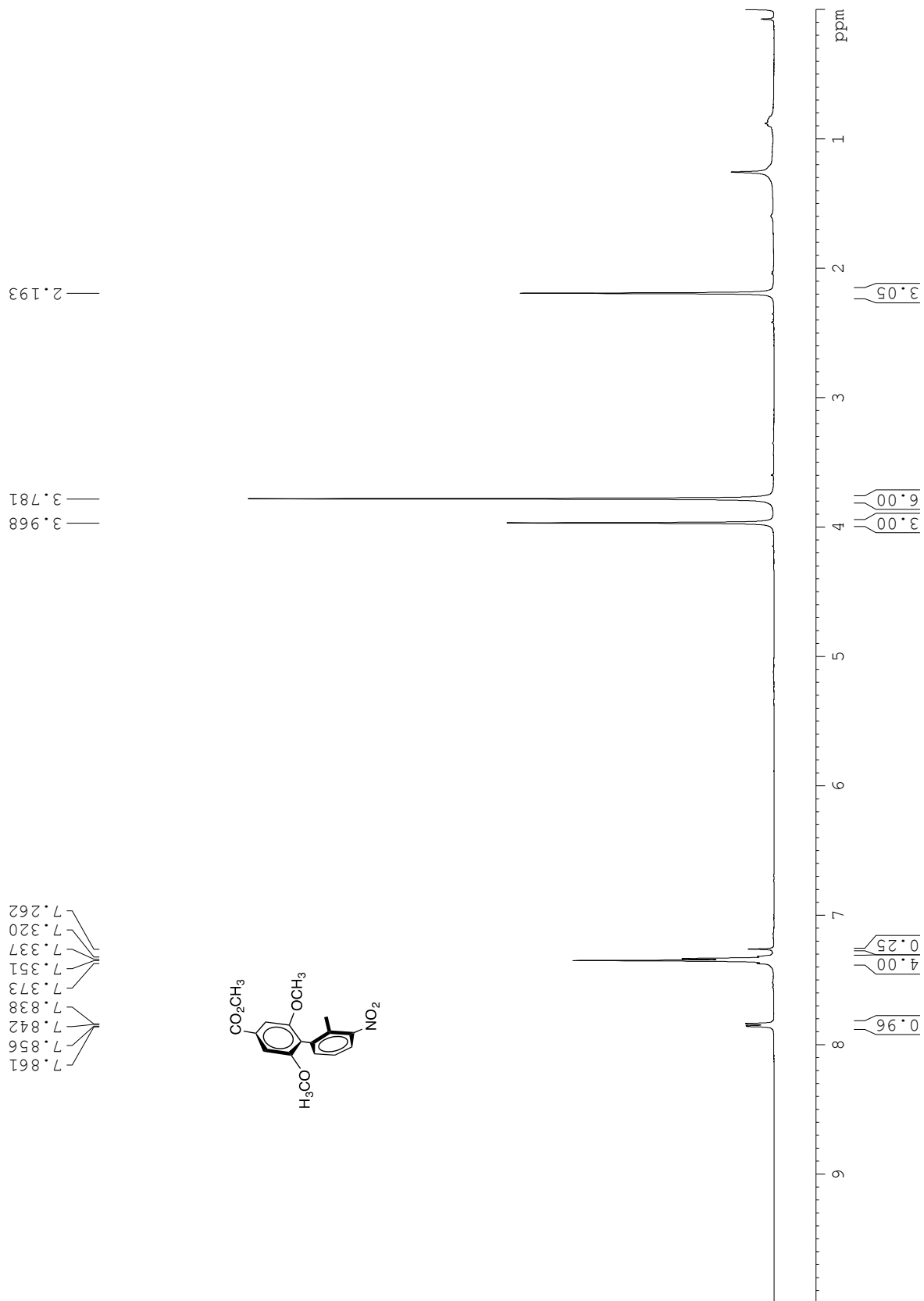


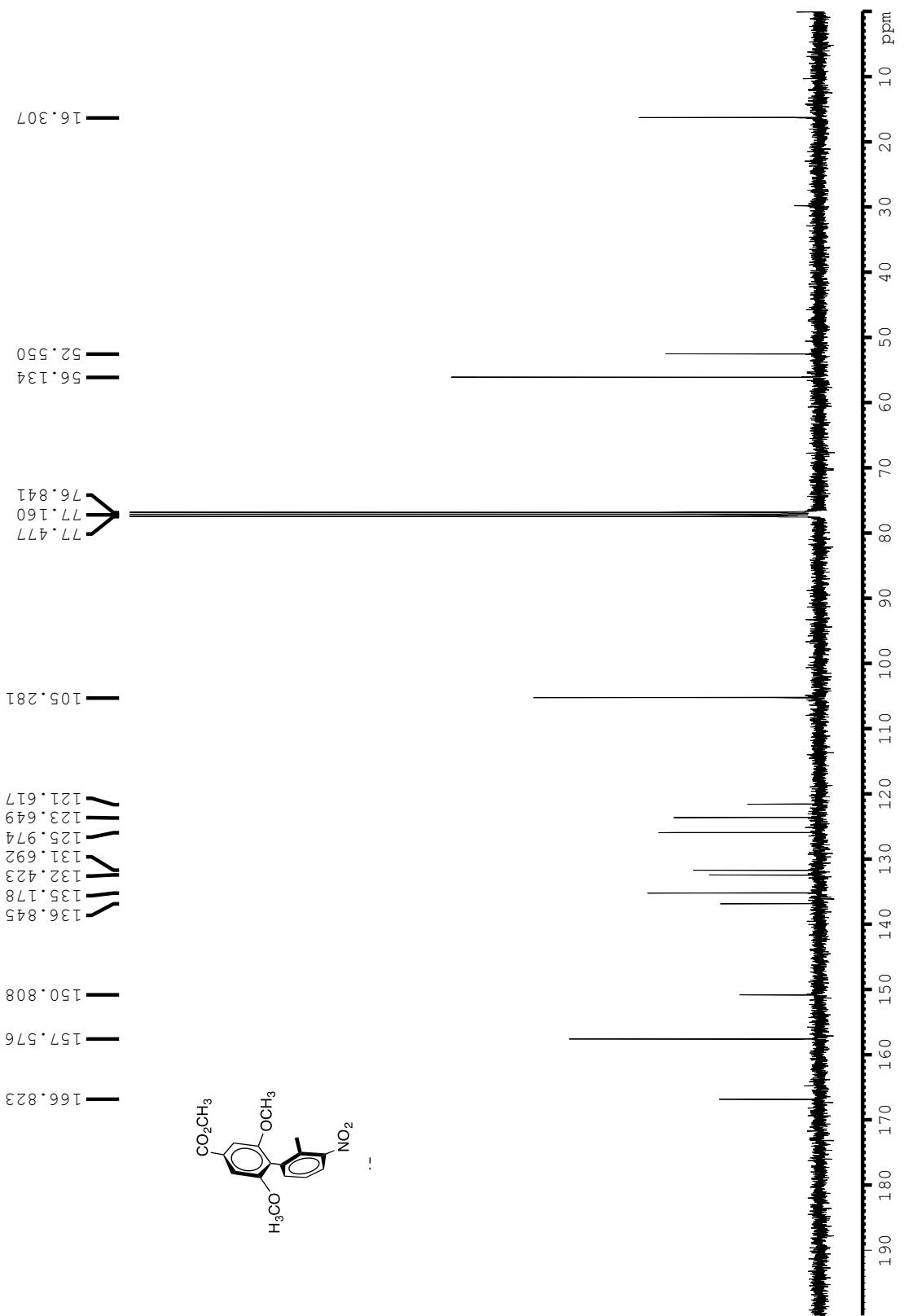


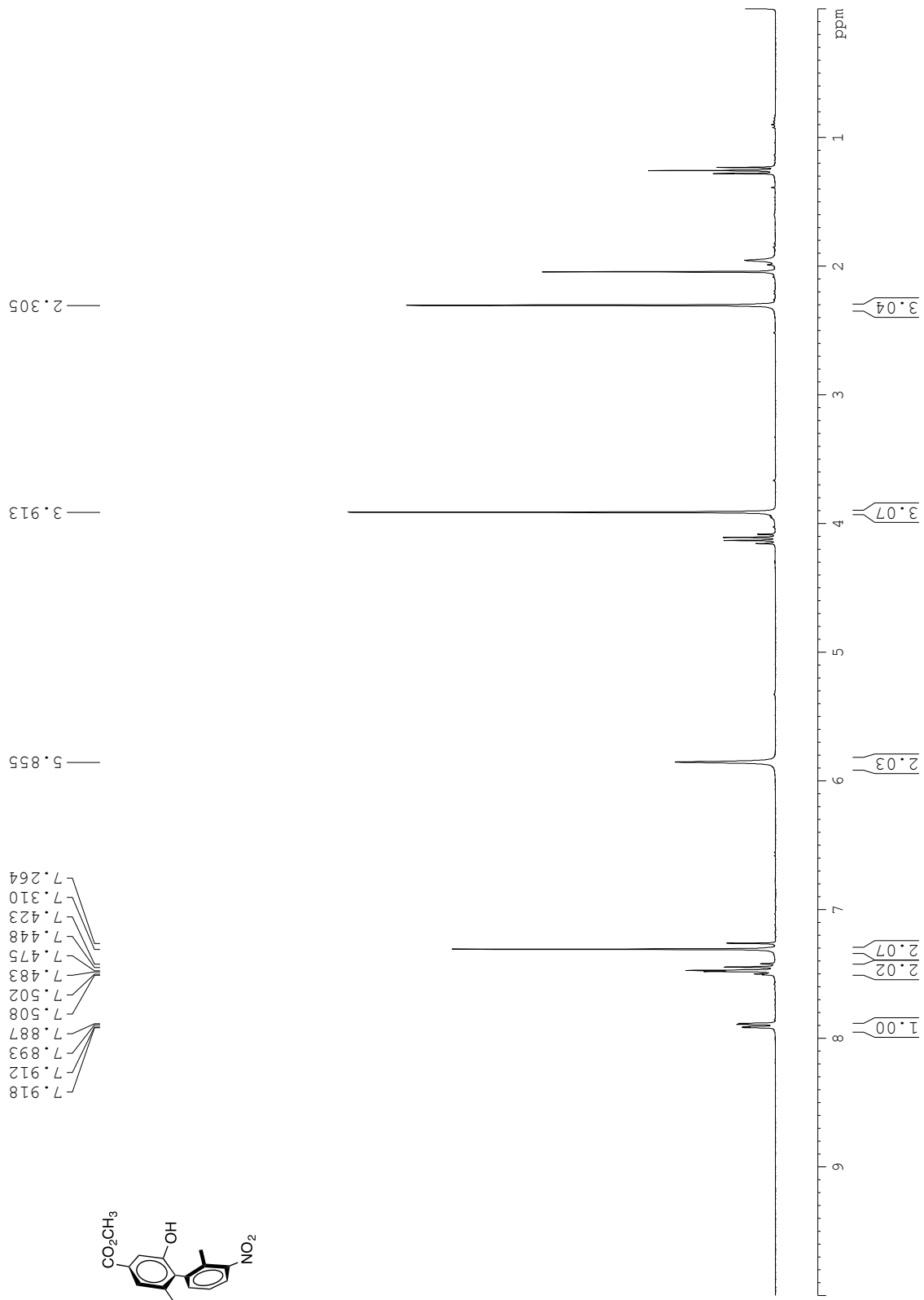


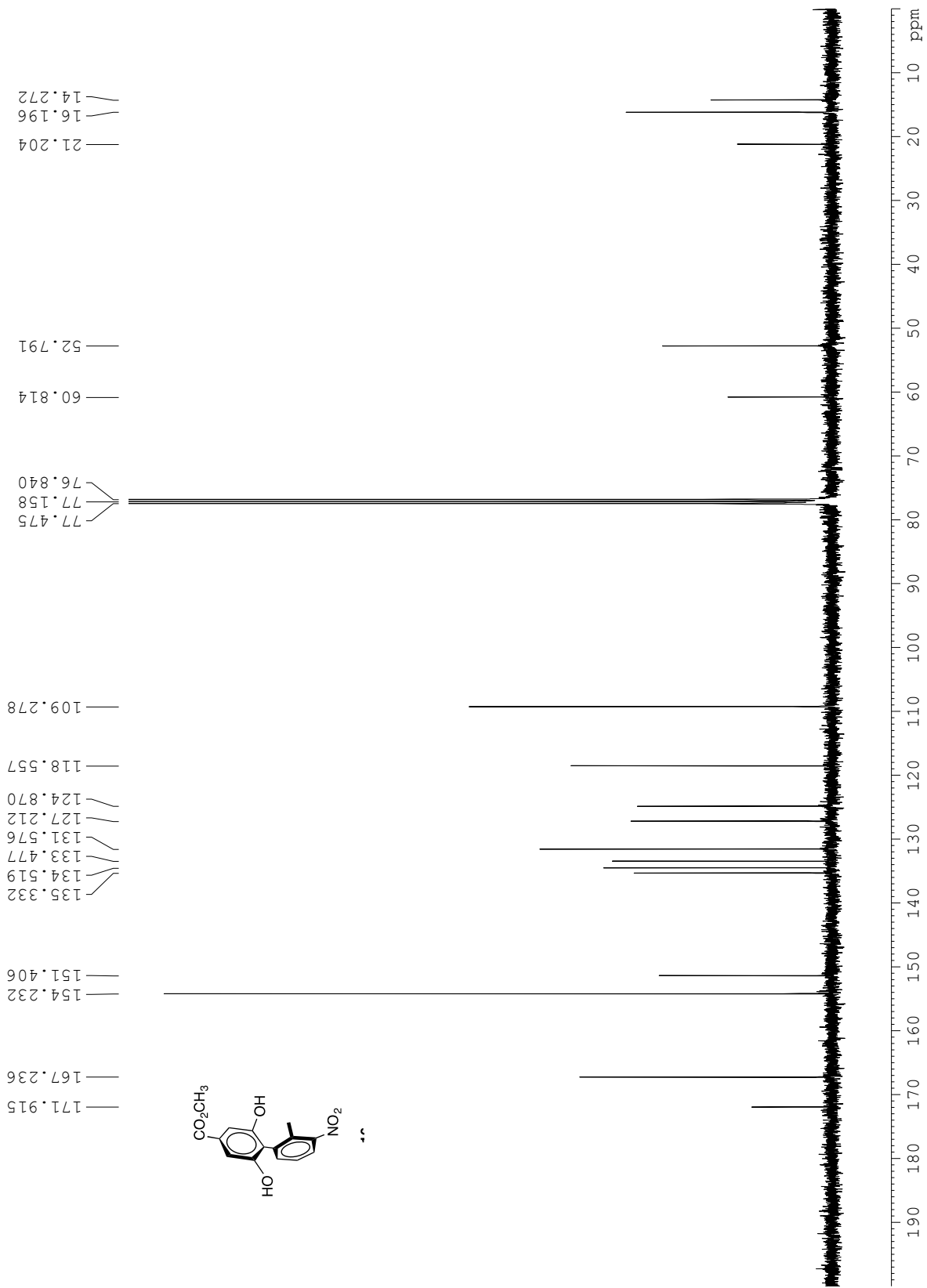


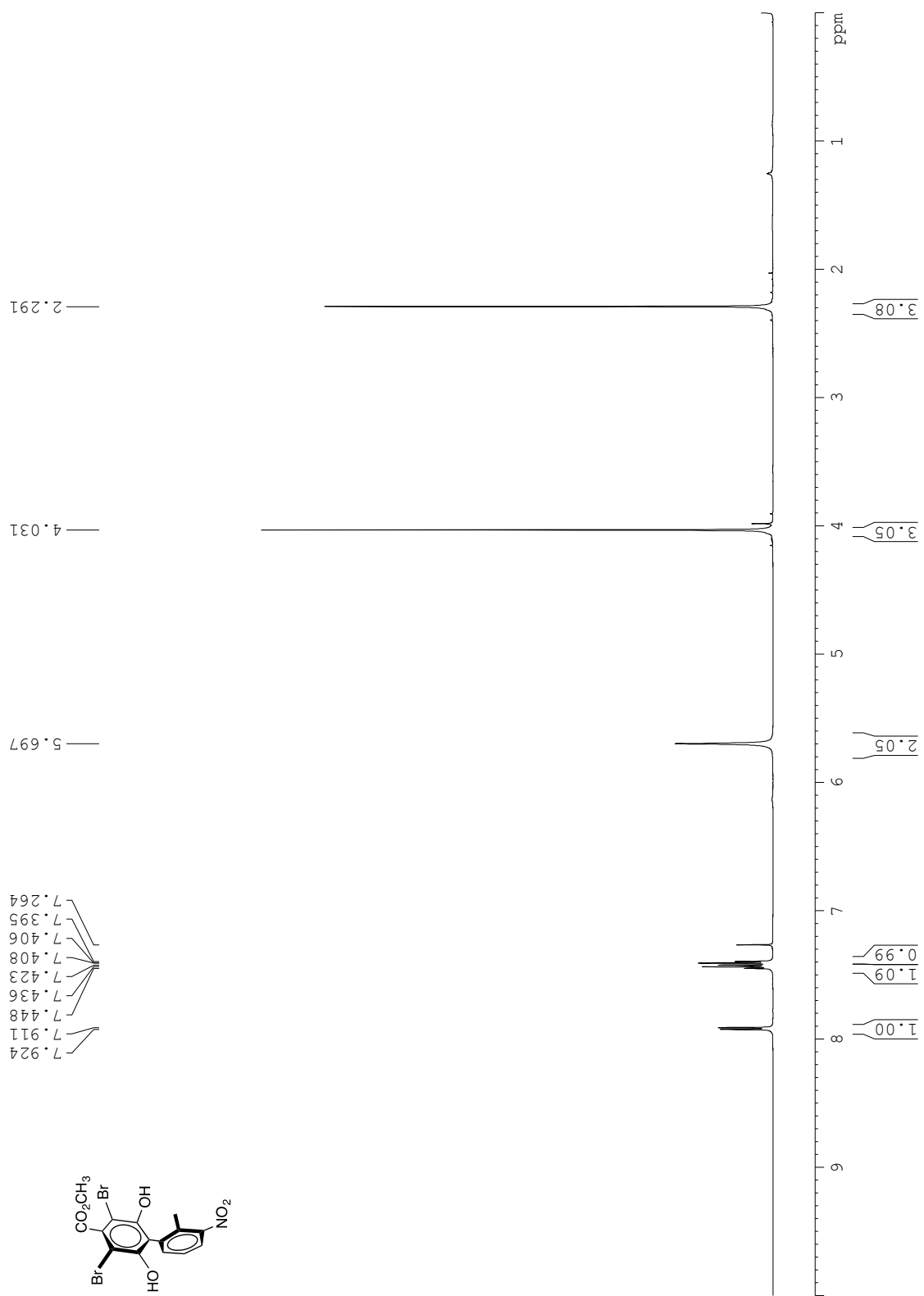


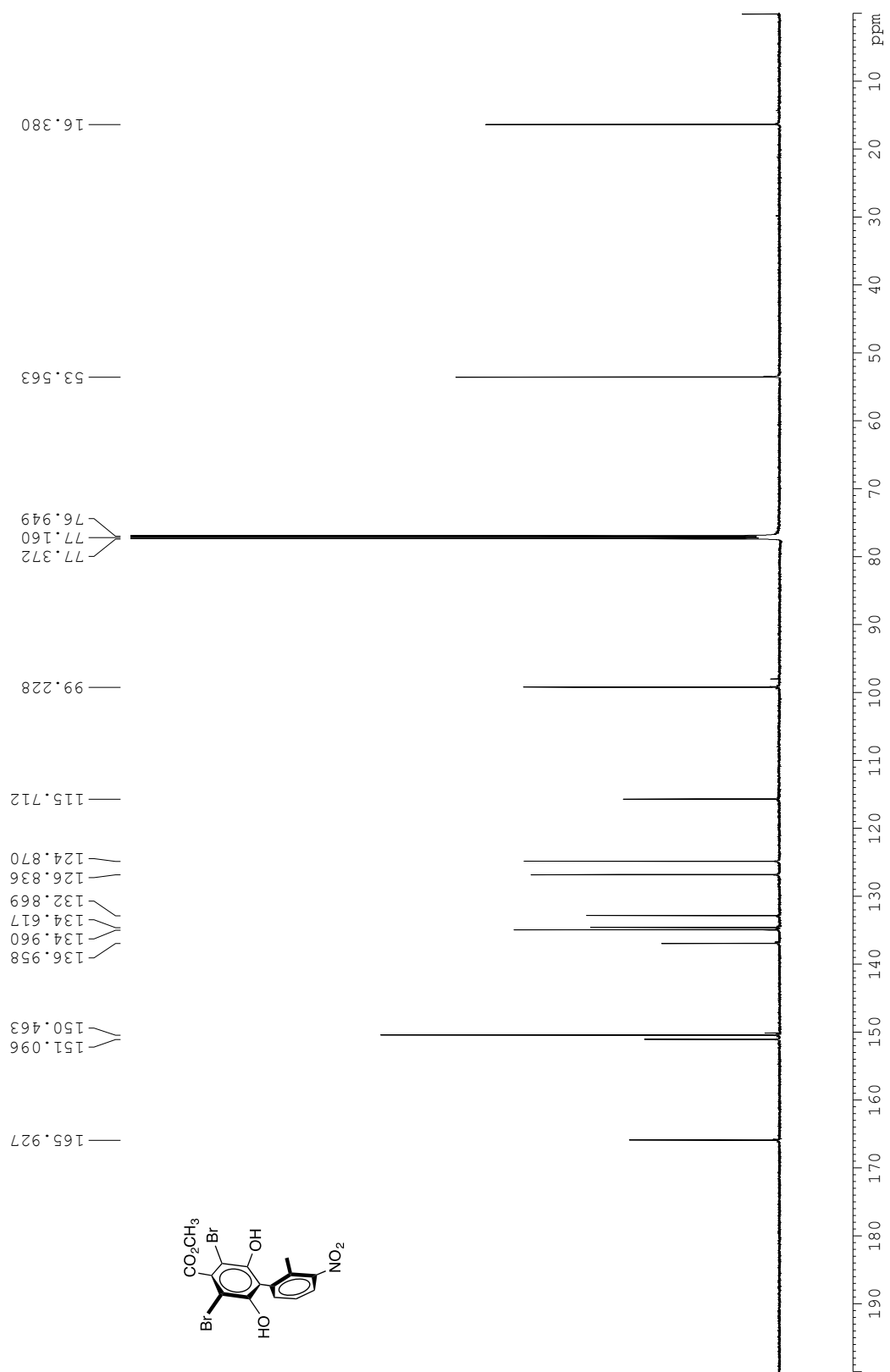


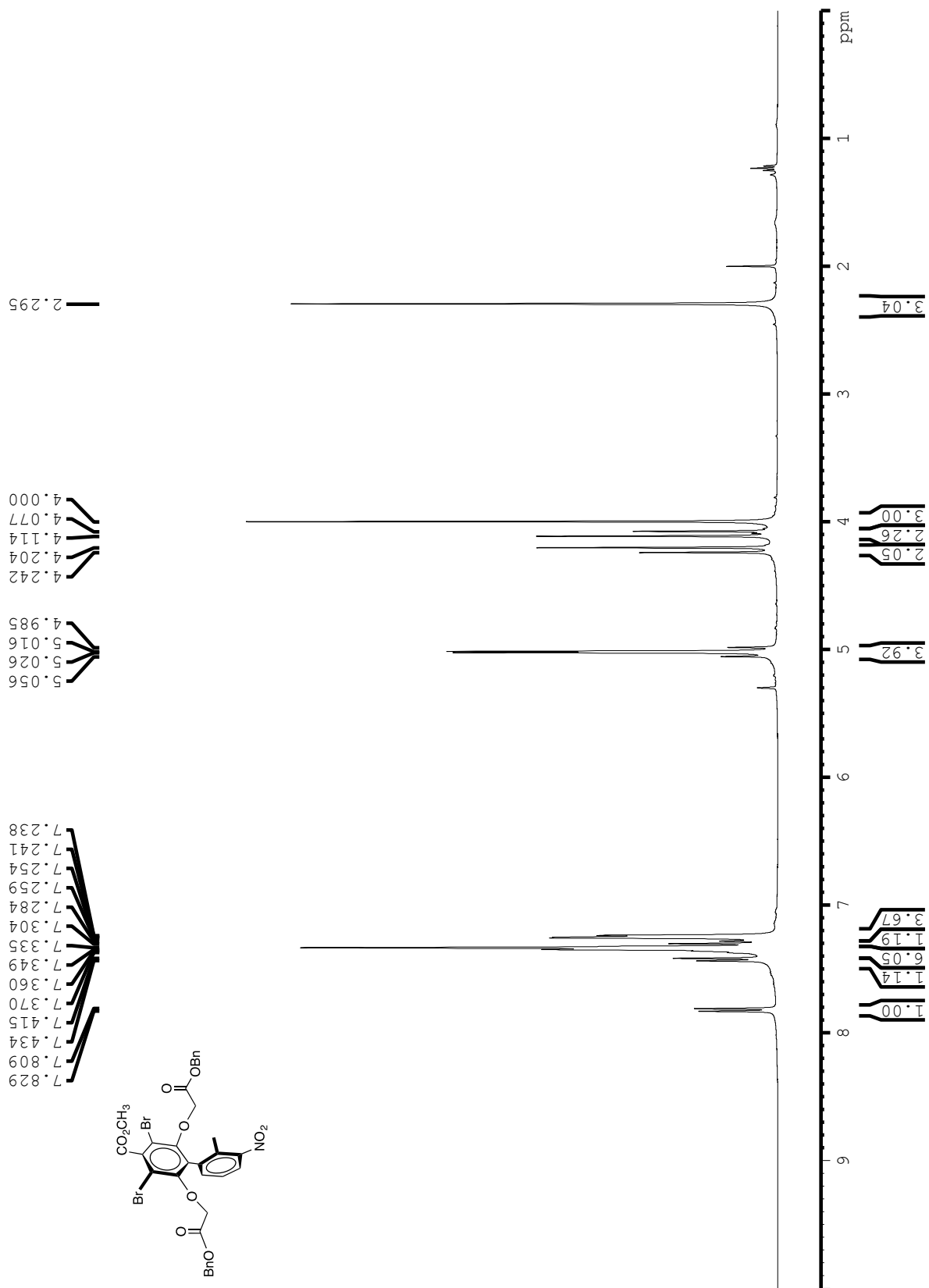


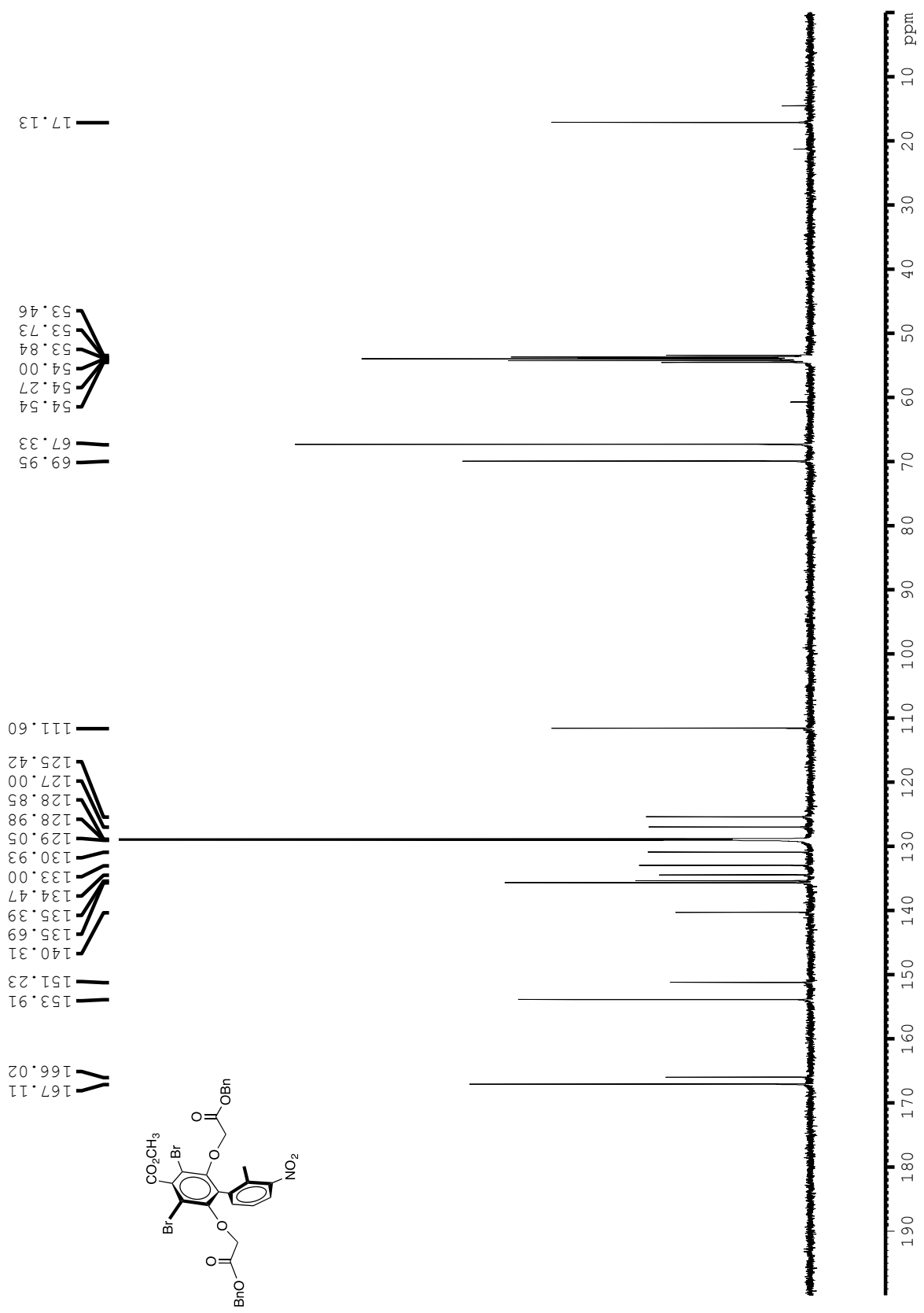


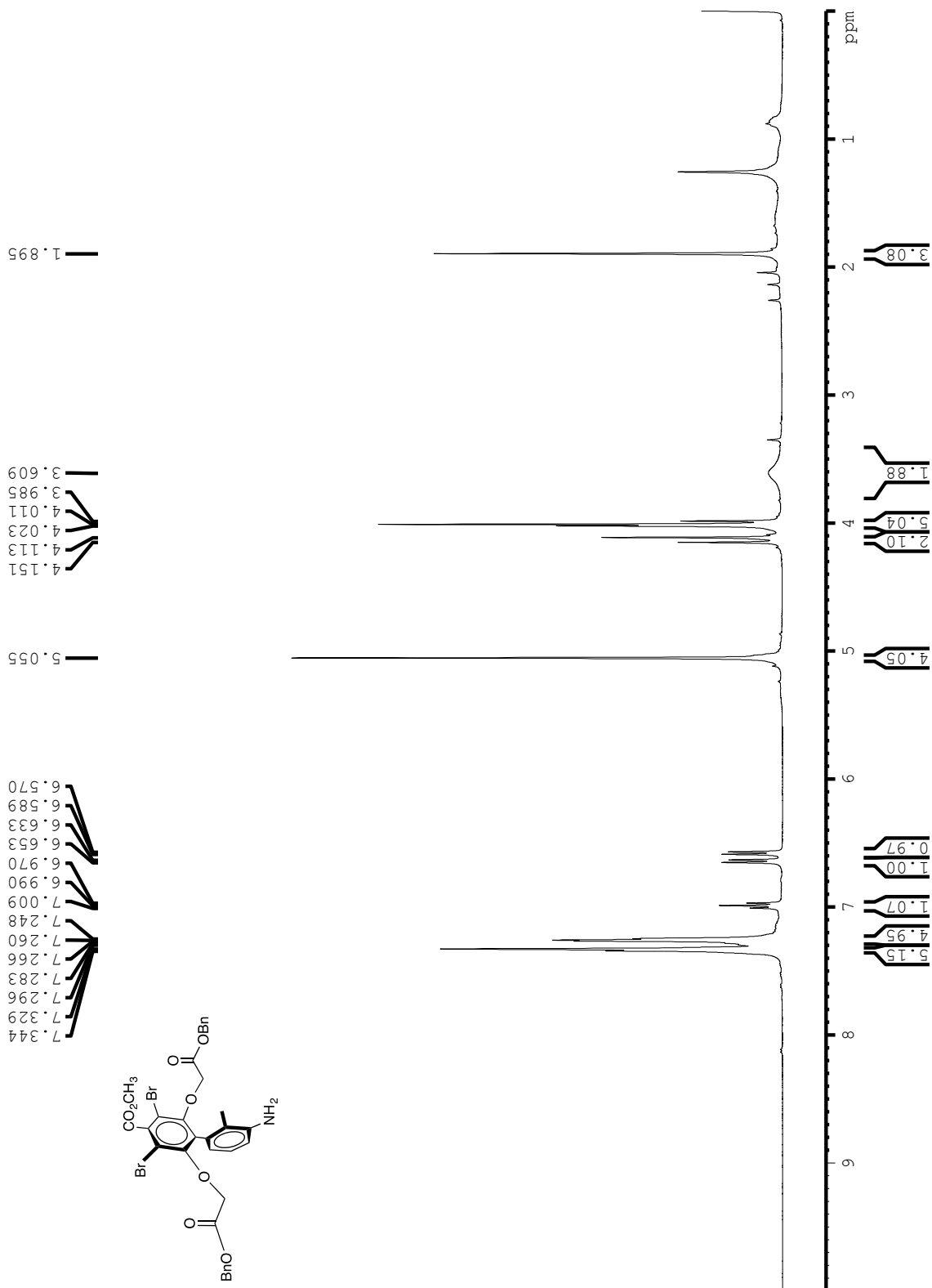


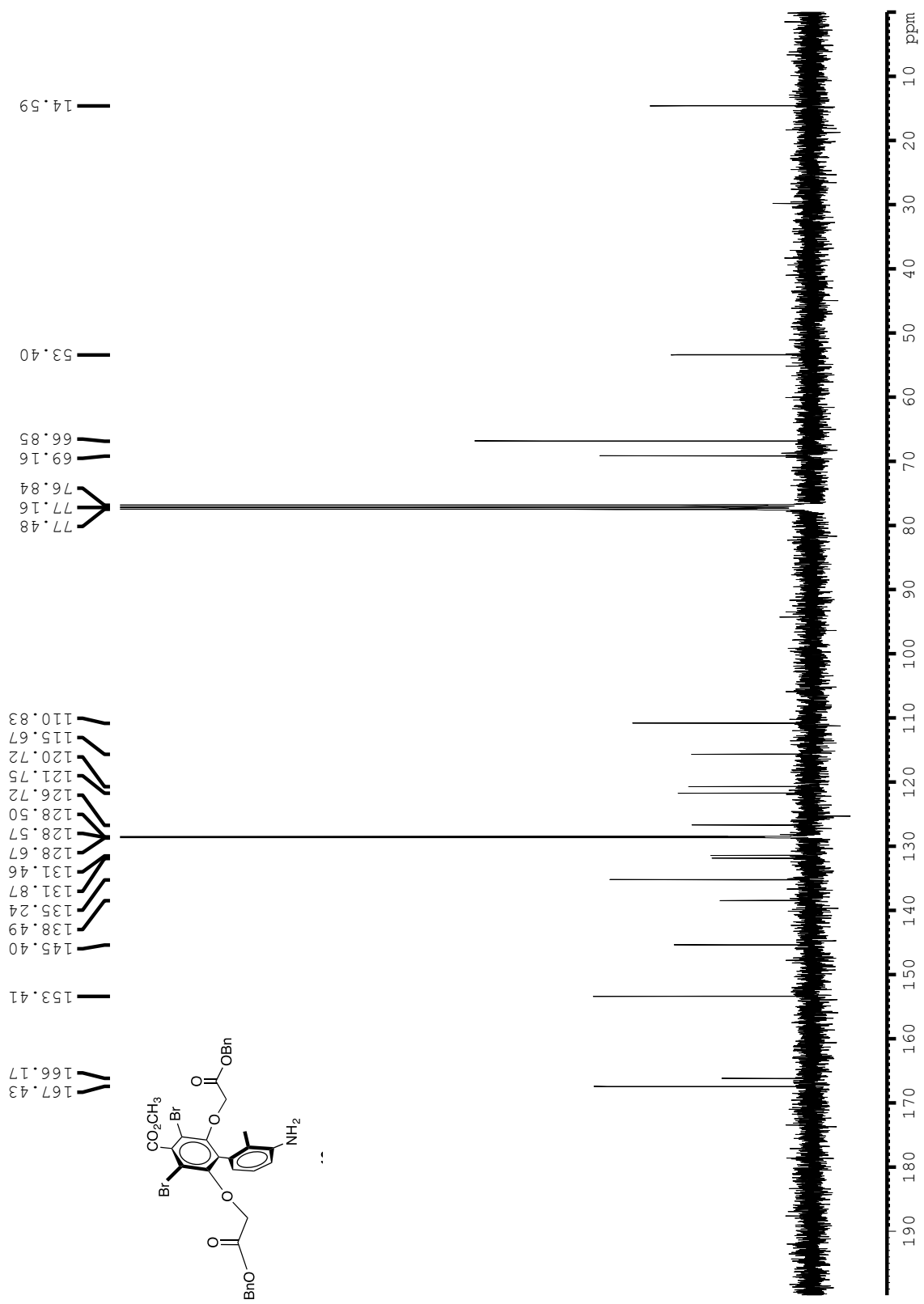


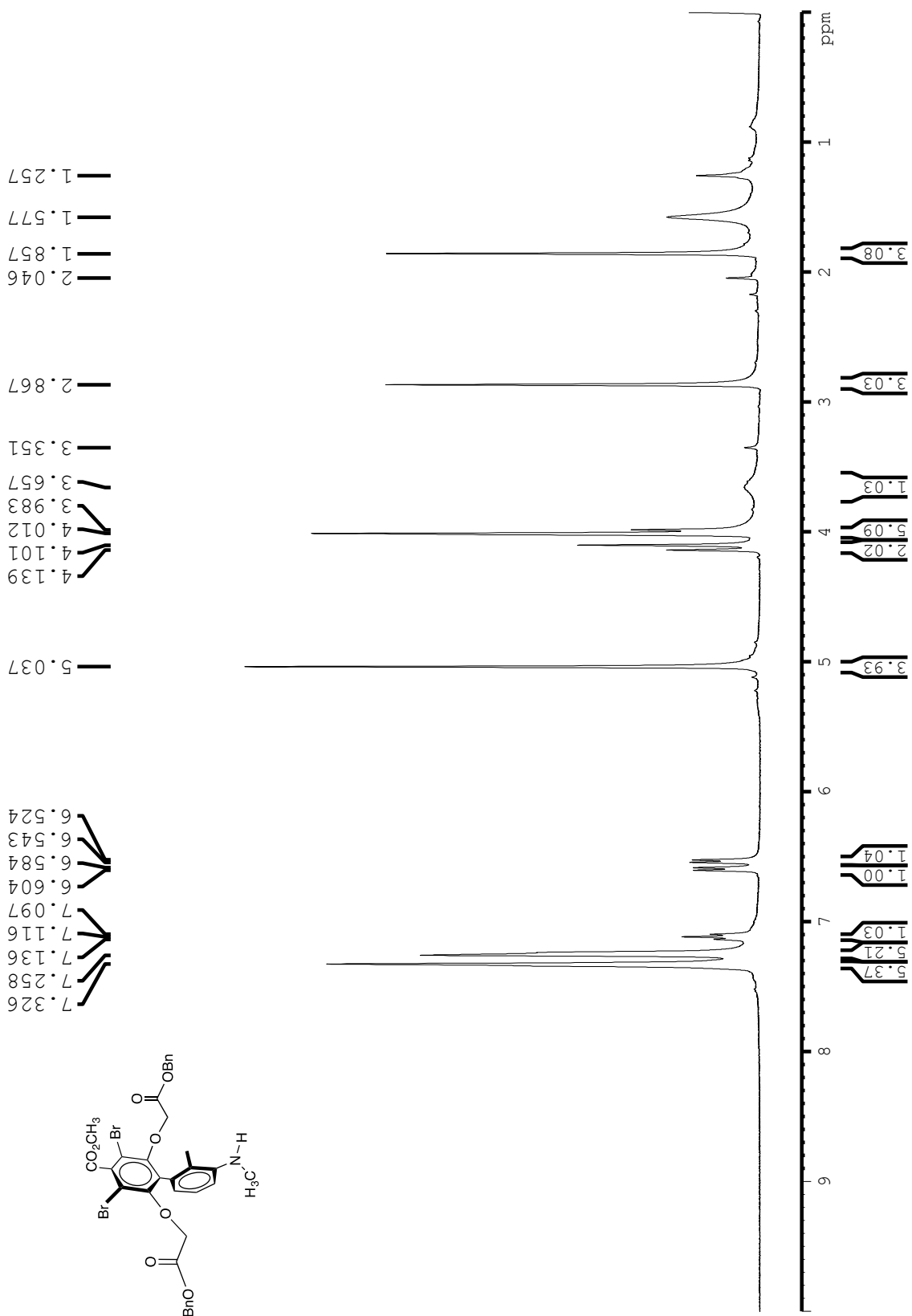


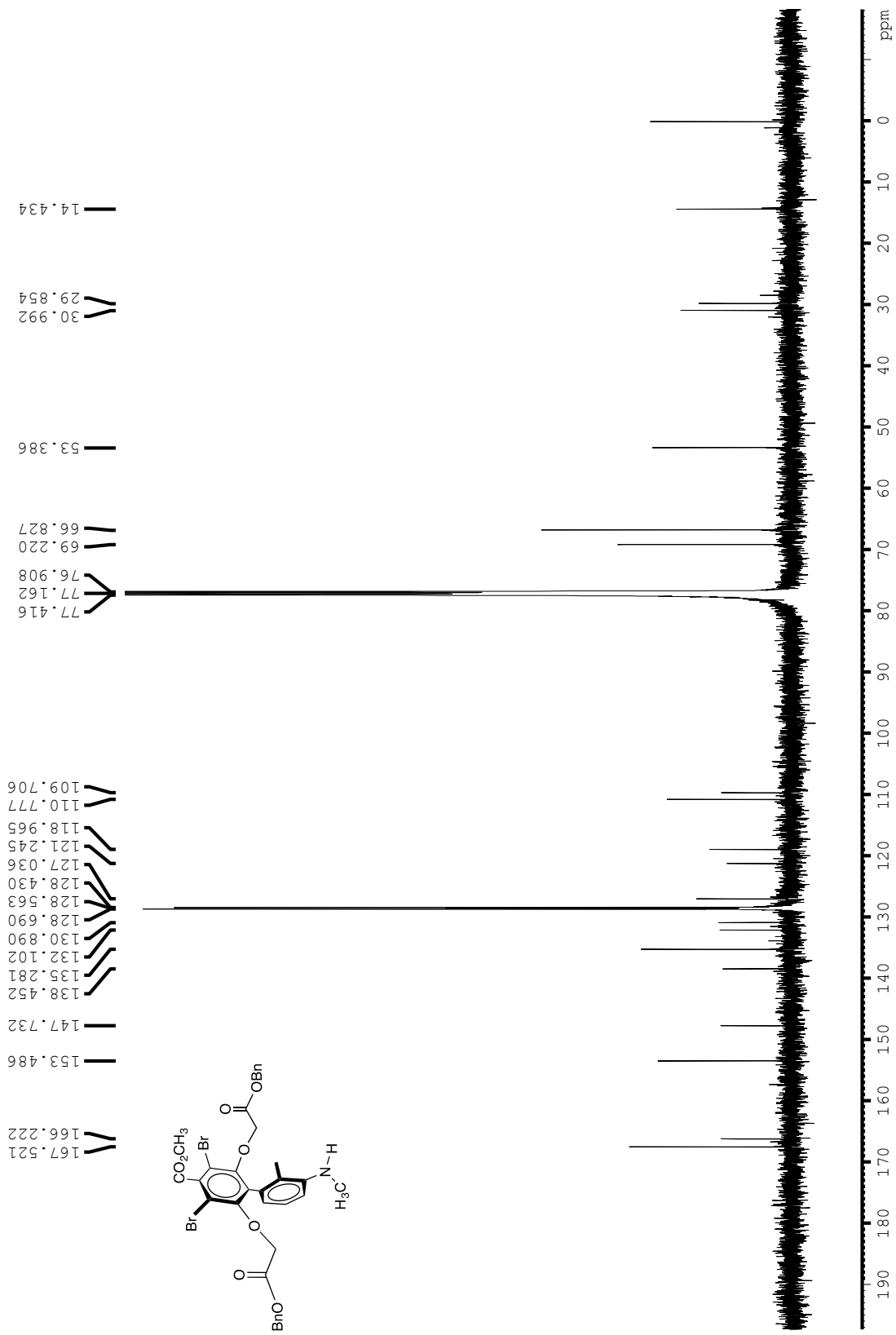


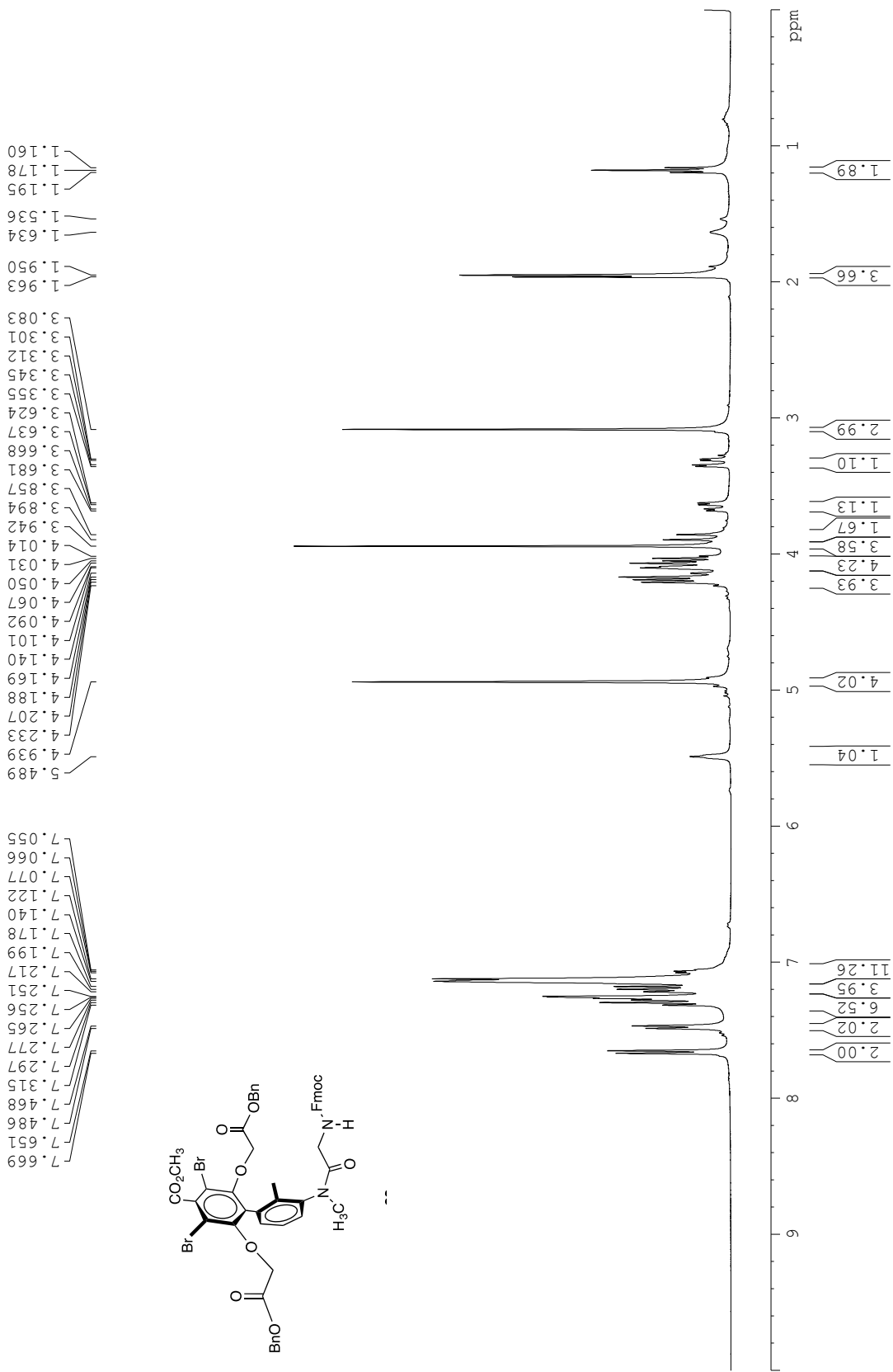


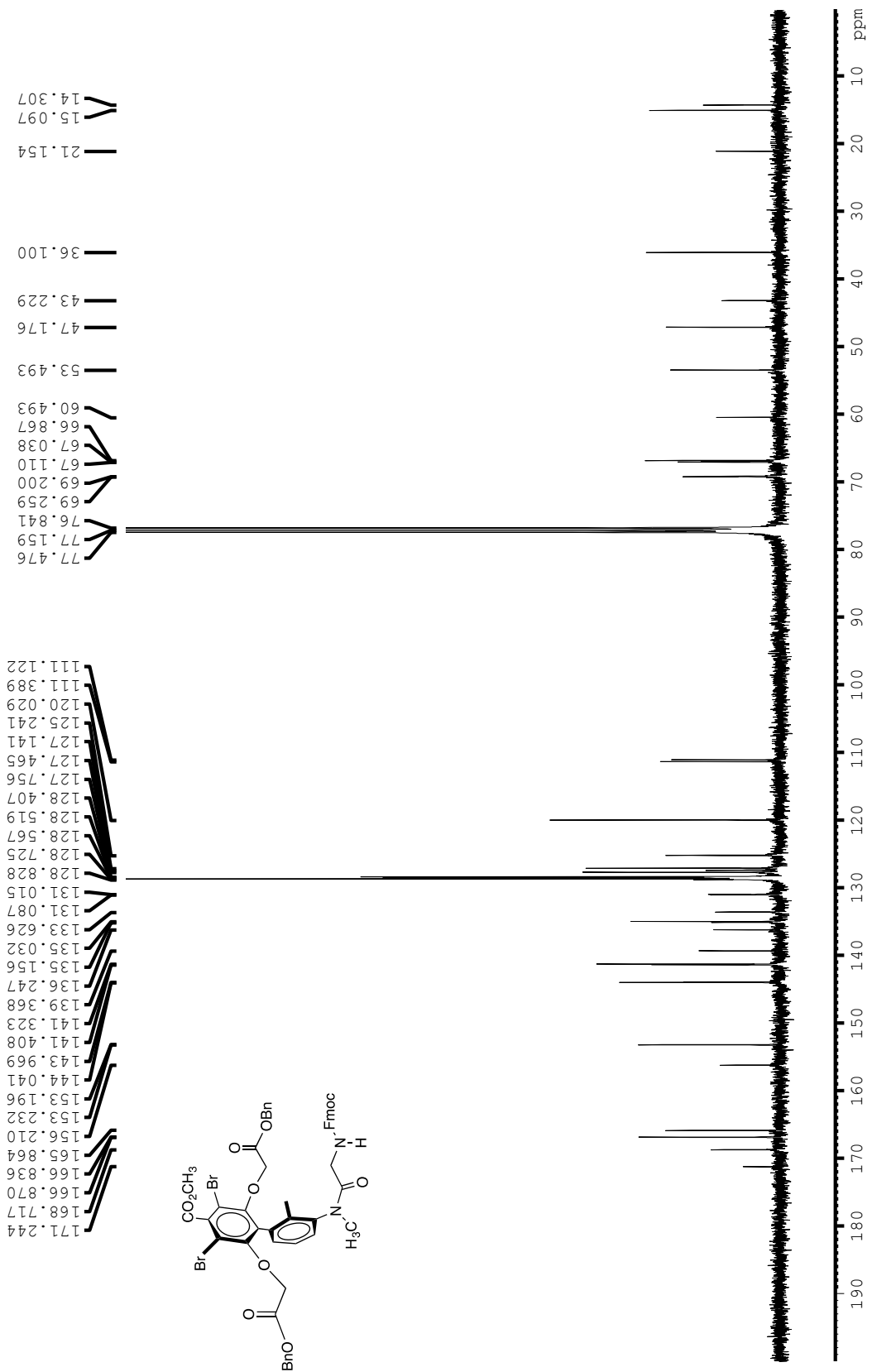


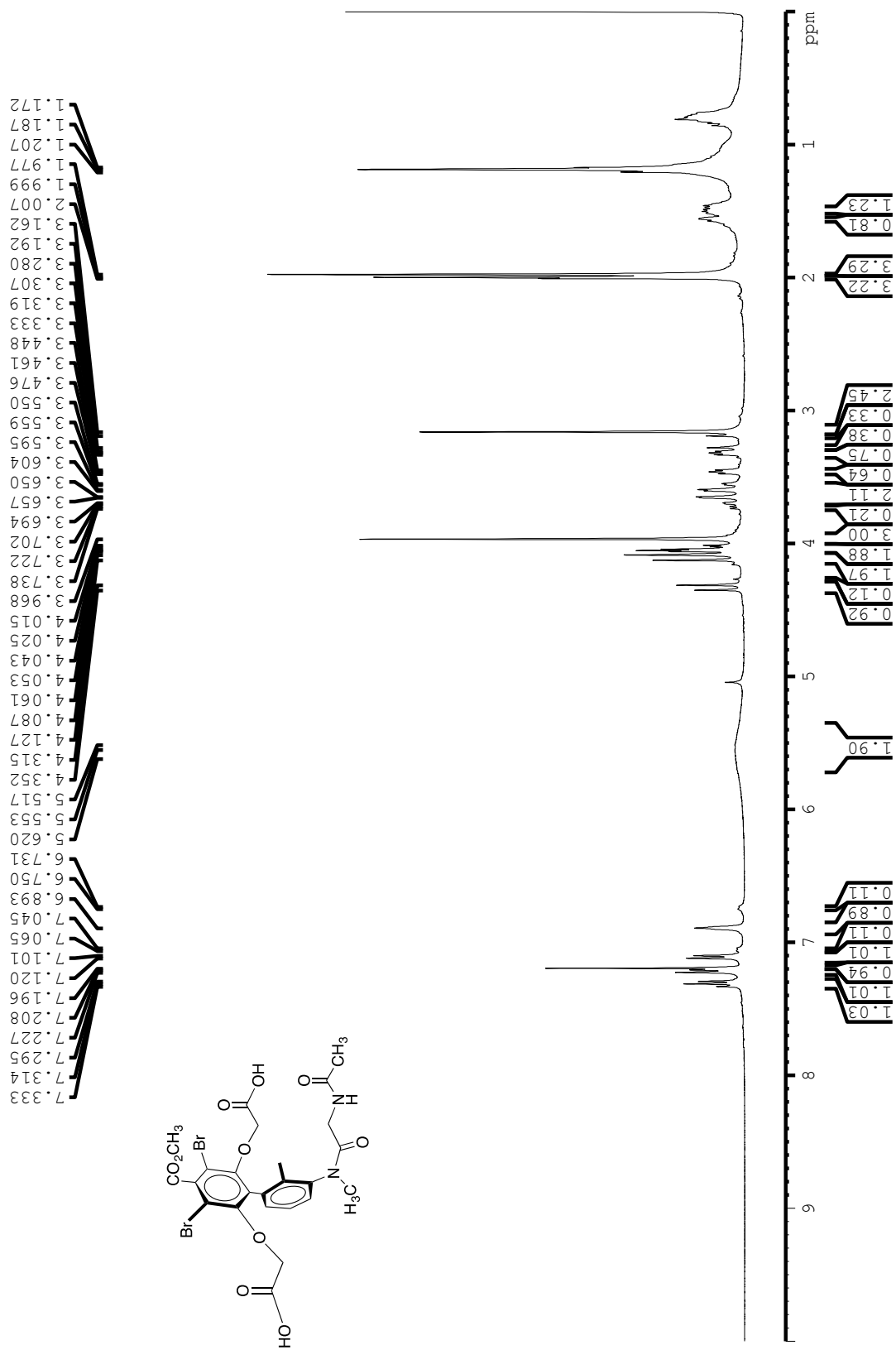


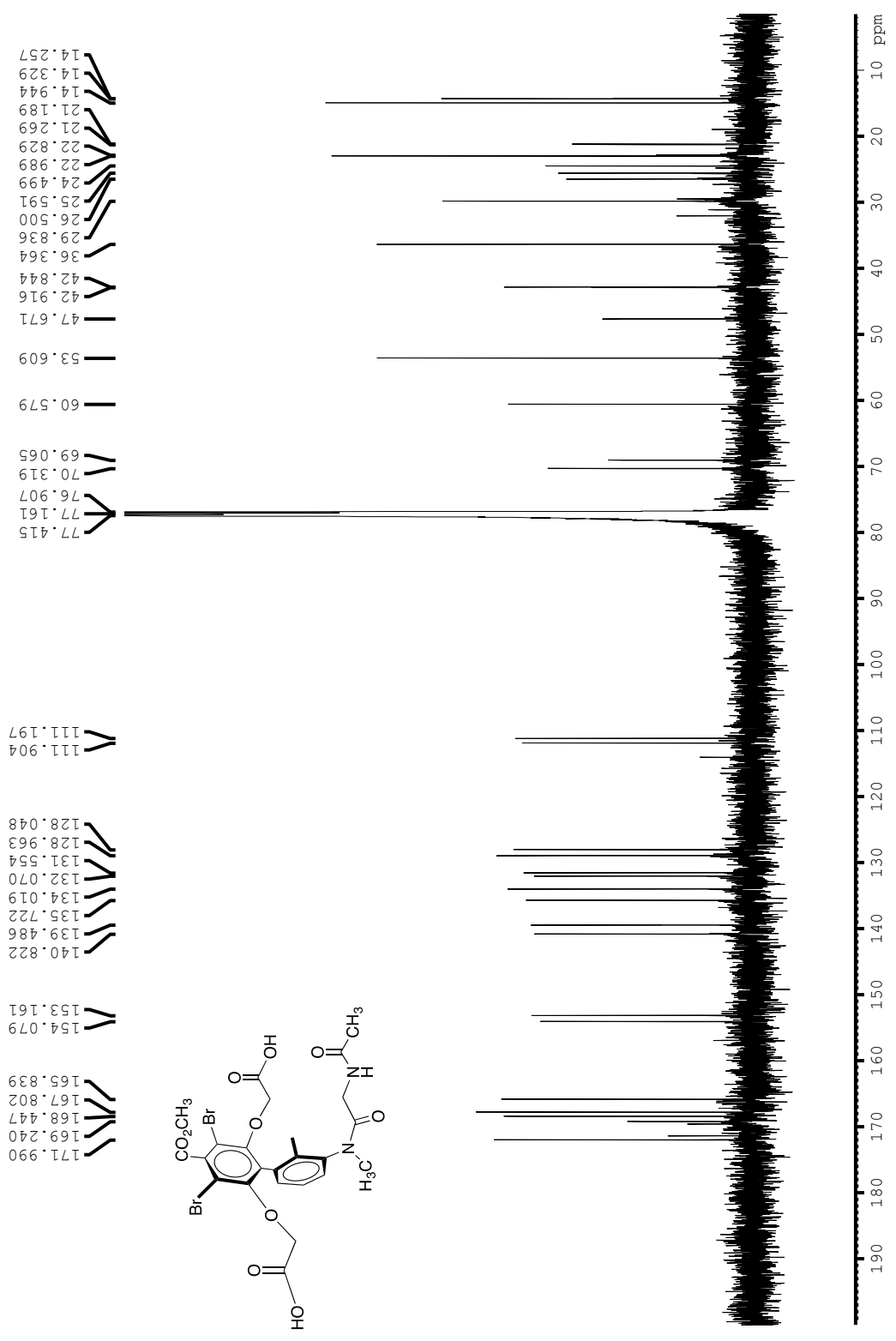


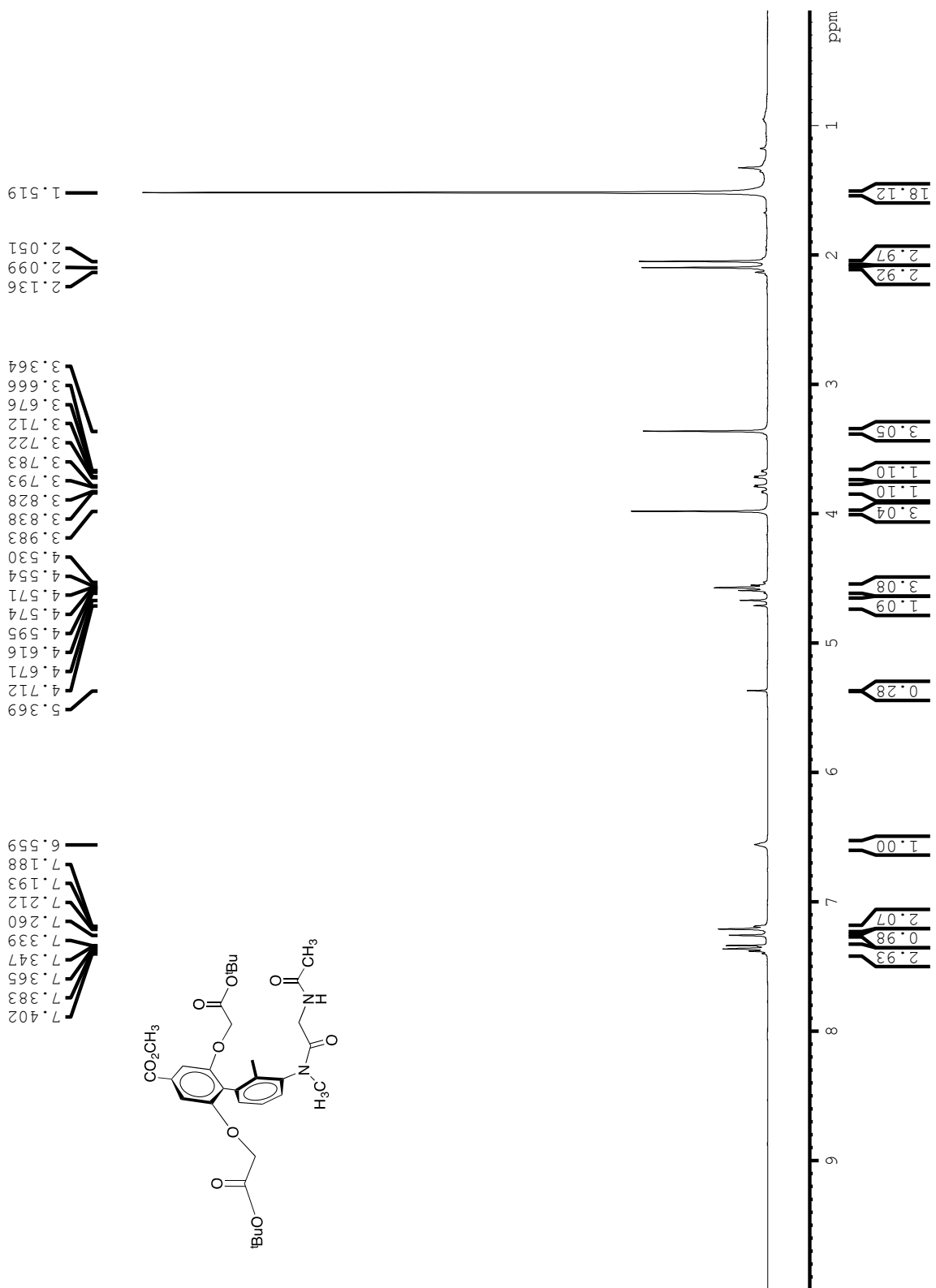


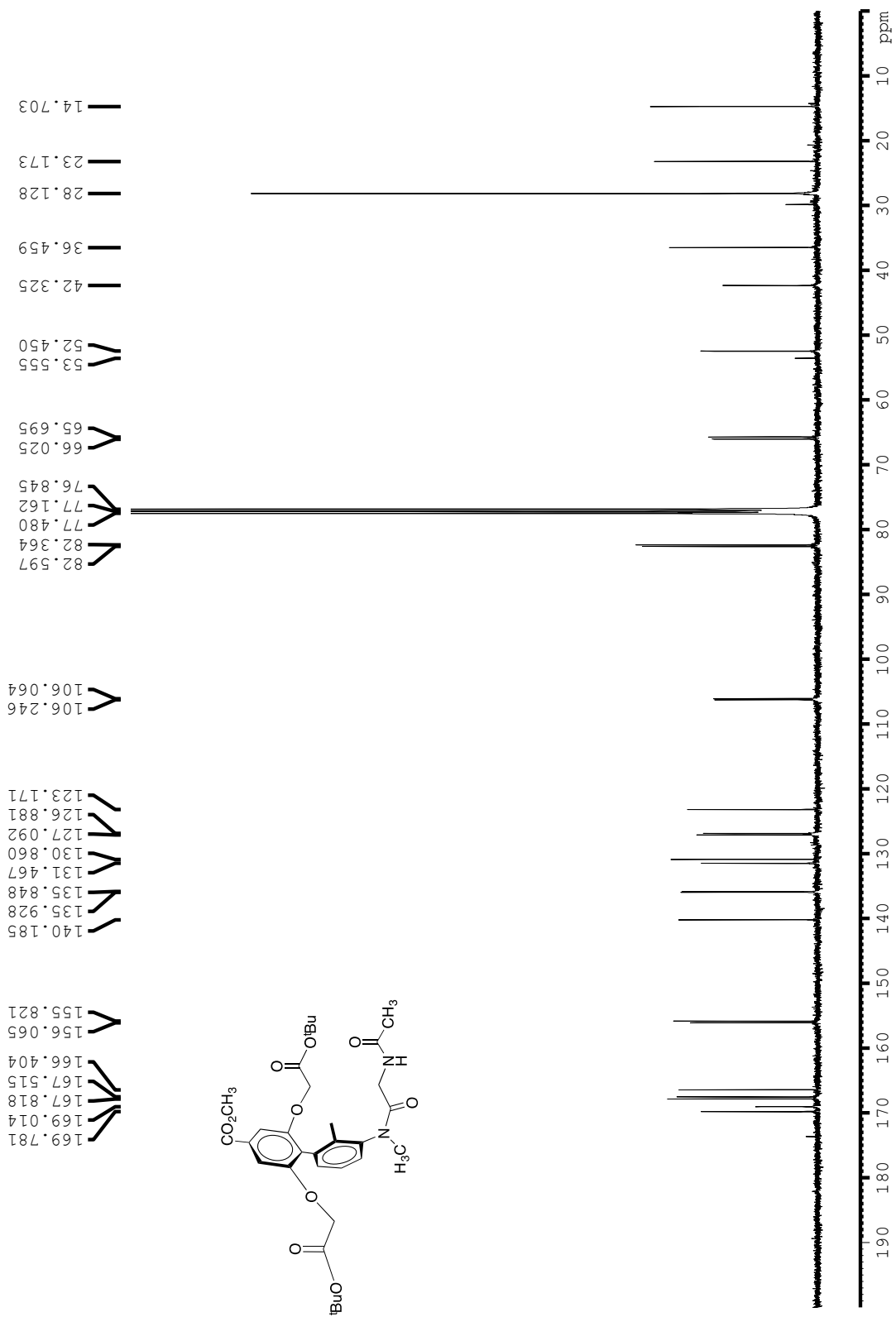


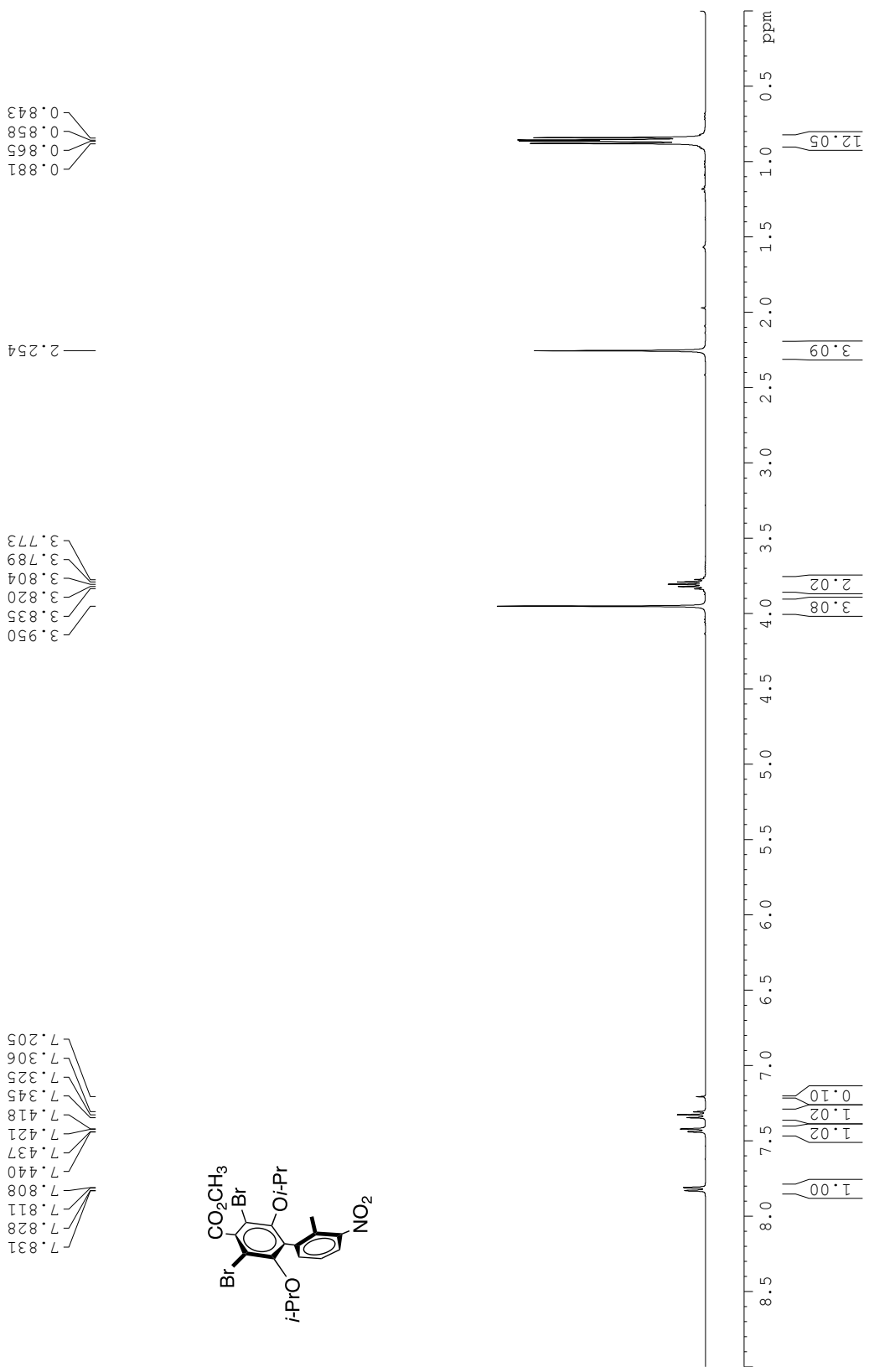


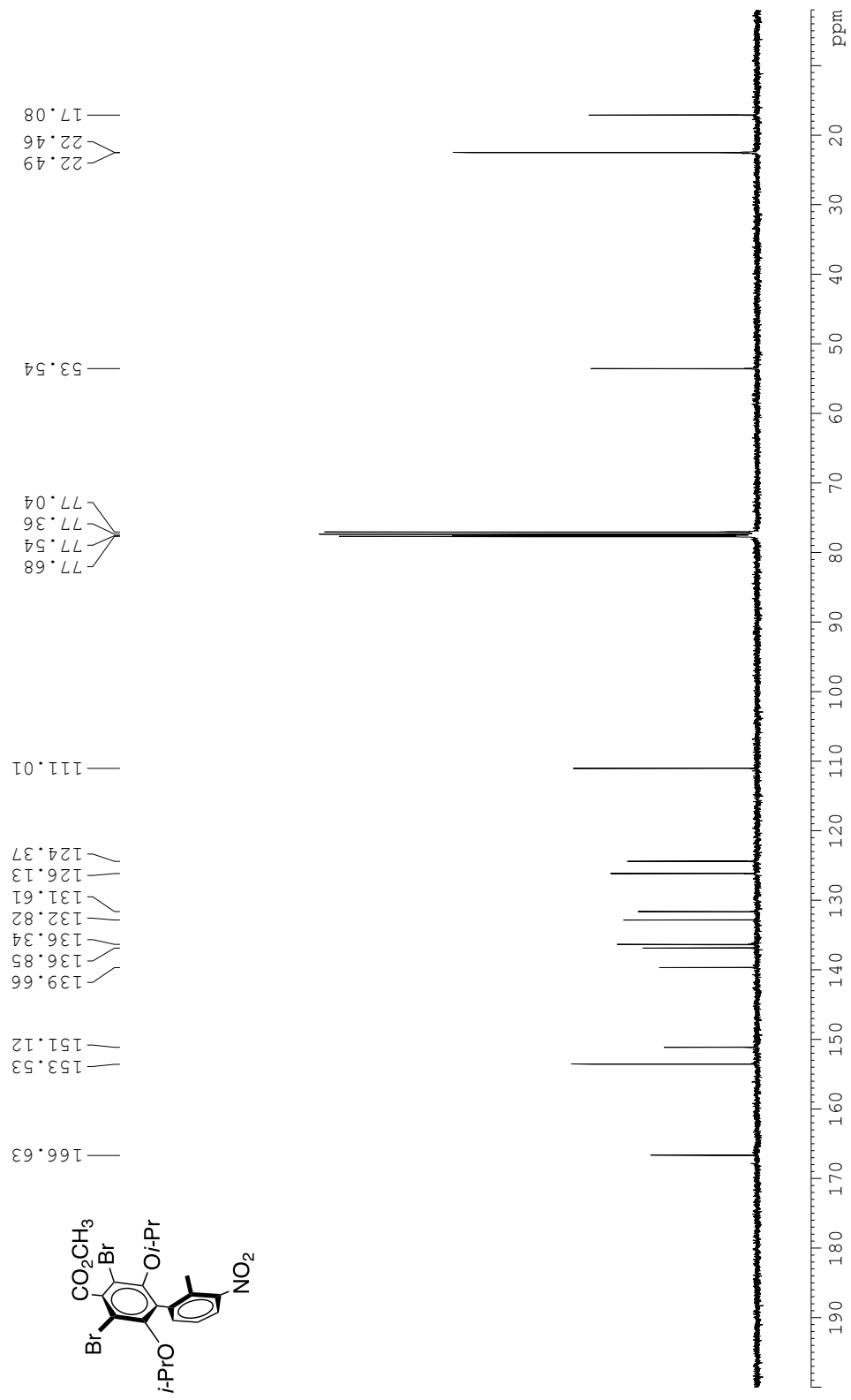


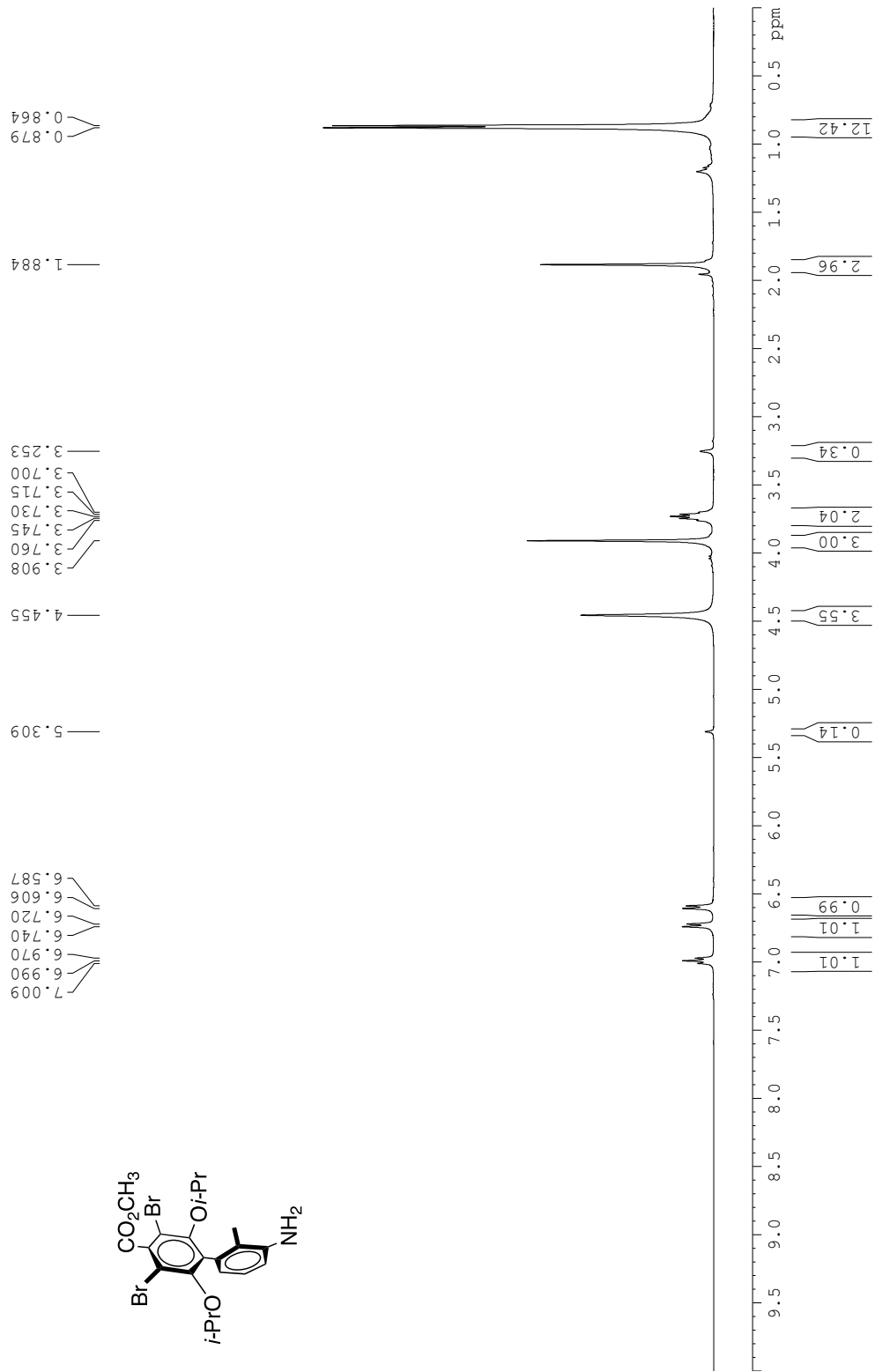
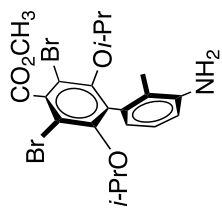


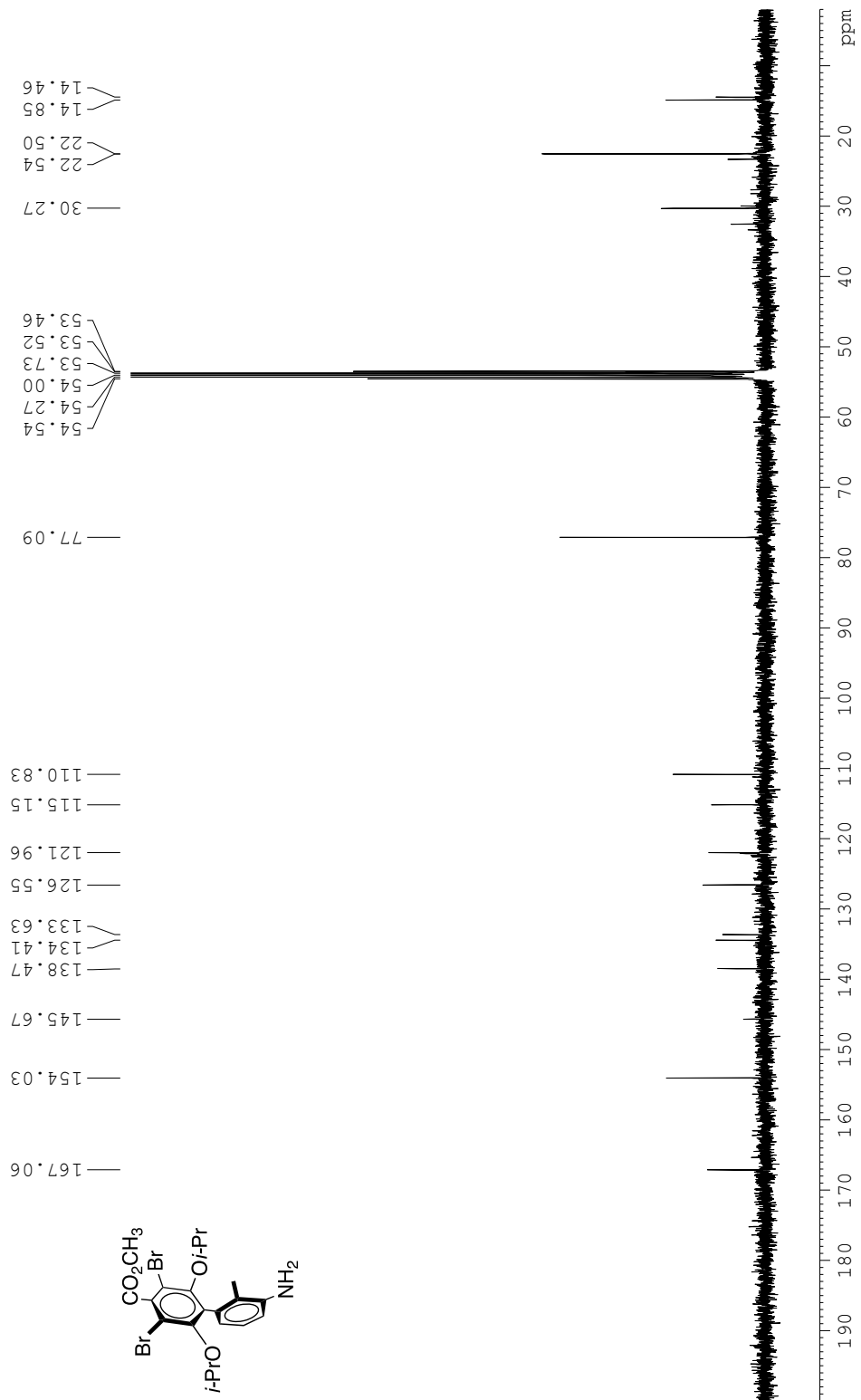


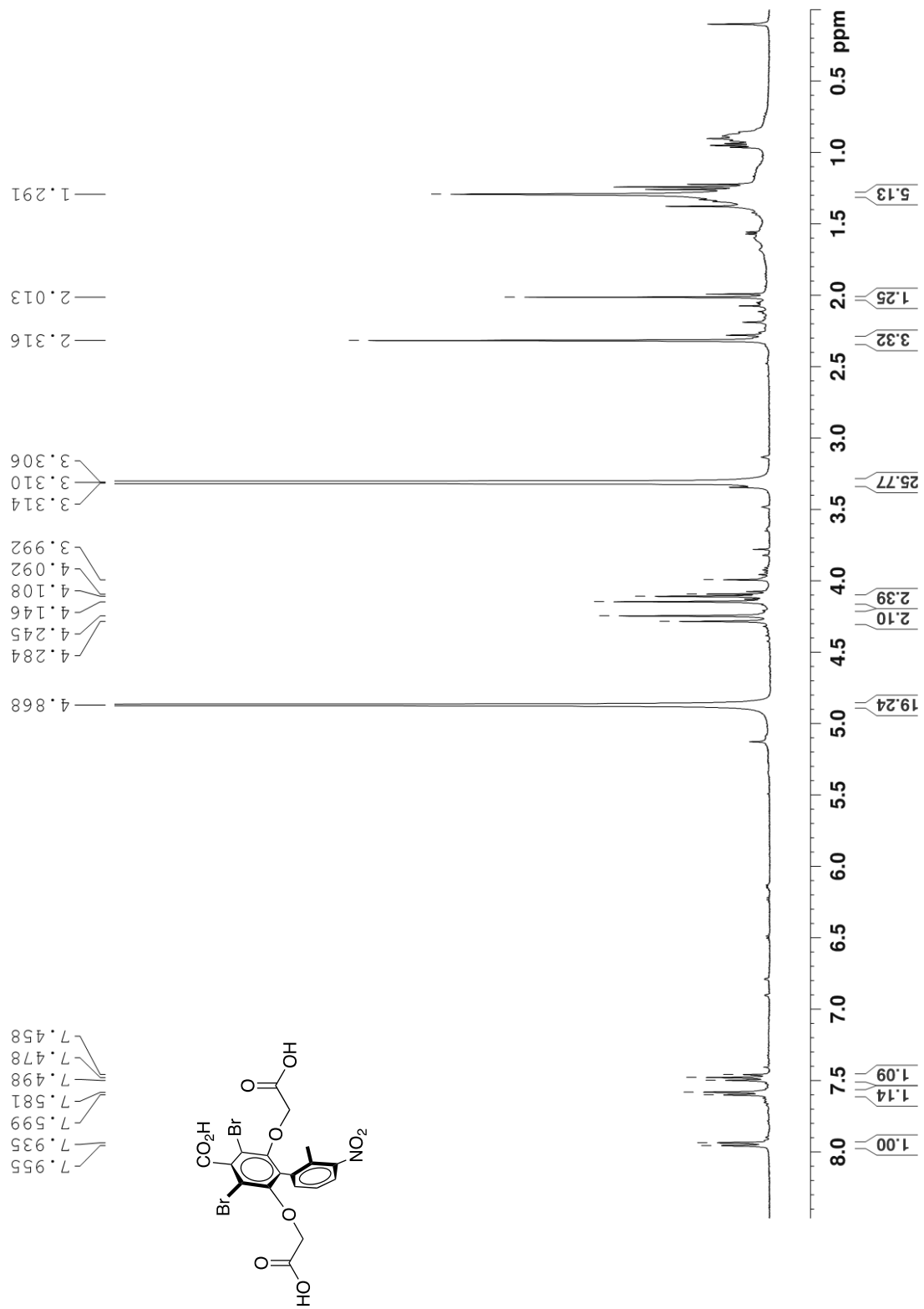


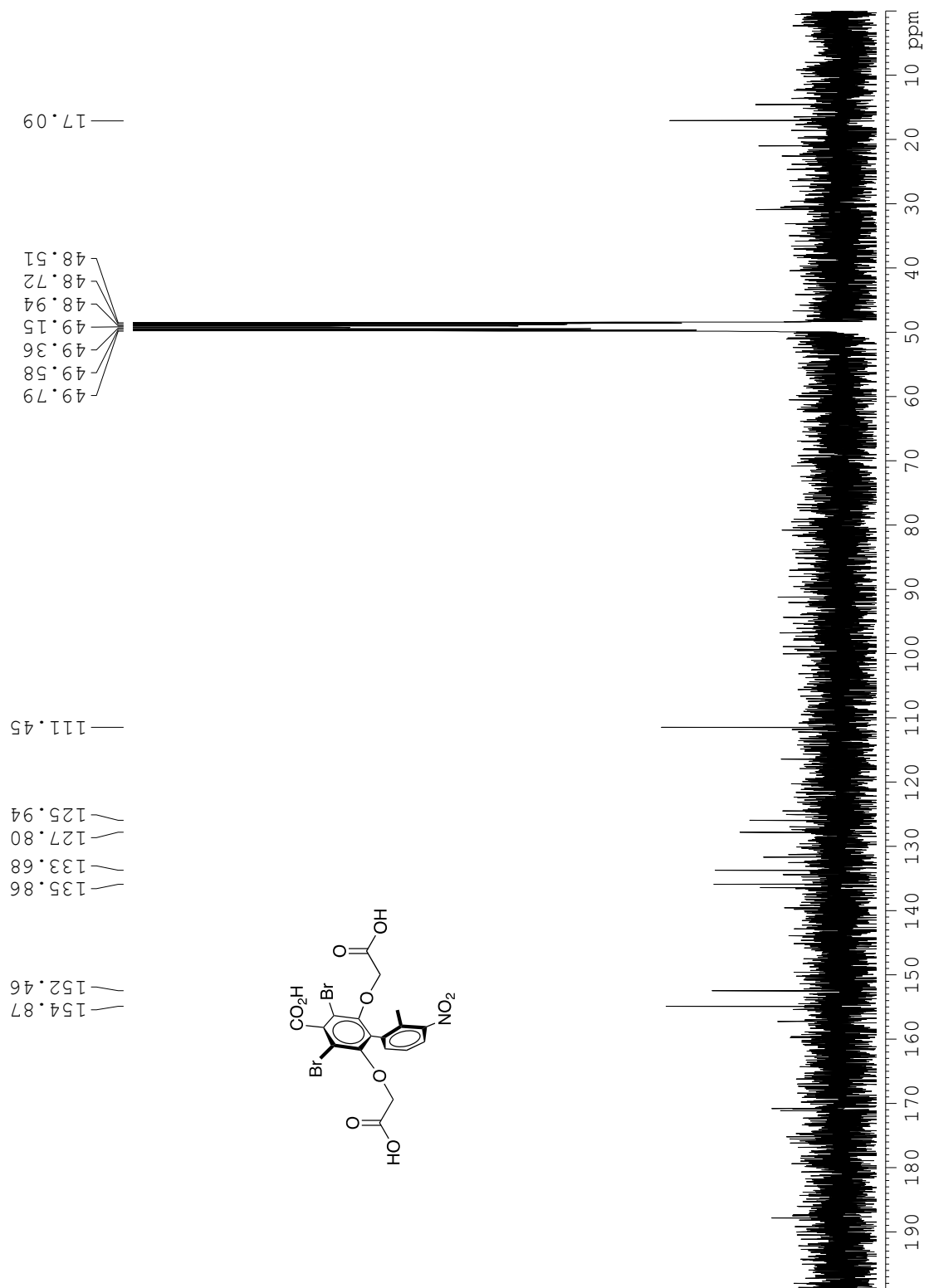


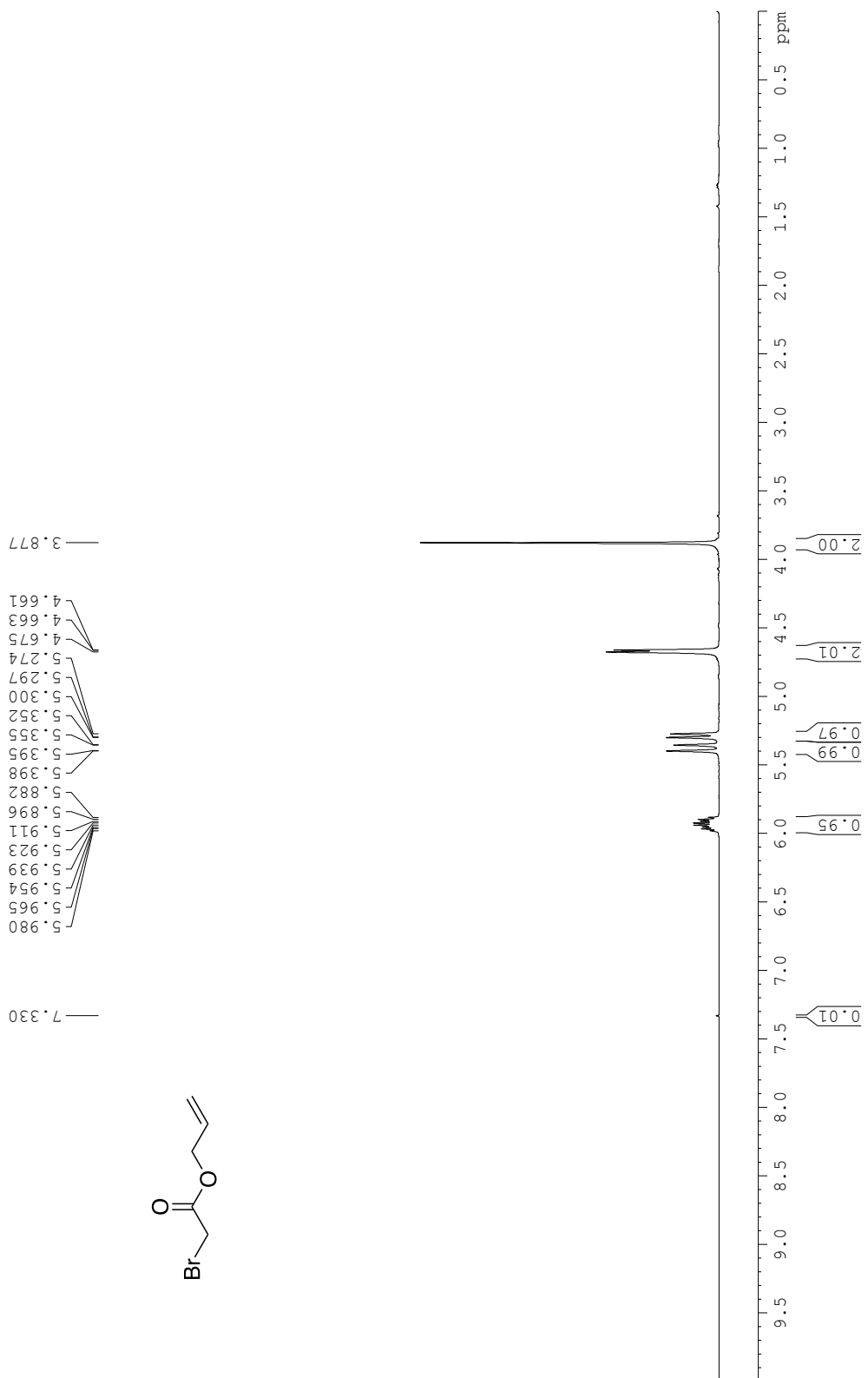
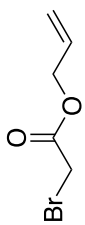


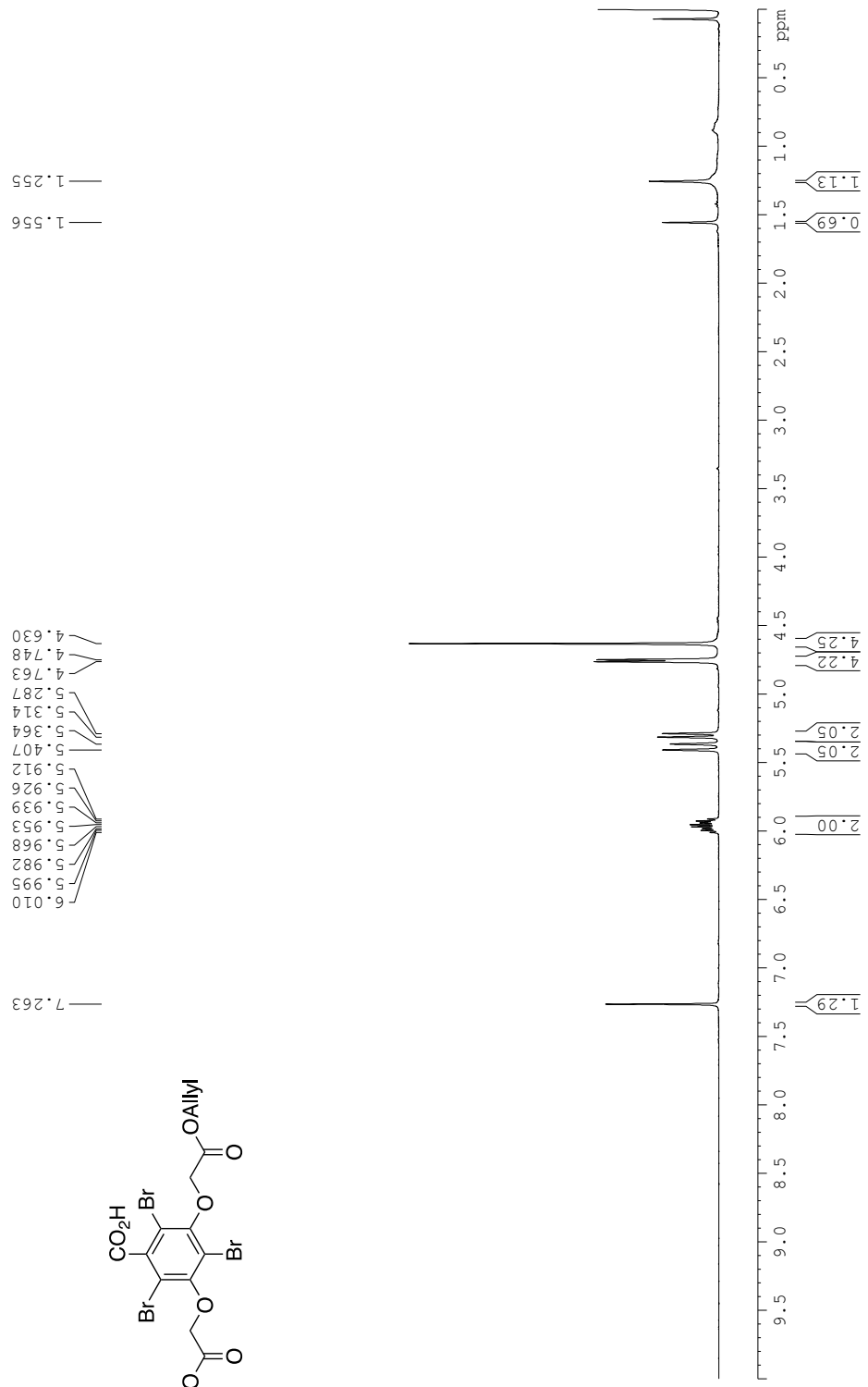


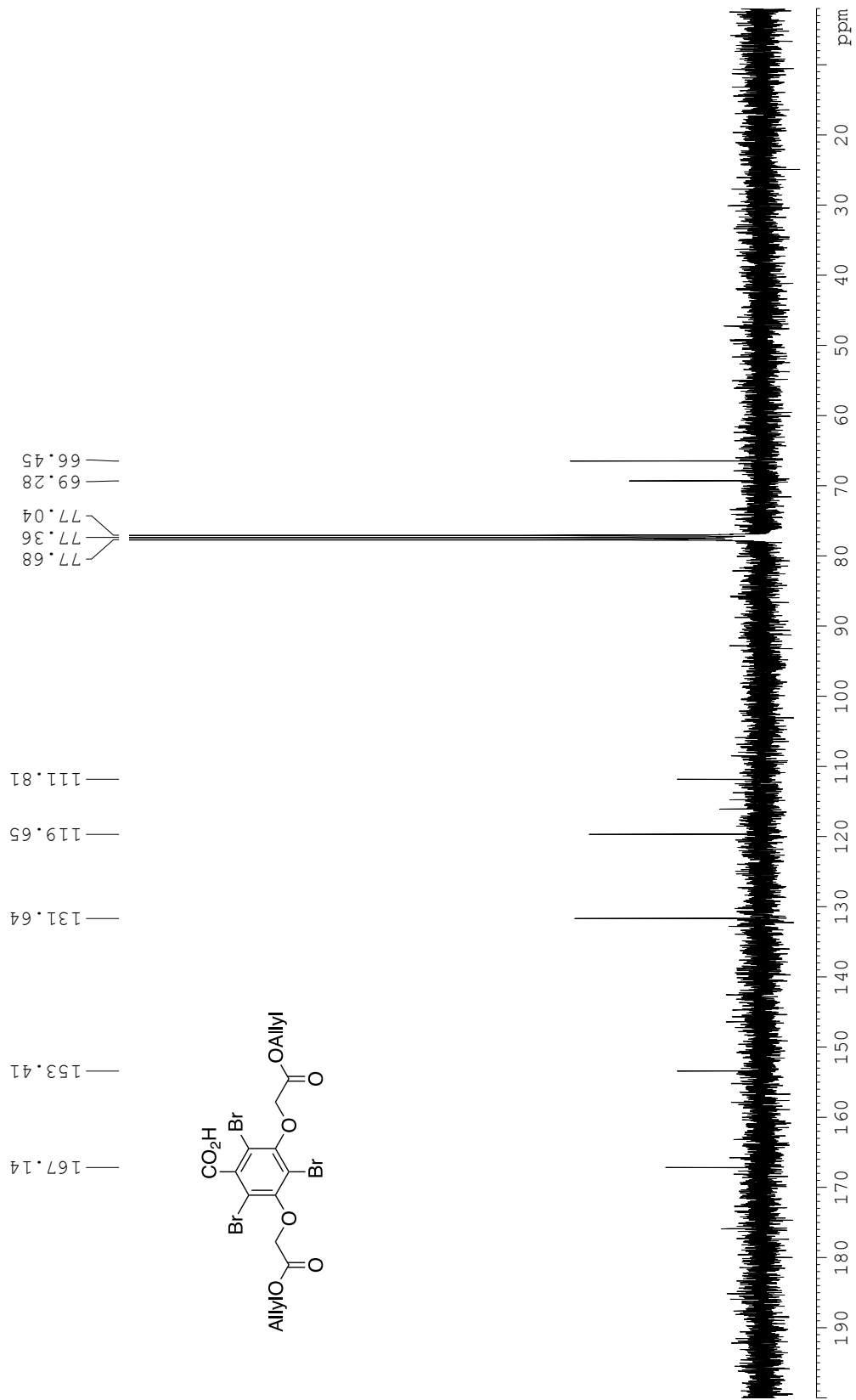


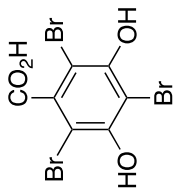






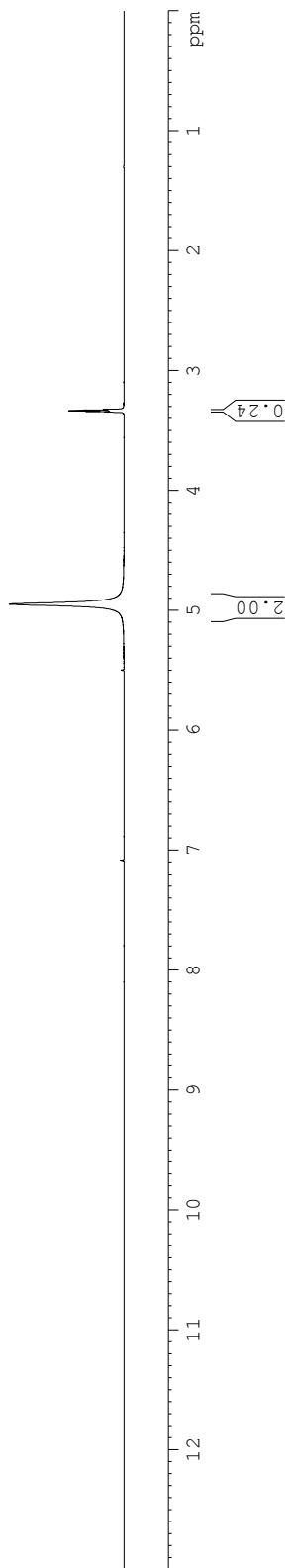


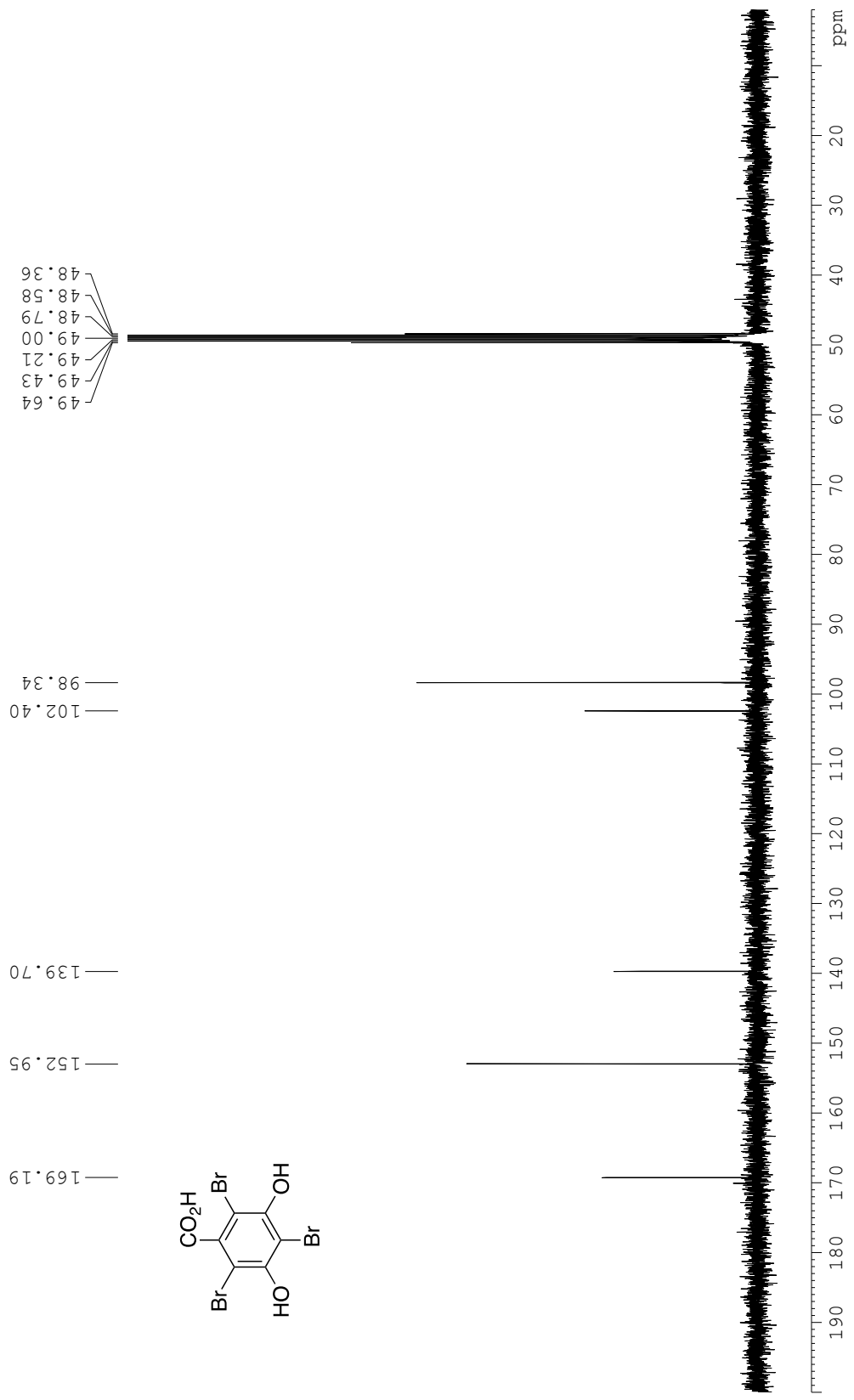


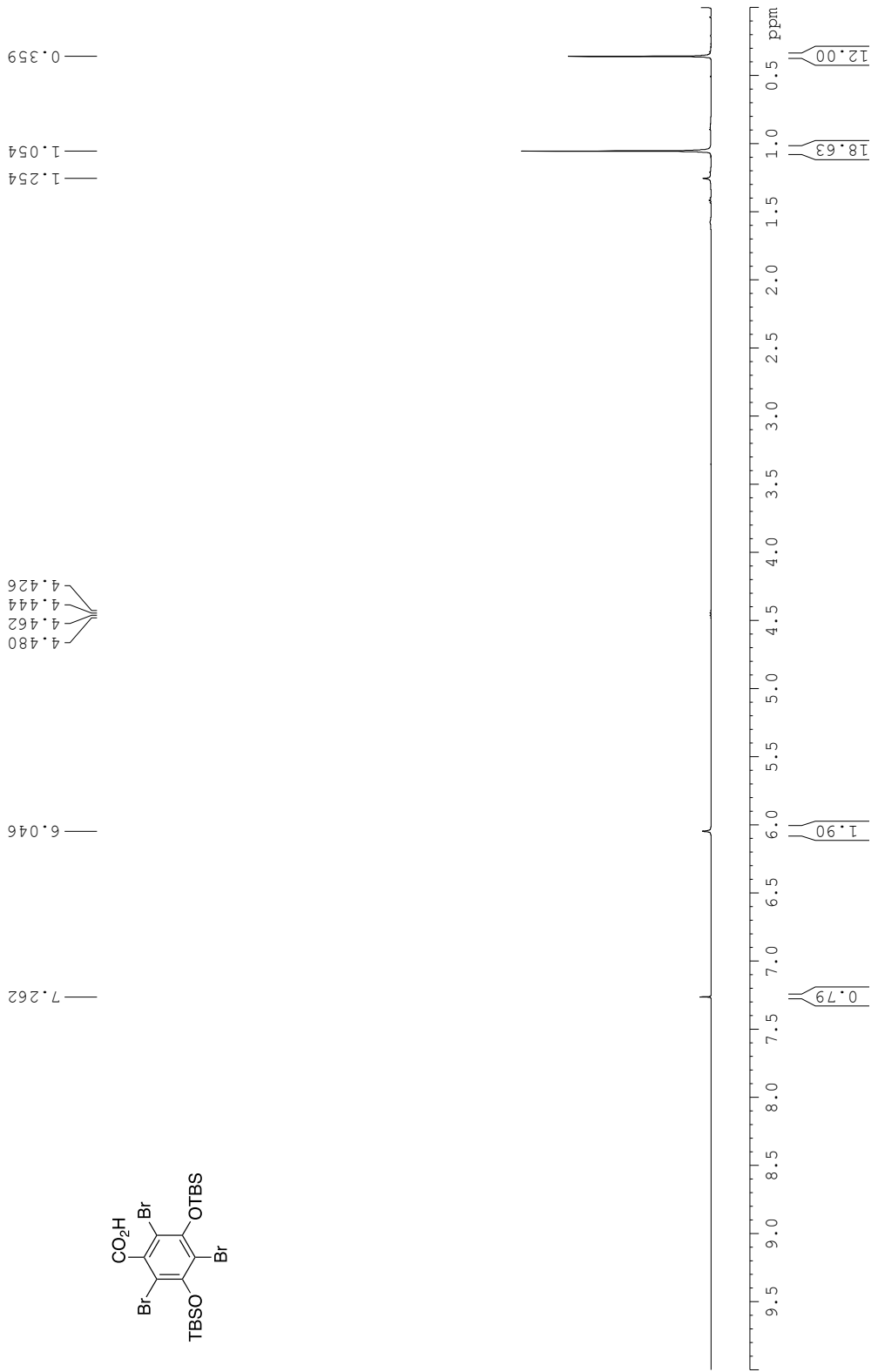
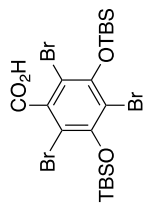


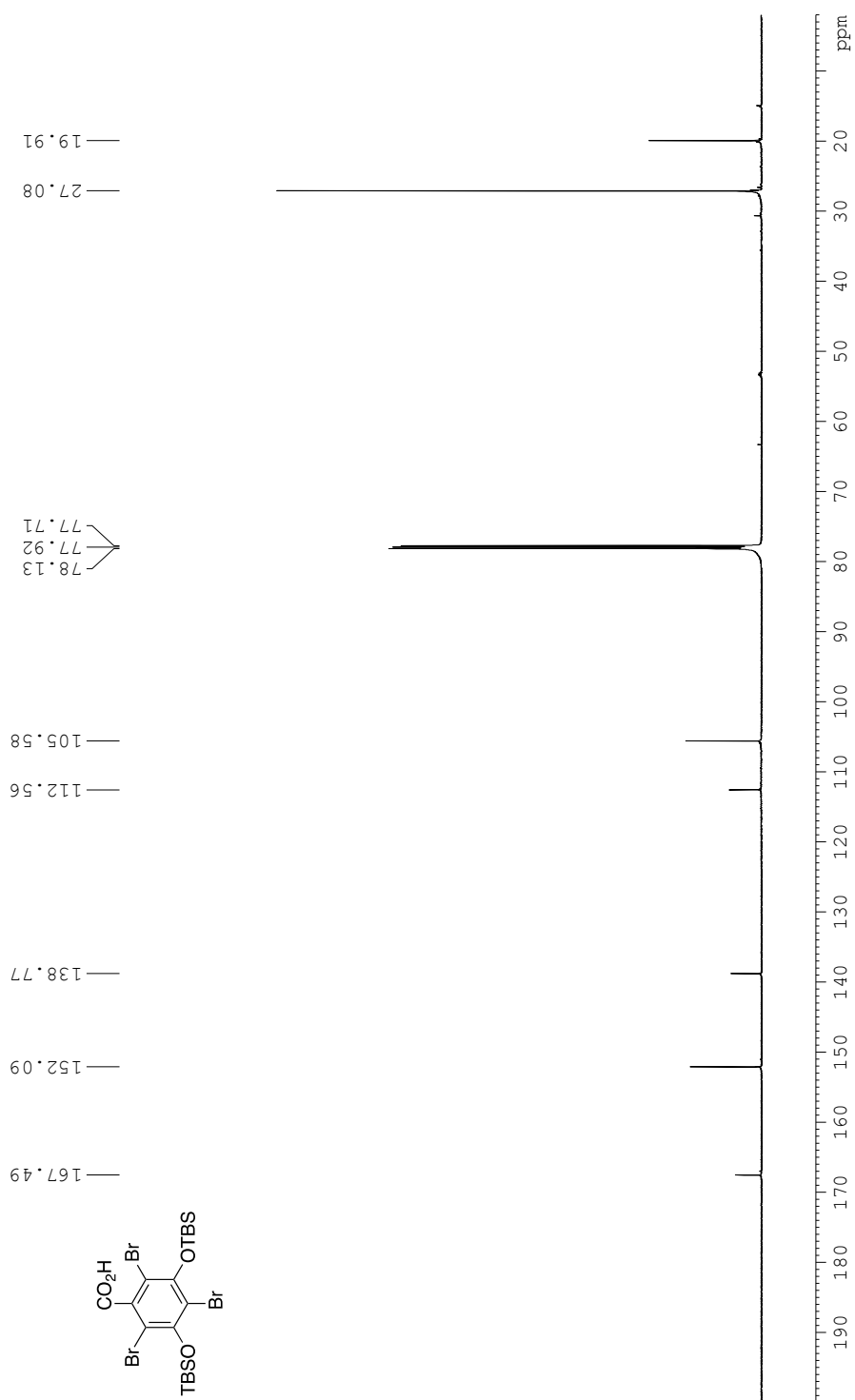
3.324
3.329
3.334
3.340
3.345

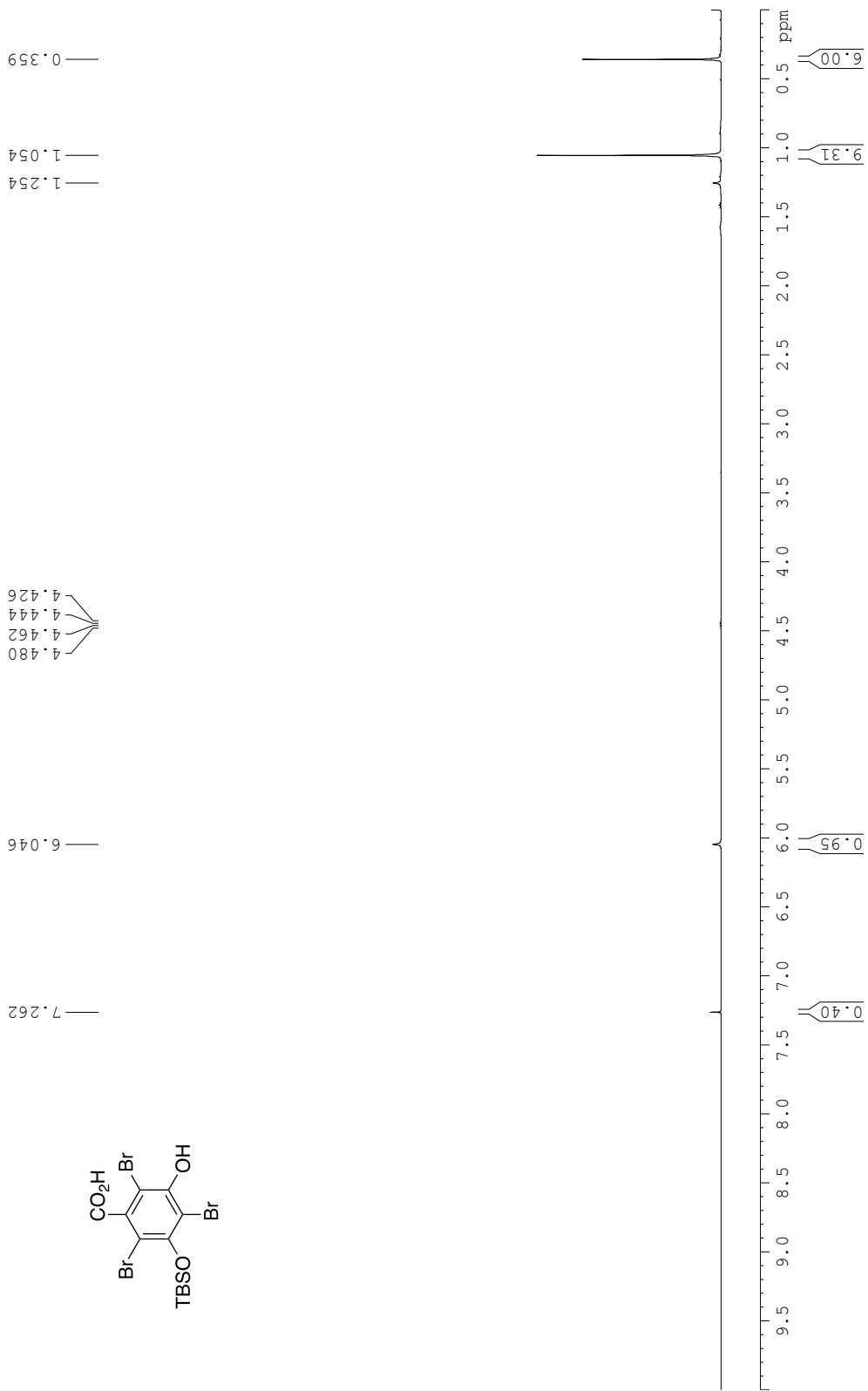
4.947

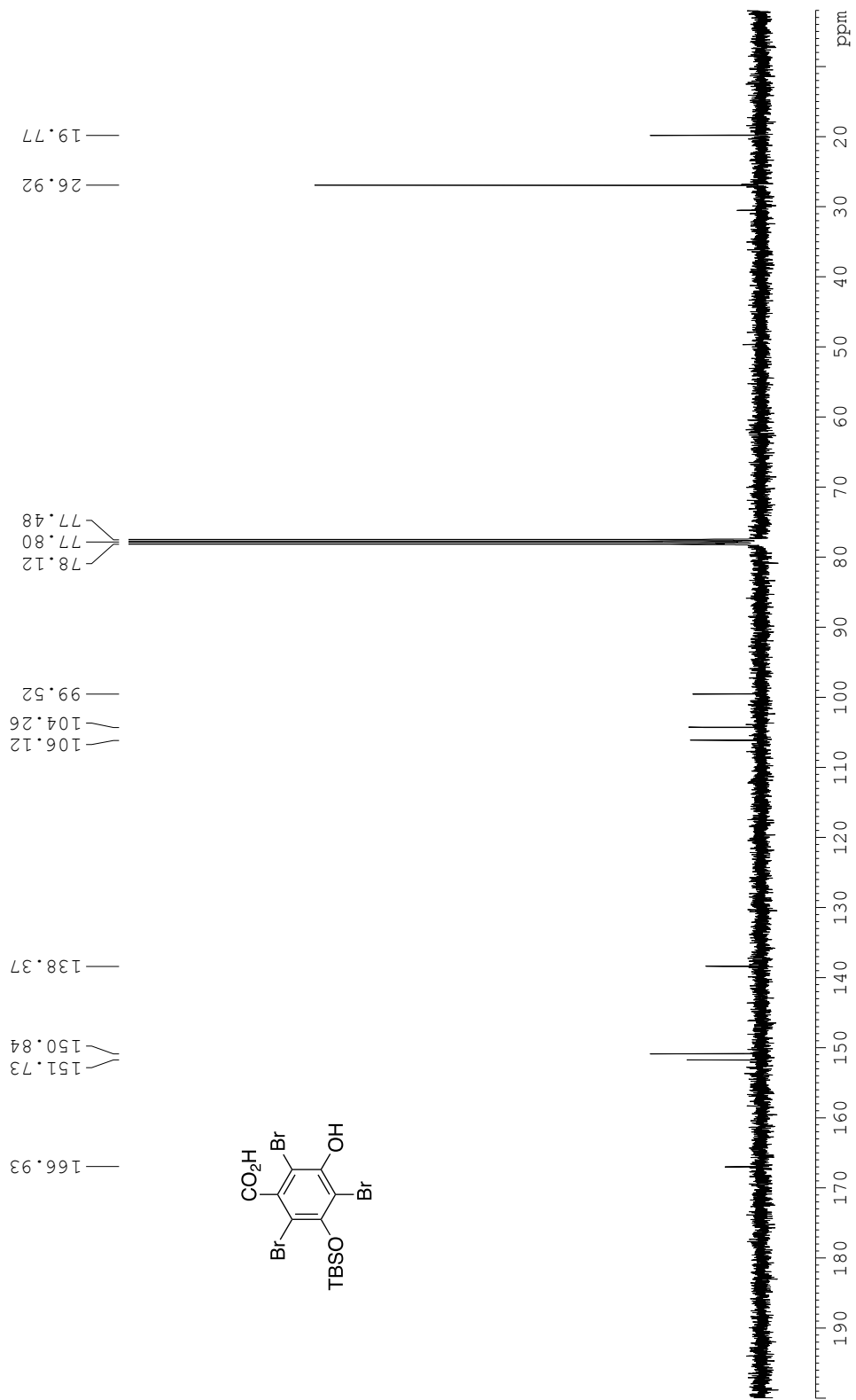


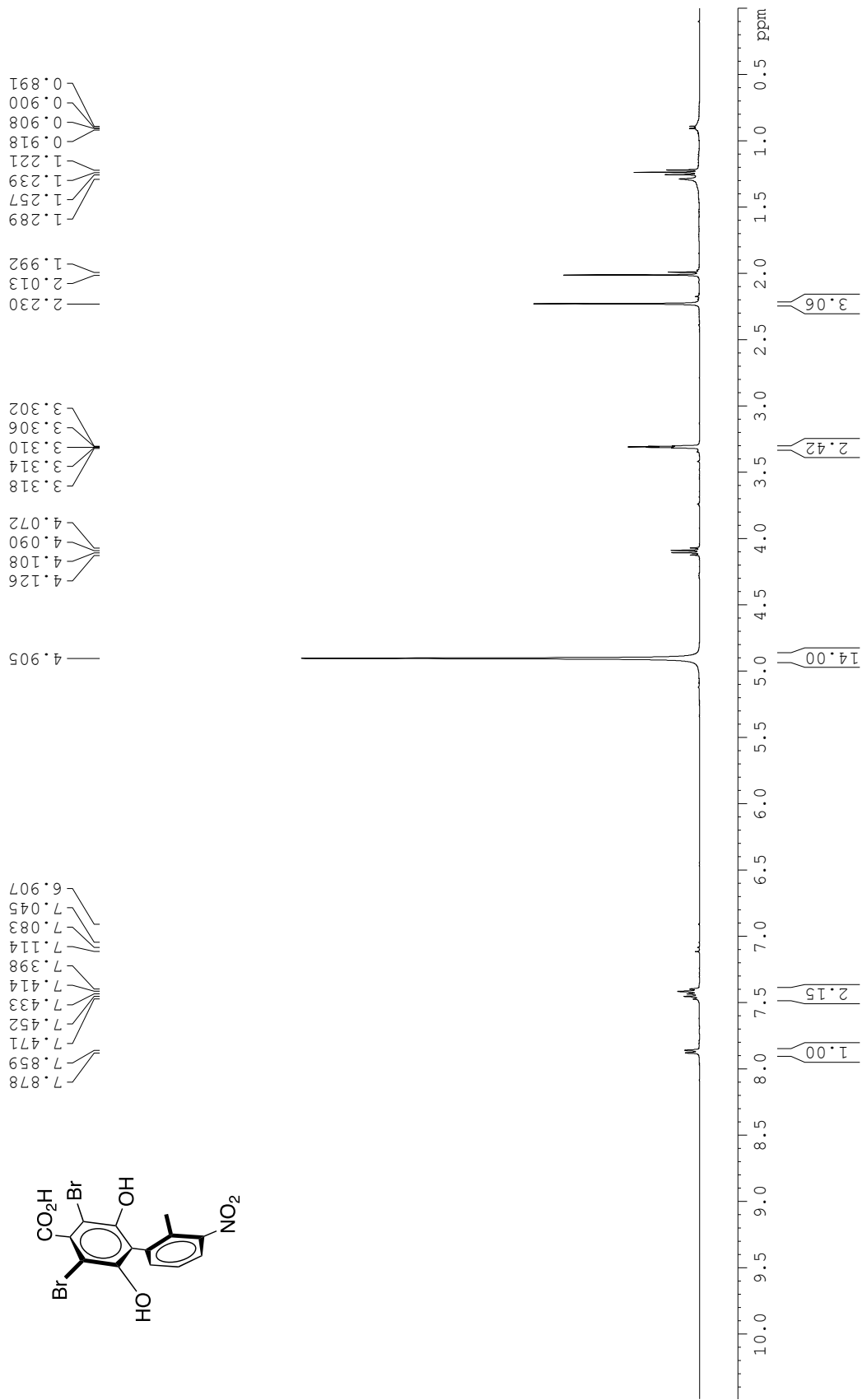


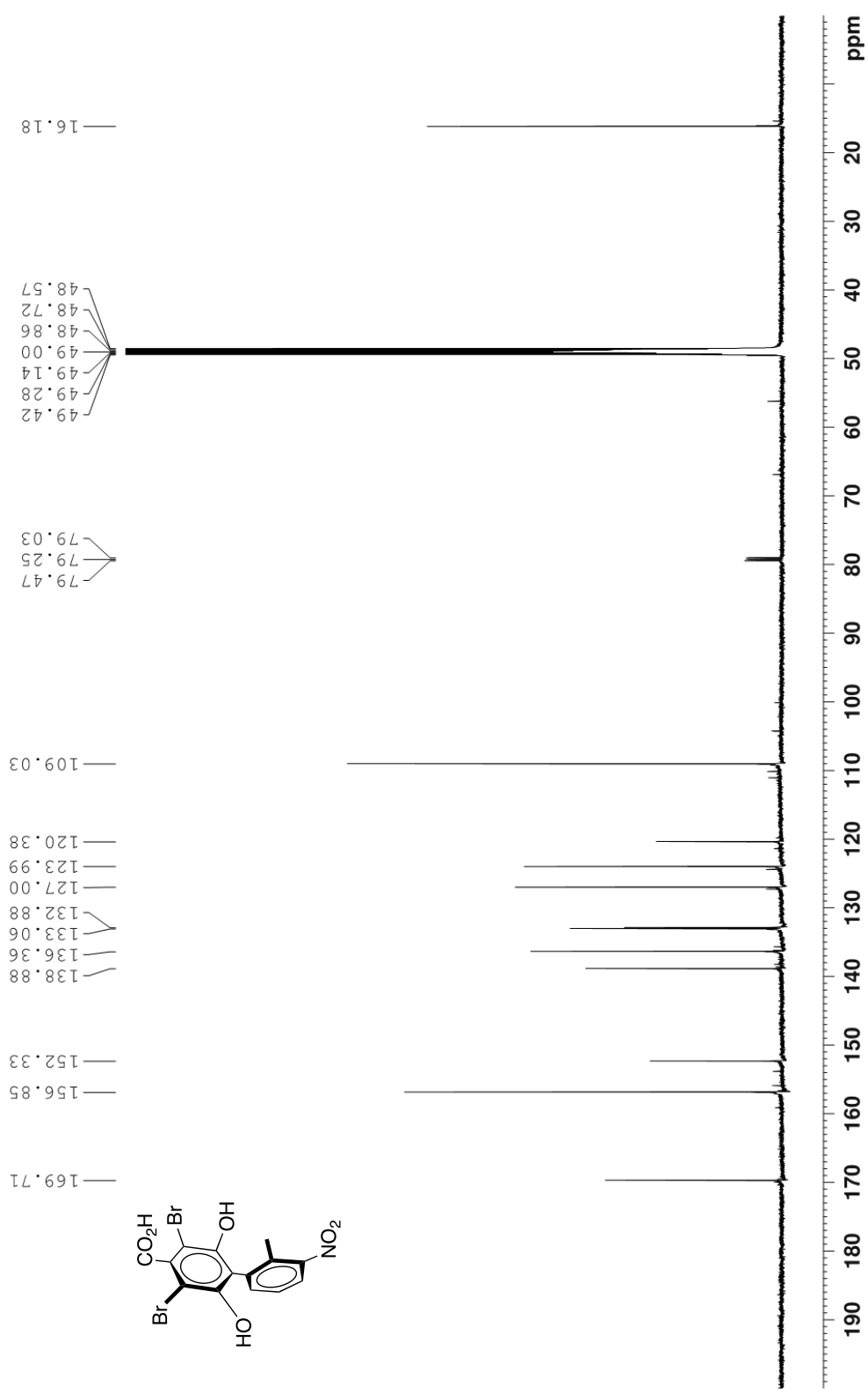


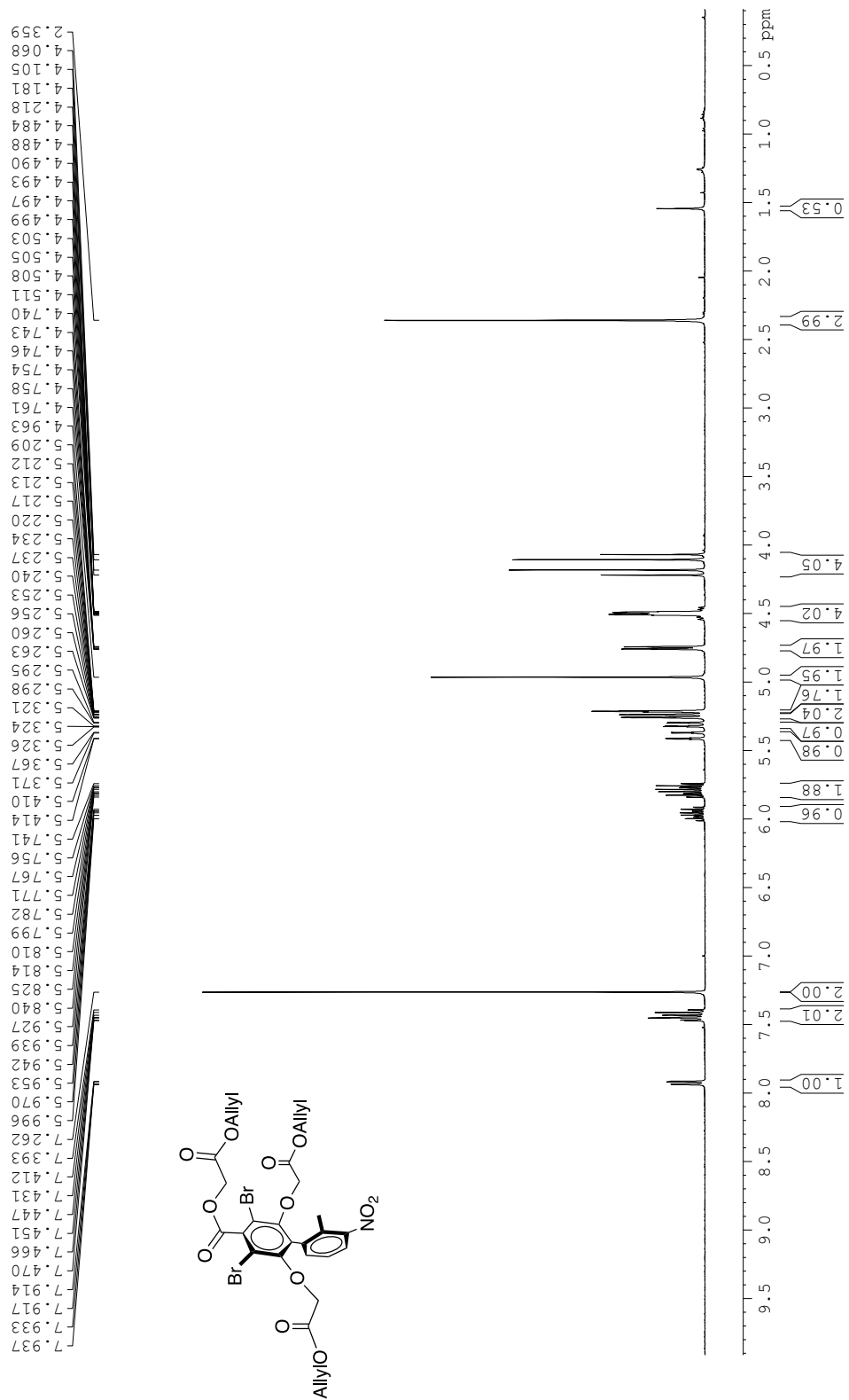


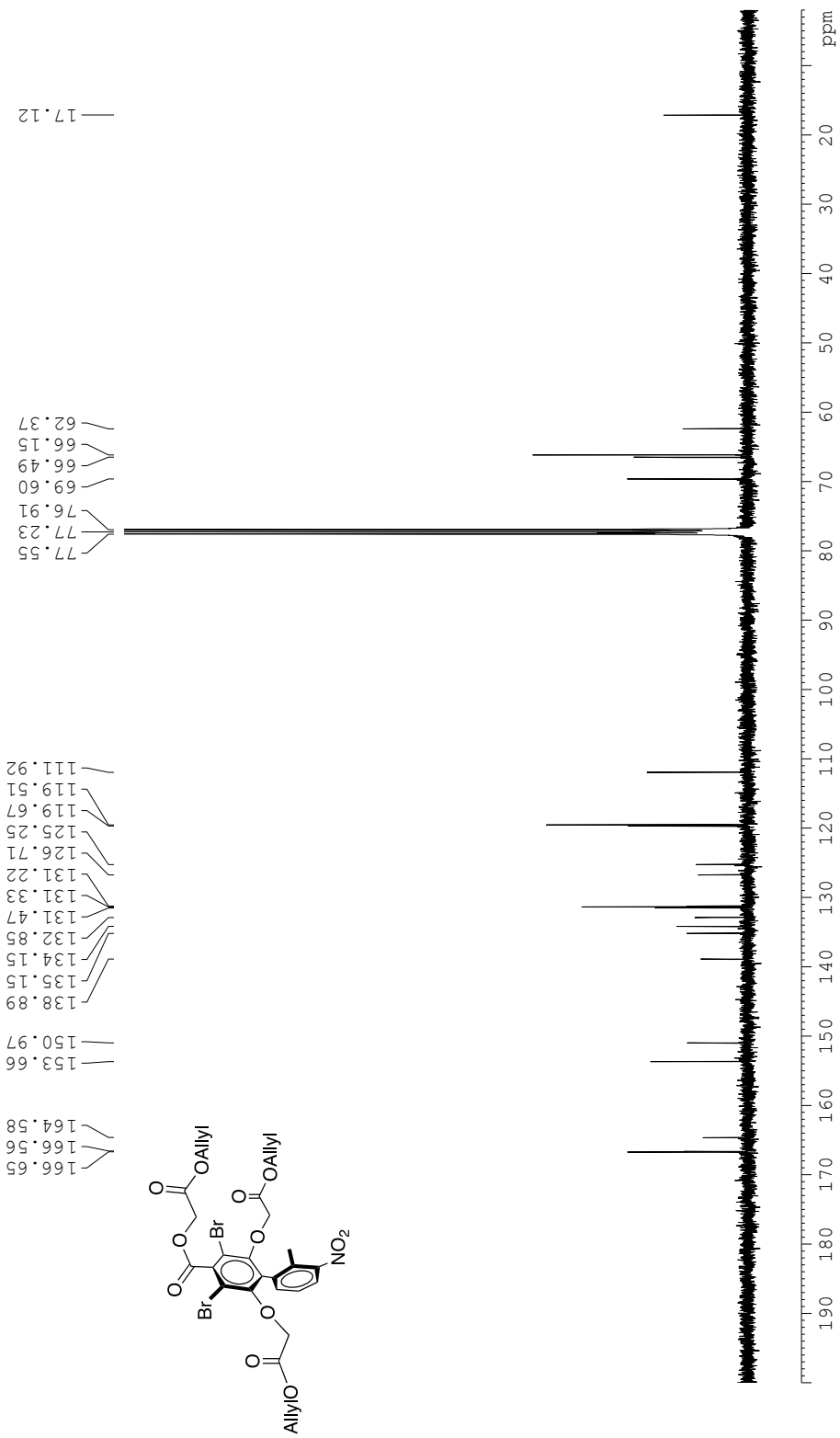


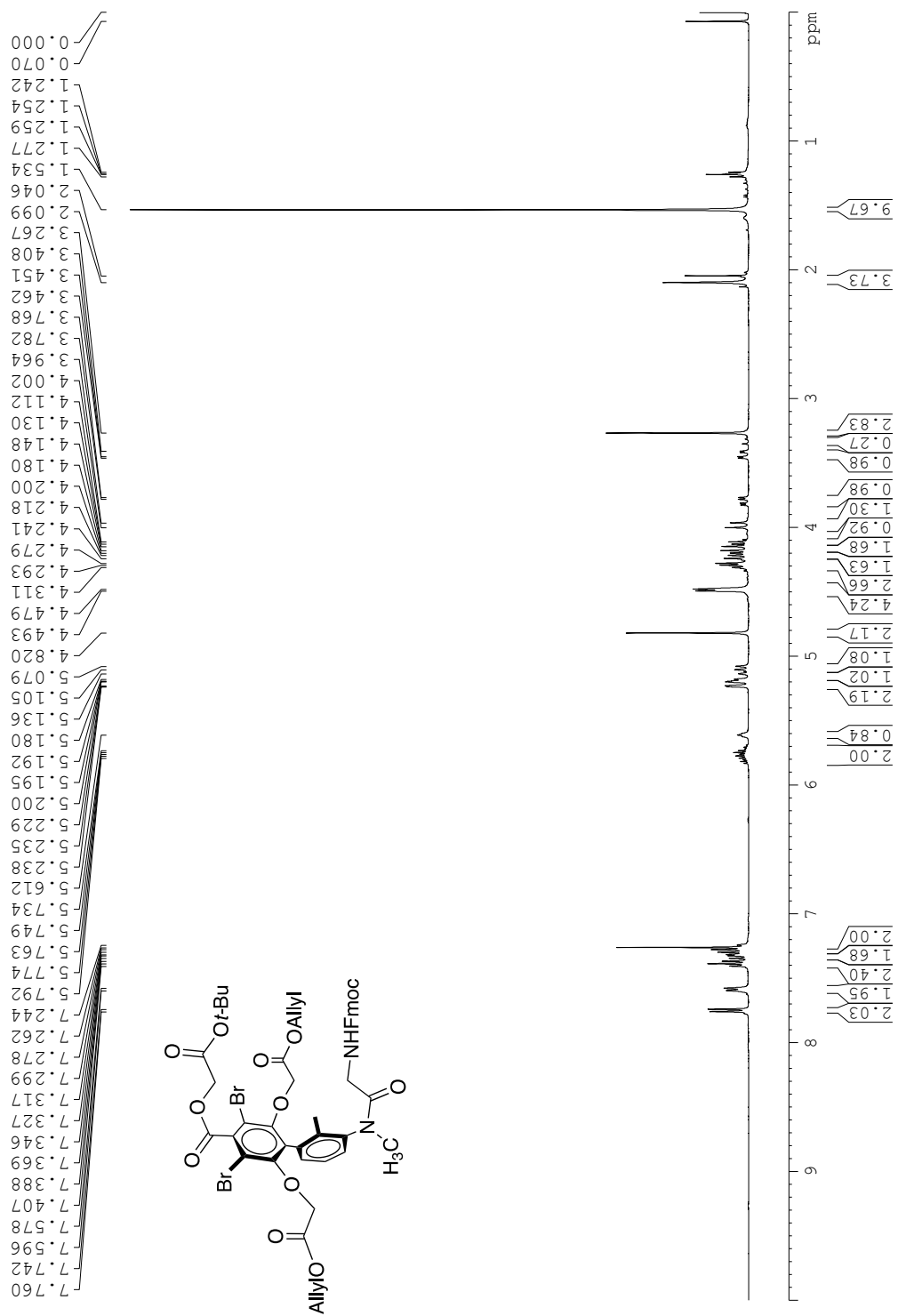


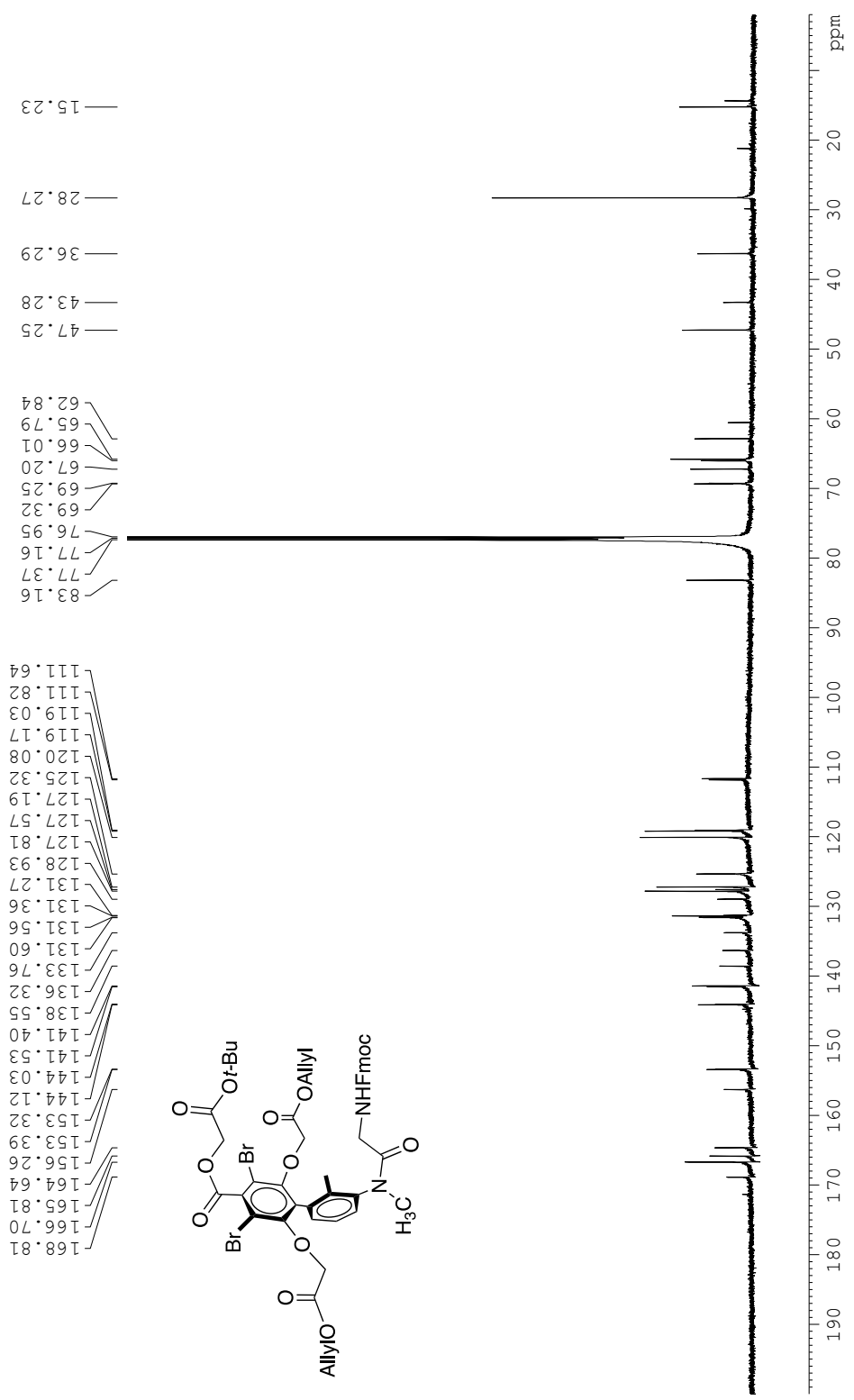


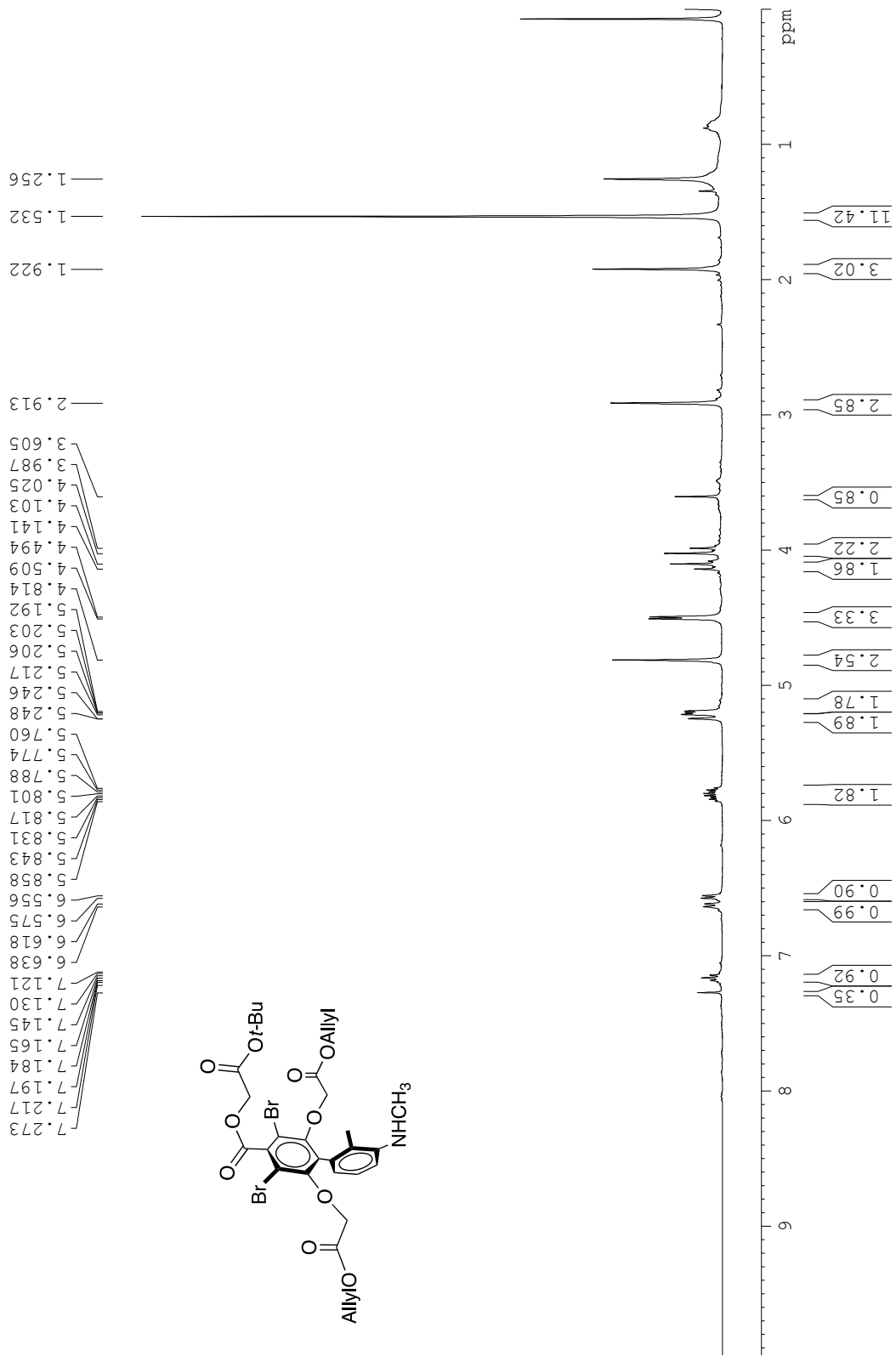


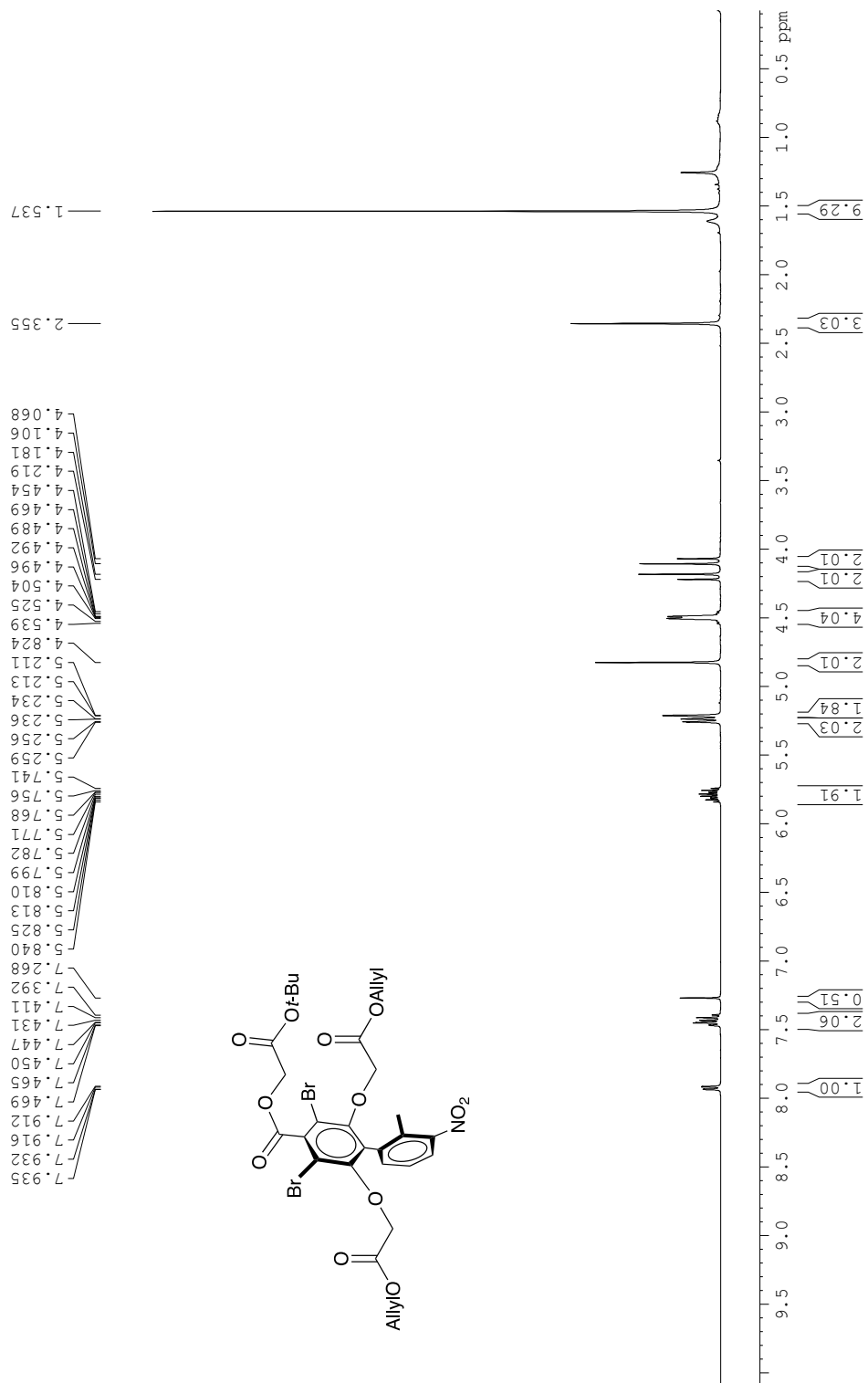


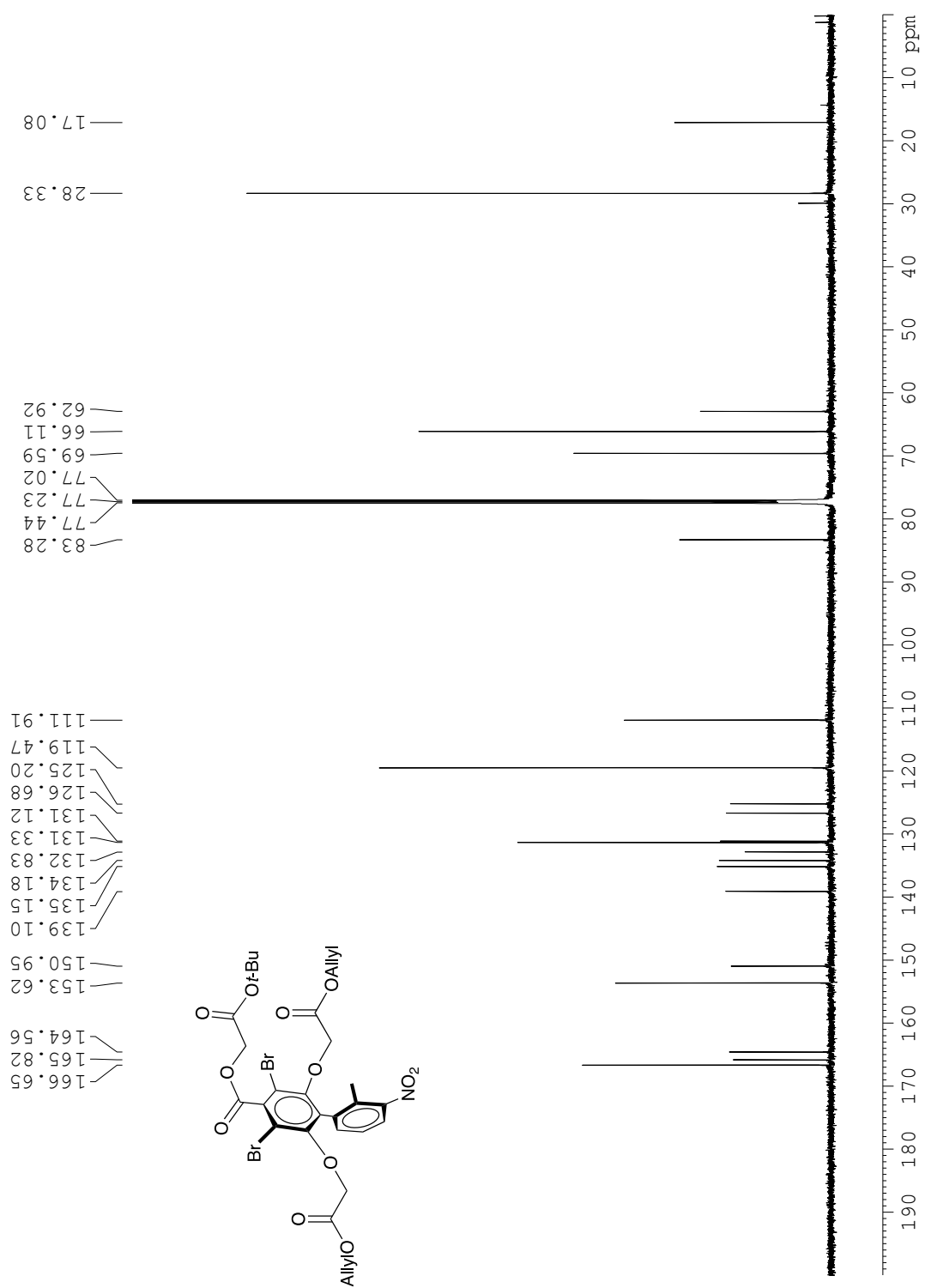


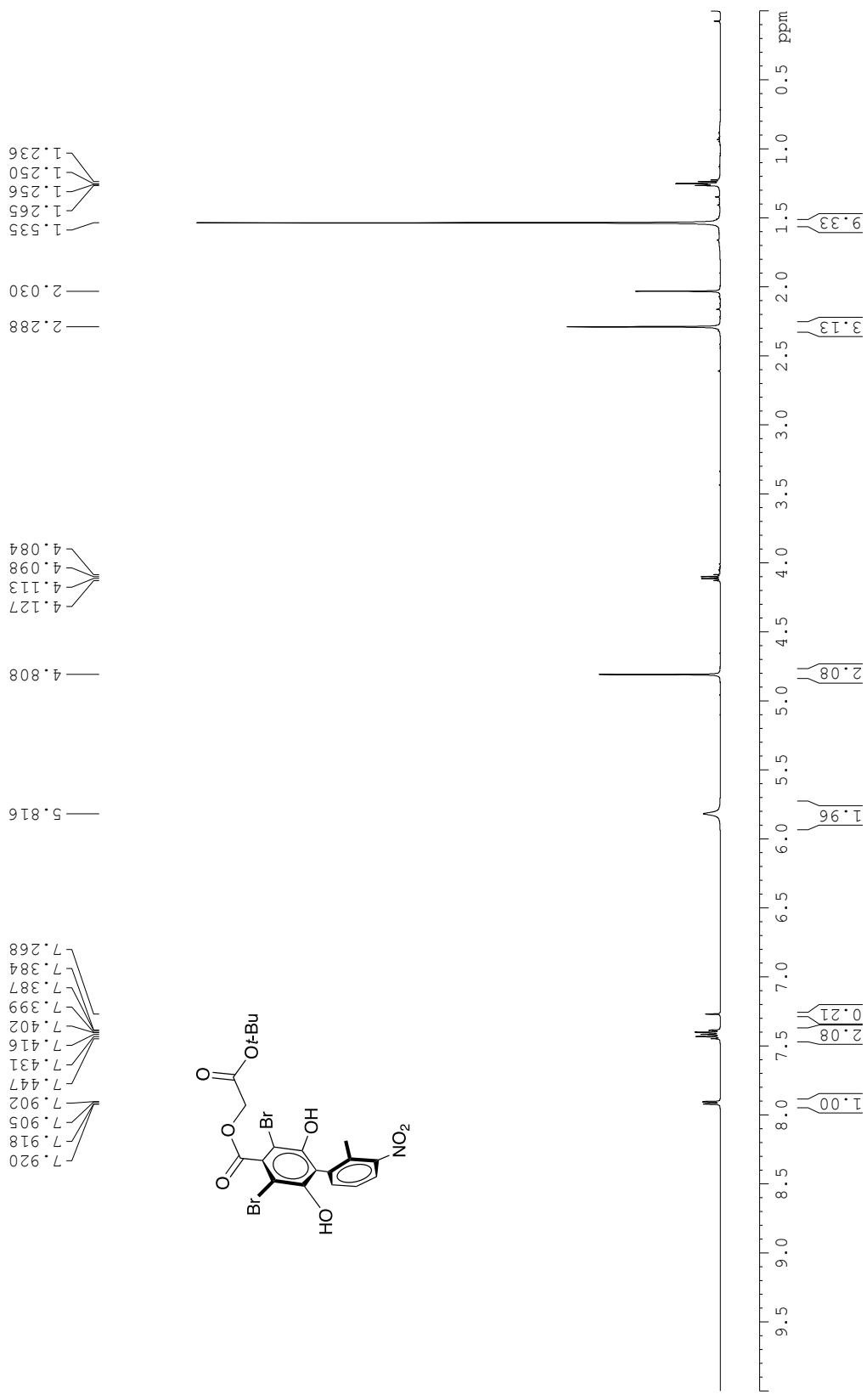


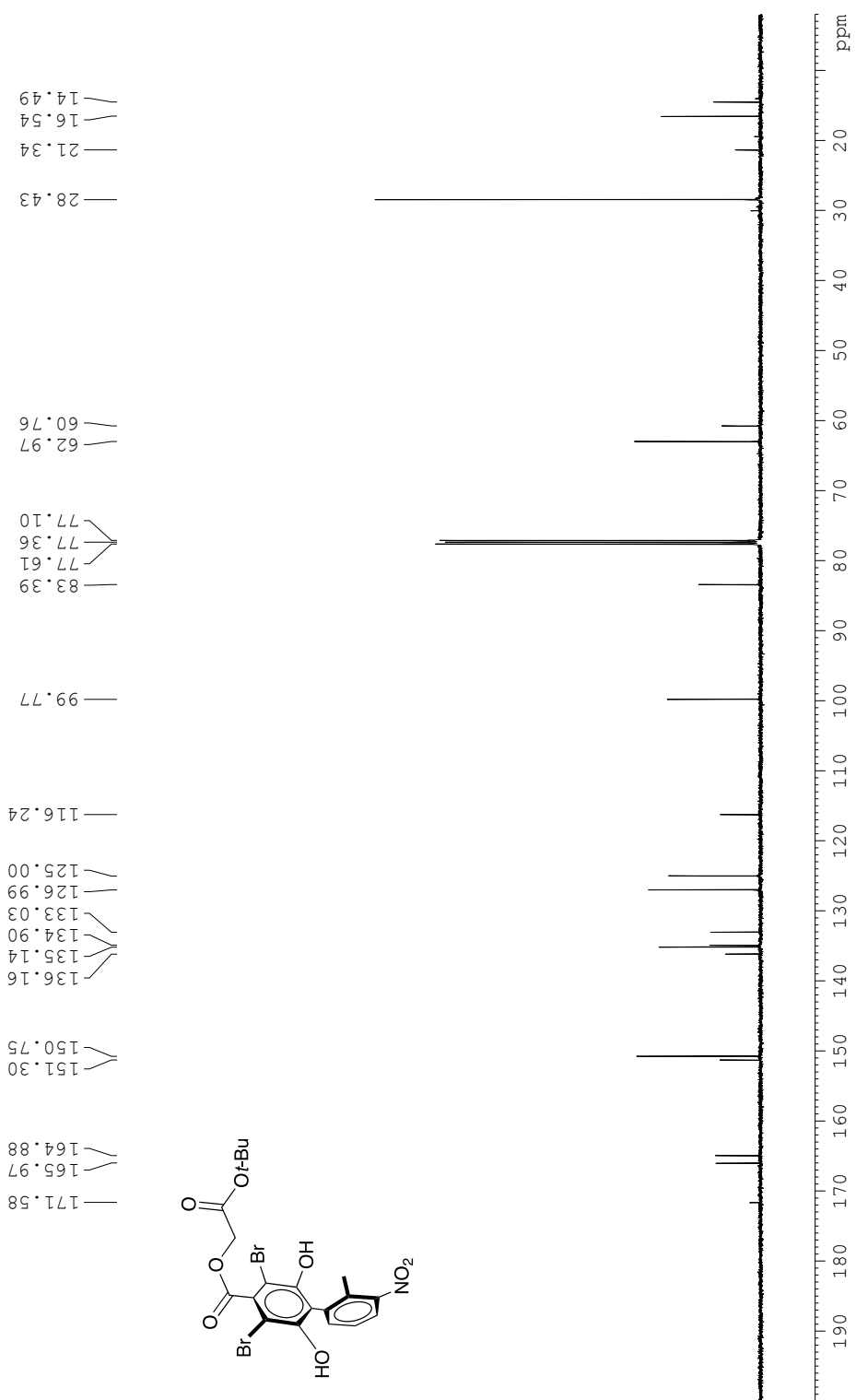








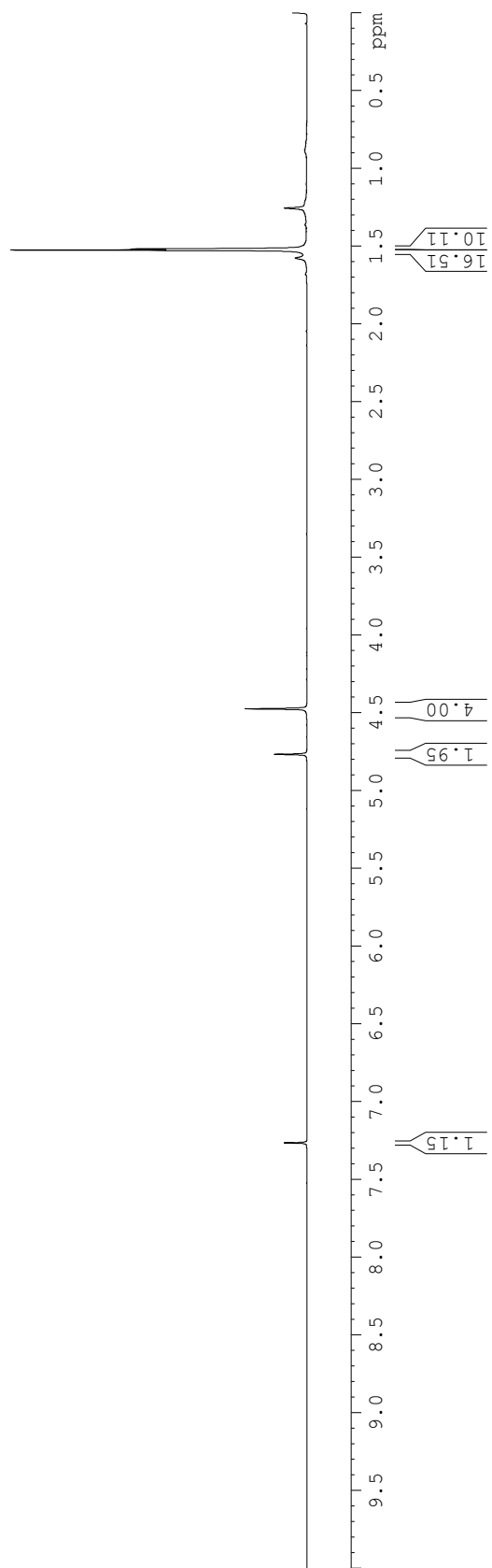
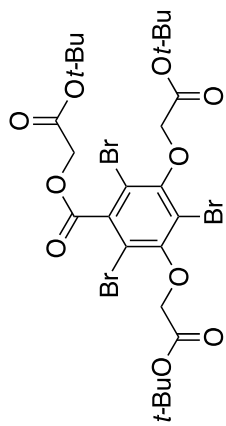


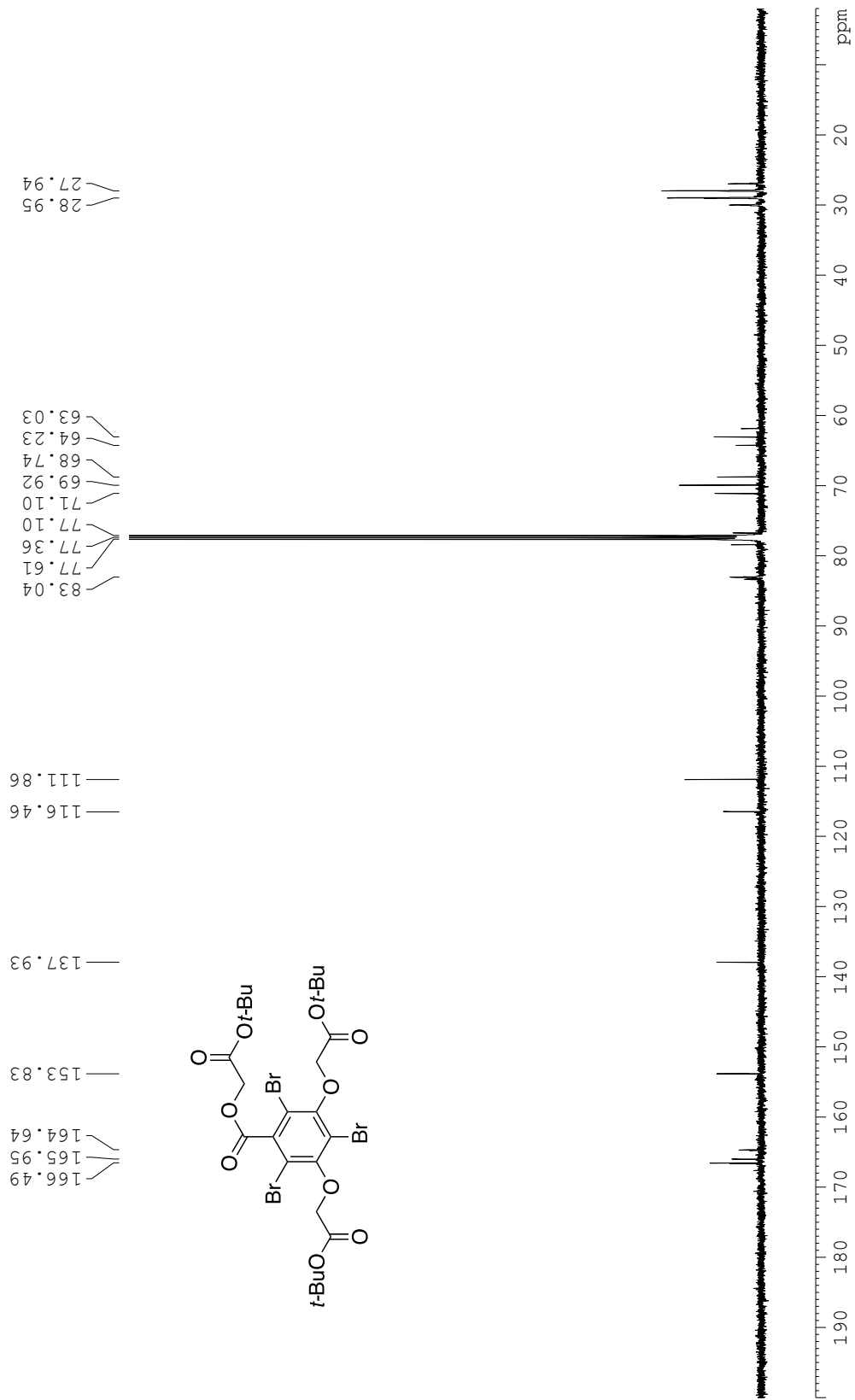


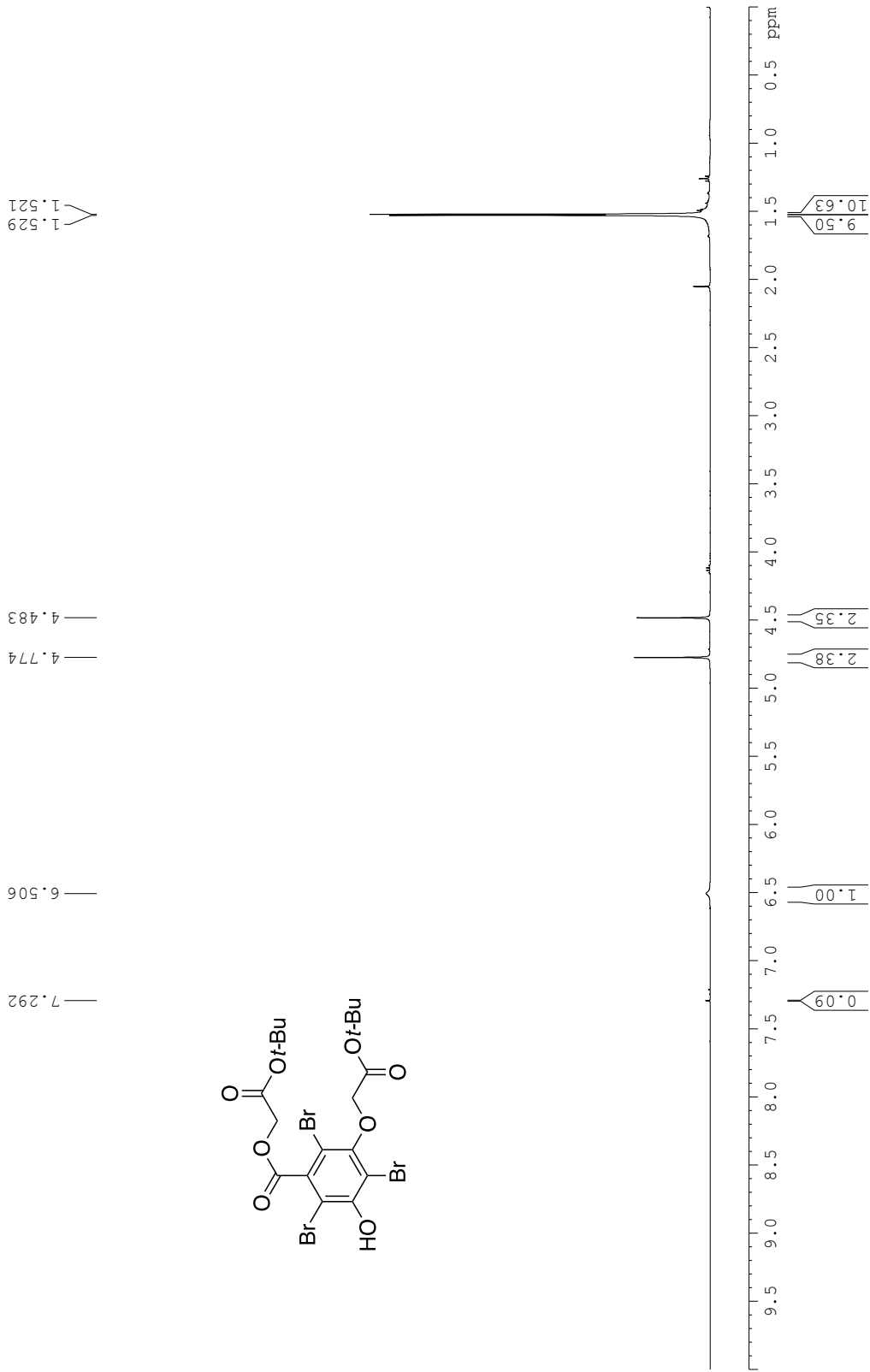
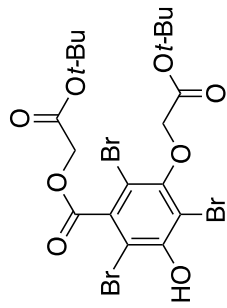
1.525
1.518
1.255

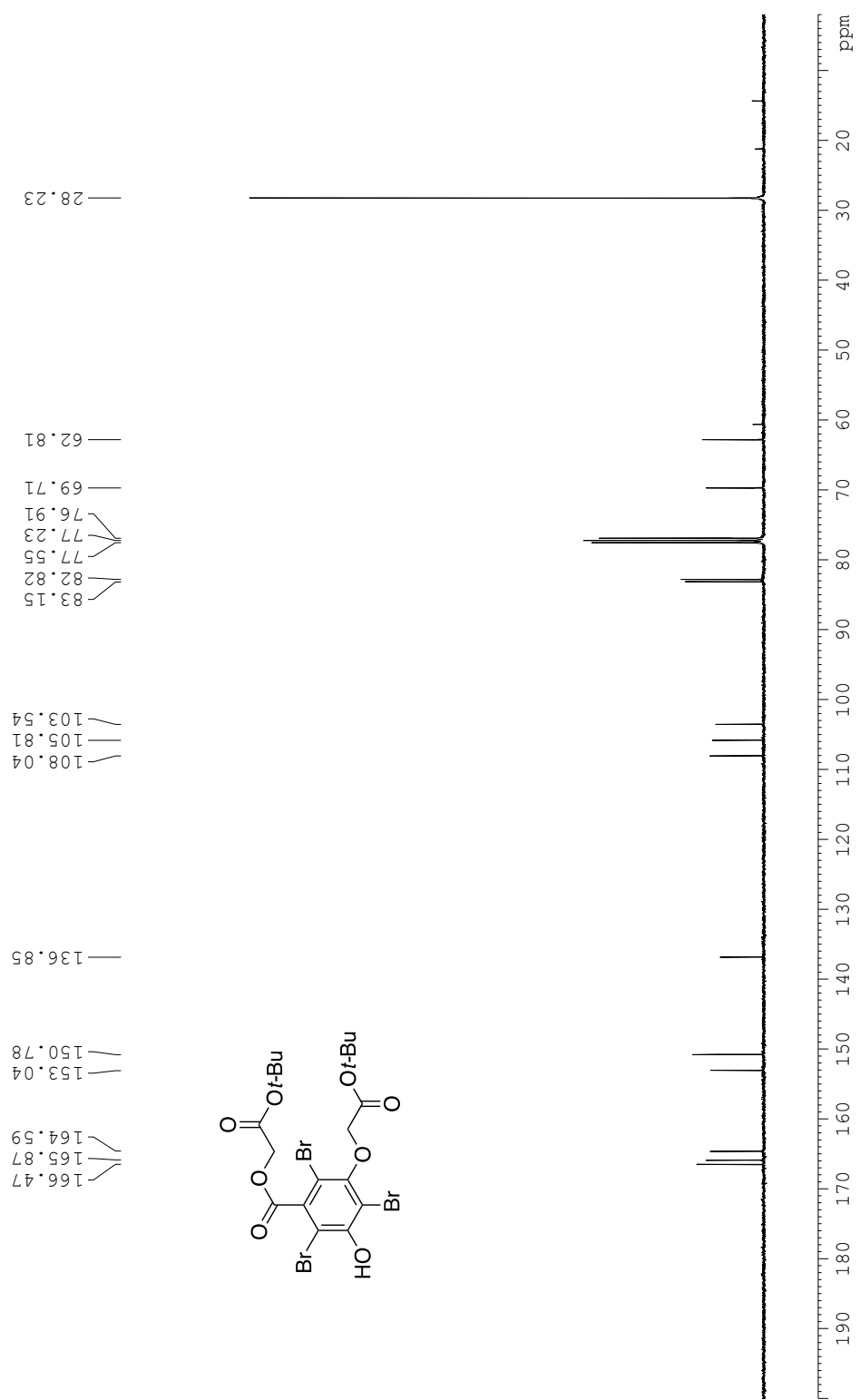
4.767
4.474

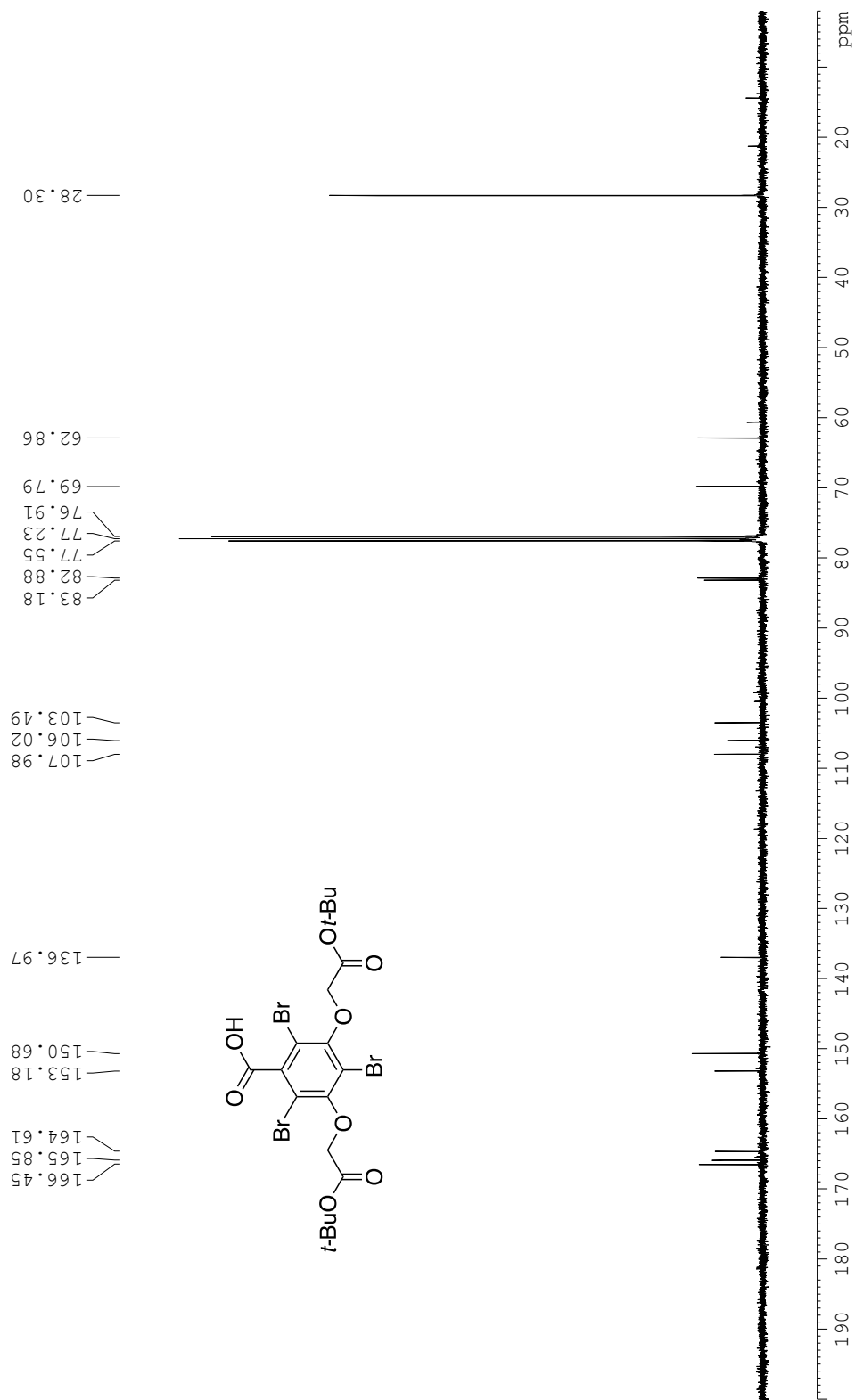
7.265

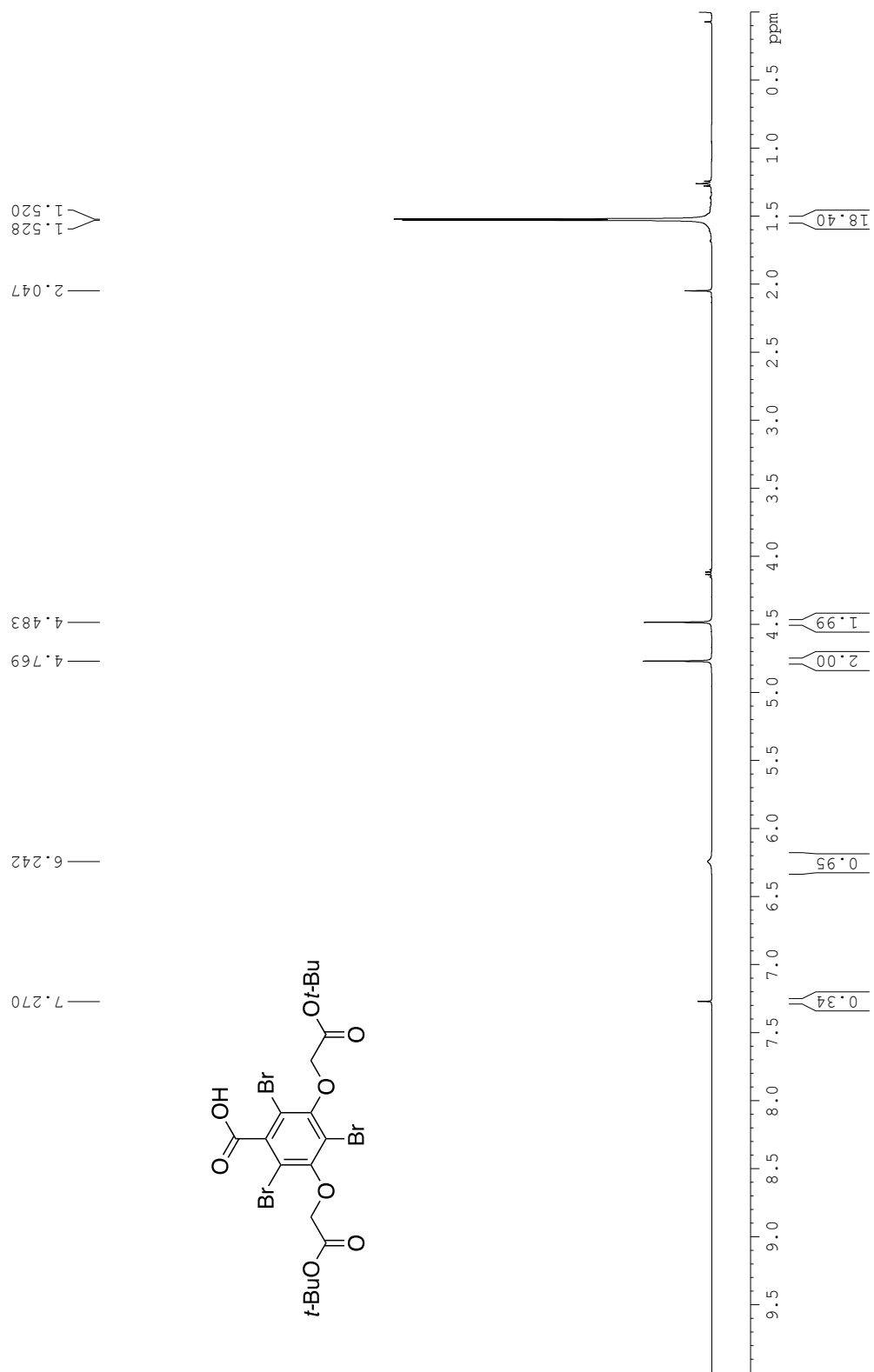


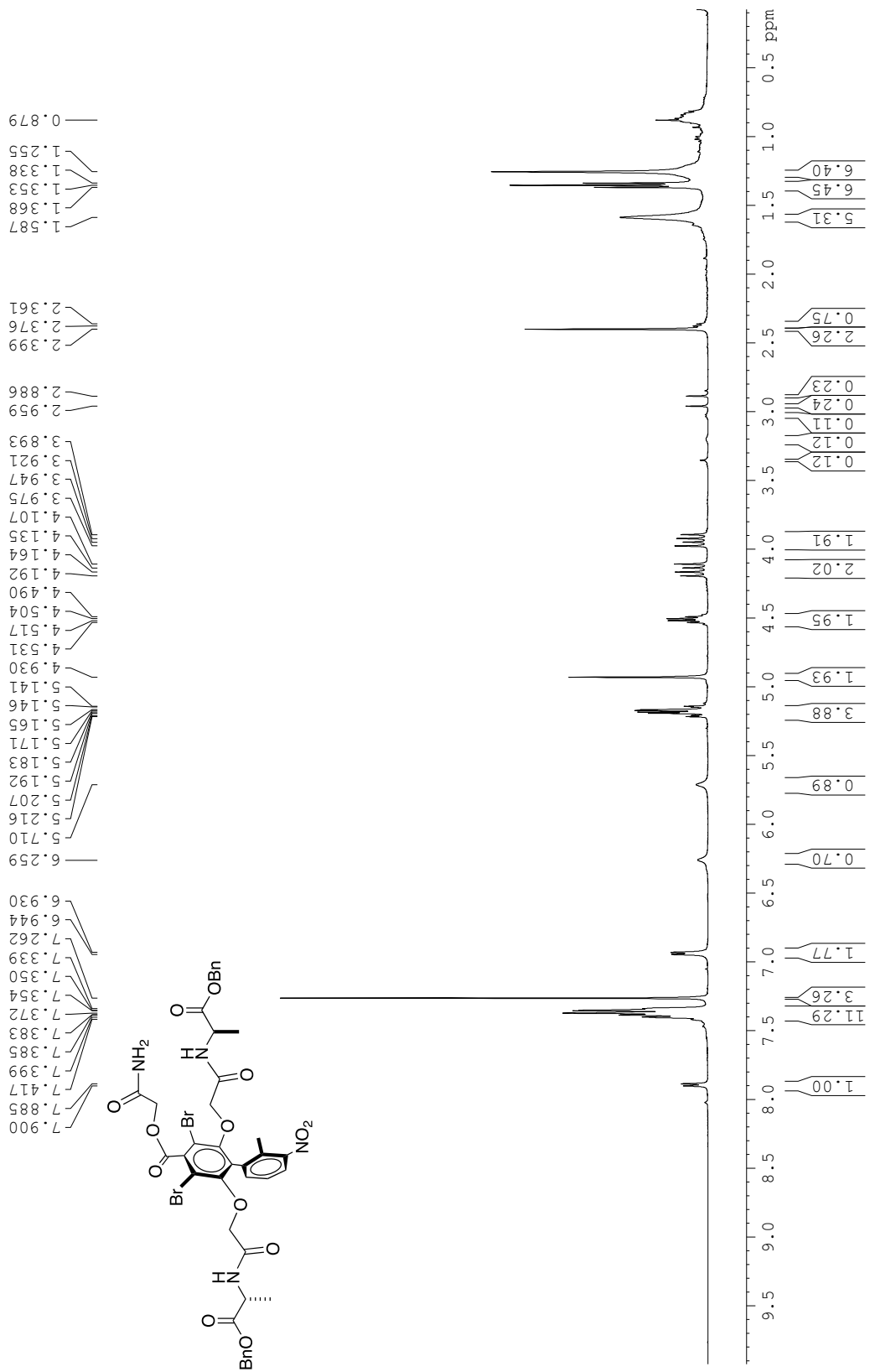


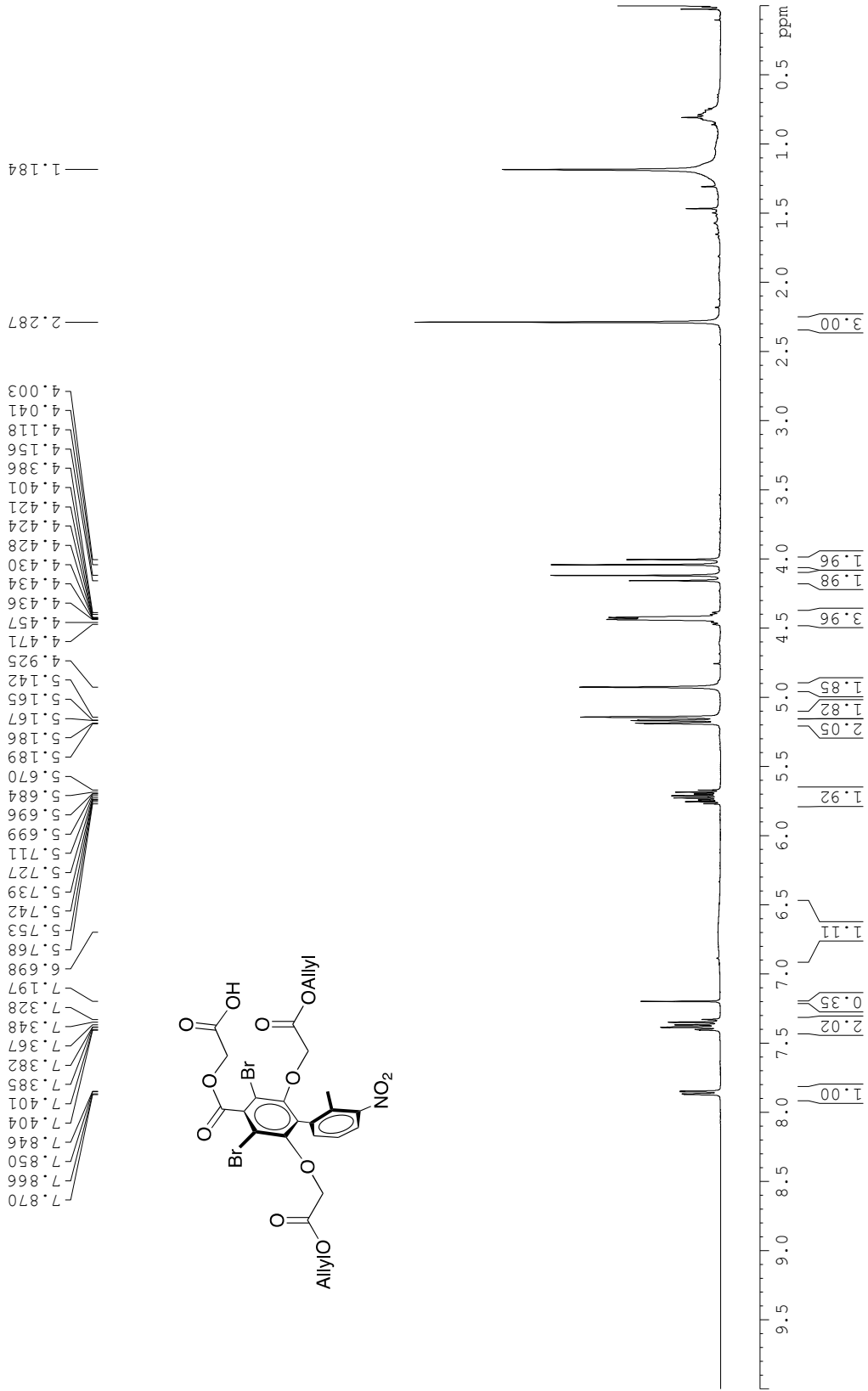


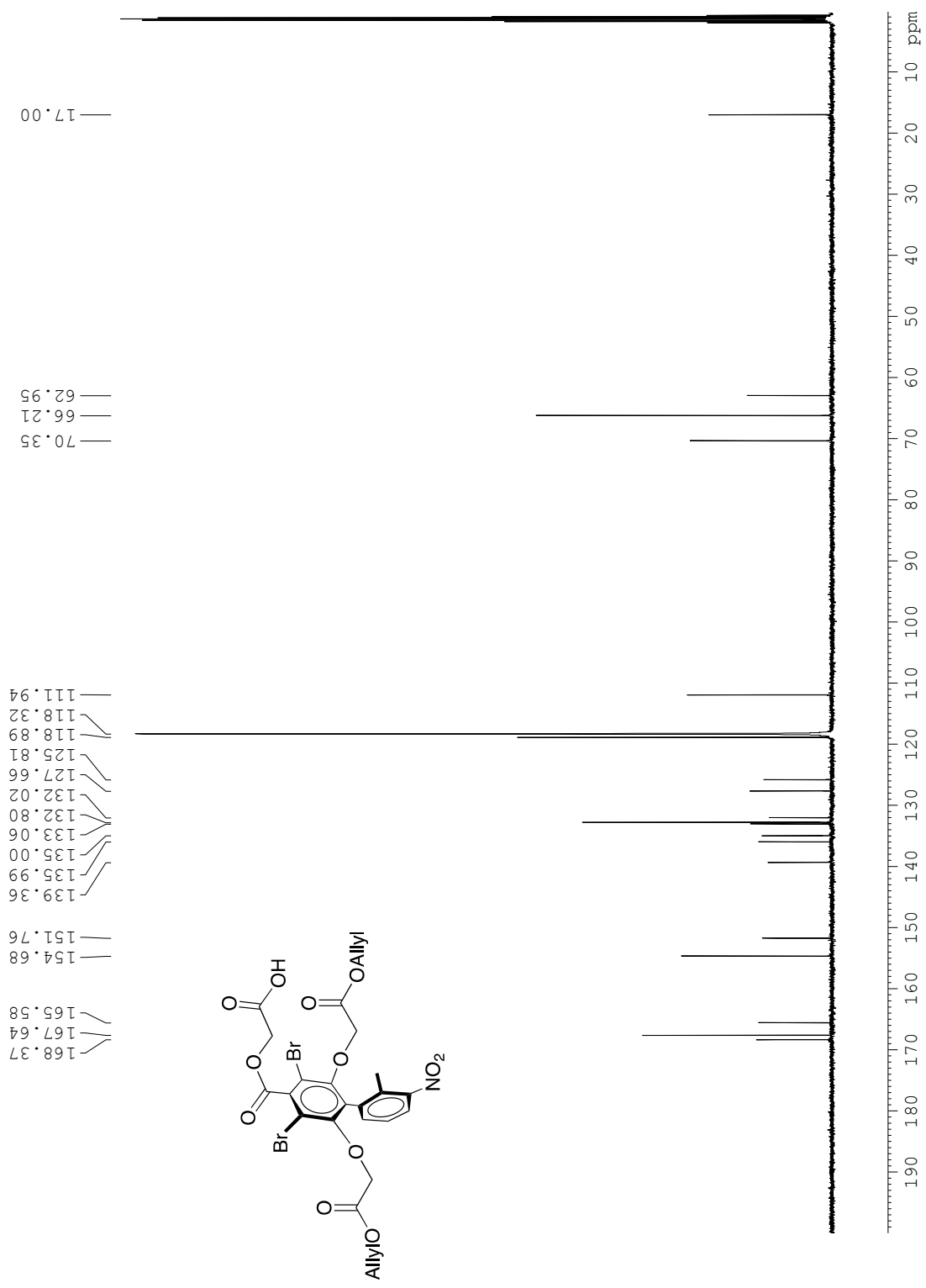


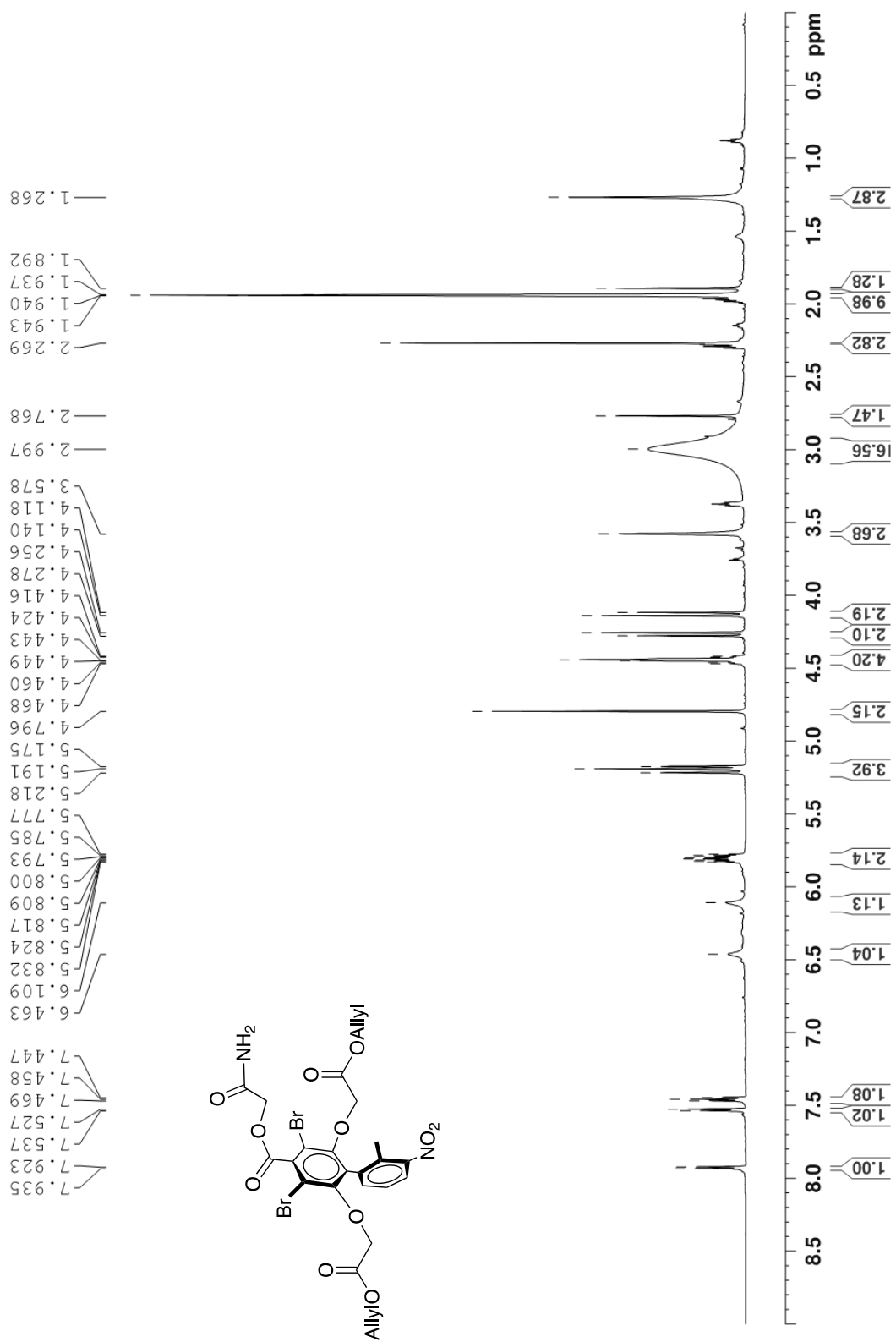


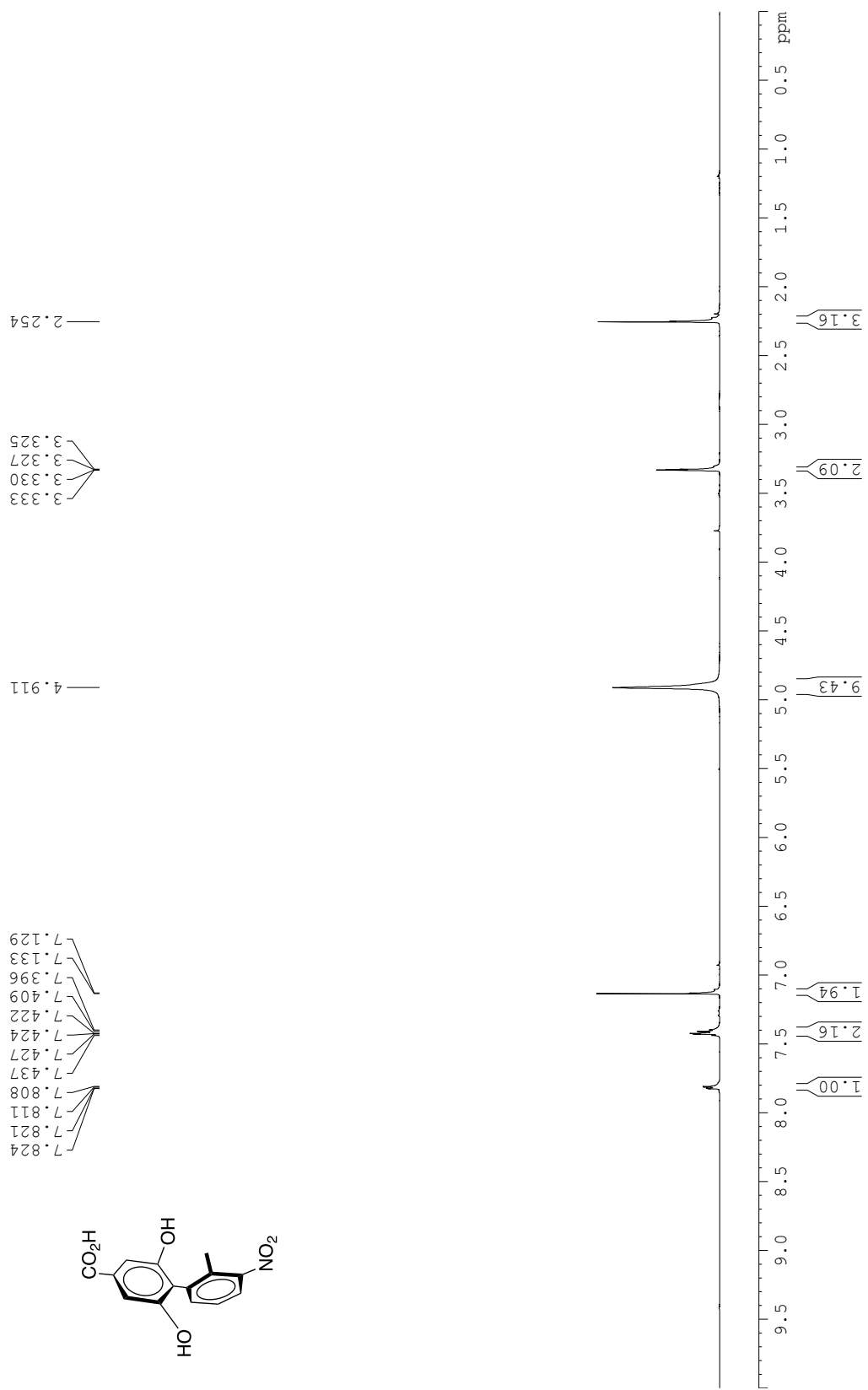


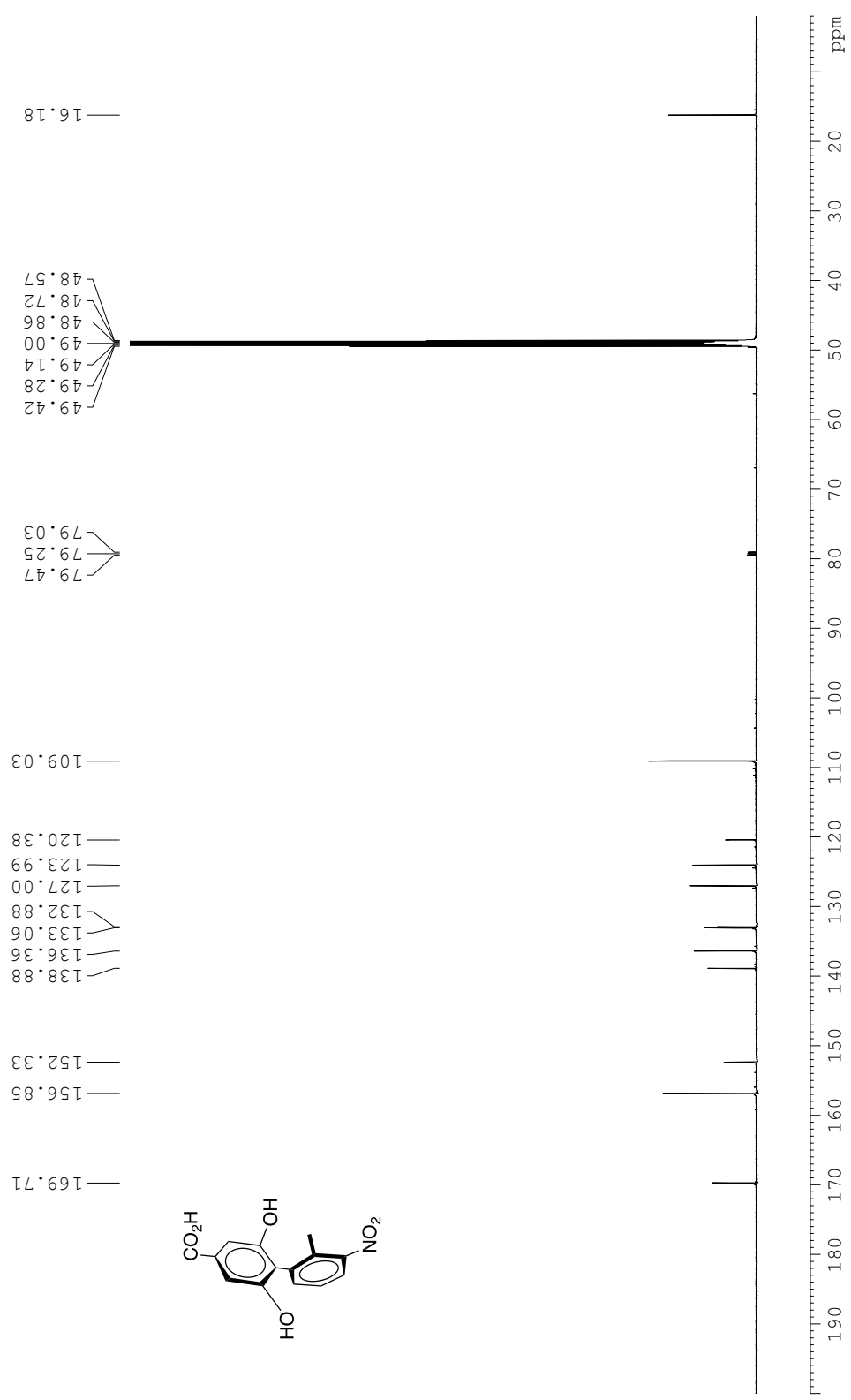


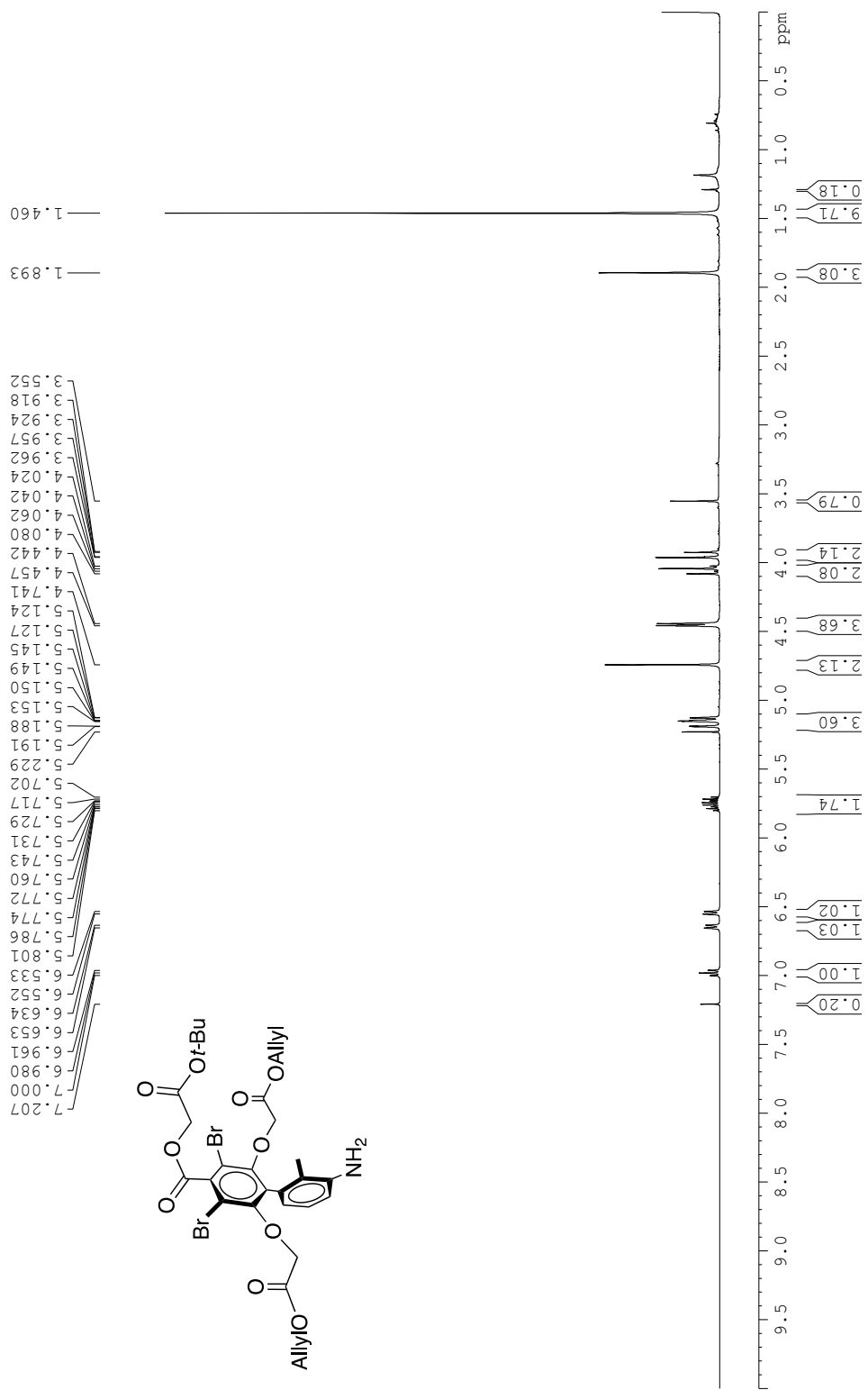


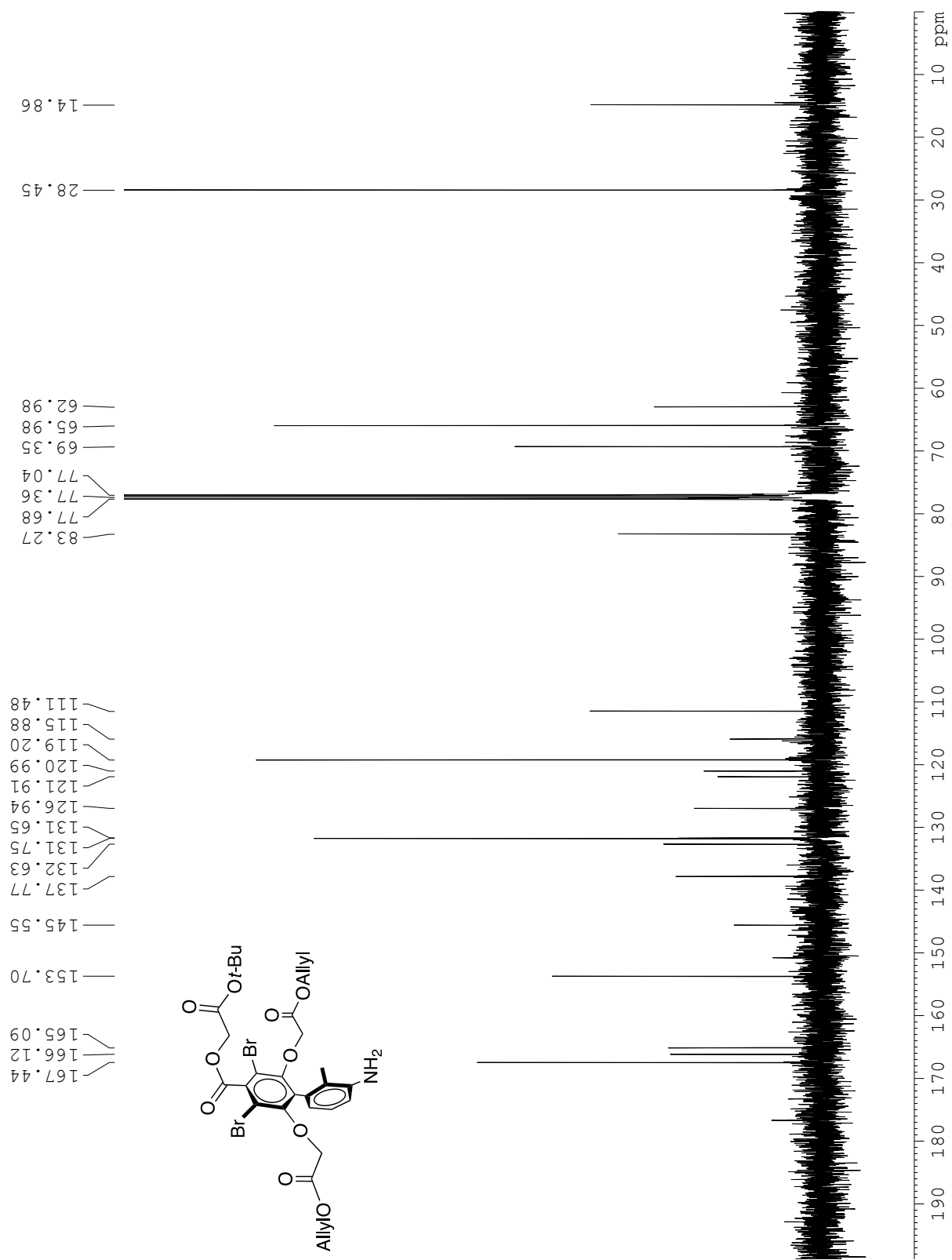












BIBLIOGRAPHY

1. (a) Kanagaraj, K.; Alagesanm, M.; Inoue, Y.; Yang, C. *Comp Supramolec. Chem.* **2017**, *2*, 11-60. (b) Janin, J. *Structure.* **1999**, *7*, 277-279.
2. (a) C. N. Pace, J. M. Scholtz and G. R. Grimsley, *FEBS Lett.*, **2014**, 588, 2177. (b) Jerome M. Fox, J.M. et al., *Annual Review of Biophysics.* **2018**, *47*, 223-250.
3. Hawkins, P.C.D. *J. Chem. Inf. Model.* **2017**, *57*, 1747-1756.
4. Berman, H. M.; Westbrook, J.; Feng, Z.; Gilliland, G.; Bhat, T. N.; Weissig, H.; Shindyalov, I. N.; Bourne, P. E. *The Protein Data Bank. Nucleic Acids Res.* **2000**, *28*, 235-42.
5. Groom, C. R.; Bruno, I. J.; Lightfoot, M. P.; Ward, S. C. *The Cambridge Structural Database. Acta Crystallogr., Sect. B: Struct. Sci., Cryst. Eng. Mater.* **2016**, *72*, 171-179.
6. Ferraro, M; Colombo, G. *Molecules*, **2018**, *23*, 2256.
7. Torchia, D.A., *Progress in Nuclear Magnetic Resonance Spectroscopy*, **2015**, *84*, 14-32.
8. (a) Verdine, G.L. and Walensky, L.D. *Clin. Cancer Res.*, **2007**, *13*, 7254-70. (b) Benilova, I; Karran, E. De Strooper, B., *Nat Neurosci.*, **2012**, *15*, 349-357.
9. Lau, J.L. and Dunn, M.K. *Bioorg. Med. Chem.* **2018**, *26*. 2700-07.
10. Wuo, M.G., Arora, P.S. *Curr. Opin. in Chem. Biol.* **2017**, *38*, 45-51.
11. Obexer, R.; Walport, L.J.; Suga, H. *Curr. Opin. in Chem. Biol.* **2017**, *38*, 52-61.
12. Gurwitz, D. *Drug. Dev. Res.*, *78*, **2017**, 231-235.
13. (a) Banting, F.G., Best, C.H., Collip, J.B., Campbell, W.R., Fletcher, A.A., *Can Med Assoc J.* **1922**, *12*, 141-6; (b) Gopalakrishnan, R.; Frolov, A.I.; Knerr, L.; Drury, III, W.J.; Valuer, E. *J. Med. Chem.* **2016**, *59*, 9599-9621.
14. (a) Dahlin, J.L. and Walters M.A. *Future Med Chem.*, **2014**, *11*, 1265-90. (b) Czodrowski, P. et al., *J. Med. Chem.*, **2016**, *59*, 9337-9349.
15. Lee, Y.; Basith, S.; Choi, S. *J. Med. Chem.* **2018**, *61*, 1-46.
16. Di, L., *The AAPS Journal*, **2015**, *17*, 134-143.
17. (a) Zorzi, A.; Deyle, K.; Heinis, C. *Curr. Opin. Chem. Biol.*, **2017**, *38*, 24-29. (b) Wang, Z.A.; Ding, X.Z.; Tiana, C.; Zheng, J. *RSC Adv.*, **2016**, *6*, 61599.
18. (a) Smith, C.K., Withka, J. Regan, L. *Biochemistry*, **1994**, *33*, 5510-5517; (b) Horne, W. S.; Gellman, S. H. *Acc. Chem. Res.*, **2008**, *41*, 1399-1408; (c) Reinert, Z.E.; Lengyel, G.A.; Horne, W.S. *J. Am. Chem. Soc.* **2013**, *135*, 12528-12531; (d) Lengyel, G.A. and Horne W. S. *J. Am. Chem. Soc.* **2012**, *134*, 15906-15913.
19. Olson, G.L.; Voss, M.E.; Hill, D.E.; Kahn, M.; Madison, V.S.; Cook C. M. *J. Am. Chem. Soc.* **1990**, *112*, 323-333.
20. Kreutzer, A.G. and Nowick, J.S. *Acc. Chem. Res.*, **2018**, *51*, 706-718.
21. (a) O. Kutzki, H. S. Park, J. T. Ernst, B. P. Orner, H. Yin and A. D. Hamilton, *J. Am. Chem. Soc.*, **2002**, *124*, 11838-11839; (b) Jayatunga, M. K. P.; Thompson, S.; Hamilton, A.D. *Bioorg. Med. Chem. Lett.* **2014**, *24*, 717-24; (c) Azzarito, V.; Long, K.; Murphy, N. S.; Wilson, A. *J. Nat. Chem.* **2013**, *5*, 161-173; (d) Thompson, S.; Vallinayagam, R. Adler, M.J. Scott, R.T.W.; Hamilton, A. D. *Tetrahedron* **2012**, *68*, 4501-05.
22. (a) Z.E. Reinert, W.S. Horne. *Org. Biomol. Chem.* **2014**, *12*, 8796-8802. (b) Kim, C., Jung, J., Tunga, T.T., Park, S.B., *Chem. Sci.*, **2016**, *7*, 2753. (c) *Int. J. Mol. Sci.* **2015**, *16*, 6513-6531.

23. Kaul, R., Deechongkit, S., Kelly, J.W. *J. Am. Chem. Soc.*, **2002**, *124*, 900–11907.
24. (a) Arnesen T. *PLoS Biol.* **2011**, *9*, 5. (b) Koehler MFT, Zobel K, Beresini MH, Caris LD, Combs D, Paasch BD, Lazarus RA. *Bioorg & Med Chem Lett.* **2002**, *12*, 2883–2886.
25. Ferrie, J.J.; Gruskos, J.J.; Goldwaser, M.E.; Guarracino, D.A. *Bioorg. Med. Chem. Lett.* **2013**, *23*, 989–995.
26. (a) Weinstain, R., Savariar, E.N., Felsen, C.N., Tsien, R.Y., *J Am Chem Soc.* **2014**, *136*, 874–877. (b) Soler M, Gonzalez M, Soriano-Castell D, Ribas X, Costas M, Tebar F, Massaguer A, Feliu L, Planas M. *Org & Biomol Chem.* **2014**. Pessi A, Langella A, Capitò E, Ghezzi S, Vicenzi E, Poli G, Ketas T, Mathieu C, Cortese R, Horvat B, Moscona A, Porotto M. *A General PLOS One.* **2012**, *7*, 36833.
27. Parsegian, V. A. “Van der Waals Forces – A Handbook for Biologists, Chemists, Engineers, and Physicists” *Cambridge University Press, Cambridge*, **2006**.
28. (a) London, F. *Trans. Faraday Soc.* **1936**, *33*, 8-26. (b) Carroll, W. R.; Pellechia, P. J.; (b) Shimizu, K. D. *Org. Lett.* **2008**, *10*, 4547-4550; (c) Cummings, C. G.; Hamilton, A. D. *Curr. Opin. Chem. Biol.* **2010**, *14*, 342-347; (c) Mati, I. K.; Cockroft, S. L. *Chem. Soc. Rev.* **2010**, *39*, 4195- 4205; (d) Carroll, W. R.; Zhao, C.; Smith, M. D.; Pellechia, P. J.; Shimizu, K. D. *Org. Lett.* **2011**, *13*, 4320-4323.
29. (a) Paliwal, S.; Geib, S.; Wilcox, C. S. *J. Am. Chem. Soc.* **1994**, *116*, 4497-4498; (b) Bhayana, B.; Ams, M. R. *J. Org. Chem.* **2011**, *76*, 3594-3596; (c) Bhayana, B. *J. Org. Chem.* **2013**, *78*, 6758-6762;
30. (a) C. S. Wilcox, M. D. Cowart, *Tetrahedron Lett.* **1986**, *27*, 5563–66. (b) Cowart, M.D.; Sucholeiki, I.; Bukownik, R.R.; Wilcox, C.S. *J. Am. Chem. Soc.* **1988**, *110*, 6204– 6210.
31. Wilcox, C.S. *Tetrahedron Lett.* Tröger base analogs - new structural units for the preparation of chiral hosts and metal ligands, **1985**, *26*, 5749–5752.
32. Rúnarsson, O.V.; Artacho, J.; Wärnmark, K. *Eur. J. Org. Chem.* **2012**, 7015–7041.
33. (a) T. H. Webb, H. Suh, C. S. Wilcox, *J. Am. Chem. Soc.* **1991**, *113*, 8554–55; (b) C. S. Wilcox, J. C. Adrian, T. H. Webb, F. J. Zawacki, *J. Am. Chem. Soc.* **1992**, *114*, 10189–97; (c) M. Miyake, C. S. Wilcox, *Heterocycles* **2002**, *57*, 515–22.
34. Goswami, S.; Ghosh, K.; Dasgupta, S. *J. Org. Chem.* **2000**, *65*, 1907-1914.
35. (a) E. Yashima, M. Akashi, N. Miyauchi, *Chem. Lett.* **1991**, 1017–1020; (b) A. Tatibouët, M. Demeunynck, J. Lhomme, *Synth. Commun.* **1996**, *26*, 4375–4395; (c) A. Tatibouët, M. Demeunynck, H. Salez, R. Arnaud, J. Lhomme, C. Courseille, *Bull. Soc. Chim. Fr.* **1997**, *134*, 495–501; (d) B. Baldeyrou, C. Tardy, C. Bailly, P. Colson, C. Houssier, F. Charmantray, M. Demeunynck, *Eur. J. Med. Chem.* **2002**, *37*, 315–322.
36. Q. Xin et al., *Org. Electron.* **2008**, *9*, 1076–1086.
37. Tröger, J. *J. Prakt. Chem.* **1887**, *36*, 225.
38. Spielman, M.A. *J. Am. Chem. Soc.* **1935**, *57*, 583–585.
39. S. B. Larson, C. S. Wilcox, *Acta Crystallogr., Sect. C: Cryst. Struct. Commun.* **1986**, *42*, 224–227; (b) Cornago, P.; Claramunt, R.M.; Bouissane, L.; Elguero, J. *Tetrahedron* **2008**, *64*, 3667–3673.
40. (a) Shokhirev, N. V.; Shokhireva, T. Kh.; Polam, J. R.; Watson, C. T.; Raffii, K.; Simonis, U.; Walker, F. A. *J. Phys. Chem.* **1997**, *101*, 2778-2786. (b)Whittaker, S. B.; Boetzel, R.; MacDonald, C.; Lian, L. Y.; Pommer, A. J.; Reilly, A.; James, R.; Kleanthous, C.; Moore, G. R. *J. Biomol. NMR* **1998**, *12*, 145-59. (c)Vassilev, N. G.; Dimitrov, V. S. *Mag. Res. Chem.* **2001**, *39*, 607-614. (d) Saudan, C.; Dunand, F. A.; Abou-Hamdan, A.; Bugnon, P.; Lye, P. G.; Lincoln, S. F.; Merbach, A. E. *J. Am. Chem. Soc.* **2001**, *123*, 10290-

10298. (e) Cossio, F. P.; De la Cruz, P.; De la Hoz, A.; Langa, F.; Martin, N.; Prieto, P.; Sanchez, L. *Eur. J. Org. Chem.* **2000**, *13*, 2407-2415.
41. Kim, E.; Paliwal, S.; Geib, S.; Wilcox, C.S. *J. Am. Chem. Soc.* **1998**, *120*, 11192–11193.
42. Olsen, J. A.; Banner, D. W.; Seiler, P.; Wagner, B.; Tschopp, T.; Obst-Sander, U.; Kansy, M.; Mueller, K.; Diederich, F. *Chem Bio Chem.* **2004**, *5*, 666-675.
43. Gouverneur, V. *Science.* **2009**, *325*, 1630-1631.
44. Diederich, F. *Science.* **2007**, *317*, 1881-1886.
45. (a) Hof, F.; Scofield, D. M.; Schweizer, W. B.; Diederich, F. *Angew. Chem., Int. Ed.* **2004**, *43*, 5056-5059. (b) Fischer, F. R.; Schweizer, W. B.; Diederich, F. *Angew. Chem., Int. Ed.* **2007**, *46*, 8270-8273.
46. Adams, H.; Carver, F. J.; Hunter, C. A.; Morales, J. C.; Seward, E. M. *Angew. Chem., Int. Ed. Engl.* **1996**, *35*, 1542-1544.
47. (a) Bhayana, B.; Wilcox, C. S. *Angew. Chem. Int. Ed.* **2007**, *46*, 6833-6836; (b) Bhayana, B., “Experimental and theoretical investigations in solid phase reaction kinetics and noncovalent interactions in water.” *University of Pittsburgh: Pittsburgh, PA, 2007*.
48. Metrangolo, P; Neukirch, H. Pilati, T., Resnati, G. *Acc. Chem Res.* **2005**, *38*, 386-95.
49. Keyser, S. K. “Evaluation of the halogen bond and the salt bridge interaction using the molecular torsion balance.” *University of Pittsburgh: Pittsburgh, PA, 2010*.
50. (a) Musafia, B.; Buchner, V.; Arad, D. *J. Mol. Bio.* **1995**, *254*, 761-70.; (b) Zubillaga R. A; Garcia-Hernandez E.; Camarillo-Cadena M.; Leon M.; Polaina, J. *Prot. Peptide Lett.* **2006**, *13*, 113-8; (c) Bosshard, H. R.; Marti, D. N.; Jelesarov, I. *J. Mol. Recognition* **2004**, *17*, 1-16; (d) Ahmed. M.C., Papaleo, E, Lindorff-Larsen, K. *Peer J* **2018**, *6*, 4967.
51. Thomas, A. S.; Elcock, A. H. *J. Am. Chem. Soc.* **2004**, *126*, 2208-2214.
52. Ling, X. “Synthesis of protein folding models and a molecular torsion balance study of neighboring group effects on hydrophobically driven folding.” Ph.D. Dissertation, **University of Pittsburgh**, Pittsburgh, PA, **2014**.
53. (a) Huang, D. M.; Chandler, D. *Proc. Natl. Acad. Sci. USA* **2000**, *97*, 8324-8327; (b) Lum, K.; Chandler, D.; Weeks, J. D. *J. Phys. Chem.* **1999**, *103*, 4570-4577; (c) Yang, L.; Adam, C.; Nichol, G. S.; Cockroft, S. L. *Nat. Chem.* **2013**, *2913*, 1006-1010; (d) Cockroft, S.L.; Hunter, C.A. *Chem. Commun.* **2006**, *36*, 3806–3808.
54. (a) Johnson, M.J.; Horne, S.; Gellman, S.H. *J. Am. Chem. Soc.* **2011**, *133*, 10038–10041. (b) Bogan, A.B. and Thorn, K.S. *J. Mol. Biol.* **1998**, *280*, 1-9. (c) Buhlage, S. J.; Bates, C. A.; Rowe, S. P.; Minter, A. R.; Brennan, B. B.; Majmudar, C. Y.; Wemmer, D. E.; Al-Hashimi, H.; Mapp, A. K. *ACS Chem. Biol.* **2009**, *4*, 335. (d) Nicholas Dominelli-Whiteley, James J. Brown, Kamila B. Muchowska, Ioulia K. Mati, Catherine Adam, Thomas A. Hubbard, Alex Elmi, Alisdair J. Brown, Ian A. W. Bell, and Scott L. Cockroft. *Angew. Chem.* **2017**, *129*, 7766–70.
55. Zhou P, Wang C, Ren Y, Yang C, Tian F. *Curr Med Chem.* **2013**, *20*, 1985–1996.
56. (a) Ciemny MP, Kurcinski M, Kozak KJ, Kolinski A, Kmiecik S. *Methods in Molecular Biology*, Vol 1561. New York, NY, *Humana Press*, **2017**. (b) Farhadi T, Fakharian A, Ovchinnikov RS. *Interdisciplin Sci.* **2017**.
57. (a) Yagi Y, Terada K, Noma T, Ikebukuro K, Sode K. *BMC Bioinformatics.* **2007**, *8*, 11. (b) Kellenberger E, Rodrigo J, Muller P, Rognan D. *Proteins.* **2004**, *57*, 225–242. (c) Farhadi T. *Int J Pept Res Ther.* **2017**, 1–12. (d) Desmet J, Wilson IA, Joniau M, de Maeyer M, Lasters I. *FASEB J.* **1997**, *11*, 164–172. (e) Antes I.D., *Proteins.* **2010**, *78* (5), 1084–1104.

58. (a) Pabo C. *Nature*. **1983**, *301*, 200. (b) Drexler KE. *Proc Natl Acad Sci USA*. **1981**, *78*, 5275–8.
59. (a) Veber, D. F.; Strachan, R. G.; Bergstrand, S. J.; Holly, F. W.; Homnick, C.F.; Hirschmann, R. *J. Am. Chem. Soc.* **1976**, *98*, 2367. (b) Veber, D. F.; Holly, F. W.; Palveda, W. J.; Nutt, R. F.; Bergstrand, S. J.; Torchiana, M.; Glitzer, M. S.; Saperstein, R.; Hirschmann, R. *Proc. Natl. Acad. Sci. U.S.A.* **1978**, *75*, 2636. (c) Veber, D.F.; Saperstein, R.; Nutt, R. F.; Freidinger, R. M.; Brady, S. F.; Curley, P.; Perlow, D. S.; Palveda, W. J.; Colton, C. D.; Zacchei, A. G.; Two, D. J.; Hoff, D. R.; Vandlen, R. L.; Gerich, J. E.; Hall, L.; Mandarino, L.; Cordes, E. H.; Anderson, P. S.; Hirschmann, R. *Life Sci.* **1984**, *34*, 1371. (d) Freidinger, R. M.; Veber, D. F.; Schwenk Perlow, D. *Science* **1980**, *210*, 656.
60. Roy A, Nair S, Sen N, Soni N, Madhusudhan MS. *Methods*. **2017**, *131*, 33–65.
61. Horne, W. S. *Expert Opin. Drug Discovery* **2011**, *6*, 1247–62.
62. Farhadi, T.; and Seyed M., Hashemian, R. *Drug Des Devel Ther.* **2018**; *12*, 1239–1254.
63. Horne, W. S.; Price, J. L.; Keck, J. L.; Gellman, S. H. *J. Am. Chem. Soc.* **2007**, *129*, 4178–80. Lengyel, G.A. and Horne W. S. *J. Am. Chem. Soc.* **2012**, *134*, 15906–13.
64. (a) Gellman, S. H. *Acc. Chem. Res.* **1998**, *31*, 173; (b) Espinosa, J.F.; Gellman, S.H. *Angew. Chem. Int. Ed.* **2000**, *39*, 2330–2333; (c) Newcomb, L.F.; Haque, T.S.; Gellman, S.H. *J. Am. Chem. Soc.* **1995**, *117*, 6509–6519; (d) Gardner, R. R.; Christianson, L.A.; Gellman, S.H. *J. Am. Chem. Soc.* **1997**, *119*, 5041–5042; (e) Gardner, R.R.; McKay, S.L.; Gellman, S.H. *Org. Lett.* **2000**, *2*, 2335–2338; (f) Gellman, S.H.; Dado, G. P.; Liang, G.B.; Adams, B.R. *J. Am. Chem. Soc.* **1991**, *113*, 1164–1173; (g) Matsumoto, M.; Lee, SJ; Marcey, W.; Gagne, M. *J. Am. Chem. Soc.* **2014**, *136*, 15817–15820.
65. (a) Nowick, J. S.; Chung, D. M.; Maitra, K.; Maitra, S.; Stigers, K. D.; Sun, Y. “An Unnatural Amino Acid that Mimics a Tripeptide beta-Strand and Forms beta-Sheetlike Hydrogen-Bonded Dimers” *J. Am. Chem. Soc.* 2000, *122*, 7654–61. (b) Harini, V. V.; Aravinda, S.; Rai, R.; Shamala, N.; Balaram, P. “Molecular Conformation and Packing of Peptide beta-Hairpins in the Solid State: Structures of Two Synthetic Octapeptides Containing 1-Aminocycloalkane-1-Carboxylic Acid Residues at the i+2 Position of the beta-Turn” *Chem. Eur. J.* 2005, *11*, 3609–3620. (c) Parisien, M.; Major, F. “A New Catalog of Protein beta-Sheets” *Proteins* 2005 *61*, 545–558. (d) Lassila, K. S.; Datta, D.; Mayo, S. L. “Evaluation of the energetic contribution of an ionic network to beta-sheet stability” *Protein Sci.* 2002 *11*, 688–690. (e) Nowick, J. S.; Lam, K. S.; Khasanova, T. V.; Kemnitzer, W. E.; Maitra, S.; Hao T. Mee, H. T.; Liu, R. “An Unnatural Amino Acid that Induces beta-Sheet Folding and Interaction in Peptides *J. Am. Chem. Soc.* 2002, *124*, 4972–4973. (f) Nowick, J. S.; Brower, J. O. “A New Turn Structure for the Formation of beta-Hairpins in Peptides” *J. Am. Chem. Soc.* 2003, *125*, 876–877. (g) Nowick, J. S.; Insaf, S. “The Propensities of Amino Acids To Form Parallel beta-Sheets *J. Am. Chem. Soc.* 1997, *119*, 10903–10908. (h) Deechongkit, S.; Kelly, J. W. “The Effect of Backbone Cyclization on the Thermodynamics of beta-Sheet Unfolding: Stability Optimization of the PIN WW Domain” *J. Am. Chem. Soc.* 2002, *124*, 4980–4986. (h) Lam, K.S.; Khasanova, T.V.; Kemnitzer, W.E.; Maitra, S.; Hao, T.; Mee, H.T.; Liu, R.; Nowick, J.S. *J. Am. Chem. Soc.* 2002, *124*, 4972–4973.
66. (a) Smith III, A.B. Hirschmann, R.F.; K. C. Nicolau, K.C.; Angeles, A.R. Chen, J.S. The beta-D-Glucose Scaffold as a beta-Turn Mimetic. (b) Krutzer, A.G. and Nowick, J.S. *Acc. Chem Res.* **2018**, *51*, 706–718.
67. (a) Kemp, D.S.; Li, Z.Q. *Tetrahedron Lett.* 1995, *36*, 4175–4178. (b) Kemp, D. S.; Li, Z. Q.

- Tetrahedron Lett.* 1995, 36, 4179–4180.
68. (a) C. L. Nesloney, J. W. Kelly, *J. Am. Chem. Soc.* 1996, 118, 5836–5845. (b) Tsang, K.Y.; Diaz, H.; Graciani, N.; Kelly, J.W. Hydrophobic Cluster Formation Is Necessary for Dibenzofuran-Based Amino Acids to Function as beta-Sheet Nucleators. *J. Am. Chem. Soc.* **1994**, 116, 3988-4005.
 69. (a) Suich, D. J.; Mousa, S.A.; Singh, G. Liapakis et al. *Bioorg. Med. Chem.*, **2000**, 8, 2229. (b) Brandmeier, V. and Feigel, M. *Tetrahedron*, **1989**, 45, 1365.
 70. (a) Walensky, L.D. et al., *Science*. **2004**, 305, 1466–1470; (b) A. M. Almeida, R. Li, S. H. Gellman, *J. Am. Chem. Soc.* **2012**, 134, 75–78; (c) White, C.J.; Yudin, A. K. *Nat. Chem.* **2011**, 3, 509.
 71. (a) Robinson, J.A.; DeMarco, S.; Gombert, F. Moehle, K.; Obrecht, D. *Drug Discovery Today*, **2008**, 13, 944-51. (b) Brust, A.; Wang, C.; Daly N.L. et al. *Angew. Chem. Int. Ed. Engl.* **2013**, 52, 12020-3. (c) Srinivas, N.; Moehle, K.; Abou-Hadeed, K.; Obrecht, D.; Robinson, J.A. *Org. Biomol. Chem.*, **2007**, 5, 3100–3105.
 72. (a) Spivey, A. C.; McKendrick, J.; Srikanan, R.; Helm, B. A. Helm, *J. Org. Chem.* **2003**, 68, 1843-51; Hamilton. (b) Lingard, H. Han. JT; Thompson, AL; Leung, KH, Scott, RTW, Thompson, Hamilton, A.D. *Angew. Chem. Int. Ed.* **2014**, 53, 3650 –3. (c) *J Pept Sci* **2014**, 20, 704-715.
 73. (a) F. Freire, S. H. Gellman, *J. Am. Chem. Soc.* **2009**, 131, 7970 – 7972; (b) Offermann, D. A.; McKendrick, J.E.; Sejberg, J. J. P.; Mo, B.; Holdom, M. D.; Helm, B. A.; Leatherbarrow, R. J.; Beavil, A. J.; Sutton, B. J.; Spivey, A. C. *J. Org. Chem.* **2012**, 77, 3197-214. (c) L. Halab, F. Gosselin and W. D. Lubell, *Biopolymers*, **2000**, 55, 101–22. (d) A. Khashper and W. D. Lubell, *Org. Biomol. Chem.*, **2014**, 12, 5052–70. (e) L. Halab, J. A. J. Becker, Z. Darula, D. Tourwe, B. L. Kieffer, F. Simonin and W. D. Lubell, *J. Med. Chem.*, **2002**, 45, 5353–57. (f) G. M. Grotenbreg, M. S. M. Timmer, A. L. Llamas-Saiz, M. Verdoes, G. A. van der Marel, M. J. van Raaij, H. S. Overklee and M. Overhand, *J. Am. Chem. Soc.* **2004**, 126, 3444–6. (g) J. Kruijtzter and R. Liskamp, *Org. Biomol. Chem.*, **2014**, 12, 4471–4478. (h) J. M. Smith, N. C. Hill, P. J. Krasniak and R. Fasan, *Org. Biomol. Chem.*, **2014**, 12, 1135–42. (i) D. Ranganathan, V. Haridas, S. Kurur, A. Thomas, K. P. Madhusudanan, R. Nagaraj, A. C. Kunwar, A. V. S. Sarma and I. L. Karle, *J. Am. Chem. Soc.* **1998**. Kokan, Z.; Glasovac, Z.; Elenkov, M.M. et al. *Organometallics*. **2014**, 33, 4005-15. (j) H. A. Lashuel, S. R. LaBrenz, L. Woo, L. C. Serpell, J. W. Kelly, *J. Am. Chem. Soc.* **2000**, 122, 5262 – 5277. (k) Y. Hamuro, A. D. Hamilton, *Bioorg. Med. Chem.* **2001**, 9, 2355 –2363; (l) J. S. Nowick, E. M. Smith, G. Noronha, *J. Org. Chem.* **1995**, 60, 7386 – 7387; (m) S. Chowdhury, G. Schatte, H.-B. Kraatz, *Angew. Chem.* **2008**, 120, 7164 – 7167; *Angew. Chem. Int. Ed.* **2008**, 47, 7056 – 7059. (n) F. Freire, S. H. Gellman, *J. Am. Chem. Soc.* **2011**, 133, 12318. (o) J. S. Nowick, *Acc. Chem. Res.* **2008**, 41, 1319 – 1330.
 74. Lysozyme: PDB Code 1EQ4; Takano, K.; Tsuchimori, K.; Yamagata, Y.; Yutani, K. *Biochemistry*, **2000**, 39, 12375-12387.
 75. (a) Smith, N.N.; Howard, A. J. Chorismate-pyruvate lyase: PDB Code 1XLR. (b) Holden, M. J.; Mayhew, M.P.; Gallagher, D.T.; Vilker, V.L. *Biochimica et Biophysica Acta* **2002**, 1594, 160-7. (c) Smith, N. N.; Howard, A. J.; Holden, M. J.; Mayhew, M.P.; Kaistha, S.B.; Gallagher, D.T. “Hydroxybenzoate Production: Structural and Dynamic Analysis of the Chorismate Lyase Mechanism”, **2004**. (d) Han, S.S; Kyeong, H.; Choi, J.M.; Sohn, Y.; Lee, J.; Kim, H. *ACS Catal.* **2016**, 6, 8440–5.
 76. (a) Shvo, Y.; Taylor, E. C.; Mislow, K.; Raban, M. *J. Am. Chem. Soc.* **1967**, 89, 4910-4917.

- (b) Petit, M.; Geib, S. J.; Curran, D. P. *Tetrahedron* **2004**, *60*, 7543-7552. (c) Alfonso, I.; Burguete, M. I.; Galindo, F.; Luis, S. V.; Vigara, L. *J. Org. Chem.* **2007**, *72*, 7947-7956.
77. (a) Theilacker, W.; Böhm, H. *Angew. Chem. Int. Ed.* **1967**, *6*, 251. (b) Mazzanti, A.; Lunazzi, L.; Minzoni, M.; Anderson, J.E. *J. Org. Chem.* **2006**, *71*, 5474-5481. (c) Kawano, N.; Okigawa, M.; Hasaka, N.; Kouno, I.; Kawahara, Y.; Fujita, Y. *J. Org. Chem.* **1981**, *46*, 389-392. (d) Hanford, W.E.; Adams, R. *Stereochemistry of Diphenyls.* **1935**, *57*, 1592-1595. (e) Meyer, W.L.; Meyer, R.B. *Communications to the Editor*, **1963**, *85*, 2170-2171. (f) Wolf, C.; Xu, H. *Tetrahedron Lett.*, **2007**, *48*, 6886-6889. (g) Schurig, V.; Glausch, A.; Fluck, M. *Tetrahedron: Asymmetry* **1995**, *6*, 2161-2164. (h) Ceccacci, F.; Mancini, G.; Mencarelli, P.; Villani, C. *Tetrahedron: Asymmetry*, **2003**, *14*, 3117-3122. (i) Grein, F. *J. Phys. Chem. A* **2002**, *106*, 3823-3827. (j) Hall, D.M.; Harris, M.M. *J. Chem. Soc.* **1960**, 490-494. (k) Casarini, D.; Lunazzi, L.; Mancinelli, M.; Mazzanti, A.; Rosini, C. *J. Org. Chem.* **2007**, *72*, 7667-7676.
78. Hollingsworth, S.A. and Karplus., P.A. *Biomol Concepts.* **2010**, *1*, 271-283.
79. (a) Arlene J. Hoogewerf et al. *Biochemistry*, **1997**, *36* (44), 13570-8; (b) Jensen, K. J.; Alsina, J.; Songster, M. F.; Vagner, J.; Albericio, F.; Barany, G. *J. Am. Chem. Soc.* **1998**, *120*, 5441-5452.
80. (a) Puglisi, E. V.; Puglisi, J. D.; Williamson, J. R.; RajBhandary, U. L., *Proc. Natl. Acad. Sci.* **1994**, *91*, 11467-11471; (b) Puglisi, J. D.; Tan, R.; Calnan, B. J.; Frankel, A. D.; Williamson, J. R., *Science* **1992**, *257*, 76-80; (c) Carlomagno, T.; Amata, I.; Williamson, J. R.; Hennig, M., *Biomol. NMR Assign.* **2008**, *2*, 167-169; (d) Schultheisz, H. L.; Szymczyna, B. R.; Williamson, J. R., *J. Am. Chem. Soc.* **2009**, *131* (40), 14571-14578.
81. (a) Lypson, A.B. Wilcox, C.S. *J. Org. Chem.*, **2017**, *82*, 898-909; (b) Lypson, A.B. "Synthesis of the Conformationally Controlled β -Turn Mimetic Molecular Torsion Balance Core Scaffold" M.S. Thesis, *University of Pittsburgh*, Pittsburgh, PA, **2018**; (c) Liberatore, M. A. "Synthesis and NMR Studies of a β -Turn Mimetic Molecular Torsion Balance." Ph.D. Dissertation, *University of Pittsburgh*, Pittsburgh, PA, **2012**.
82. Vutukuri, D. R.; Basu, S.; Thayumanavan, S. *J. Am. Chem. Soc.* **2004**, *126*, 15636-15637.
83. Baudoin, O.; Guenard, D.; Gue'ritte, F. *J. Org. Chem.* **2000**, *65*, 9268-9271.
84. Nacario, R.; Kotakonda, S.; Fouchard, D. M. D.; Tillekeratne, L. M. V.; Hudson, R. A. *Org. Lett.* **2005**, *7*, 471-474.
85. (a) Carpino, L.A.; Cohen, B.J.; Stephens Jr., K.E.; Sadat-Aalae, S.Y.; Tien, J-H.; Langridge, D.C. *J. Org. Chem.* **1986**, *51*, 3732-3734. (b) Carpino, L.A.; Chao, H.G.; Beyermann, M.; Bienert, M. *J. Org. Chem.* **1991**, *56*, 2635-2642. (c) Beyermann, M.; Bienert, M.; Niedrich, H.; Carpino, L.A.; Sadat-Aalae, D. *J. Org. Chem.* **1990**, *55*, 721-728.
86. Bo, Z.; Schafer, A.; Franke, P.; Schluter, A. D. *Org. Lett.* **2000**, *2*, 1645-1648.
87. Vutukuri, D.R.; Basu, S.; Thayumanavan, S. *J. Am. Chem. Soc.* **2004**, *126*, 15636-15637.
88. Barder, T.E.; Walker, S.D.; Martinelli, J.R.; Buchwald, S. L. *J. Am. Chem. Soc.* **2005**, *127*, 4685-4696.
89. (a) Ishiyama, T.; Murata, M.; Miyaura, N. *J. Org. Chem.* **1995**, *60*, 7508-7510. (b) CGI Pharmaceuticals, Inc. Kinase Inhibitors and Methods of Using and Identifying Kinase Inhibitors. Patent WO2008/33858, **2008**.
90. (a) Hashem, A.I.; Shaban, M.E.; El-Kafrawy, A.F. *J. Chem. Soc. Pak.* 1983, *5*, 19-21. (b) Bloomer, J.L.; Zheng, W. *Syn. Comm.* **1998**, *28*, 2087-2095. (c) Anbar, M.; Dostrovsky, I.; Samuel, D.; Yoffe, A.D. *J. Chem. Soc.* **1954**, *0*, 3603-3611.

91. (a) Fillion, E.; Fishlock, D. *J. Am. Chem. Soc.* **2005**, *127*, 13144–13145. (b) Denmark, S. E. *Tetrahedron* **2010**, *66*, 4745–59.
92. (a) Lee, K.S.; Kim, K.D.; *Bull. Korean Chem. Soc.* **2010**, 3842–3843; (b) Boovanahalli, S.K.; Kim, D.W.; Chi, D.Y. *J. Org. Chem.* **2004**, *69*, 3340–3344; (c) Hammond, G.S.; Wu, C.-H.S. *J. Am. Chem. Soc.* **1973**, *95*, 8215–8222.
93. (a) Kuehne, M.E.; Pitner, J.B. *J. Org. Chem.* **1989**, *54* (19), 4553–4569; (b) Ranu, B.C.; Bhar, S. *S. Org. Prep. Proced. Int.* **1996**, *28*, 371–409; (c) Kaboudin, B.; Abedi, Y. *Synthesis*. **2009**, *12*, 2025; (d) Morita, T.; Okamoto, Y.; Sakurai, H. *J. Chem. Soc., Chem. Comm.* **1978**, 874–875; (e) McOmie, J.F.W.; Watts, M.L.; West, D.E. *Tetrahedron* **1968**, *24*, 2289–2292.
94. (a) Kaiser, F.; Schmalz, H.-G. *Tetrahedron* **2003**, *59*, 7345–7355; (b) Ganieva, E.S.; Ganiev, I.M.; Grabovskii, S.A.; Kabal'nova, N.N. *Russ. Chem. Bull. (Int. Ed.)*, **2008**, *57*, 2332.
95. (a) Day, J.D.; McFadden, R.M.; Virgil, S.; Kolding, H.; Alleva, J.L.; Stolz, B. *Ang Chem. Int. Ed.* **2011**, *50*, 6814–6818; (b) Shiohara, H.; Nakamura, T.; Kikuchi, N.; Ozawa, T.; Nagano, R.; Matsuzawa, A.; Ohnota, H.; Miyamoto, T.; Ichikawa, K.; Hashizume, K. *Bioorg. Med. Chem.* **2012**, *20*, 3622–3634; (c) William, A.D. et al., *J. Med Chem.* **2012**, *55*, 169–196; (d) Simon, L.; Muniz, F.M.; Saez, S.; Raposo, C.; Sanz, F.; Moran, J.R.; *Hel. Chim. Acta.* **2005**, *88*, 1682–1701; (e) Li, Y. et al. *Bioorg. Med. Chem.* **2012**, *20*, 4582–4589. (f) Sharma, U.; Verma, P.K.; Kumar, N.; Kumar, V.; Bala, M.; Singh, B. *Chem. Eur. J.* **2011**, *17*, 5903–5907; (g) Gowda, D., Maheseh, B.; Shankare, G. *Ind. Sect. J. Chem.* **2001**, *40*, 75–77.
96. (a) Le Pera, A. Leggio, A.; Ligouri, A. *Tetrahedron* **2006**, *62*, 6100–6106; (b) Prechter, A.; Heinrich, M.R. *Synthesis* **2011**, *10*, 1515–1525.
97. (a) Di Gioia, M.L.; Leggio, A.; Le Pera, A.; Liguori, A.; Napoli, A.; Siciliano, C.; Sindona, G. *J. Org. Chem.* **2003**, *68*, 7416–7421; (b) De Marco, R.; Di Gioia, M.L.; Ligouri, A.; Perri, F.; Siciliano, C.; Spinella, M. *Tetrahedron* **2011**, *67*, 9708–9714.
98. Golding, B.T.; Bleasdale, C.; McGinnis, J.; Muller, S.; Rees, H.T.; Rees, N.H.; Farmer, P.B.; Watson, W.P. *Tetrahedron* **1997**, *53*, 4063–4082.
99. (a) Katritzky, A.R.; Akutagaw, K. *Org. Prep. Proc. Int.* **1989**, *21*, 340–341; (b) Katritzky, A.R.; Rachwal, S.; Rachwal, B. *J. Chem. Soc. Perkin Trans.* **1987**, *1*, 781–809; Katritzky, A.R.; Wu, J.; Wrobel, L.; Rachwal, S.; Steele, P.J. *Acta Chemica Scandinavica.* **1993**, *47*, 167–175.
100. (a) Moraczewski, A.L.; Banaszynski, L.A.; From, A.M.; White, C.E.; Smith, B.D. *J. Org. Chem.* **1998**, *63*, 7258–7262; (b) Deetz, M.J.; Forbes, C.C.; Jonas, M.; Malerich, J.P.; Smith, Yoshimura, T.; Tomohara, K.; Kawabata, T. *J. Am. Chem. Soc.* **2013**, *135*, 7102–7105.
101. (a) B.D.; Wiest, O. *J. Org. Chem.* **2002**, *67*, 3949–3952; (b) Smith, B.D.; G-Lashua, D.M.; D'Souza, C.J.E.; Norton, K.J.; Schmidt, L.M.; Tung, J.C. *Tetrahedron Lett.* **2004**, *45*, 2747–2749.
102. Jiang, W.; Wanner, J. Lee, R.J.; Bounaud, P.-Y.; Boger, D.L. *J. Am. Chem. Soc.* **2002**, *124*, 5288–5290.
103. (a) Merrifield, R. B., *J. Am. Chem. Soc.* **1963**, *85*, 2149–2154; (b) White, P.; Keyte, W.; Bailey, K.; Bloomberg, G., *J. Pept. Sci.* **2004**, *10*, 18–26.
104. (a) Collins, J.M., Porter, K.A., Singh, S.K. and Vanier, G.S. *Org. Lett.*, **2014**, *16*, 940–3; (b) Wang, S. S. *J. Am. Chem. Soc.*, **1973**, *95*, 1328; (c) Lu, G. et al., *J. Org. Chem.*, **1981**,

- 46, 3433. (d) Blanco, F. J.; Jimenez, M. A.; Pineda, A.; Rico, M.; Santoro, J.; Nieto, J. L. *Biochemistry*, **1994**, *33*, 6004.
105. Blanco, F. J. R., G.; Serrano, L. *Nature Structural & Molecular Biology* **1994**, *1*, 584.
106. (a) Bauer, M.C.; Xue, W-F.; Linse, S. *Int. J. Mol. Sci.* **2009**, *10*, 1552-1566; (b) Frick, I. M.; Wikström, M.; Forsén, S.; Drakenberg, T.; Gomi, H.; Sjöbring, U.; Björck, L. *Proc. Natl. Acad. Sci.* **1992**, *89*, 8532.
107. (a) Lorschach, B.A.; Kurth, M.J. *Chem. Rev.* **1999**, *99*, 1549–1581; (b) Colombel, V.; Presset, M.; Oehlich, D.; Rombouts, F.; Molander, G.A. *Org. Lett.* **2012**, *14*, 1680–1683. (c) Kiselyov, S., & Armstrong, R.W.; *Tetrahedron Lett.*, **1997**, *38*, 6163; (d) Wipf, P.; Cunningham, A. *Tet. Lett.* **1995**, *36*, 7819-7822; (e) Valverde, M. G.; Dallinger, D.; Kappe, C. O. *Synlett*, **2001**, *6*, 741-744; (f) Kappe, C. O. *Bioorg. Med. Chem. Lett.* **2000**, *10*, 49-51.
108. (a) Frericks Schmidt, H. L.; Sperling, L. J.; Gao, Y. G.; Wylie, B. J.; Boettcher, J. M.; Wilson, S. R.; Rinstral, C. M., *J. Phys. Chem. B.* **2007**, *111*, 14362-14369; (b) Gronenborn, A.; Filpula, D.; Essig, N.; Achari, A.; Whitlow, M.; Wingfield, P.; Clore, G., *Science*. **1991**, *253*, 657-661.
109. (a) Byeon, I.-J. L.; Louis, J. M.; Gronenborn, A. M., *J. Mol. Biol.* **2003**, *333*, 141-152; (b) Li, H.; Wang, H. C.; Cao, Y.; Sharma, D.; Wang, M., *J. Mol. Biol.* **2008**, *379*, 871-80; (c) Minor, D. L.; Kim, P. S., *Nature*. **1994**, *367*, 660-663; (d) Minor, D. L.; Kim, P. S., *Nature*, **1994**, *371*, 264-267; (e) Smith, C. K.; Withka, J. M.; Regan, L., *Biochemistry*, **1994**, *33*, 5510-5517; (f) King D.S., Fields, C.G., Fields, G.B., *Int. J. Pept. Protein Res.* **1990**, *36*, 255-26; (g) Albericio F, et al. *J.Org. Chem.* **1990**, *55*, 3730–3743; (h) Solé, N.A. and Barany G., *J. Org. Chem.* **1992**, *57*, 5399–5403.
110. Doan, N.-D.; Bourgault, S.; Létourneau, M.; Fournier, A. *J. Comb. Chem.* **2008**, *10*, 44–51.
111. V. Krchnák, et al., *Tetrahedron Lett.*, **1995**, *36*, 6193; (b) Wang, Y. and Wilson, S.R. *Tetrahedron Lett.*, **1997**, *38*, 4021; (c) Dahan, A. et al., *Macromolecules*, **2003**, *36*, 1034; (d) Hauske, J.R. et al., *Tetrahedron Lett.*, **1995**, *36*, 1589. (e) Giraud, M.; Cavalier, F.; Martinez, J. *J. Pept. Sci.* **1999**, *5*, 457–461; (e) Yraola, F.; Ventura, R.; Vendrell, M.; Colombo, A.; Fernandez, J.-C.; de la Figuera, N.; Fernandez-Forner, D.; Royo, M.; Forns, P.; Albericio, F. *QSAR Comb. Sci.* **2004**, *23*, 145–152; (f) Stanger, K. J.; Krchnack, V. *J. Comput. Chem.* **2006**, *8*, 652–654.
112. (a) Ngu, K. and Patel, D.V. *Tetrahedron Lett.* **1997**, *38*, 973-976; (b) Davies, S.G. et al., *Org. Biomol. Chem.*, **2008**, *6*, 1625–1634; (c) Lahiri, P.; Verma, H; Ravikumar, A.; Chatterjee, *J. Chem. Sci.* **2018**, *9*, 4600–4609; (d) Han, S-Y. and Kim, Y-A. *Tetrahedron* **2004**, *60*, 2447–2; (e) Cossu, F. *Biochem. Biophys. Res. Commun.* **2009**, *378*, 162-7. (f) Monfardini, I. et al., *J. Med. Chem.* **2011**, *54*, 890-900.